Thermal buckling of metal oil tanks subject to an adjacent fire

Ying Liu

Doctor of Philosophy

The University of Edinburgh – 2011

Declaration

This thesis entitled “Thermal buckling of metal oil tanks subject to an adjacent fire” is submitted to the College of Science and Engineering, The University of Edinburgh, for the degree of Doctor of Philosophy.

The work in this thesis was completed solely by Ying Liu, under the supervision of Dr. Jian-Fei Chen, Prof. J. Michael Rotter and Prof. Jose L. Torero. Where other sources were used, full references are given.

Publications based on this thesis:

Liu, Y., Chen, J.F., Rotter J.M. and Torero, J.L. (2010), “Buckling analysis of an oil tank exposed to heating from an adjacent tank fire”, *Proceedings (CD-ROM) of the 13th International Conference on Structural Faults + Repair*, 15-17 June 2010, Edinburgh, UK, 12pp.

Liu, Y., Chen, J.F., Rotter, J.M. and Torero, J.L. (2008). “Buckling of oil tanks under elevated temperature”, *Proceedings, 5th European Conference on Steel and Composite Structures (EUROSTEEL 2008)*, 3-5 September, Graz, Austria, pp1527-1532.

Ying LIU

July 2011

Abstract

Fire is one of the main hazards associated with storage tanks containing flammable liquids. These tanks are usually closely spaced and in large groups, so where a petroleum fire occurs, adjacent tanks are susceptible to damage leading to further development of the fire. The structural behaviour such as thermal stability and failure modes of the tanks under such fire scenario are very important to the safety design and assessment of oil depots. However, no previous studies on this problem are known to the best knowledge of the author.

This thesis presents a systematic exploration of the potential thermal and structural behaviours of an oil tank when one of its neighbour tanks is on fire. Under such scenario, the oil tanks are found to easily buckle under rather moderate temperature rises. The causes of such buckling failures are the reduced modulus of steel at elevated temperatures, coupled with thermally-induced stresses due to the restraint of thermal expansion. Since the temperatures reached in such structures can be several hundred Centigrade degrees, any restraint to thermal expansion can lead to the development of compressive stresses. The high susceptibility of thin shell structures to elastic buckling under low compressive stresses means that this type of failure can be easily provoked.

The main objectives of this thesis were to reveal the thermal distribution patterns developed in an oil tank under the heating from an adjacent tank fire, to understand the underlying mechanism responsible for the buckling of tank structure, and to explore the influences of various thermal and geometrical parameters on the buckling temperature of the tanks.

The study began with analytical solutions for stresses and deformations in a partially filled roofless cylindrical tank under an idealised axisymmetrical heating regime involving thermal discontinuity at the liquid level. The results demonstrate that large compressive circumferential membrane stresses occur near the bottom boundary for an empty tank and near the liquid level for a partially-filled tank. Heat transfer

analysis was conducted to explore the temperature distribution developed in the tank when the fire reaches a steady state. Parameters and assumptions used in the adopted pool fire model were carefully examined. The results show that a rather non-uniform distribution of temperature is developed in the tank especially around the tank circumference. A simple model was then proposed to describe the temperature distribution based on the numerical heat transfer analysis. The accuracy of the proposed temperature distribution model for predicting the structure behaviour was evaluated by comparing its predictions with those using directly the temperature distribution obtained from the numerical heat transfer analysis. Extensive geometric and material nonlinear analyses were carried out to capture the buckling behaviour of the tank using both the proposed temperature distribution and that from heat transfer analysis. It was found large vertical compressive membrane stresses are induced in the tank, causing buckling. The influence of fire diameter, location, liquid filling level and tank geometry were investigated.

Acknowledgements

The author is deeply grateful to her supervisors Dr. Jian-Fei Chen, Prof. J. Michael Rotter and Prof. Jose L. Torero for their tremendous guidance and encouragement during her research as well as their kindness and care for her life in Edinburgh.

Many thanks to Dr. Stephen Welch, Prof. Asif Usmani, Prof. Dougal Drysdale, Dr. Martin Gillie and Dr. J. Mark F. G. Holst for their valuable comments and suggestions during her study.

Thanks go to her colleagues in the Silos & Granular Solids Group and Fire Safety Engineering Group and her friends in Edinburgh, particularly Haiying, Jin, Kuan, Zhong, Guo, Yong and Yanan. Their care and love accompanied her through the difficult time and made her life more colourful and filled with joy.

The author would like to acknowledge the financial support from Dorothy Hodgkin Postgraduate Award (DHPA) which is jointly sponsored by Engineering and Physical Science Research Council (EPSRC) and Shell UK Ltd. Travel fund provided by BRE Centre for Fire Safety Engineering is also gratefully acknowledged.

Finally the author would like to thank her husband Jun and parents for their constant love and support throughout her study and life, also thank her daughter Meng-Yao who has made her life much more meaningful.

To my beloved family

Contents

Declaration i
Abstract ii
Acknowledgements iv
Contents vi
List of figures xi
List of tables xviii
1. Introduction 1
1.1 Motivation 1
1.1.1 The Buncefield oil storage depot incident 1
1.1.2 Major causes of oil tank failures in a large oil depot fire 3
1.1.3 Current research status and aim of this study 5
1.2 Methodologies 6
1.2.1 Analytical solutions 7
1.2.2 Heat transfer analysis 7
1.2.3 Proposition of empirical models 8
1.2.4 Thermal shell buckling analysis 8
1.3 Structure of this thesis 9
2. Literature review 12
2.1 Introduction 12
2.2 Storage tank accidents 13
2.3 Large pool fire and fire models 14
2.3.1 Large pool fires 14
2.3.2 Pool fire modelling 15
2.3.3 Solid flame models 17
2.4 Thermal buckling of thin shells 25
2.4.1 Buckling of shells 25
2.4.2 Shell buckling under mechanical loads 30
2.4.3 Classification of buckling analyses 32
2.4.4 Thermal buckling of thin shells 33
2.5 Design standards for liquid storage tanks 38
2.6 Finite element analysis package Abaqus 39
2.7 Conclusions 40
3. An analytical solution for a cylindrical tank under axisymmetric thermal loading 42
3.1 Introduction 42

3.2 Governing equations for a cylindrical shell under axisymmetric loading 44
3.2.1 General equations 44
3.2.2 Equations considering thermal effect and axisymmetric loading condition 49
3.2.3 General solution 53
3.3 Solution for a cylindrical shell with temperature variation along its height 55
3.4 Deformation in an example shell 59
3.4.1 An example problem 59
3.4.2 Validation of the analytical solutions 61
3.4.3 Behaviour of empty and half-filled tank 62
3.5 Parametric study 65
3.5.1 Effect of radius to wall thickness r/t ratio (r/t) 65
3.5.2 The effect of temperature rise ΔT 71
3.5.3 Deformation and stress envelops 75
3.6 Conclusions 79
4. A cylindrical tank under axisymmetric thermal loading with a transition zone near the liquid level 80
4.1 Introduction 80
4.2 Analytical solution 81
4.2.1 Shell bending equations considering thermal effect and axisymmetric loading condition 81
4.2.2 Solution for a cylindrical shell under axisymmetric loading and with a tri-linear temperature rise 83
4.2.3 Internal forces and deformations near the bottom boundary 91
4.3 Validation of analytical solutions against FE prediction 92
4.3.1 An example problem 92
4.3.2 Finite element model 93
4.3.3 Validation of the analytical solutions 93
4.4 The effect of transition zone size 100
4.5 Conclusions 104
5. Heat transfer modelling of a non-uniformly heated tank 105
5.1 Introduction 105
5.2 Pool fire model 106
5.2.1 Heat transfer governing equation 107
5.2.2 Flame geometry 108
5.2.3 Emissive power 110
5.2.4 Viewfactor 111
5.3 Heat exchange between storage tank and environment 111
5.3.1 Heat exchange mechanisms 111

5.3.2 Temperature of the burning liquid 112
5.3.3 Heat transfer coefficient of liquid 113
5.3.4 Emissivity of the target tank 115
5.3.5 Tank spacing 116
5.4 Test cases 117
5.4.1 1D model 118
5.4.2 2D model 120
5.4.3 3D Model 122
5.5 Temperature distribution in tanks 127
5.5.1 Model setup 127
5.5.2 Temperature distribution in the reference case 128
5.5.3 Sensitivity of input parameters in the fire model 134
5.5.4 Effect of liquid filling height 142
5.5.5 Effect of vertical fire location and flame height 145
5.5.6 Effect of horizontal fire location 151
5.5.7 Effect of fire diameter 155
5.6 Conclusions 160
6. Simple temperature distribution models for heated tanks 163
6.1 Introduction 163
6.2 Proposed simple mode of temperature distribution 164
6.3 Determination of parameters in the proposed model 172
6.4 Examination of the proposed temperature model in various fire scenarios 179
6.4.1 Fire diameter 179
6.4.2 Fire locations 181
6.4.3 Liquid level 183
6.5 A further simplified model 185
6.6 Conclusions 189
7. Buckling behaviour of a tank under a simplified temperature distribution 190
7.1 Introduction 190
7.2 Finite element modelling 191
7.2.1 An example problem 191
7.2.2 Thermal loading 192
7.3 Analysis procedure 195
7.3.1 Linear buckling analysis (LBA) 196
7.3.2 Geometrically non-linear elastic analysis (GNA) 204
7.3.3 Geometrically nonlinear analysis with materially nonlinear analysis (GMNA) 212
7.3.4 Geometrically nonlinear elastic analysis with imperfections (GNIA) 216

7.4 Parametric study ... 218
7.4.1 Effect of roof stiffness ... 218
7.4.2 Effect of temperature pattern around circumference ... 224
7.4.3 Effect of roof slope ... 226
7.4.4 Effect of heating range ... 228
7.4.5 Effect of liquid level ... 232
7.4.6 Effect of tank radius-to-thickness ratio ... 235
7.4.7 Effect of transition zone ... 236
7.5 Conclusions ... 237
8. Realistic post-buckling analysis of tanks ... 240
8.1 Introduction ... 240
8.2 Analysis procedure ... 241
8.2.1 Limitations of the Riks method ... 241
8.2.2 The Artificial Damping Method (Simulia 2008) ... 242
8.3 Predicting the thermal buckling behaviour ... 244
8.3.1 Model and thermal loading pattern ... 244
8.3.2 Examination of the predictions ... 245
8.3.3 Predictions of successive buckling behaviour ... 252
8.4 Selection of suitable numerical parameters ... 258
8.4.1 Initial value of dissipated energy fraction ... 258
8.4.2 Loading increment ... 260
8.5 Conclusions ... 261
9. Buckling behaviour of tank structures under various thermal and geometrical parameters ... 263
9.1 Introduction ... 263
9.2 Effect of material nonlinearity - GMNA vs. GNA ... 264
9.3 Effect of wall thickness – uniform vs. stepped thickness ... 267
9.4 Sensitivity study of heat transfer parameters ... 272
9.4.1 Flame height ... 273
9.4.2 Emissivity of the tank surface ... 275
9.4.3 Convective heat transfer coefficient of liquid h_{liq} ... 277
9.5 Buckling behaviours under various fire scenarios ... 278
9.5.1 Effect of vertical fire location ... 278
9.5.2 Effect of horizontal fire distance ... 283
9.5.3 Effect of fire diameter ... 286
9.6 Effect of filling level in target tank ... 290
9.7 Conclusions ... 293
10. Conclusions and future work ... 297

10.1 Introduction 297
10.2 Conclusions 298
10.2.1 Background knowledge and literature review 298
10.2.2 Analytical solution for a cylindrical tank under axisymmetric thermal loading 299
10.2.3 A cylindrical tank under axisymmetric thermal loading with a transition zone near the liquid level 300
10.2.4 Heat transfer modelling of a non-uniformly heated tank 301
10.2.5 Simple temperature distribution models for heated tanks 302
10.2.6 Buckling behaviour of a tank under a simplified temperature distribution 303
10.2.7 Realistic post-buckling analysis of tanks 304
10.2.8 Buckling behaviour of tank structures under various thermal and geometrical parameters 305
10.2.9 Summary 306
10.3 Future research 307
11. References 309
12. Appendix 319
12.1 Heat transfer analysis 319
12.2 Thermal buckling analysis (Riks) 321
12.3 Thermal buckling analysis (ADM) 325

List of figures

Figure 1-1 Buncefield oil depot fire incident, Dec. 2005 (Board 2010) 3
Figure 2-1 Pool fire models 16
Figure 2-2 Model flame shape for tank fire (Rew and Hulbert 1996) 20
Figure 2-3 Emissive power as a function of the pool diameter 23
Figure 2-4 Schematic of viewfactor calculation (Simulia 2008) 25
Figure 2-5 Load-deflection curves showing limit and bifurcation points (Arbocz 1987) 27
Figure 2-6 Three basic types of bifurcation (TWG8.4 Shells 2008) 28
Figure 2-7 Effects of imperfection on bifurcation behaviour of structural systems (TWG8.4 Shells 2008) 30
Figure 3-1 A cylindrical shell 44
Figure 3-2 Assumed linear temperature profile through the thickness of the shell 53
Figure 3-3 Load and temperature distribution in the shell and its deformed shape of the shell 56
Figure 3-4 An example cylindrical tank 60
Figure 3-5 Reduction of elastic modulus with temperature (EN1993 1-2 2007) 60
Figure 3-6 Case 1 (upper segment heated): radial displacement of tank wall 61
Figure 3-7 Case 1 (upper segment heated): circumferential membrane stress in tank wall 62
Figure 3-8 Radial deformation of empty and half-filled tanks 63
Figure 3-9 Circumferential membrane stresses in empty and half-filled tank walls 64
Figure 3-10 Meridional bending stresses in empty and half-filled tanks 64
Figure 3-11 Effect of r/t ratio on radial deformation 67
Figure 3-12 Effect of r/t ratio on circumferential membrane stress 70
Figure 3-13 Effect of temperature rise on radial deformation 72
Figure 3-14 Effect of temperature rise on circumferential membrane stress 74
Figure 3-15 Maximum radial displacement in the tank wall with different temperature difference in the half-full tank 75
Figure 3-16 Effect of temperature rise on the maximum meridional bending stress in the half-full tank 76
Figure 3-17 Effect of temperature rise on the maximum normalised membrane stress in the half-full tank 77
Figure 3-18 Maximum radial displacement in the empty and hall full tank (r/t=500) 78
Figure 3-19 Maximum radial displacement in the empty and hall full tank (r/t=500) 78
Figure 4-1 Sketch of load and temperature distribution in the shell and its deformed shape 84
Figure 4-2 Equilibrium of the shell 85
Figure 4-3 Verification: radial displacement 94
Figure 4-4 Verification: circumferential membrane stress 96

Figure 4-5 Verification: circumferential moment 97
Figure 4-6 Verification: meridional moment 98
Figure 4-7 Verification: shear force 99
Figure 4-8 Radial displacement in the tank wall with transition zone heights 100
Figure 4-9 Maximum radial displacement versus normalise transition zone length l/t 101
Figure 4-10 Circumferential membrane stress versus transition zone size l/t 102
Figure 4-11 Meridional moment in the tank wall with different l/t values 102
Figure 4-12 Shear force versus transition zone size l/t 103
Figure 4-13 Maximum circumferential membrane stress versus transition zone size l/t 103
Figure 5-1 Oil tank fire scenario 107
Figure 5-2 Cylindrical solid flame model 109
Figure 5-3 Variation of flame height with pool fire diameter 110
Figure 5-4 Convection in a tank 114
Figure 5-5 Conservation of energy for a plate 118
Figure 5-6 2-D FE model for calculating the view factor ($D=D_f$=20m, d=20m) 121
Figure 5-7 Temperature distribution on the outer surface of the tank ($D=D_f$=20m, d=20m) 122
Figure 5-8 3D heat transfer analysis model ($D=D_f$=20m, d=20m, H_{f0}=0m, H_f=100m) 123
Figure 5-9 Effect of vertical mesh size on the temperature along the most heated meridian ($D=D_f$=20m, d=20m, H_{f0}=0m, H_f=100m) 124
Figure 5-10 Effect of circumferential mesh size on the temperature distribution around the circumference at z=50m ($D=D_f$=20m, d=20m, H_{f0}=0m, H_f=100m) 124
Figure 5-11 Temperature distribution along the most heated meridian ($D=D_f$=20m, d=20m) 125
Figure 5-12 Temperature distribution around circumference at mid-height of the tank ($D=D_f$=20m, d=20m) 126
Figure 5-13 Highest temperature on the outer surface of the tank (°C); $D=D_f$=20m, d=20m 126
Figure 5-14 The numerical model in Abaqus for heat transfer analysis 127
Figure 5-15 A close-up look of the mesh pattern at the cylinder-to-roof joint 128
Figure 5-16 Temperature distribution in the target tank (°C) 129
Figure 5-17 Effect of flame height on temperature distribution along the meridian of θ=0° of an empty tank ($D=D_f$=20m, d=6.67m, H_{f0}=0m) 129
Figure 5-18 Temperature distribution around the circumference of an empty tank at different heights ($D=D_f$=20m, d=6.67m, H_{f0}=0m, H_f=20m) 130
Figure 5-19 Temperature distribution around the circumference of an empty tank at different heights ($D=D_f$=20m, d=6.67m, H_{f0}=0m, H_f=40m) 130
Figure 5-20 Temperature distribution on the conical roof at θ=0° ($D=D_f$=20m, d=6.67m, H_{f0}=0m) 131
Figure 5-21 Temperature distribution around the circumference at roof (h=21m, $D=D_f$=20m, d=6.67m, H_{f0}=0m) 131
Figure 5-22 Effect of wall thickness on the maximum temperature at tank surfaces ($D=D_f$=20m, d=6.67m, H_f=20m, H_{f0}=0m) 133

Figure 5-23 Effect of heat transfer coefficient of the liquid inside of the tank on the temperature distribution along the most heated meridian in a half filled tank (D=D_f=20m, d=6.67m, H_f=20m, H_{f0}=0m) 135

Figure 5-24 Effect of the heat transfer coefficient on the maximum temperature in an empty tank (D=D_f=20m, d=6.67m, H_f=20m, H_{f0}=0m) 136

Figure 5-25 Effect of external tank surface emissivity on temperature distribution around the circumference at z=10m (inner surface radiation neglected; D=D_f=20m, d=6.67m, H_f=20m, H_{f0}=0m) 137

Figure 5-26 Effect of external tank surface emissivity on temperature distribution along the meridian at θ=0° (inner surface radiation neglected; D=D_f=20m, d=6.67m, H_f=20m, H_{f0}=0m) 138

Figure 5-27 Effect of inner surface emissivity on the temperature distribution around the circumference (D=D_f=20m, d=6.67m, H_f=20m, H_{f0}=0m) 139

Figure 5-28 Effect of surface emissivity on the maximum wall temperature (D=D_f=20m, d=6.67m, H_f=20m, H_{f0}=0m)..... 140

Figure 5-29 Effect of fire emissive power on the predicted maximum temperature in the tank (D=D_f=20m, d=6.67m, H_f=20m, H_{f0}=0m) 141

Figure 5-30 Effect of thermal conductivity on the predicted maximum temperature in the tank (D=D_f=20m, d=6.67m, H_f=20m, H_{f0}=0m) 142

Figure 5-31 Temperature distribution along the most heated meridian in a partially filled tank (D=D_f=20m, d=6.67m, H_f=20m, H_{f0}=0m) 143

Figure 5-32 Temperature distribution near the liquid level along the most heated meridian (D=D_f=20m, d=6.67m, H_f=20m, H_{f0}=0m) 144

Figure 5-33 Temperature distribution near the roof along the most heated meridian (D=D_f=20m, d=6.67m, H_f=20m, H_{f0}=0m) 145

Figure 5-34 Temperature distribution at the most heated meridian of an empty tank: effects of vertical fire location and flame height (D=D_f=20m, d=6.67m) 147

Figure 5-35 Temperature distribution at the most heated meridian of a fully filled tank: effects of vertical fire location and flame height (D=D_f=20m, d=6.67m) 148

Figure 5-36 Temperature distribution around the circumference of an empty tank at h=2m: effect of vertical fire location (D=D_f=20m, d=6.67m, H_f=20m) 148

Figure 5-37 Temperature distribution around the circumference of an empty tank at h=10m: effect of vertical fire location (D=D_f=20m, d=6.67m, H_f=20m) 149

Figure 5-38 Temperature distribution around the circumference of an empty tank at h=18m: effect of vertical fire location (D=D_f=20m, d=6.67m, H_f=20m) 149

Figure 5-39 Temperature distribution in the diametric section through θ=0° on the conical roof (D=D_f=20m, d=6.67m) 150

Figure 5-40 Temperature distribution around the circumference at r=6.27m (h=21m) on the roof (D=D_f=20m, d=6.67m) 150

Figure 5-41 Effect of horizontal fire location on temperature distribution in an empty tank (D=D_f=20m, H_f=20m;H_{f0}=0m) 153

Figure 5-42 Effect of horizontal fire location on the temperature distribution of an empty tank (D=D_f=20m, H_f=40m, H_{f0}=0m) 154

Figure 5-43 Effect of fire-to-tank distance on the maximum temperature in an empty tank (D=D_f=20m, H_{f0}=0m) 155

Figure 5-44 Effect of fire diameter on temperature distribution of an empty tank (H_{f0}=0m, Case 1) 157

Figure 5-45 Effect of fire size on temperature distribution of an empty tank (H_{f0}=0m, Case 2)..... 159

Figure 5-46 Effect of fire size on the maximum temperature in the cylindrical tank wall (H_{f0}=0m) 160

Figure 6-1 A Simplified 2D model of tank-fire viewfactor..... 166

Figure 6-2 Quantities of the four terms in Eq.6-4 for the reference case (d=20/3m; H_f=20m, H_{f0}=0m) 168

Figure 6-3 Normalised viewfactor F (d=20/3m H_f=20m) 170

Figure 6-4 Comparison of predicted temperature distribution around the circumference and fitted temperature at different vertical locations (d=20/3m; H_f=20m; H_{f0}=0m) 174

Figure 6-5 Variation of fitted θ_0 along the vertical coordinate..... 175

Figure 6-6 Temperature distribution along the vertical coordinate: proposed expression vs. numerical heat transfer analysis (d=20/3m; H_f=20m; H_{f0}=0m) 176

Figure 6-7 Conservation of energy for a plate..... 177

Figure 6-8 Effect of material emissivity on the equivalent heat transfer coefficient - tank surface temperature 179

Figure 6-9 Effect of fire size on θ_0..... 180

Figure 6-10 Variation of θ_0 with the normalised fire size 181

Figure 6-11 Normalised temperature distribution along the vertical coordinate (d=6.67m; H_f=40m; H_{f0}=0m) 182

Figure 6-12 Normalised temperature distribution along the vertical coordinate (d=6.67m; H_f=20m; H_{f0}=10m) 182

Figure 6-13 Normalised temperature distribution along the vertical coordinate (d=15m; H_f=20m; H_{f0}=0m) 183

Figure 6-14 Normalised temperature distribution along the vertical coordinate (d=6.67m; H_f=20m; H_{f0}=0m) 185

Figure 6-15 Temperature distribution along the vertical coordinate: proposed further simplified model vs. heat transfer analysis (d=6.67m; H_f=20m; H_{f0}=0m)..... 188

Figure 6-16 Normalised temperature distribution along the vertical coordinate: further simplified model vs. heat transfer analysis (d=6.67m; H_f=20m) 188

Figure 7-1 Example tank..... 191

Figure 7-2 Reduction of elastic modulus with temperature (EN 1993-1-2, 2007)..... 191

Figure 7-3 Temperature distribution patterns..... 193

Figure 7-4 Temperature variation with vertical coordinate..... 194

Figure 7-5 Mesh scheme along vertical coordinate..... 197

Figure 7-6 Mesh convergence study for an empty tank under smooth-edge temperature distribution with a cool roof (t_f=2t_c). The dashed curves are 3rd order polynomial fittings of the data lines. 199

Figure 7-7 FE model of an empty tank in Abaqus 200

Figure 7-8 Bucking mode shape of an empty tank (Smooth-edge; cool roof; t_f=2t_c) 202

Figure 7-9 Bucking mode shape of an empty tank (Half-cosine; cool roof; t_f=2t_c)..... 203

Figure 7-10 Mesh scheme 1: uniform mesh around circumference with non-uniform mesh along meridian..... 205

Figure 7-11 Comparison of post-buckling modes between two mesh schemes 206

Figure 7-12 Temperature-radial displacement curves of the node at θ=0, h=2.5m 207

Figure 7-13 Buckling and post-buckling modes of an empty tank under smooth-edge pattern with hot roof (t_f=2t_c) 208

Figure 7-14 Axial membrane stresses down most heated meridian (smooth-edge: hot roof) 209

Figure 7-15 Axial membrane stresses around circumference at h=2m (smooth-edge: hot roof)..... 209

Figure 7-16 Circumferential membrane stress down most heated meridian (smooth-edge: hot roof) 210

Figure 7-17 Circumferential membrane stresses around circumference at h=2m (smooth-edge: hot roof) 210

Figure 7-18 Stress-strain relationship for steel at elevated temperatures with a yield stress of 300MPa at T=20°C 213

Figure 7-19 Effect of yield stress on the buckling temperature..... 213

Figure 7-20 The equivalent plastic strain contour in an empty tank from a GMNA analysis ($\sigma_y = 275$ MPa)..... 215

Figure 7-21 Effect of material nonlinearity on the prediction..... 216

Figure 7-22 Imperfection sensitivity of empty tank under smooth-edge temperature distribution with cool roof..... 217

Figure 7-23 Buckling and post-buckling modes in an empty tank under smooth-edge temperature distribution (deformation scale factor=20) 219

Figure 7-24 Axial membrane stress distribution of empty tanks with various roof stiffness 221

Figure 7-25 Buckling temperature rises in empty and half-filled tanks 223

Figure 7-26 Post-buckling mode of an empty tank under half-cosine temperature distribution pattern (cool roof)..... 225

Figure 7-27 Axial membrane stresses down most heated meridian (cool roof) 225

Figure 7-28 Axial membrane stresses around circumference at mid-height of tank (cool roof) 226

Figure 7-29 The effect of roof slope on the buckling temperature of an empty tank 227

Figure 7-30 The effect of roof slope on the buckling temperature of a half-filled tank 228

Figure 7-31 The effect of heating ranges on the buckling temperature..... 229

Figure 7-32 Effect of heating ranges θ_0 on axial membrane stress around circumference in an empty tank (stresses taken at the mid-height of the tank)..... 230

Figure 7-33 Post buckling modes in an empty tank with a slender roof (t_f=2t_c)..... 231

Figure 7-34 Post buckling modes in an empty tank with a very stiff roof (t_f=100t_c)..... 231

Figure 7-35 Post buckling modes in a half filled tank with a slender roof (t_f=2t_c)..... 231

Figure 7-36 Post buckling modes in a half filled tank with a very stiff roof (t_f=100t_c)..... 232

Figure 7-37 The effect of liquid surface level on the buckling temperature 233

Figure 7-38 Post buckling modes in a slender roof tank (t_f=2t_c) with different liquid surface levels 234

Figure 7-39 Post-buckling modes in a stiff roof tank (t_f=1000t_c) with different liquid surface levels 235

Figure 7-40 Buckling temperature of half-filled tanks with different aspect ratios (t_f/t_c=10) 236

Figure 7-41 Post-buckling modes of half filled tanks with different aspect ratios (r/t=1000) 236

Figure 7-42 Effect of transition length on the buckling temperature 237

Figure 8-1 Numerical model 245

Figure 8-2 Evolution of energy dissipation fraction (t_f=2t_c, cool roof) 246

Figure 8-3 Temperature vs. radial displacement curves of node at θ=0°, z=10m from Artificial Damping Method and Riks method (cool roof; t_f=2t_c) 248

Figure 8-4 Temperature rise - radial displacement curves of node at θ=0°, z=10m from Artificial Damping Method and Riks method (hot roof; t_f=2t_c) 249

Figure 8-5 Deformation of the tank at some critical stages (t_f=2t_c, cool roof, scale factor = 5) 251

Figure 8-6 Dissipated energy fraction history (t_f=2t_c) 253

Figure 8-7 Roof buckling followed by shell buckling of a thin roof tank (t_f=t_c, cool roof)..... 254

Figure 8-8 Temperature vs. radial displacement curves of node at θ=0°, z=10m (t_f=t_c, cool roof)... 257

Figure 8-9 Evolution of energy dissipation fraction with different input initial values (t_f=2t_c, cool roof) 260

Figure 8-10 Effect of step size on the buckling temperature prediction (t_f=2t_c, cool roof) 261

Figure 9-1 Effect of material nonlinearity on the tank buckling temperature 265

Figure 9-2 History of dissipated energy fractions of an GMNA analysis 266

Figure 9-3 The equivalent plastic strain contour at T=200°C from a GMNA analysis ($\sigma_y = 300$ MPa)..... 267

Figure 9-4 Stepped wall profile..... 268

Figure 9-5 History of dissipated energy fractions (uniform wall vs. stepped wall) 269

Figure 9-6 Temperature rise - displacement curve of the node at θ=0°, z=9m (uniform wall vs. stepped wall)..... 270

Figure 9-7 Deformations in an empty tank (uniform wall thickness vs. stepped wall thickness; deformation scale factor =5)..... 271

Figure 9-8 Comparison of tank deformation modes (Buncefield accident vs. numerical prediction) 272

Figure 9-9 Effect of flame height on the buckling temperature of an empty tank; D=D_f=20m, d=6.67m, H_{f0}=0m..... 273

Figure 9-10 Temperature distribution contours in an empty tank exposed to an adjacent tank fire arising from ground level; D=D_f=20m, d=6.67m, H_{f0}=0m 274

Figure 9-11 Axial membrane stress distribution around circumference at mid-height of the tank (T=100°C); D=D_f=20m, d=6.67m, H_{f0}=0m 275

Figure 9-12 Effect of surface emissivity on the buckling temperature (empty tank); D=D_f=20m, d=6.67m, H_f=20m, H_{f0}=0m..... 276

Figure 9-13 Steady state deformations in an empty tank with various values of surface emissivity (deformation scale factor =5); D=D_f=20m, d=6.67m, H_f=20m, H_{f0}=0m 277

Figure 9-14 The effect of heat transfer coefficient of the liquid inside of the tank on the buckling temperature; D=D_f=20m, d=6.67m, H_f=20m, H_{f0}=0m..... 278

Figure 9-15 Buckling temperature of an empty tank exposed to adjacent tank fire starting from various vertical locations (t_f=2t_c); D=D_f=20m, d=6.67m, H_f=20m 280

Figure 9-16 Temperature contour in an empty tank exposed to adjacent tank fire starting from roof level; D=D_f=20m, d=6.67m, H_f=20m 280

Figure 9-17 Steady state deformations in an empty tank under an adjacent fire starting from various vertical locations (t_f=2t_c); deformation scale =5; D=D_f=20m, d=6.67m, H_f=20m 281

Figure 9-18 Buckling temperature of an empty tank exposed to an adjacent fire starting from different vertical locations (t_f=t_c); D=D_f=20m, d=6.67m, H_f=20m..... 282

Figure 9-19 Steady state deformations of an empty tank under an adjacent fire starting from various vertical locations (t_f=t_c); deformation scale factor=5; D=D_f=20m, d=6.67m, H_f=20m..... 283

Figure 9-20 Buckling temperature of an empty tank under various tank-fire distances (t_f=2t_c); D=D_f=20m, H_f=20m, H_{f0}=0m 285

Figure 9-21 Steady state deformations of an empty tank under an adjacent fire; deformations are the same for various tank-fire distances; deformation scale factor =5; D=D_f=20m, d=6.67m, H_f=20m, H_{f0}=0m 285

Figure 9-22 Buckling temperature of an empty tank under various tank-fire distances (t_f=t_c); D=D_f=20m, H_f=20m, H_{f0}=0m 286

Figure 9-23 Buckling temperature of an empty tank under an adjacent fire with various fire diameters (t_f=2t_c); D=20m, d=6.67m, H_f=20m, H_{f0}=0m 287

Figure 9-24 Steady state deformations in an empty tank under fires with various diameters (t_f=2t_c); deformation scale factor =5; D=20m, d=6.67m, H_f=20m, H_{f0}=0m..... 288

Figure 9-25 Buckling temperature of an empty tank under an adjacent fire with various fire diameters (t_f=t_c): comparison of roof and wall buckling; D=20m, d=6.67m, H_f=20m, H_{f0}=0m..... 289

Figure 9-26 Steady state deformations of an empty tank under fire with various diameters (t_f=t_c); deformation scale factor =5; D=20m, d=6.67m, H_f=20m, H_{f0}=0m..... 289

Figure 9-27 Buckling temperature of a tank filled with various levels of liquid (t_f=2t_c); D=D_f=20m, d=6.67m, H_f=20m, H_{f0}=0m 290

Figure 9-28 Steady state deformations of a tank filled with various levels of liquid (flame height=20m; t_f=2t_c); deformation scale factor =5; D=D_f=20m, d=6.67m, H_f=20m, H_{f0}=0m.... 291

Figure 9-29 Buckling temperature of a tank filled with various levels of liquid (t_f=t_c); D=D_f=20m, d=6.67m, H_f=20m, H_{f0}=0m 292

Figure 9-30 Steady state deformations of a tank filled with various levels of liquid (t_f=t_c); deformation scale factor =5; D=D_f=20m, d=6.67m, H_f=20m, H_{f0}=0m 293

List of tables

Table 5-1 Heat transmission mechanisms in different parts of the system (thermal boundary conditions) 112

Table 5-2 Heat transfer coefficient change with liquid depth 115

Table 5-3 Minimum Tank Spacing (Shell-to-Shell) (NFPA 30 1996) 116

Table 5-4 Summary of parameters used in the reference case 117

Table 7-1 Buckling temperature in LBA (t_f=2t_c, °C) 201

Table 7-2 Comparisons of different mesh schemes for empty tank 206

Table 7-3 Buckling temperatures for different cases (t_f=2t_c) 224

Chapter 1

1. Introduction

1.1 Motivation

1.1.1 The Buncefield oil storage depot incident

Storage tanks in refineries and chemical plants contain large volumes of flammable and hazardous chemicals. A small accident may lead to serious property damage, business interruption, and loss of money and life. According to an investigation of 242 accidents (Chang and Lin 2006) related to storage tanks, fire and explosion account for 85% of the accidents. The event of a massive conflagration at the Buncefield Oil Storage Depot north of London on December 11, 2005, drew international attention to the serious risks associated with fires in petroleum storage tanks. This fire is the ever largest peacetime fire in Europe, in which 23 large oil storage tanks were destroyed (Board 2010).

(a) A global view of fire ground in the burning stage

(b) Damage of tanks during fire (with visible buckles in both roofs and walls of the tanks)

(c) Tanks with different extents of failure after the fire

Figure 1-1 Buncefield oil depot fire incident, Dec. 2005 (Board 2010)

A global view of the site during the burning stage is shown in Figure 1-1a, pictures of damage to tanks during and after the fire are shown in Figures 1-1b and c. This striking recent fire incident offers the direct motivation of this study.

1.1.2 Major causes of oil tank failures in a large oil depot fire

The main hazards associated with storage tanks containing flammable liquids are fire and explosion (Chang and Lin 2006). Fires or explosions are likely to occur when vapours or liquids are released into areas where there may be an ignition source, or when an ignition source is introduced into an area where there may be flammable atmospheres. The extent of the fire or explosion hazard, depends largely on the temperature of the liquid, how much of the surface area is exposed, how long it is exposed for, and the air movement over the surface.

From the structural safety point of view, explosion is without doubt the most dangerous hazard for the adjacent tanks, as the shockwave from explosions is easy to cause structural damage (Baker *et al.* 1982, Ruiz *et al.* 1989, Islam *et al.* 1992). Explosions are believed to be the major reason of the failure of tanks in Buncefield as in the Report (Board 2010). Another possibility of causing the tank failure could be heating from the fire, however this factor was somehow less mentioned in the Buncefield Report.

In the presence of a fire impinging on the tank shell, the metal undergoes a degradation of mechanical properties therefore causes structural weakening and eventual collapse. In other situations, where the fire is not spreading on the tank, the adjacent tank may still be in danger of failure. The hazards arising from such a situation are due to fire radiation. Radiation heats up the neighbouring tanks and results in a non-uniform temperature rise in the tank where the part facing the fire is hotter than the part opposite to it. This can lead to the buckling failure of tanks, because the modulus of the steel (or other metals) used for constructing the tank is reduced at elevated temperatures, coupled with thermally-induced stresses due to the restraint of thermal expansion. Since the temperatures reached in such structures can be several hundred degrees in Centigrade, any restraint to thermal expansion can lead to the development of large compressive stresses. The high susceptibility of thin shell structures to elastic buckling under very low stresses means that this type of failure is easily provoked. However, no previous studies on this problem are known to the best knowledge of the author.

Back to the Buncefield incident, although the pressure wave generated by explosions are believed to be the major cause of the tremendous damage to the outlying area and the huge fires involving 23 large oil fuel tanks (Johnson 2010, Board 2010), it is possible that thermal buckling was an important triggering event for the leakage or spill of the stored oil that occurred before the explosion. In fact, thermal buckling of the tank may actually induce or accelerate the following explosion thus contributed to the catastrophic failure. Indeed, it is difficult and even impossible to judge whether some of the failures in Fig. 1-1 were due to explosion or thermal buckling. The

buckling of the green tank in Fig. 1-1c was more likely caused by thermal buckling rather than explosion, as will be seen in this thesis. Therefore, a safety evaluation of the possibility of thermal buckling and its role in the possible tank failures is urgently needed.

1.1.3 Current research status and aim of this study

To date, thermal buckling of oil tanks under fire scenario is a poorly studied problem, relevant research is very rare. The current oil tank design codes (e.g. API 650 2007, NFPA 30 1996, EN1993 4-2 2007) have not provided any guidance for tanks under such fire scenarios either. The role of thermal loading in structural failure has been almost ignored in the past research or industrial tank design practices. This study stands as a complementary work to the past investigations of oil tank failures.

A basic approach to minimise the risk of storages under fire condition is to do a proper layout for the whole tank farm with safe separation distances. Various regulatory and professional bodies like American Petroleum Institute (API) and National Fire Protection Association (NFPA) have suggested standards on such issue. The tanks are arranged in groups by dike wall or bunds and separated from each other within one group. However, for economic reasons, the minimum spacing specified in the codes does not guarantee the safety of tanks from a fire. The researches on safe separation distance between two storage tanks in a tank farm from fire therefore emerge (Sengupta *et al.* 2010, Atallah and Allan 1971).

The safe separation distance is defined as that at which the thermal radiation flux is equal to a prescribed level. This level depends on what is required to conserve or protect (Atallah and Allan 1971). The critical heat flux of 4.732kW/m^2 is considered to be the safe inter-tank distances on the basis of that no material is expected to ignite (Crowl and Louvar 2002, Lees 1996, DiNenno 1995). This heat flux is equal to the energy radiated from a black body with a temperature of 260°C. In another research a critical temperature of 540°C is deemed to be a threshold for the safety of steel tanks (Beyler 2004b) in determining safe separations. However, would the steel

tank really be ’safe’ under these critical temperature? Although this defined temperature seems not very high to soften the steel tank, the most important issue here is not the reduction of strength of steel under the given temperature, but the stresses arisen from nonuniform temperature distribution in the steel tank which may easily lead to catastrophic failure even if the maximum temperature is much lower.

The aim of this study is to reveal and understand the behaviour of a steel oil tank when it is exposed to an adjacent fire, from a thermal buckling prospective view. The objectives include revealing the thermal distribution patterns developed in an oil tank under the heating from an adjacent tank fire, exploring the underlying mechanism responsible for the buckling of tank structure, and discovering the influences of various thermal and geometrical parameters on the buckling temperature of the tanks. A method which facilitates understanding of tank behaviour under fire environment will be performed to fill this gap in current knowledge.

1.2 Methodologies

The starting effort is put on the enhancement of the analytical solutions of stresses and deformations in a cylindrical shell under an axisymmetric heating regime involving thermal discontinuity at the liquid level. The thermal buckling behaviour of tanks is then studied by numerical simulations. First a solid flame model is chosen to represent the tank fire after due consideration, and the heat transfer analysis is conducted using Abaqus to determine the temperature distribution in the adjacent tank. The heat transfer analysis will be followed by an extensive nonlinear finite element analysis of tanks under such scenarios. The results from this study offers general understanding and provides useful information on how serious the temperature gradient developed in the tank under such fire heating may be for the thin-shell tank structure.

Being the first study on tank buckling under thermal loading, this study suffers some limitations, especially the lack of direct experimental measurement, and also some simplifications of both the fire model and tank model. However, results indicate

clearly that the fire loading is a major threat to the safety of adjacent tanks even if they are designed satisfying all the requirements of current design standards.

1.2.1 Analytical solutions

Analytical solutions for problems of any complexity in shell structures are typically very difficult mathematically. For this reason, the study began by developing an analytical solution for the simplest known problem, to see whether this might possibly be extended to more complex and realistic conditions. The simplest case, which does not appear to have been studied before, is the condition of axisymmetric heating of a circular partially-filled tank, which may be supposed to be caused by multiple other tanks on fire in the area around this tank. In addition, this study served the purpose of demonstrating the critically important role of partial filling in producing discontinuities in the shell response, and also showed that relatively small thermal changes could produce relatively large local stresses. However, it was quickly realised that an extension of this analytical treatment to the more complex conditions that occur in practical unsymmetrically heated tanks was not very feasible, so the study turned towards numerical solutions thereafter. Nevertheless, these analytical solutions remain the only known ones for conditions of this kind, and there may be applications for these solutions in problems unrelated to fire.

1.2.2 Heat transfer analysis

A structural heat transfer analysis by using a proper fire model is next employed to explore the temperature profiles in the tank.

Oil tank fires are large pool fires. Methods of estimating the thermal radiation from pool fires are available in many references. A semi-empirical solid flame model is chosen for the pool fire in the oil tank in this thesis. The flame is assumed to be a cylindrical blackbody and a homogeneous radiator with an average emissive power. This model provides a constant value of the radiation from the flame but does not give information of fire evolution with time. It is deemed suitable for the current study of exploring tank buckling behaviour under fire heating.

A steady state heat transfer analysis of a typical oil tank exposed to an adjacent fire is then performed using the commercial software Abaqus (Simulia 2008). Three heat transfer mechanisms - radiation, convection and conduction are all taken into consideration in the simulations.

1.2.3 Proposition of empirical models

Two temperature distribution models are then proposed to describe the temperature distribution developed in the tank obtained from the numerical heat transfer analysis. Algebraic expressions are extremely useful to structural researchers and designers who have no knowledge of heat transfer analysis but need to assess or design the structural behaviour. Based on the fact that some idealisations and assumptions that have been made in the solid flame model for heat transfer analysis, effort is put on seeking an expression which can capture the most important temperature distribution features, but without employing many curve fitting coefficients whose physical meanings are obscure. Eventually two models with only a very few parameters which all possess physical meanings such as the diameter of the fire, location of fire and liquid level inside of the target tank are proposed.

1.2.4 Thermal shell buckling analysis

Geometric and material nonlinear analyses are conducted in the finite element analysis (FEA) software Abaqus (Simulia 2008) to investigate the buckling failure modes of an oil tank under the fire heating regime and the influences of relevant parameters. A typical fixed roof oil tank with uniform wall thickness is chosen to be the representative example for investigation.

As the first attempt to analysing the buckling failure of the tank, the arc-length method (Riks subroutine in Abaqus) is employed, which is the conventional method used in shell buckling analysis (Teng and Lou 1997). In the simulations, the proposed temperature pattern is applied as the thermal loading. Although this method can accurately predict the buckling temperature, the temperature loading has to reduce once the structure passes the buckling point. While in reality, the post-

buckling procedure of the structure should be accompanied by either a constant or a continuously ascending temperature as usually the thermal loading due to fire may often develop a much higher temperature than the buckling temperature of a structure. To overcome this discrepancy, another nonlinear static analysis method incorporating an “artificial damping” is used to make the simulation able to continue after the first buckling occurs.

By using the artificial damping method, extensive geometric and material nonlinear analyses are carried out to simulate the tank behaviour using the temperature distribution obtained directly from the numerical heat transfer analysis. The influence of fire diameter, location, liquid filling level and tank geometry are investigated. The accuracy of the proposed temperature distribution model for predicting the structure behaviour is also evaluated by comparing its predictions with those using directly the temperature distribution obtained from the numerical heat transfer analysis.

1.3 Structure of this thesis

This thesis contains seven core chapters, plus three chapters on introduction, literature review and conclusions. If they are divided following the adopted methodologies, the core chapters may fall into three groups: derivation of analytical solutions, heat transfer analysis and nonlinear thermal shell buckling analysis. A brief description of the following chapters is given below.

Chapter 2 reviews the relevant background literature including the information of oil tank accidents, large pool fire models, thermal buckling of thin shells, design standards for liquid storage and the FEA package Abaqus.

Chapter 3 derives solutions of deformations and stresses for a cylindrical shell under an axisymmetrical heating regime involving abrupt temperature change at the liquid level. The analytical solutions are then validated using numerical predictions using the finite element method (FEM). A parametric study is performed using the analytical solution to investigate the effects of radius to thickness ratio and temperature gradient on the stresses and deflections in the tank wall.

Chapter 4 extends the solution of a cylindrical shell under axisymmetric thermal loading in Chapter 3 by taking account a temperature transition zone near the liquid level. The effect of the size of the temperature transition zone is studied and compared with solutions omitting the transition zone as in Chapter 3.

Chapter 5 presents a steady state heat transfer analysis of thermal distributions in a tank heated by an adjacent tank fire. The details of pool fire model adopted and thermal mechanisms considered in the simulations are introduced. This chapter also explores the temperature distribution in a typical steel cylindrical oil tank with conical roof under different fire scenarios such as fire size and locations. The effect of the filling level on the temperature distribution is also studied.

Chapter 6 deals with the generalisation of the numerical predictions of temperature distributions obtained in Chapter 5 with algebraic expressions. Two models are proposed: a rigorous model based on semi-analytical solution and a simple model simplified from it. They provide the form of thermal loading for structural analysis of tanks exposed to an adjacent fire.

Chapter 7 explores the buckling behaviour of a thin cylindrical tank with conical roof that is subjected to the simple temperature distribution model proposed in Chapter 6. The arc-length method is employed to trace the buckling behaviour. Linear bifurcation analysis (LBA), geometrically non-linear analysis (GNA), and geometrically and materially non-linear analysis (GMNA) are conducted. The effects of roof stiffness, temperature distribution around the circumference, roof slope, heating range, liquid level in the tank and tank radius-to-thickness ratio are investigated.

Chapter 8 presents the thermal buckling behaviour of oil tank predicted by using the artificial damping method. The buckling behaviour of the tank involving successive buckling events is successfully captured. The numerical mechanism of this procedure is introduced and two important input parameters which affect the accuracy of the results are discussed. The predictions using the artificial damping method are compared with those obtained using the Riks method.

Chapter 9 conducts a parametric numerical study on tank behaviour under various fire scenarios such as different fire diameters and locations. Both the temperature distribution predicted directly by numerical heat transfer analysis in Chapter 5 and the temperature distribution model proposed in Chapter 6 are adopted and their predictions are compared.

Chapter 10 presents the conclusions produced from the study and suggestions for future work on the topic.

Chapter 2

2. Literature review

2.1 Introduction

This chapter presents a review of current knowledge related to the research of this study.

Firstly, a review of storage tank incidents is presented in Section 2.2. Secondly, in Section 2.3, relevant studies on pool fire modelling are reviewed. The solid flame model which is adopted in this thesis to describe the burning tank fire is elaborately described. Thirdly, in Section 2.4 the knowledge of structural buckling of thin shell is briefly reviewed with an emphasis on the thermal buckling that is the key topic of the present research. Different buckling analysis procedures and modelling techniques including popular software are also briefly reviewed. Finally, current design standards and specifications for liquid storage tanks are reviewed in Section 2.5.

2.2 Storage tank accidents

Storage tanks in refineries and chemical plants contain large volumes of flammable and hazardous chemicals. A small accident may lead to serious property damage, business interruption, and loss of life and money. The event of a massive conflagration at the Buncefield Oil Storage Depot north of London on December 11, 2005, drew international attention to the serious risks associated with fires in petroleum storage tanks (Board 2010). Fire engulfed 23 tanks and was the ever largest peacetime fire in Europe, and caused massive disruption to the adjacent community, road usage, and air travel through restrictions on fuel supplies. The total economic cost was around £1 billion. It occurred due to the loss of primary containment by overfilling of a vessel resulting in the formation of large flammable vapour cloud that subsequently was ignited.

Buncefield was not a unique oil depot fire. A survey of 728 accidents occurred in process plants and in the transportation of hazardous material (Planas Cuchi *et al.* 1999) showed that 8% of accidents were caused during a filling or emptying operation, in which fire and explosion are the most frequent major accidents. Pool-fire and flash-fire are the most common types of fire accidents.

A review of 242 accidents of storage tanks that occurred in industrial facilities over last 40 years (Chang and Lin 2006) showed that 74% of accidents occurred in petroleum refineries, oil terminals or storage. Fire and explosion account for 85% of the accidents. There were 80 accidents (33%) caused by lightning and 72 (30%) caused by human errors including poor operations and maintenance. Most of these tank accidents would have been avoided if good engineering in design, construction, maintenance and operation has been practiced and safety management program has been implemented and executed. Davie *et al.* 1994) studied 73 case histories of incidents involving heated bitumen storage tanks and concluded that the majority of incidents was due to operations such as filling and discharging of tanks, including overfilling which can lead to lagging fires and exposure of heater tubes. It is proposed that regular cleaning of tanks would reduce the number of these incidents.

Ignited flammable substances, lightning and human errors are the top three causes among 139 oil tank fires in China (Li *et al.* 2004). Fewtrell and Hirst (1998) studied high-cost accidents that have occurred in the UK chemical and petrochemical section since 1974 and showed that the intense heat generated by fire posed a real threat of escalation to involve adjacent storage tanks. A review of the 100 largest property damage losses that have occurred in the hydrocarbon-chemical industries over the last 30 years (Property-Risk-Consulting 2003) showed that nearly all of the losses involved fires or explosions. The losses at terminals and distribution locations have been attributed to the overfilling of storage tanks and natural hazard related incidents. According to this report, total losses for these facility incidents are approximately $363m . These incidents demonstrate the potential dangers posed to workers, the public, and the environment when these storage tanks fail catastrophically.

2.3 Large pool fire and fire models

This section presents the basics of a large pool fire and fire models which will be used in the current thesis for tank fire modelling.

2.3.1 Large pool fires

There are several types of fire occurring in an oil tank farm, depending on the circumstances and conditions leading to the fire. For example, ignited releases can produce pool fires, jet flames, vapour cloud fires, or fireballs. Pool fires from storage tanks of hydrocarbons are the most common type of tank fires.

A pool fire is a type of buoyancy controlled turbulent diffusion flame which burns above a pool of vaporizing fuel, where the fuel vapour has negligible initial momentum. Radiation and convection are the main mechanisms for transferring heat from the fire to its surroundings. Thermal radiation is particularly the dominant mechanism of damage from such fires.

The main efforts being currently undertaken on pool fire research can be divided into experimental and modelling. Howell et al. (2001) presented a review of large-scale

experiments on pool fires. Pool fire models have been developed based on the observed flame shapes and measured thermal radiation levels. They are used to assess the consequence of pool fires over a range of weather conditions.

2.3.2 Pool fire modelling

The mathematical tools for predicting the consequences associated with pool fires can be divided into three classes: field models, semi-empirical models, and integral models.

Field models known as Computational Fluid Dynamics or CFD models are mathematically complex, embodied in large computer programs and require significant run times on large computer systems. They are often based on numerical solutions to the Navier-Stokes equations but also often require the use of some empirical data. The advantages of CFD models are that they can provide detailed information in modelling effects on objects engulfed in fire and are capable of modelling fires with irregular geometry. However, CFD models are not normally used for typical pool fire hazard assessments because they require significantly more efforts to apply but provide little or no benefits over the solid flame model when the goal is the prediction of heat flux at significant distances from the fire.

Semi-empirical models are currently the best models available for the prediction of heat fluxes to objects outside flames. They are usually designed to predict only those quantities of direct relevance to consequence assessments, such as radiative and convective heat fluxes, rather than to provide a detailed description of the fire itself. It characterizes the geometry and radiative characteristics of a pool fire using correlations derived from a wide range of experimental data. Due to their relative ease of use and mathematical simplicity, semi-empirical models are ideally suited for hazard assessment.

There are two types of semi-empirical models. The basic strategy for calculating the amount of radiation received from a flame by a target surface is the point source model (Figure 2-1 a). In this case the assumption is that the flame radiates either

from a single point or from a number of points along the central axis of the flame. The calculated energy is multiplied by a fraction that accounts for the fact that only part of the energy is emitted as thermal radiation. In some circumstances the point source model can be appropriate, but it has the disadvantage of not producing valid estimates for receptors close to the fire.

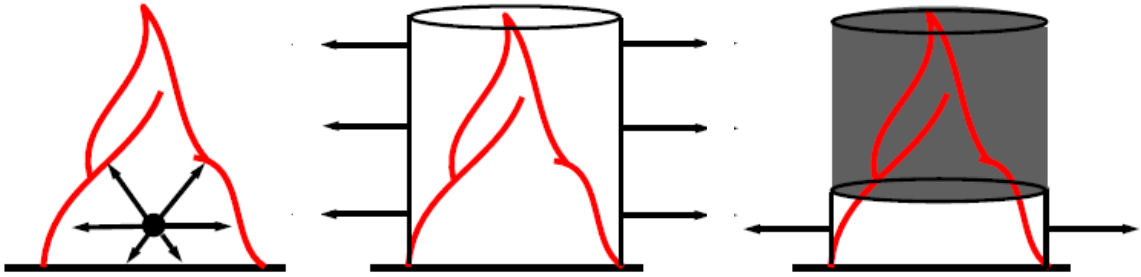

a) Point source model b) Solid flame model (one zone) c) Solid flame model (two-zones)

Figure 2-1 Pool fire models

Another possibility is to model the flame as a solid surface (Figure 2-1 b, c), which assumes that heat is radiated from the surface of a solid object (usually a cone or cylinder). In principle these models can produce accurate radiation predictions within a flame length away, but fluctuations in real flame behaviour render the use of models under near impingement conditions highly questionable.

The key parameters which affect the predictions from solid flame models are the flame shape, the model average surface emissive power, atmospheric absorption of radiation and the view factor calculation method. In solid flame model, the incident heat flux to the a target outside, q'', is given by the expression

$$q'' = \tau F E_f \tag{2-1}$$

where τ is the atmospheric transmissivity; F is the view factor between the flame and the receiver; E_f is the surface emissive power of the fire (kW/m^2).

The fire surface may be taken as a grey surface in Fig. 2-1b, c, and can be written as the net rate of radiation heat transfer from fire surface is

$$E_f = \varepsilon_f \sigma \left(T_f^4 - T_a^4 \right) \tag{2-2}$$

where ε_f is the emissivity of the fire; σ is the Stefan-Boltzmann constant (σ=5.67×10^{-8}W/m^2·K^4); T_f is the temperature of the fire; T_a is the temperature of the ambient air.

The third approaches of pool fire model are integral models, which represent a compromise between semi-empirical models and field models. The models that incorporate a more rigorous description of physics can be used over a wider range of circumstances than semi-empirical models. Integral models are formulated mathematically in a similar way as the field models. They solve the same equations but expressed in a simplified form in integral models, so the computing time of these models is far less than that of the field model. At present, there are no integral models of pool fires which could be used for the prediction of large-scale pool fire hazard consequences.

Available pool fire models for hazard assessment purposes are predominantly based on the solid flame model. Thus the solid flame model is chosen in this study. The details of solid flame modelling is discussed in the following section.

2.3.3 Solid flame models

Detailed descriptions of solid flame models are available in many references. Perhaps the best overall reference on the topic is Section 3 in Chapter 11 of The SFPE Hand Book of Fire Protection Engineering (DiNenno 1995). Others include TNO (Mercx and van den Berg 1997) and Rew (1996).

POOLFIRE6 (Rew and Hulbert 1996), sponsored by HSE has been validated against a wide range of test data and found to give good results for all fuel types except

methanol. Other pool fire models widely used include that of Mudan (1984) and the pool fire models contained in Shell's hazard consequence modelling package Shell FRED software (Shell FRED 4.0 April 2004), Det Norske Veritas (DNV) PHAST (DNV 2007) and NEPTUNE software packages which are used in offshore industry and the 'Yellow' Book (Mercx and van den Berg 1997) and associated software EFFECTS.

The differences of all the solid flame models lie mainly on the flame geometry, view factor and the value of the surface emissive power.

The fire descirbed in most analyses generally has an arbitrary shape with a perimeter length, *P*, and a height , H , with a total heat release rate (HRR), $\dot{Q}$. The radiated energy from the fire can be expressed as

$$\chi_r \dot{Q} = PH_f E_f \tag{2-3}$$

where χ_r is the radiative fraction representing the ratio of the rate of energy radiated to the surroundings to the total HRR of the fire. The value of χ_r is based on curve fit of experimental data involving a range of different combustible liquids and it is a function of both the fuel and pool diameter. The value of χ_r decreases with an increase of the fire diameter due to smoke obscuration (Beyler 2004a).

The total HRR of the fire, $\dot{Q}$, can also be expressed as the product of the heat release rate per unit area q_f'' and the area of the base of the fire *A*

$$\dot{Q} = q_f'' A \tag{2-4}$$

For a given fuel, the heat release rate per unit area q_f'' is relatively constant because the fuel mass burning rate per unit area is relatively constant (Walton 1993).

Flame geometry

The flame shape can be described by its diameter D_f, height H_f, its tilt and the stretching of its base in the direction of the wind (flame drag). Alternatively, the shape could be based on an idealized non-dimensional form derived from flame image analysis (Pritchard and Binding 1993). The most commonly adopted shapes are an upright circular cylinder, a sheared elliptical cylinder, or a tilted circular cylinder.

The upright circular cylindrical shape is the simplest and commonly adopted model for pool fire modelling (Fig. 2-4b) by researchers (e.g. McGrattan *et al.* 2000; Lehr and Simecek-Beatty 2004). The sheared elliptical shape (Johnson 1992) attempts to describe the real flame shape more accurately and accounts for the effects of wind on the fire. However, the disadvantage of this model is that the computation of the view factors between the target and the flame cannot be conducted analytically. An alternative tilted circular cylinder enables quick analytical evaluation of radiation in the downwind plane but it tends to under-predict radiation to lateral targets due to reduced flame surface area compared to the sheared model (Rew and Hulbert 1996). All the above flame shapes are based on observations of flame with its base at the ground.

For tank fire modelling, the upright cylinder is usually used to model fire without the presence of wind (Beyler 2004b). According to Rew et al. (1997), the sheared elliptical cylinder produces good predictions when compared with experimental observations, but the flame sag needs to be considered. The flame from a tank fire may spill over the edge of the tank and drop to a level below the top edge of the tank. This flame sag H_s is defined as the maximum vertical distance that the flame shape drops below the tank top (Figure 2-2).

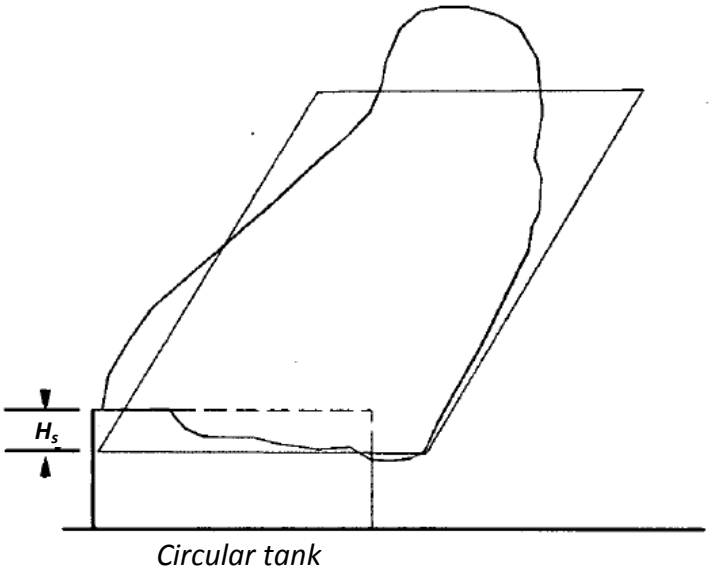

Figure 2-2 Model flame shape for tank fire (Rew and Hulbert 1996)

The flame height used for the model is usually the maximum visible flame height which is the distance from the base of the flame to the highest point at which puffs of bright flame occasionally emerge from the dark soot on the outside of the upper part of the flame. The visible flame height depends on the flame diameter and the type of fuel characterised by the burning rate.

Many different correlations have been proposed for the visible flame height. All the correlations are for a time-averaged flame shape, since the actual flame height fluctuates greatly with time. There are some discrepancies between them, partly due to the way in which the flame height is defined. For example, it can be defined as the maximum visible flame height, or the height of a given model flame shape which best fits the visible crosswind profile of the flame.

Two correlations widely used to determine the flame height (H_f) of pool fires are those of Thomas (1963) and Heskestad (1995). The flame height correlation derived by Thomas (1963) was based on the experimental data of laboratory-scale wood crib fires and dimensional analysis considerations. The mean visible flame height in the calm wind situation is given by:

$$H_f = 42D\left[\frac{\dot{m}''}{\left(\rho_0\sqrt{gD_f}\right)}\right]^{0.61} \tag{2-5}$$

where H_f is the average visible flame height (m); D_f is the equivalent fire diameter (m); $\dot{m}''$ is the burning rate per unit pool area (kg/m^{2}s); ρ_o is the density of the ambient air (kg/m^3) and g is the gravity acceleration. This correlation has been shown to predict reasonably well the flame height for pool fires ranging from 2.4 to 80m (Mudan 1984).

The correlation of Heskestad (1995) was based on data from a wide variety of sources including pool fires and buoyant jets. The simplified Heskestad correlation is given by

$$H_f = 0.23\dot{Q}^{2/5} - 1.02D_f \tag{2-6}$$

where H_f is the flame height (m) above the top of the fuel; D_f is the equivalent fire diameter (m); $\dot{Q}$ is the actual rate of heat release (kW), satisfying $7 < \dot{Q}^{2/5}/D_f < 700$ (kW$^{2/5}$/m) (Drysdale 1999).

The general equation for heat release rate of pool fire burning in a confined area or an open top tank with unlimited air access is given by

$$\dot{Q} = \dot{m}''\Delta H_c \chi_{chem} \pi D_f^{\,2}/4 \tag{2-7}$$

where ΔH_c is the heat of combustion of the volatiles (kJ/g) and χ_{chem} is the efficiency factor that takes into account incomplete combustion, and D_f is the pool fire diameter (m).

Zabetakis and Burgess (1961) describes the variation of mass burning rate $\dot{m}''$ with D_f for pool fire diameters greater than 0.2m as

$$\dot{m}'' = \dot{m}''_{\infty}\left(1 - e^{-k\beta D_f}\right) \tag{2-8}$$

where $\dot{m}''_{\infty}$ is the asymptotic burning rate for large pools, k is an extinction coefficient and β is a mean-beam-length corrector. Babrauskas (1983) proposed values of $\dot{m}''_{\infty}$ and $k\beta$ for deferent liquids.

Flame surface emissive power

Measurement of the emissive power of large fires is difficult and subject to considerable uncertainty.

Shokri and Beyler (1989) and Mudan (1984) use an emissive power averaged over the flame height of the fire (Figure 2-1b) by fitting experimental measurements of radiant heat flux from pool fires q''_f. Understandably, the value of emissive power estimated from these models is significantly less than what can be attained locally. The mean surface emissive power fall below 31.5 kW/m^2 for fires larger than 30m in diameter due to the increasing prominence of black smoke outside the flame that obscures the radiation from the luminous flame (Figure 2-3).

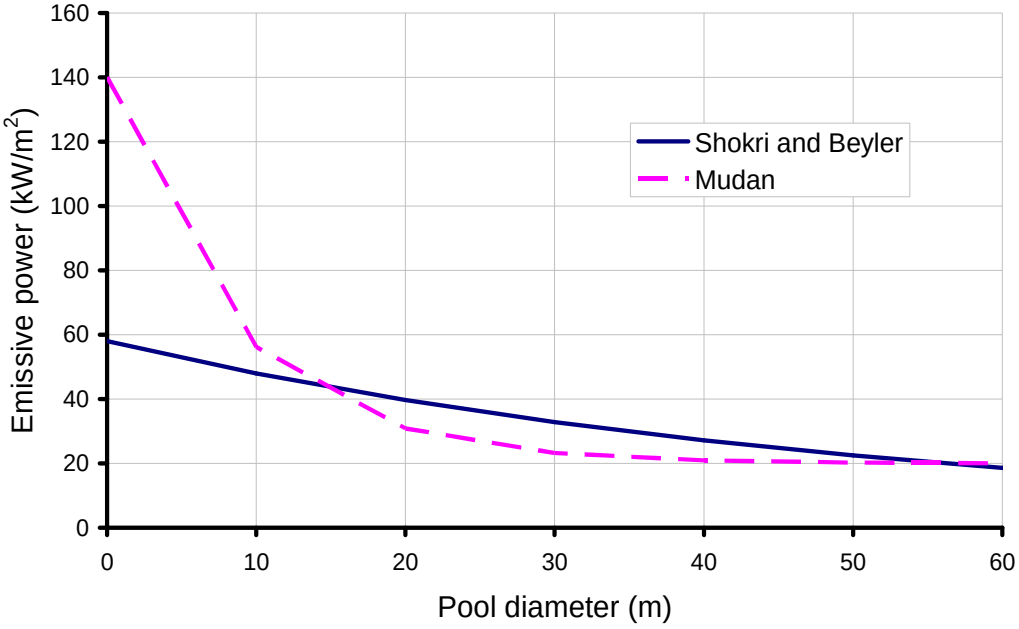

Figure 2-3 Emissive power as a function of the pool diameter

Another type of emissive power model is multiple layer model, in which different values of emissive power are assigned to different parts of the fire. A two layer model as shown in Figure 2-1c is the most widely used one. This assumption is based on the fact that most liquid hydrocarbon fuels burn with a sooty flame. Depending on the fuel and the size of the fire, up to 20% of the fuel mass is converted to smoke particulates in the combustion process (SFPE 1999). This smoke shields much of the luminous flame region from the viewer, and the shielding effect is most pronounced for fires that are tens or hundreds of meters in diameter because of the decreased efficiency of combustion at these scales (McGrattan *et al.* 2000). This two zone model thus usually uses a high emissive power for the luminous flame zone on the bottom and a low value for the smoky upper zone (Burgess and Hertzberg 1974; Beyler 1995; McGrattan *et al.* 2000; Engelhard 2005).

View factor

In the equation for radiative heat transfer (Eq. 2-1), the view factor parameter plays a significant role. The view factor is sometimes also known as the configuration factor, form factor or shape factor.

In a complex 'scene' there can be any number of different objects, which can be divided in turn into even more surfaces and surface segments. The view factor indicates the extent to which two objects can “see” each other.

The dimensionless view factor F_{ij} between two elementary areas, A_i and A_j, is the ratio of the amount of energy reaching the destination surface j to the total energy leaving the source surface i. It satisfies the following relation (Incropera *et al.* 1996)

$$F_{ij} = \frac{1}{A_i} \int_{A_i} \int_{A_j} \frac{\cos\phi_i \cos\phi_j}{\pi R_{ij}^2} dA_i dA_j \tag{2-9}$$

where R_{ij} is the distance between the two areas and ϕ_i, ϕ_j are the angles between R_{ij} and the normals to the surfaces of the areas (Figure 2-4). The view factor also satisfies the reciprocity relation

$$A_i F_{ij} = A_j F_{ji} \tag{2-10}$$

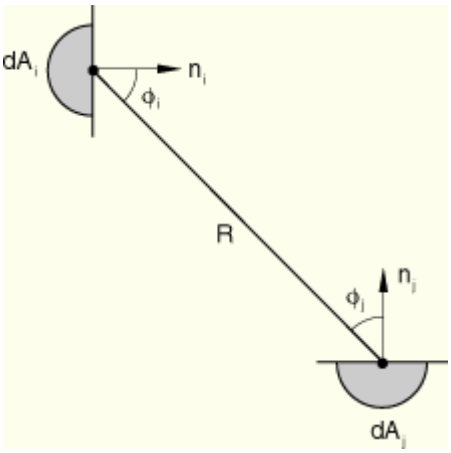

Figure 2-4 Schematic of viewfactor calculation (Simulia 2008)

For some simple geometries, the calculation of the view factor is straightforward and are available in many heat transfer textbooks (Siegel and Howell 2002, Incropera *et al.* 1996).

The solid flame model POOLFIRE6 (Rew and Hulbert 1996) uses the contour integral approach (Sparrow and Cess 1978) to calculate the view factor. The general-purpose finite element program Abaqus (Simulia 2008) adopts a technology originally developed by Johnson (1987) in view factor calculation. Shokri and Beyler (1989) and Mudan (1984) provided the expressions of maximum view factors at a point away from fire in their fire models respectively.

2.4 Thermal buckling of thin shells

2.4.1 Buckling of shells

Definition of buckling

Oil tanks are generally constructed of steel and have a large radius to thickness ratio. Usually the strength of this kind of thin shell structure is not controlled by the material strength but by the elastic or elastic-plastic stability instead. In thin shell structures, the membrane stiffness is much greater than the bending stiffness. A thin

cylindrical shell can store strain energy by membrane straining without deforming too much, while it must deform a lot in order to absorb an equivalent amount of bending strain energy. If the shell is loaded in such a way that most of its strain energy is stored in the form of membrane compression, and if there exists a disturbance making this stored membrane energy converted into bending energy, the shell may fail dramatically in a process called 'Buckling'(Bushnell 1981). The pre-buckling process is often nonlinear if there is a reasonably large percentage of bending energy being stored in the shell throughout the loading history.

Equilibrium paths and critical states

To predict buckling failure and obtain the critical load one can carry out an asymptotic analysis (Hutchinson and Koiter 1970, Tvergaard 1976, Hutchinson 1974) or a general nonlinear analysis. The asymptotic analyses rest on the theoretical foundation established by Koiter (1945). Its primary aims are to calculate the maximum loads for perfect and imperfect structures.

Two types of instability failure can be found through these two analyses. One is snap-through buckling where a structure collapses at the maximum point in a load vs. deflection curve. The state is called limit point. The change in the shape often occurs in a violent way. The other one is bifurcation buckling which occurs when the primary (or pre-buckling) equilibrium path intersects with a secondary equilibrium path (or post-buckling) causing a rapid change in the deformed shape of the structure.

Applying the asymptotic analysis to an axially compressed perfect shell (also applied for orthotropic shells e.g. Arbocz 1987), initially the buckling displacement W_b is zero until the bifurcation load λ_c at point B is reached (Figure 2-4a). Following bifurcation the initial failure of the perfect structure is characterized by a rapidly growing asymmetric deformation along the path BD with a decreasing axial load λ.

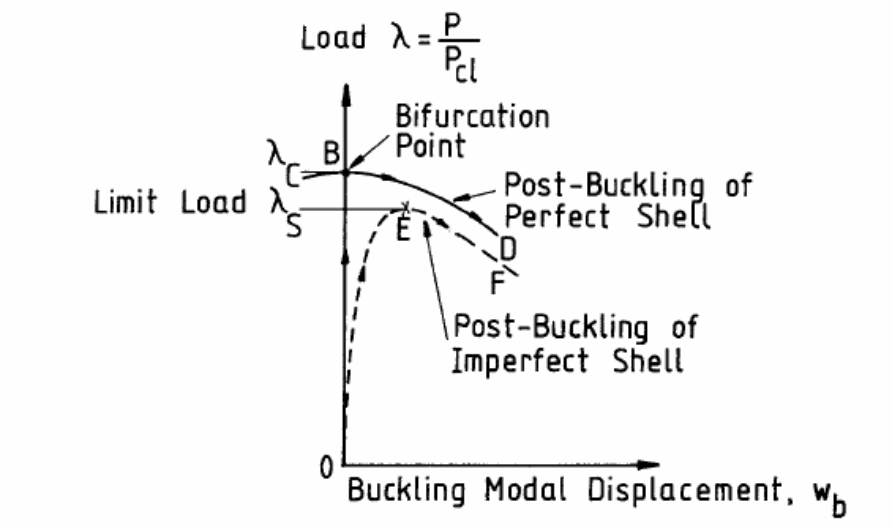

a) Asymptotic analysis

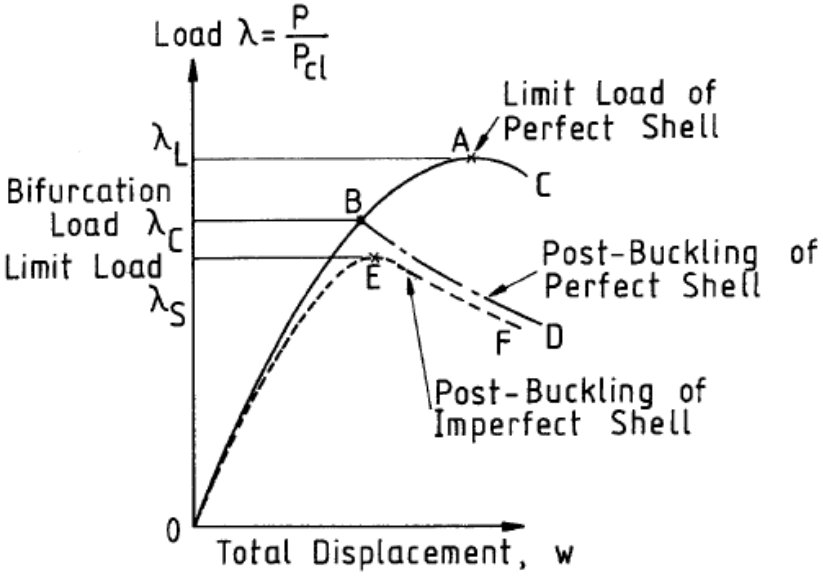

b) General nonlinear analysis

Figure 2-5 Load-deflection curves showing limit and bifurcation points (Arbocz 1987)

If the general nonlinear analysis is employed, the axially compressed perfect shell deforms axisymmetrically along the path OA (Figure 2-4b) until a maximum (or

limit) load λ_L is reached at point A. However, here a bifurcation point B lies between O and A. Once the bifurcation load λ_C is reached, the initial failure of the perfect structure is characterized by a rapidly growing nonaxisymmetric deformation along the path BD with a decreasing axial load λ. Thus, in this case, the collapse load of the perfect structure λ_L is of no engineering significance.

For real shells, which contain unavoidable initial imperfections, in both approaches the structural response follows a fundamental path OEF, with failure occurring as a "snap through" at point E at the limit (collapse) load λ_s. In this case there are no bifurcation points between O and E. However, considering Figures 2-5a and b, one can state that if there are no significant pre-buckling load redistributions then the bifurcation model often leads to a good approximation of the failure load and mode, especially in cases involving significant pre-bifurcation symmetries (Arbocz 1987).

Not all structures and mathematical models behave as Figure 2-5b. Koiter (1945) showed that the critical states of bifurcation may be of the following types (Figure 2-6):

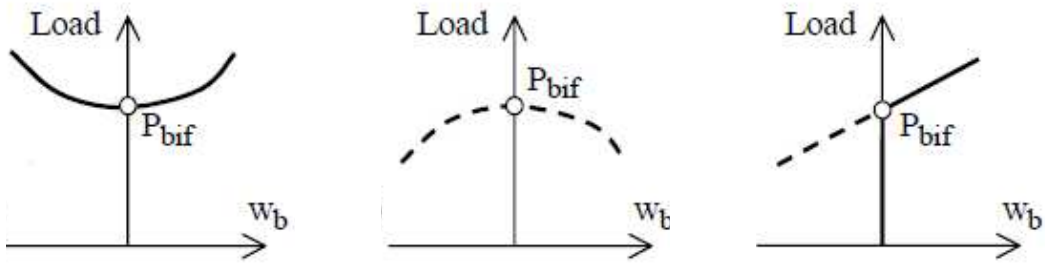

(a) Stable symmetric (b) Unstable symmetric (c) Asymmetric

Figure 2-6 Three basic types of bifurcation (TWG8.4 Shells 2008)

1) Stable symmetric bifurcation (Figure 2-6a): The post-buckling path has a horizontal tangent at the critical point (bifurcation load P_{bif}), and the path is stable, so that the structure can carry further load increments. This behaviour is often found in columns and plates.

2) Unstable symmetric bifurcation (Figure 2-6b): The post-buckling path has a horizontal tangent at the critical point, but the path is unstable, so that the structure cannot carry any further load increments. The behaviour is typically found in shells.

3) Asymmetric bifurcation (Figure 2-6c): The post-buckling path has a non-horizontal tangent at the critical point, and the path is stable on one side and unstable on the other, depending on the displacements, so that the structure can carry further load increments only on the stable branch. This behaviour is often found in frames.

There are also cases where more than one mode is associated to the same critical load, which is known as a coincident critical state. For example, cylindrical shells under axial load or spherical shells under uniform external pressure develop many coincident modes for the lowest critical state.

Effect of imperfections

All real structures have imperfections, which arise from geometry, loading, non-uniform boundary conditions, residual stresses, local thickness variations and other conditions. The most important and most studied effects are those due to geometric imperfections. The effect of these geometric imperfections on snap-through and bifurcation instabilities is illustrated in Figure 2-7, where ε represents the amplitude of imperfection.

In snap-through buckling (Figure 2-7a), the response of the imperfect structure is similar to that of the corresponding perfect structure, though the value of the limit load P_{lim} varies with the value of the imperfection parameter ε.

For bifurcation instability, imperfections may play a significant role in changing both the response of the system and the type of instability load. Structural systems that display asymmetric bifurcations have a maximum load on the unstable branch (Figure 2-7b). Structural systems that display stable symmetric bifurcations have a nonlinear path due to imperfections, and the bifurcation point can be passed (Figure 2-7c). System with unstable symmetric bifurcation in the perfect configuration, when

an imperfection is included has a nonlinear path with a maximum in the load, after which the path descends (Figure 2-7d).

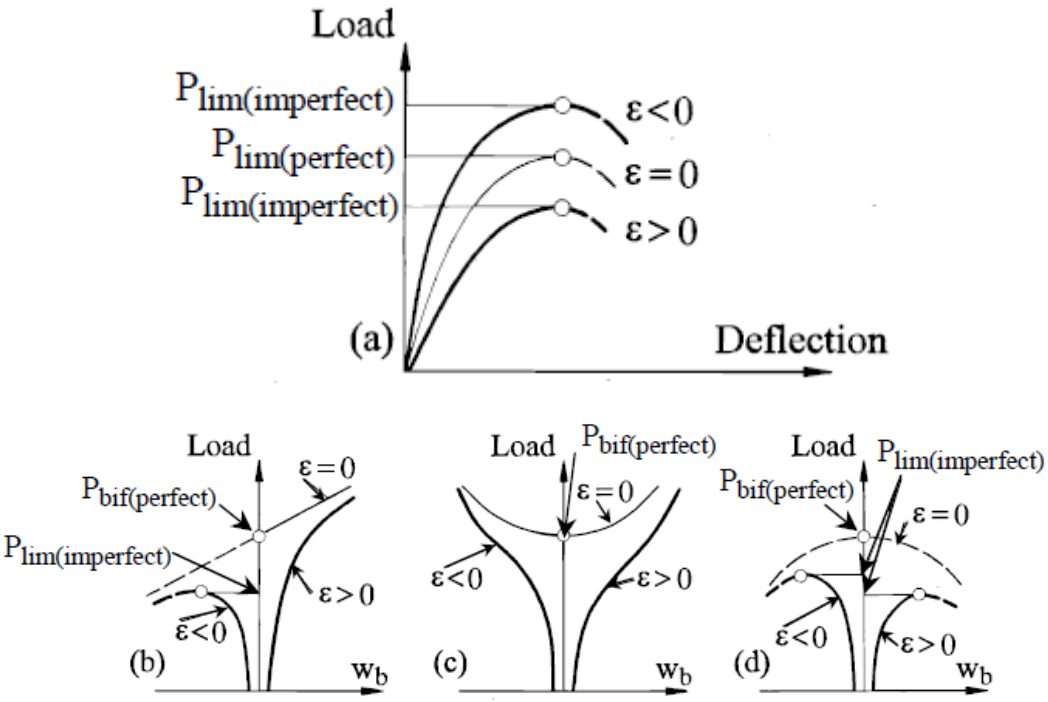

Figure 2-7 Effects of imperfection on bifurcation behaviour of structural systems (TWG8.4 Shells 2008)

2.4.2 Shell buckling under mechanical loads

The buckling of thin shells under mechanical loadings has been extensively studied since the early of the twentieth century. The first theoretical shell buckling problem was to solve the linear bifurcation stress for a cylinder under axial compression with simply supported ends and a uniform membrane pre-buckling stress distribution. The linear bifurcation stress is referred to as the 'classical elastic buckling stress' σ_{cr} (Timoshenko 1910, Lorenz 1908; Southwell 1914):

$$\sigma_{cr} = \frac{E}{\sqrt{3(1-\nu^2)}}\frac{t}{r} = 0.605\frac{t}{r} \tag{2-11}$$

in which ν is the Poisson's ratio; t is the thickness of the cylindrical wall; r is the radius of the cylinder; and E is the elastic modulus.

However, experimental values of buckling load are much lower than those calculated using the above equation (Robertson 1928,Wilson and Newmark 1933). Four causes are responsible for the discrepancy between the experimental and theoretical strengths (Teng and Rotter 2004): pre-buckling deformations and their contributions in changing the stress distribution, boundary conditions, eccentricities and non-uniformities in the applied load or support, and geometric imperfections and residual stresses.

The influence of pre-buckling deformations for a uniformly axially compressed shell is generally small ~15% (Yamaki and Kodama 1972). For shells under non-uniform loading, for example, under wind load (Brendel and Ramm 1980), the pre-buckling deformation does play an important role on predicting the critical buckling load.

The effect of boundary conditions on the buckling strength was discovered to have little influence on the buckling strength. Great sensitivity to boundary conditions occurs only when the shell ends are free to displace in the circumferential direction during buckling (Teng and Rotter 2004). Small eccentricities in line of action of the total load do not have a major influence on the buckling strength for axially compressed isotropic cylinders (Simitses et al. 1985) and eccentricities of the applied load relative to the middle surface of the shell at the boundary are usually avoided both in tests and in practice by detailing.

The effect of residual stresses can account for some of the discrepancies between experimental observations and theoretical predictions, but they do not play a major role (Rotter 1988; Holst *et al.* 1996; Rotter 1996; Holst *et al.* 2000).

The most important factor contributing to the discrepancy between the theory and experiment for axially compressed isotropic cylinders is now widely accepted to be the initial imperfections in the shell geometry (Teng and Rotter 2004). The imperfection sensitivity of shell buckling has been widely studied over the past half century, however, determining the most critical imperfection shape that leads to the

lowest collapse load of an axially compressed cylindrical shell is still an open research issue.

There are two types of common geometrical imperfections: fabric imperfection and stochastic imperfection. The former arises in the construction and fabrication and is measurable in practice (Teng and Rotter 1992; Ding *et al.* 1996; Rotter 1997; Holst *et al.* 2000). The latter is difficult to measure in reality but has been shown to be critical in some structures, though a most critical stochastic mode for a structure is never known (Rotter 2004). Usually the stochastic imperfection mode can be chosen as certain combination of eigenmodes from a linear buckling analysis and the critical mode is studied by trial and error (Simitses 1986; Teng and Song 2001; Greiner and Guggenberger 2004; Song et al. 2004).

2.4.3 Classification of buckling analyses

Different buckling analysis methods are classified depending on whether geometrical and material nonlinearities and geometrical imperfections are considered. Eurocode (EN1993 1-6 2007) and ECCS (TWG8.4 Shells 2008) provide detailed requirements for these shell buckling analysis.

Linear elastic shell analysis (LA) is based on the linear elastic material law and the linear small deflection theory. The assumed geometry remains that of the un-deformed structure. The classic shell membrane theory and linear bending theory is a LA analysis.

Linear eigenvalue analysis (LBA) is based on LA stress. It produces the buckling loads and buckling modes at various bifurcation points. The lowest buckling load and buckling mode usually provide a reference for all the following analyses.

Geometrically nonlinear elastic analysis (GNA) includes the effect of pre-buckling deformations using the large displacement theory. It can be used to identify the possible occurrence of snap-through buckling or a bifurcation in the load path. The material is assumed to be elastic and no imperfection is taken into account.

Materially nonlinear analysis (MNA) is a buckling analysis of a perfect shell with the assumption of small deflections. An MNA analysis gives the plastic limit load.

Geometrically and materially nonlinear analysis (GMNA) is a buckling analysis considering both geometrically nonlinear and material nonlinearity, but still without taking explicit account of geometric imperfections. The GMNA defines the strength of the perfect structure or the structures that are not imperfection sensitive.

Geometrically nonlinear elastic analysis with imperfections (GNIA) is an elastic buckling analysis of an imperfect shell with the assumption of large deflections. However, this analysis is difficult to perform because many different imperfection forms must be investigated.

Geometrically and materially nonlinear analysis with imperfections (GMNIA) is a fully nonlinear analysis which includes all the effects of geometric and material nonlinearity with explicit modelling of imperfections. Similar to GNIA, there exist difficulties for imperfection modelling.

2.4.4 Thermal buckling of thin shells

History

Research on thermal buckling of thin shells started in 1950s. At that time, the design of lightweight structures for high speed aircraft and missiles provided strong motivation for the first studies of thermal buckling. Due to aerodynamic heating, the thin cylindrical shells experience higher temperature than the heavier reinforcing frames. The hotter shell tends to expand radially more than the restraining frame, inducing compressive circumferential membrane stresses in the thin shell. The research includes experimental, analytical (for simple models) and computer codes based numerical studies. Good reviews of these early studies on thermal buckling of shells can be found in the paper of Ziegler and Rammenrstorfer (1989), Moulin et al. (1989), Keene and Hetnarski (1990) and Thornton (1993).

The analysis methods used in the research of thermal buckling of shell were reviewed by Moulin et al. (1989). Many of the studies have been analytical particularly through the 1950s and 1960s, but since 1970, many computer programs have been used in investigating thermal buckling behaviour based on finite element and finite difference methods. Between 1950s and 1970s, experiments on shell thermal buckling of shells were also conducted. Most of the experiments considered monocoque shells (Ross *et al.* 1965, Hill 1959), except the study of stiffened shells by Anderson and Card (1962).

The analytical methods that dominated in the work before 1970s were based on the asymptotic theories, where bifurcation load λ_C was given. These methods can provide certain practical predictions but was limited to certain mechanical configurations. The numerical methods that gradually got popular since 1970 include incremental methods such as finite element or finite difference methods and a special method used to develop BOSOR code by Bushnesll (1971a; 1971b; 1985). The code BOSOR is a finite difference computer code adapted to axisymmetrical structures. This code can also solve thermal stress and buckling under heating that varies in both the axial and the circumferential directions but this is based on linear theory.

Thermal buckling of cylindrical thin shells

As the interest of this thesis mainly lies in the thermal buckling behaviour of an oil tank which particularly has a form of cylindrical shell connected with possible end structure (e.g. roof), the researches on thermal buckling of shells of revolution, such as cylindrical shells are briefly reviewed. It is worth pointing out that Thornton (1993) has conducted a detailed review of the research on thermal buckling of plates and shells reported before 1990. The majority of the following review is a quotation of the key information from his review.

According to Thornton (1993), the initial work on thermal buckling of thin circular cylindrical shells was reported by Hoff (1957a) who has discussed various aspects of

thermal buckling such as the temperature dependent material properties, creep, and the effect of non-uniformity of temperature distribution.

The simply supported cylindrical shells under axisymmetric heating was investigated in a few studies (e.g., Hoff 1957b; Anderson 1962a; Johns 1962; Sunakawa 1962; Johns 1965) A conclusion from their work is that circumferential thermal stresses due to the uniform temperature rise are not likely to cause elastic buckling except when the radius to thickness ratio is very large.

At about the same time as the research on uniform circumference heating, research on cylindrical shells under non-uniform circumferential heating have also been conducted. For simply supported circular cylindrical shells that buckle due to the variation of axial membrane force, Abir and Nardo (1959) and Bijlaard and Gallagher (1960) concluded that the critical axial thermal stress occurs at the same value as the critical stress under uniform axial compression (Eq. 2-11), thus the critical buckling temperature for a fully restraint cylinder is

$$\Delta T_{cr} = \frac{1}{\left[3\left(1-\nu^2\right)\right]^{1/2}} \frac{t}{\alpha r} \tag{2-12}$$

Hoff *et al.* (1964) analytically studied the buckling of a thin cylinder heated along an narrow axial strip. They reached the same conclusion as above unless the heated strip is very small.

Hill (1959) and Ross *et al.* (1965) performed analytical and experimental studies of the thermal buckling of cylindrical shells heated along an axial strip. They tested a series of steel cylinders with fully-fixed end supports heated by infrared heat lamps. The heating ranging around shell circumference varied from 1.5% to 18%. They observed two types of failure for thin and thick cylinders. The thin cylindrical shells tended to have localised snap through buckling under narrow heated strip widths; and the localised buckling emerged simultaneously within the heated strip at several locations. The thick wall cylinders had a different yielding failure mode at the clamped ends.

A review of theoretical and experimental studies on thermal buckling of cylinders by Anderson (1962b) demonstrated the strong dependence of the buckling deformation on the exact boundary conditions. It was also shown very difficult to obtain analytical predictions for the thermal buckling stresses due to localised temperature distributions.

Hoff and Ross (1967) reported that the experimental critical buckling temperature was higher than the analytical solution. This trend obviously contradicts to that of the buckling problem under mechanical loading where experimental critical buckling loads are consistently found lower than the analytical prediction. This anomaly was explained by Ross *et al.* (1966) through further experiments. They found the pre-buckling behaviour of the cylinders is non-linear, so the axial compressive stress is somewhat relieved when the cylinder 'barrels out' during heating, thus a higher critical temperature can be reached than that is predicted by the linear buckling theory.

All the early solutions reviewed above were within the framework of small-deflection theory. The computer code based analysis appeared from the late 1960s and early 1970s. For example, Chang and Card (1970; 1971) developed programs using finite difference method for analysing axisymmetric thermal buckling problems. The program was validated by comparisons with the analytical solutions of Hoff (1957b), Sunakawa (1962) and Anderson (1962b). The problem of thermal buckling due to circumferential stresses raised by Hoff (1957b) was studied by Bushnell (1973) using program BOSOR. It was concluded that the prebuckling rotations need to be considered in the analysis and the elastic buckling does not occur for simply supported cylinders under uniform temperature (Chang and Card 1971; Bushnell 1973).

An experimental study was carried out by Belov (1978) on the stability of a cylindrical shell filled with liquid. Although he claimed the experiment data and calculations matched fairly, no details of the analysis and tests were given.

Experimental studies of buckling of cylinders under combined mechanical and thermal loads were reported in Frum and Baruch (1976) and Ari Gur (1979). Frum and Baruch (1976) studied the buckling of cylindrical shells heated along two opposite generators with fixed ends. They reached the conclusion that the radial displacement boundary condition has a significant effect on buckling results. Ari Gur *et al.* (1979) developed a temperature-torque interaction curve by conducting tests of cylindrical shells under combined axial preload, non-uniform heating and torque.

Eslami *et al.* (1996) conducted a significant number of theoretical studies on thermal buckling of shells using the modified Donnell equations. The temperature effects related to creep (Eslami and Shariyat 1997) and imperfections (Eslami and Javaheri 1999; Eslami and Shahsiah 2001) on thin cylindrical shells were also investigated. Johnson and Card (2009) conducted a buckling analysis of stiffened cylindrical shell subjected to a combination of mechanical and thermal loading using BOSOR4 computer program. This research extended the work of Chang and Card (1970) and further studied the effects of boundary conditions and eccentricity of longitudinal stiffeners on the buckling of cylindrical shells.

Above studies are about isotropic shells. In recently years, attention has been moved to anisotropic shells such as laminated composite cylindrical shells (Ma 1989; Thangaratnam *et al.* 1990; Eslami and Javaheri 1999; Shahsiah and Eslami 2003; Panda and Singh 2011) and functionally graded cylindrical shells (Shahsiah and Eslami 2003). These researches mostly aimed to develop theoretical stability solutions of simple shell geometry under assumed temperature change. As they are not closely related to the current thesis, details of these studies are not further reviewed.

It should be noted that the majority of previous thermal buckling research involves temperature distribution patterns that is very simple in form (e.g., linear variation or axisymmetrical) and is usually based on various assumptions. To the best knowledge of the author, there has been no specific research concerned with the thermal buckling under fire loading, where the large temperature gradient occurs both around circumference and along meridian of the cylindrical shell and the roof. Furthermore,

the structural geometries considered in the above papers are usually a simple cylindrical shell without any connected boundary structures (e.g., the end plate and stiffeners). The existence of a roof for a tank plays a significant role in thermal buckling behaviour of the tank. The roof offers certain amount of restraint to the shell, this restraint is especially important for the thermal stain induced stress distribution in the tank. Thus the thermal buckling behaviour of a roofed tank under fire heating is still waiting to be revealed.

2.5 Design standards for liquid storage tanks

Most of the liquid storage tanks were constructed from steel. There are numerous Standards covering a whole variety of subjects such as materials, site layout and tank spacing requirements, safety issues, etc which are necessary for tank designers and manufacturers. The current most widely used design and construction standards for ambient temperature tanks are as follows.

1) American standards

Flammable and Combustible Liquids Code NFPA 30 (1996), the National Fire Protection Association (NFPA)

Welded Steel Tanks for Oil Storage APl 650 (2007), the American Petroleum Institute (API).

2) British standards

BS EN 14015:2004 Specification for the design and manufacture of site built, vertical, cylindrical, flat-bottomed, above ground, welded, steel tanks for the storage of liquids at ambient temperature and above (BS EN14015:2004 2004).

3) European standards

EN 1993-1-6 Eurocode 3: Design of steel structures, Part 1-6: General rules - Strength and stability of shell structures (EN1993 1-6 2007).

EN 1993-1-2 Eurocode 3: Design of steel structures, Part 1-2: General rules - Structural fire design (EN1993 1-2 2007).

EN 1993-4-2 Eurocode 3- Design of steel structures, Part 4-2: Tanks (EN1993 4-2 2007).

prEN 14015-1: Specification for the Design and Manufacture of Site Built Vertical Cylindrical Flat-Bottomed Above Ground Welded Metallic Tanks for the Storage of Liquids at Ambient Temperature and Above - Part 1: Steel Tanks EN 14015, draft issued for public comment in 2000 (prEN 14015-1 2000).

4) Company Standards

Some of the major companies involved with the use of or the design and construction of storage tanks produced their own Standards such as the Shell standards, and some of these have become influential within the industry and have attained the status of unofficial Standards.

2.6 Finite element analysis package Abaqus

In the above reviewed buckling analysis, available analytical solutions can only deal with some buckling problems but they are limited to very simple geometries, loading patterns and boundary conditions. Moreover, the mathematics of closed-form algebraic solution of the governing equations is very un-manageable for slightly complex problems in terms of geometry, loading and boundary conditions. Numerical analyses such as the finite element method (FEM) and the finite difference method (FDM) have many advantages in handling shell buckling problems (Rotter 1998; Rotter 2002).

Abaqus is a general-purpose finite element program, and it delivers accurate, robust, high-performance solutions for nonlinear problems, large-scale linear dynamics applications, and routine design simulations (Simulia 2008). Abaqus provides implicit (Abaqus/Standard) and explicit (Abauqs/Explicit) methods.

Abaqus/Standard employs solution technology ideal for static and low-speed dynamic events and Abaqus/Explicit is particularly well-suited to simulate brief transient dynamic events.

Abaqus/Standard is popular in use for shell buckling research. The Modified Riks algorithm was powerful to deal with nonlinear problem such as shell snap-through problems, where the load and/or the displacement may decrease as the solution evolves.

Another feature of Abaqus is that the results at any point within an Abaqus/Standard run can be used as the starting conditions for continuation in Abaqus/Explicit. The researches on structural behaviour under fires always take advantage of this flexibility in which Abaqus/Standard was used to conduct a static analysis to calculate the stress state in the structure under mechanic load and Abaqus/Explicit was employed to investigate transient response of the preloaded structure under fire loading.

Abaqus also enables one to use the results of previous simulation directly in a subsequent analysis to capture the effects of prior history. This is especially useful for the fire related structure analysis, as the temperature pattern in the structure is obtained from a heat transfer analysis and a structural analysis is conducted afterwards.

Based on the above advantages, Abaqus is therefore chosen to conduct simulations in this thesis.

2.7 Conclusions

This chapter has provided the background knowledge of the research presented in this thesis. A brief review has been presented on oil tank accidents, pool fire modelling, thermal buckling of thin cylindrical shells and numerical buckling analysis.

Oil storage accidents were firstly reviewed which shows fire accounts for a large percentage of the accidents. How to protect the storage from collapsing in such circumstances is the concern of many researchers.

The adjacent fire is a kind of pool fire, thus knowledge on pool fire and available pool fire models were reviewed next. Emphasis is put on the solid flame model which will be adopted in the thesis to model the adjacent tank fire.

The research on thermal buckling of thin shells has been motivated by the design of lightweight structures for high speed aircrafts and missiles. There is no research till now on thermal buckling under fire loading. The only known study that addresses a similar problem is the classic study of Hoff of the buckling of a cylinder under stresses induced by heating on a single axial strip. Because the roof of the tank offers only a small restraint to thermal expansion, most of the restraint derives from the incompatibility of the thermal expansions in the hot and adjacent cool parts of the shell wall, leading to shear stresses between the two parts. As a result, the studies of thermal buckling in the literature cannot be directly applied to a fire-heated tank. To date, the structural response of an oil tank under an adjacent fire scenario is a poorly studied problem and relevant research is very rare.

Finally, the relevant codes and standards relevant to this research are summarised.

Chapter 3

3. An analytical solution for a cylindrical tank under axisymmetric thermal loading

3.1 Introduction

When a partially filled tank is heated by an adjacent tank fire, the section of the tank wall below the liquid surface remains cool, since the thermal inertia of the fluid is usually large enough to keep the wall cool for a rather long period. By contrast, the upper section of the tank wall is hot, since the air above the fluid does not cool the steel wall significantly. Consequently, a large temperature gradient occurs in the wall at the liquid surface level, which results in an abrupt change of thermal stresses and deflections, leading to potential structural damage by yielding and buckling. An evaluation of these stresses is necessary for the prediction and control of the structural failure in such a situation.

This chapter presents an analytical solution for the stresses in a partially filled cylindrical tank under axisymmetrical heating with thermal discontinuity at the liquid

level. In a more general fire situation, there also exists a circumferential temperature gradient around the tank. However, such a more complex situation is not considered in this chapter that mainly deals with the development of an analytical solution. Instead, those more complex thermal patterns will be studied using comprehensive finite element calculations in the following chapters.

The material properties of the steel tank are temperature dependent. In particular, the elastic modulus of steel reduces rapidly with an increase of temperature. Therefore, earlier calculations of the cylindrical shell problem adopting constant elastic modulus (Fluegge 1973) are not valid for the current scenario and may lead to non-conservative predictions. Apart from the temperature dependent steel elastic modulus, this study also considers the temperature gradient across the shell thickness which has been neglected in previous studies (e.g. Fluegge 1973).

This chapter firstly conducts a linear elastic analysis (LA) of cylindrical shells using the classical theory of shells. The analytical solutions for a cylindrical shell under internal pressure, axial force and axisymmetric thermal discontinuities are obtained. The analytical solutions are then validated by comparing with the finite element (FE) predictions obtained using a reliable commercial FEM package Abaqus (Simulia 2008). In the numerical examples, two storing conditions of the tank are investigated: a partially filled tank and an empty tank. The former represents the situation where an abrupt temperature discontinuity occurs in the tank wall at the liquid level, while the latter represents the scenario where the temperature rise is uniform along whole tank height. Finally, a parametric study is performed using the analytical solution to investigate the effects of radius to thickness ratio and temperature gradient on the stress and deflection in the tank wall.

3.2 Governing equations for a cylindrical shell under axisymmetric loading

3.2.1 General equations

Consider a cylindrical shell of mean radius r in a cylindrical coordinate system (x, θ, z), as shown in Figure 3-1a, where x is axial direction, θ is circumferential direction and z is the normal coordinate with origin at the middle surface of the shell.

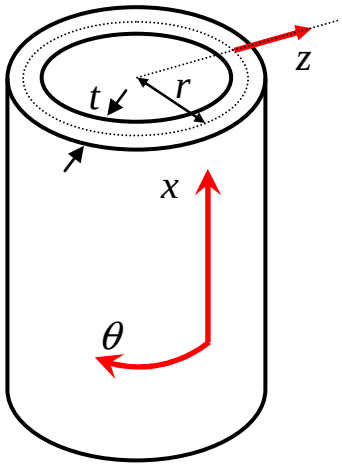

a) Coordination system

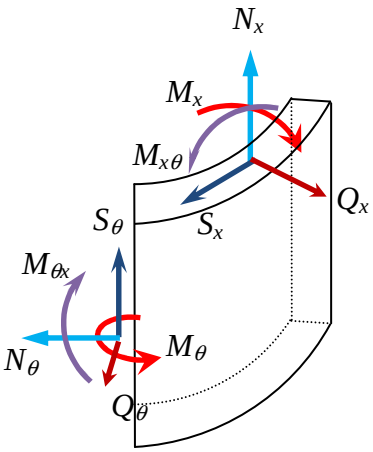

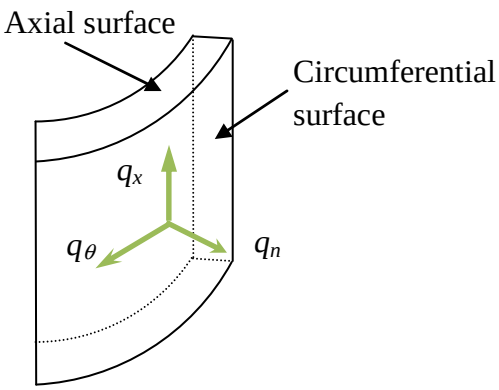

b) Stress resultants on a shell element c) External forces on a shell element

Figure 3-1 A cylindrical shell

According to the classical shell theory (e.g. Timoshenko and Woinowsky-Krieger 1959; Gould 1999) , the strains at the middle surface of the cylindrical shell (Figure 3-1a) are given by

$$\begin{Bmatrix} \varepsilon_x^0 \\ \varepsilon_\theta^0 \\ \gamma_{x\theta}^0 \end{Bmatrix} = \begin{Bmatrix} \dfrac{\partial u}{\partial x} \\ \dfrac{1}{r}\left(\dfrac{\partial v}{\partial \theta} + w\right) \\ \dfrac{1}{r}\dfrac{\partial u}{\partial \theta} + \dfrac{\partial v}{\partial x} \end{Bmatrix} \tag{3-1a}$$

where ε_x^0 and ε_θ^0 are the strains in axial and circumferential directions respectively; $\gamma_{x\theta}^0$ is the in-plane shear strain; *u*, *v* and *w* are displacements in axial, circumferential and radial directions respectively. The induced change of curvatures at the middle surface of the cylindrical shell are given by

$$\begin{Bmatrix} \kappa_x \\ \kappa_\theta \\ \chi_{x\theta} \end{Bmatrix} = \begin{Bmatrix} -\dfrac{\partial^2 w}{\partial x^2} \\ -\dfrac{1}{r^2}\dfrac{\partial^2 w}{\partial \theta^2} \\ -\dfrac{1}{r}\dfrac{\partial^2 w}{\partial x \partial \theta} \end{Bmatrix} \tag{3-1b}$$

where κ_x and κ_θ are curvatures in axial and circumferential directions respectively; $\chi_{x\theta}$ is the torsional curvature. The strains in a surface at a distance *z* from the middle surface of the shell along the normal direction are given by

$$\begin{Bmatrix} \varepsilon_x \\ \varepsilon_\theta \\ \gamma_{x\theta} \end{Bmatrix} = \begin{Bmatrix} \varepsilon_x^0 + \kappa_x z \\ \varepsilon_\theta^0 + \kappa_\theta z \\ \gamma_{x\theta}^0 + 2\chi_{x\theta} z \end{Bmatrix} \tag{3-2}$$

where ε_x^z and ε_θ^z are strains in axial and circumferential directions respectively; $\gamma_{x\theta}$ is the in-plane shear strain.

Under mechanical loading, the stresses at a distance *z* along the normal direction from the middle surface of the shell are

$$\begin{Bmatrix} \sigma_x \\ \sigma_\theta \\ \tau_{x\theta} \end{Bmatrix} = \begin{Bmatrix} \dfrac{E}{1-\nu^2}\left(\varepsilon_x + \nu\varepsilon_\theta\right) \\ \dfrac{E}{1-\nu^2}\left(\varepsilon_\theta + \nu\varepsilon_x\right) \\ \dfrac{E}{2(1+\nu)}\gamma_{x\theta} \end{Bmatrix} \tag{3-3}$$

in which σ_x and σ_θ are the axial and circumferential stresses respectively; $\tau_{x\theta}$ is the shear stress; *E* is the elastic modulus and ν is Poisson's ratio.

Substituting Eq. 3-2 into 3-3 gives

$$\begin{Bmatrix} \sigma_x \\ \sigma_\theta \\ \tau_{x\theta} \end{Bmatrix} = \begin{Bmatrix} \dfrac{E}{1-\nu^2}\left[\varepsilon_x^0 + \kappa_x z + \nu\left(\varepsilon_\theta^0 + \kappa_\theta z\right)\right] \\ \dfrac{E}{1-\nu^2}\left[\varepsilon_\theta^0 + \kappa_\theta z + \nu\left(\varepsilon_x^0 + \kappa_x z\right)\right] \\ \dfrac{E}{2(1+\nu)}\left(\gamma_{x\theta}^0 + 2\chi_{x\theta} z\right) \end{Bmatrix} \tag{3-4}$$

The membrane stress resultants, bending moments, shear forces and twisting moments per unit width of the shell as denoted in Figure 3-1b are given respectively by

$$\begin{Bmatrix} N_x \\ N_\theta \\ M_x \\ M_\theta \\ S_x \\ S_\theta \\ M_{x\theta} \\ M_{\theta x} \end{Bmatrix} = \int_{-t/2}^{t/2} \begin{Bmatrix} \sigma_x\left(1+\frac{z}{r}\right) \\ \sigma_\theta \\ \sigma_x\left(1+\frac{z}{r}\right)z \\ \sigma_\theta z \\ \tau_{x\theta}\left(1+\frac{z}{r}\right) \\ \tau_{x\theta} \\ \tau_{x\theta}\left(1+\frac{z}{r}\right)z \\ \tau_{x\theta} z \end{Bmatrix} dz \tag{3-5a}$$

where N_x and N_θ are stress resultants in the axial, circumferential directions respectively; M_x and M_θ are the meridional moment and circumferential moment respectively; S_x and S_θ are in plane shear forces in the axial, circumferential directions per unit width of the shell respectively; $M_{x\theta}$ and $M_{\theta x}$ are twisting moments on axial and circumferential surfaces respectively; t is the thickness of the cylindrical shell wall (Figure 3-1a).

For thin shell structures where $z/r<<1$, $1+\frac{z}{r} \approx 1$ and Eq. 3-5a reduces to

$$\begin{Bmatrix} N_x \\ N_\theta \\ M_x \\ M_\theta \\ S_x \\ S_\theta \\ M_{x\theta} \\ M_{\theta x} \end{Bmatrix} = \int_{-t/2}^{t/2} \begin{Bmatrix} \sigma_x \\ \sigma_\theta \\ \sigma_x z \\ \sigma_\theta z \\ \tau_{x\theta} \\ \tau_{x\theta} \\ \tau_{x\theta} z \\ \tau_{x\theta} z \end{Bmatrix} dz \tag{3-5b}$$

Substituting Eq. 3-4 into 3-5b gives

$$\begin{Bmatrix} N_x \\ N_\theta \\ M_x \\ M_\theta \\ S_x \\ S_\theta \\ M_{x\theta} \\ M_{\theta x} \end{Bmatrix} = \begin{Bmatrix} \frac{Et}{1-\nu^2}\left(\varepsilon_x^0 + \nu\varepsilon_\theta^0\right) \\ \frac{Et}{1-\nu^2}\left(\varepsilon_\theta^0 + \nu\varepsilon_x^0\right) \\ \frac{Et^3}{12\left(1-\nu^2\right)}\left(\kappa_x + \nu\kappa_\theta\right) \\ \frac{Et^3}{12\left(1-\nu^2\right)}\left(\kappa_\theta + \nu\kappa_x\right) \\ \frac{E}{2(1+\nu)}\gamma_{x\theta}^0 \\ \frac{E}{2(1+\nu)}\gamma_{x\theta}^0 \\ \frac{Et^3}{12\left(1-\nu^2\right)}\chi_{x\theta} \\ \frac{Et^3}{12\left(1-\nu^2\right)}\chi_{x\theta} \end{Bmatrix} \tag{3-6}$$

The equilibrium equations are given below（Gould 1999）

$$\begin{Bmatrix} r\frac{\partial N_x}{\partial x} + \frac{\partial S_\theta}{\partial \theta} + rq_x \\ \frac{\partial N_\theta}{\partial \theta} + r\frac{\partial S_x}{\partial x} + Q_\theta + rq_\theta \\ -N_\theta + r\frac{\partial Q_x}{\partial x} + \frac{\partial Q_\theta}{\partial \theta} + rq_n \\ \frac{\partial M_{x\theta}}{\partial x} + \frac{1}{r}\frac{\partial M_\theta}{\partial \theta} - Q_\theta \\ \frac{\partial M_x}{\partial x} + \frac{1}{r}\frac{\partial M_{\theta x}}{\partial \theta} - Q_x \end{Bmatrix} = \begin{Bmatrix} 0 \\ 0 \\ 0 \\ 0 \\ 0 \end{Bmatrix} \tag{3-7}$$

in which $q_{x,}$ q_θ and q_n are the distributed surface loadings in axial, circumferential and normal directions; Q_x is transverse shear force in the axial direction; Q_θ is transverse shear force in the circumferential direction (Figure 3-1b).

3.2.2 Equations considering thermal effect and axisymmetric loading condition

Considering temperature effects, the total strains can be written as

$$\begin{Bmatrix} \varepsilon_x \\ \varepsilon_\theta \\ \gamma_{x\theta} \end{Bmatrix} = \begin{Bmatrix} \frac{1}{Et}\left(N_x - \nu N_\theta\right) + \alpha T(z) \\ \frac{1}{Et}\left(N_\theta - \nu N_x\right) + \alpha T(z) \\ \frac{2(1+\nu)S_x}{Et} \end{Bmatrix} \tag{3-8}$$

where α is the coefficient of thermal expansion coefficient of the material and $T(z)$ is the temperature change at location *z*.

Inverting Eq. 3-8 and using the expressions for ε_x^z, ε_θ^z and $\gamma_{x\theta}^z$ as in Eq. 3-2, gives the stress-strain law**:**

$$\begin{Bmatrix} \sigma_x \\ \sigma_\theta \\ \tau_{x\theta} \end{Bmatrix} = E\begin{bmatrix} \frac{1}{1-\nu^2} & \frac{\nu}{1-\nu^2} & 0 \\ \frac{\nu}{1-\nu^2} & \frac{1}{1-\nu^2} & 0 \\ 0 & 0 & \frac{1}{2(1+\nu)} \end{bmatrix} \begin{Bmatrix} \varepsilon_x^0 + \kappa_x z \\ \varepsilon_\theta^0 + \kappa_\theta z \\ \gamma_{x\theta}^0 + 2\chi z \end{Bmatrix} - \varepsilon\alpha E T(z) \begin{Bmatrix} \frac{1}{1-\nu} \\ \frac{1}{1-\nu} \\ 0 \end{Bmatrix} \tag{3-9}$$

Considering the expression for N_x in Eq. 3-5b, we have

$$\begin{aligned} N_x &= \int_{-t/2}^{t/2} \sigma_x dz \\ &= \frac{E}{1-\nu^2}\int_{-t/2}^{t/2} \left(\varepsilon_x^0 + z\kappa_x + \nu\varepsilon_\theta^0 + \nu z\kappa_\theta\right)dz - \frac{E\alpha}{1-\nu}\int_{-t/2}^{t/2} T(z)dz \end{aligned} \tag{3-10}$$

As the origin of *z* is at the middle plane, so that

$$\int_{-t/2}^{t/2} z dz = 0 \tag{3-11}$$

and the second and fourth terms in the integral of Eq. 3-10 vanish, giving

$$N_x = \frac{E}{1-\nu^2}\left(\varepsilon_x^0 + \nu\varepsilon_\theta^0\right) - N_T \tag{3-12}$$

where

$$N_T = \frac{E\alpha}{1-\nu}\int_{-t/2}^{t/2} T(z)dz \tag{3-13}$$

Next consider the expression for M_x in Eq. 3-5b

$$\begin{aligned} M_x &= \int_{-t/2}^{t/2} \sigma_x z dz \\ &= \frac{E}{1-\nu^2}\int_{-t/2}^{t/2} \left(\varepsilon_x + z\kappa_x + \nu\varepsilon_\theta + \nu z\kappa_\theta\right) z dz - \frac{E\alpha}{1-\nu}\int_{-t/2}^{t/2} T(z) z dz \end{aligned} \tag{3-14}$$

Similar to Eq.3-10, the first and third terms of the integral vanish, so it reduces to

$$M_x = \frac{Et^3}{12\left(1-\nu^2\right)}\left(\kappa_x + \nu\kappa_\theta\right) - M_T \tag{3-15}$$

where

$$M_T = \frac{E\alpha}{1-\nu}\int_{-t/2}^{t/2} T(z) z dz \tag{3-16}$$

For axisymmetric loading conditions, the circumferential derivatives vanish and Eq.3-1 is reduced to

$$\begin{Bmatrix} \varepsilon_x^0 \\ \varepsilon_\theta^0 \\ \kappa_x \\ \gamma_{x\theta}^0 \\ \kappa_\theta \\ \chi_{x\theta} \end{Bmatrix} = \begin{Bmatrix} \dfrac{du}{dx} \\ \dfrac{w}{r} \\ -\dfrac{d^2w}{dx^2} \\ 0 \\ 0 \\ 0 \end{Bmatrix} \tag{3-17}$$

So, the equilibrium equations Eq.3-7 become

$$\frac{dN_x}{dx} + q_x = 0 \tag{3-18a}$$

$$\frac{dQ_x}{dx} - \frac{N_\theta}{r} + q_n = 0 \tag{3-18b}$$

$$\frac{dM_x}{dx} - Q_x = 0 \tag{3-18c}$$

Eq, 3-6 considering temperature effects becomes

$$N_x = \frac{Et}{1-\nu^2}\left(\frac{du}{dx} + \nu\frac{w}{r}\right) - N_T \tag{3-19a}$$

$$N_\theta = \frac{Et}{1-\nu^2}\left(\frac{w}{r} + \nu\frac{du}{dx}\right) - N_T \tag{3-19b}$$

$$M_x = -D\frac{d^2w}{dx^2} - M_T \tag{3-19c}$$

$$M_\theta = -\nu D\frac{d^2w}{dx^2} - M_T \tag{3-19d}$$

in which $D = \dfrac{Et^3}{12(1-\nu^2)}$ is the flexural rigidity of the shell.

From Eq. 3-18c,

$$Q_x = \frac{dM_x}{dx} = -D\frac{d^3w}{dx^3} - \frac{dM_T}{dx} \tag{3-19e}$$

Substituting Eq.3-19b into 3-19a, gives

$$N_\theta = \frac{Et}{r}w + \nu N_x - N_T(1-\nu) \tag{3-20}$$

Substituting Eq. 3-20 and 3-19e into 3-18b, gives

$$D\frac{d^4w}{dx^4} + \frac{Et}{r^2}w = q_n + \frac{(1-\nu)}{r}N_T - \frac{d^2M_T}{dx^2} - \frac{\nu}{r}N_x \tag{3-21}$$

Assume that the temperature varies linearly through the shell thickness so that

$$T(z) = T_m + \frac{z}{t/2}T_a \tag{3-22}$$

where T_m and T_a are respectively the mean and differential temperatures (Fig. 3-2). From Eq.3-13 and Eq. 3-16, N_T and M_T can be expressed as

$$\begin{Bmatrix} N_T \\ M_T \end{Bmatrix} = \begin{Bmatrix} \dfrac{E\alpha}{1-\nu}\displaystyle\int_{-t/2}^{t/2} T(z)dz = \dfrac{E\alpha t}{(1-\nu)} T_m \\ \dfrac{E\alpha}{1-\nu}\displaystyle\int_{-t/2}^{t/2} T(z)zdz = \dfrac{E\alpha t^2}{6(1-\nu)} T_a \end{Bmatrix} \tag{3-23}$$

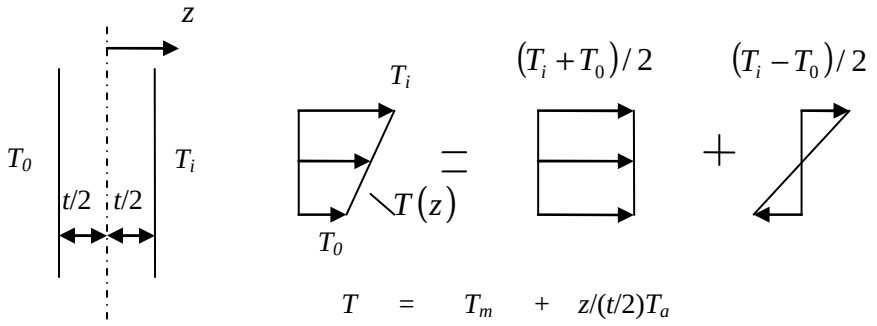

Figure 3-2 Assumed linear temperature profile through the thickness of the shell

3.2.3 General solution

The general solution of Eq. 3-21 is

$$w(x) = (C_1 \cos\frac{\pi x}{\lambda} + C_2 \sin\frac{\pi x}{\lambda})e^{-\pi x/\lambda} + \left(C_3 \cos\frac{\pi x}{\lambda} + C_4 \sin\frac{\pi x}{\lambda}\right)e^{+\pi x/\lambda} + w_m(x)$$

(3-24)

in which $w_m(x)$ is the radial displacement according to the membrane theory :

$$w_m(x) = \frac{r^2 q(x)}{Et} + \alpha T_m r - \frac{\nu r N_x(x)}{Et} \tag{3-25a}$$

and λ is the half-wavelength for meridional bending of the shell (Rotter 1985; Rotter 1987):

$$\lambda = \frac{\pi\sqrt{rt}}{\left[3\left(1-\nu^2\right)\right]^{1/4}} = 2.444\sqrt{rt} \quad \text{for } \nu = 0.3 \tag{3-25b}$$

If the shell is not short, i.e. $l > 4\lambda$, for the part close to the origin (x=0), Eq. 3-24 can be simplified to

$$w(x) = \left(C_1\cos(\pi x/\lambda) + C_2\sin(\pi x/\lambda)\right)e^{-\pi x/\lambda} + w_m(x) \tag{3-26a}$$

where C_1 and C_2 are constants of integration to be determined from the boundary conditions at $x = 0$. Similarly, for the part close to x=l, the radial displacement at the end distant from the origin (x=0) can be expressed as

$$w(x) = (C_3\cos(\pi x/\lambda) + C_4\sin(\pi x/\lambda))e^{+\pi x/\lambda} + w_m(x) \tag{3-26b}$$

where C_3 and C_4 are constants of integration which can be obtained from the boundary condition at x=l.

The constants C_1 and C_2 can be expressed in terms of a transverse shear force Q_0 and bending moment M_0 applied axisymmetrically around the circumference at $x = 0$ (Chen *et al.* 2006), as

$$\begin{Bmatrix} C_1 \\ C_2 \end{Bmatrix} = \begin{Bmatrix} -\dfrac{1}{2(\pi/\lambda)^3 D}\left(Q_0 + \dfrac{\pi}{\lambda}M_0\right) \\ \dfrac{M_0}{2(\pi/\lambda)^2 D} \end{Bmatrix} \tag{3-27}$$

From Eqs. 3-19c, 3-19d, 3-19e and 3-20, the circumferential membrane stress resultant, meridional bending moment, circumferential moment and shear force per unit width of shell can be expressed in terms of radial displacements by

$$\begin{Bmatrix} N_\theta \\ M_x \\ M_\theta \\ Q \end{Bmatrix} = \begin{Bmatrix} \dfrac{Et}{r} w + \nu N_x - N_T (1-\nu) \\ -D \dfrac{d^2 w}{dx^2} - M_T \\ -\nu D \dfrac{d^2 w}{dx^2} - M_T \\ -D \dfrac{d^3 w}{dx^3} - \dfrac{dM_T}{dx} \end{Bmatrix} \tag{3-28}$$

3.3 Solution for a cylindrical shell with temperature variation along its height

Consider a cylindrical shell under a loading condition analogous to that of an oil tank, as shown in Figure 3-3. The lower segment of the shell is subjected to a temperature rise T_1 on the outer surface and hydrostatic pressure $q_1(x)$ inside while the upper segment is subjected to a temperature rise T_2 on the outer surface and constant pressure $q_2(x)$. An axial stress resultant $N_x(x)$ is applied on the top edge of the shell. The elastic modulus of the shell is affected by the temperature and it is taken as E_1 and E_2 for the lower and upper segments of the shell respectively. The whole shell is assumed to have a uniform thickness *t*. The two segments are associated with the meridional coordinates x_1 and x_2 respectively, as shown in Figure 3-3. Consider a situation where $l_1 > 4\lambda$ and $l_2 > 4\lambda$, so both segments can be treated as long shells.

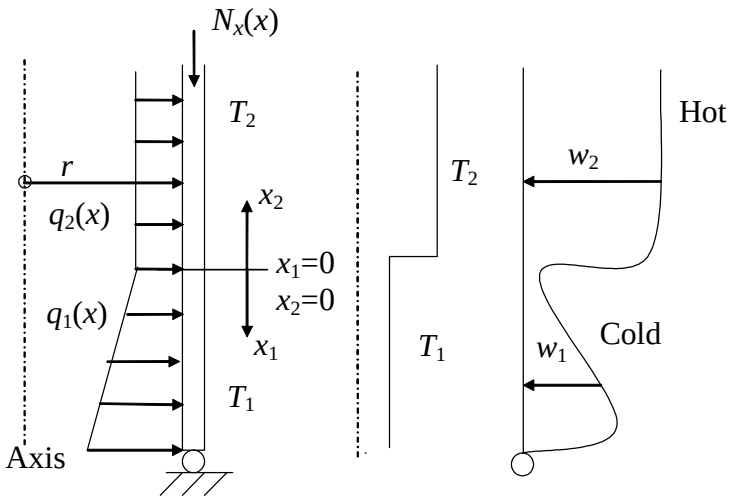

Figure 3-3 Load and temperature distribution in the shell and its deformed shape of the shell

The lower Segment 1 (coordinate x_1) is subjected to an internal hydrostatic pressure $q_1(x)$, uniform temperature rise T_1 through the wall thickness and a uniformly distributed vertical force $N_x(x)$. Assume that the stress resultants are M_{10} and Q_{10} at x_1=0. According Eq. 3-25, the membrane radial expansion w_{1m} and its derivative under the internal hydrostatic pressure $q_1(x) = \gamma x$, temperature change T_1 and vertical load $N_x(x)$, at $x_1 = 0$ are

$$\begin{cases} w_{1m}\Big|_{x_1=0} = \dfrac{r^2 q_1(0)}{E_1 t} + \alpha T_{m1} r - \dfrac{\nu r N_x(0)}{E_1 t} \\ \dfrac{dw_{1m}}{dx_1}\Big|_{x_1=0} = \dfrac{r^2 \gamma}{E_1 t} \end{cases} \tag{3-29}$$

Under the end actions M_{10} and Q_{10} alone, the bending radial expansion w_{1b} and its derivative at x_1=0 are (Chen *et al.* 2006)

$$\begin{cases} w_{1b}\Big|_{x_1=0} = -\dfrac{1}{2(\pi/\lambda)^3 D_1}\left(\dfrac{\pi}{\lambda}M_{10} + Q_{10}\right) \\ \dfrac{dw_{1b}}{dx_1}\Big|_{x_1=0} = \dfrac{1}{2(\pi/\lambda)^2 D_1}\left(2\dfrac{\pi}{\lambda}M_{10} + Q_{10}\right) \end{cases} \tag{3-30}$$

So the displacement $w_1 = w_{1m} + w_{1b}$ and rotation $\dfrac{dw_1}{dx_1}$ at x_1=0 become

$$\begin{cases} w_1(x)\Big|_{x_1=0} = \dfrac{r^2 q_1(0)}{E_1 t} + \alpha r T_{m1} - \dfrac{vrN_x(0)}{E_1 t} - \dfrac{1}{2(\pi/\lambda)^3 D_1}\left(\dfrac{\pi}{\lambda}M_{10} + Q_{10}\right) \\ \dfrac{dw_1}{dx_1}\Big|_{x_1=0} = \dfrac{1}{2(\pi/\lambda)^2 D_1}\left(2\dfrac{\pi}{\lambda}M_{10} + Q_{10}\right) + \dfrac{r^2\gamma}{E_1 t} \end{cases} \tag{3-31}$$

Following the same procedure, the upper Segment 2 (coordinate x_2) is governed by

$$\begin{cases} w_2(x)\Big|_{x_2=0} = \dfrac{r^2 q_2(0)}{E_2 t} + \alpha r T_{m2} - \dfrac{vrN_x(0)}{E_2 t} - \dfrac{1}{2(\pi/\lambda)^3 D_2}\left(\dfrac{\pi}{\lambda}M_{20} + Q_{20}\right) \\ \dfrac{dw_2}{dx_2}\Big|_{x_2=0} = \dfrac{1}{2(\pi/\lambda)^2 D_2}\left(2\dfrac{\pi}{\lambda}M_{20} + Q_{20}\right) \end{cases} \tag{3-32}$$

Satisfying equilibrium and compatibility conditions between the two segments

$$\begin{cases} w_1(x)\Big|_{x_1=0} = w_2(x)\Big|_{x_2=0} \\ \dfrac{dw_1}{dx_1}\Big|_{x_2=0} = \dfrac{dw_2}{dx_2}\Big|_{x_2=0} \end{cases} \tag{3-33}$$

the stress resultants at the boundary of the two segments Q_{10} an M_{10} can be given by

$$\begin{cases} Q_{10} = \dfrac{4k^3(\xi+1)D_1 r[q_1(0)r - \xi q_2(0)r + E_1\alpha t(T_1 - T_2) + N_x(0)\nu(\xi-1)]}{E_1 t(\xi^2+6\xi+1)} \\ \qquad \underline{+4k\xi E_1 t(M_{T1} - M_{T2}) + 2\gamma k^2 \xi D_1 r^2(1-\xi)} \\ M_{10} = \dfrac{2k^2(\xi\text{-}1)D_1 r[q_1(0)r - \xi q_2(0)r + E_1\alpha t(T_1 - T_2) + N_x(0)\nu(\xi-1)]}{E_1 t(\xi^2+6\xi+1)} \\ \qquad \underline{+E_1 t(\xi^2+3\xi)(M_{T2} - M_{T1}) - 2\gamma k\xi D_1 r^2(\xi+1)} \end{cases} \tag{3-34}$$

with

$$\xi = \frac{E_1}{E_2} = \frac{D_1}{D_2} \tag{3-35}$$

from which the deflection in the upper Segment 2 can be found as

$$\begin{aligned} w_2(x) = &-\frac{e^{-(\pi x/\lambda)}}{2(\pi/\lambda)^3 D_2}\left[\frac{\pi}{\lambda}M_{20}\left(\cos\frac{\pi x}{\lambda} - \sin\frac{\pi x}{\lambda}\right) + Q_{20}\cos\frac{\pi x}{\lambda}\right] \\ &+ \frac{r^2 q_2(x)}{E_2 t} + \alpha T_{m2} r - \frac{vrN_x(x)}{E_2 t} \end{aligned} \tag{3-36}$$

and using pinned base boundary conditions at $x_1 = l$,

$$\begin{cases} -D\dfrac{d^2 w_1}{dx^2} - M_T = 0 \\ w_1\big|_{x=l} = 0 \end{cases} \tag{3-37}$$

the lower Segment 1 deflection becomes

$$w_1(x) = -\frac{e^{-(\pi x/\lambda)}}{2(\pi/\lambda)^3 D_1}\left[\frac{\pi}{\lambda}M_{10}\left(\cos\frac{\pi x}{\lambda}-\sin\frac{\pi x}{\lambda}\right)+Q_{10}\cos\frac{\pi x}{\lambda}\right] + e^{\pi x/\lambda}\left(C_3\cos\frac{\pi x}{\lambda}+C_4\sin\frac{\pi x}{\lambda}\right)+\frac{r^2 q_1(x)}{E_1 t}+\alpha T_{m1} r-\frac{vrN_x(x)}{E_1 t} \tag{3-38}$$

in which,

$$\begin{cases} C_3 = -w_{m1}(l)e^{-\pi l/\lambda}\cos\dfrac{\pi l}{\lambda}+\dfrac{M_{T1}e^{-\pi l/\lambda}\sin(\pi l/\lambda)}{2(\pi/\lambda)^2 D} \\ C_4 = -\dfrac{M_{T1}e^{-\pi l/\lambda}\cos(\pi l/\lambda)}{2(\pi/\lambda)^2 D}-w_{m1}(l)e^{-\pi l/\lambda}\sin\dfrac{\pi l}{\lambda} \end{cases} \tag{3-39}$$

For other kind of boundary conditions, C3 and C4 can be obtained accordingly following the same procedure as above.

In summary, the radial displacement in the cylindrical shell can be calculated from Eqs 3-36 and 3-38, and the stress resultants within the shell can be calculated from Eq. 3-28.

3.4 Deformation in an example shell

3.4.1 An example problem

A cylindrical shell analogous to an oil tank with absence of the roof is examined here. A 20m high and 10m in diameter steel cylindrical tank as shown in Figure 3-4 is analysed in this section as an example. The tank wall has a uniform thickness t=10mm. The steel wall has a Poisson's ratio ν=0.3 and coefficient of thermal expansion $\alpha = 12\times10^{-6}$ /°C. The elastic modulus is temperature dependent and follows EN 1993-1-2 (2007) as shown in Figure 3-5. The shell is pinned at the bottom edge and free at the top. The density of the fluid stored in the tank is taken as γ= 1000 kg/m^3. Two load cases were considered to model the situation of a half-

full tank where the bottom half shell was subjected to the hydrostatic pressure and an empty tank where no hydrostatic pressure is present. In case 1, a temperature rise of 500ºC is applied on the upper half of the tank. In case 2, a temperature rise of 500ºC is applied throughout its whole height. The self-weight of the shell is neglected in the calculation.

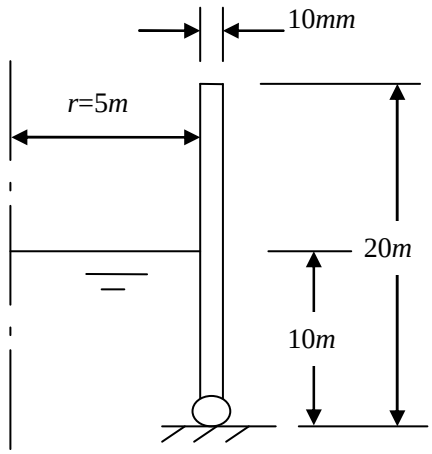

Figure 3-4 An example cylindrical tank

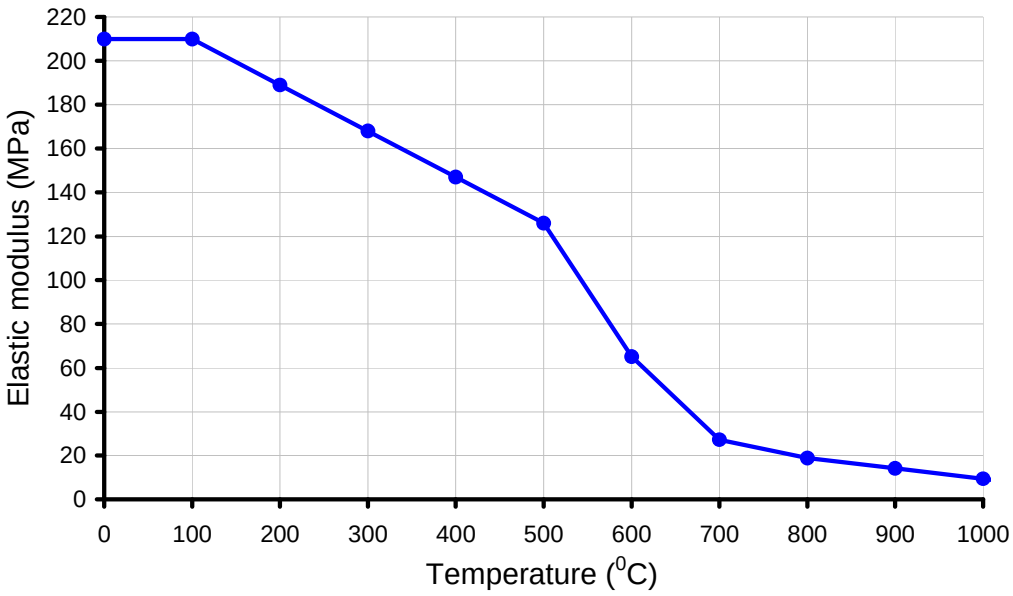

Figure 3-5 Reduction of elastic modulus with temperature (EN1993 1-2 2007)

3.4.2 Validation of the analytical solutions

In this section, the analytical solutions are validated by comparing its predictions with FE analysis using the above example. The shell was modelled using a 2 node axisymmetric element in the FE program Abaqus.

The radial defections of the tank wall predicted by the analytical solution are compared with the FE predictions in Figure 3-6. The lower segment of the shell behaves in the classic manner for a pressurised cylinder, but the upper half thermally expands, resulting in a discontinuity at the boundary between the heated and cool segments. Local bending occurs at this discontinuity, which is reflected in the circumferential membrane stresses (Figure 3-7). The circumferential membrane stresses in the lower part of the tank relate simply to the internal pressure. The difference in magnitude between these and the stresses arising from the thermal discontinuity shows what a severe load case is this due to the large temperature change.

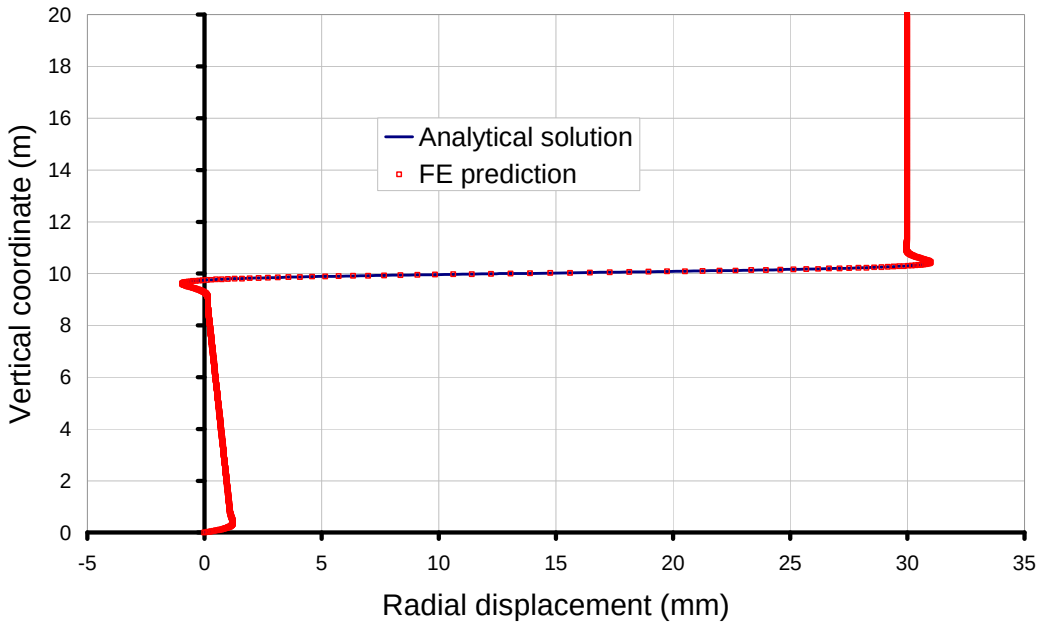

Figure 3-6 Case 1 (upper segment heated): radial displacement of tank wall

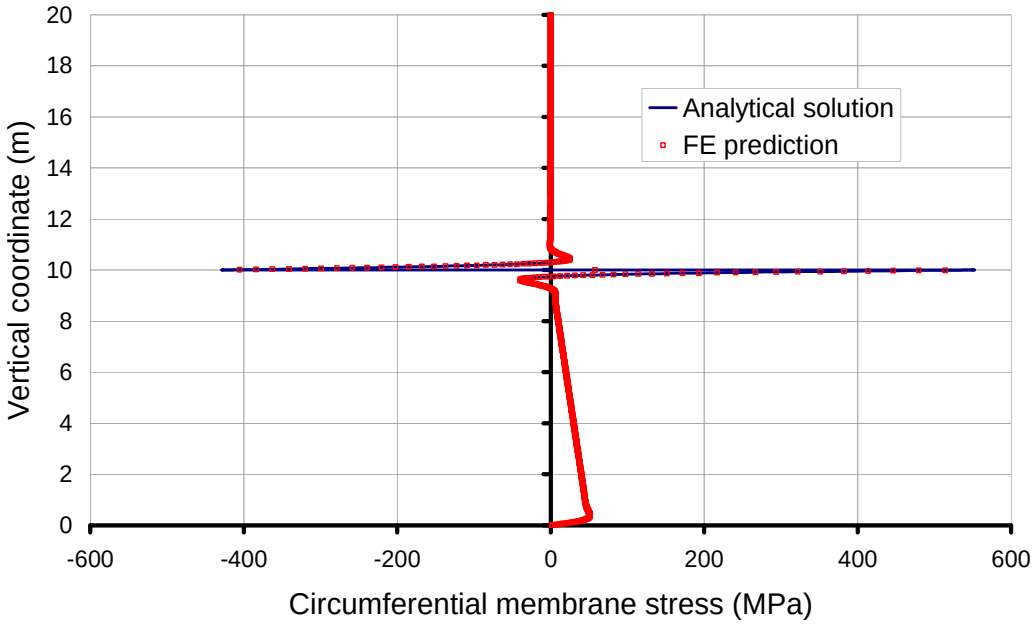

Figure 3-7 Case 1 (upper segment heated): circumferential membrane stress in tank wall

The close match between the predictions of the FEA and analytical solutions shown in Figures 3-5 and 3-6 validate the analytical solution given above.

3.4.3 Behaviour of empty and half-filled tank

The differences in the stress patterns developed in the tank walls between the two fluid conditions: empty and half-filled, are shown in Figures 3-8, 3-9 and 3-10.

As shown in Figure 3-8, the radial displacement of the upper-half tank wall in the half-filled case is the same as that of the empty tank. This indicates that the radial displacement at a point of the tank wall, except near the discontinuities or boundaries where local bending occurs, is controlled by the temperature rise there when under pure thermal loading (without internal hydrostatic pressure).

Local bending occurs near the bottom boundary for the empty tank, because the thermal expansion is restrained there. Significant circumferential membrane and meridional bending stresses are developed near the boundary. As for the half-filled

tank, apart from near the bottom boundary, local bending is also induced at the thermal discontinuity at the liquid level.

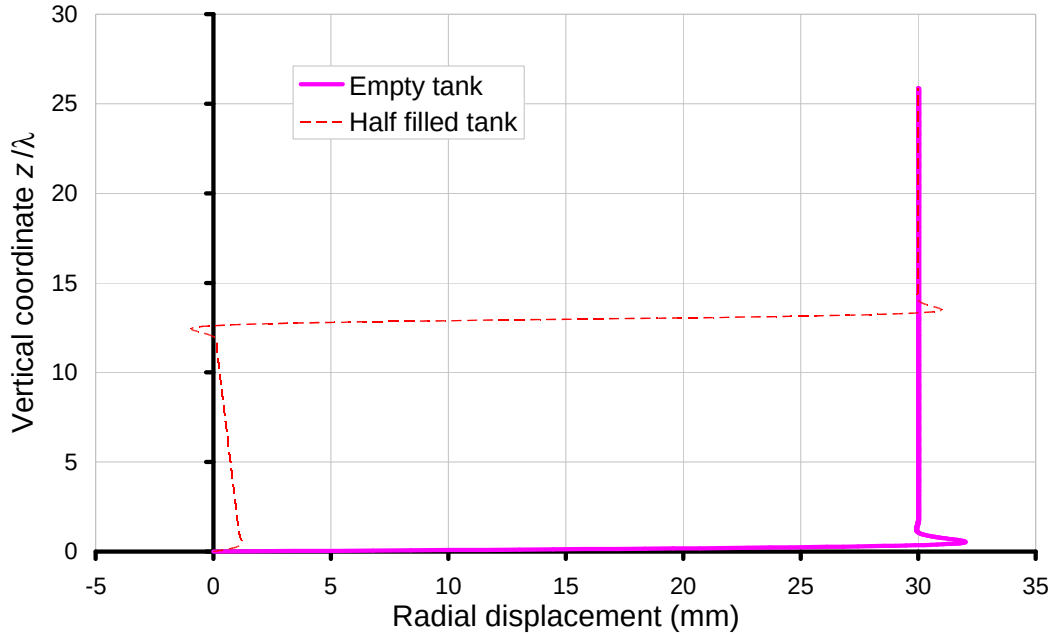

Figure 3-8 Radial deformation of empty and half-filled tanks

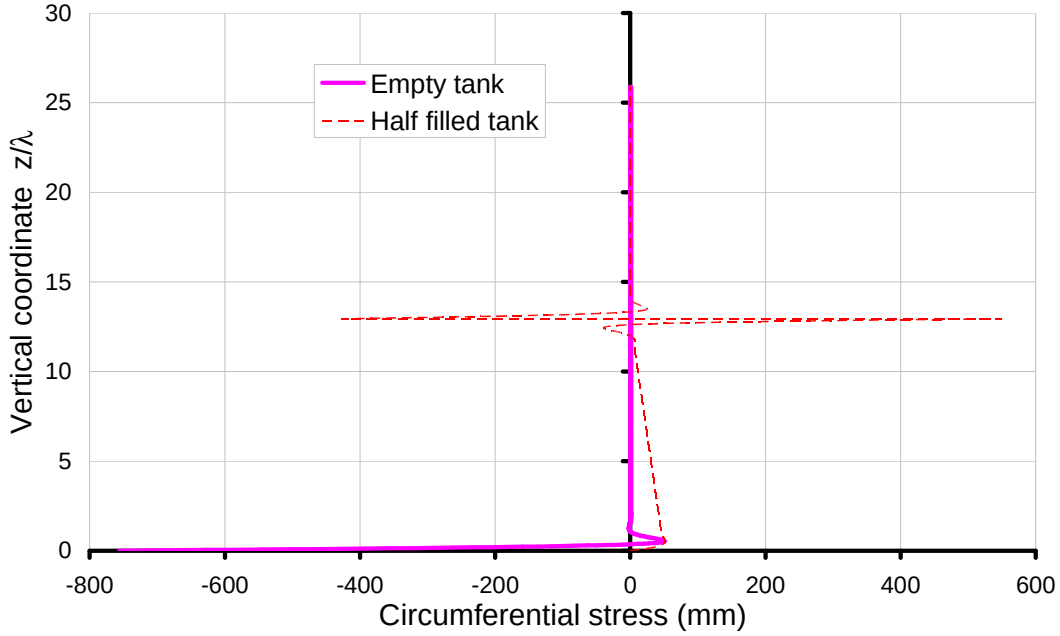

Figure 3-9 Circumferential membrane stresses in empty and half-filled tank walls

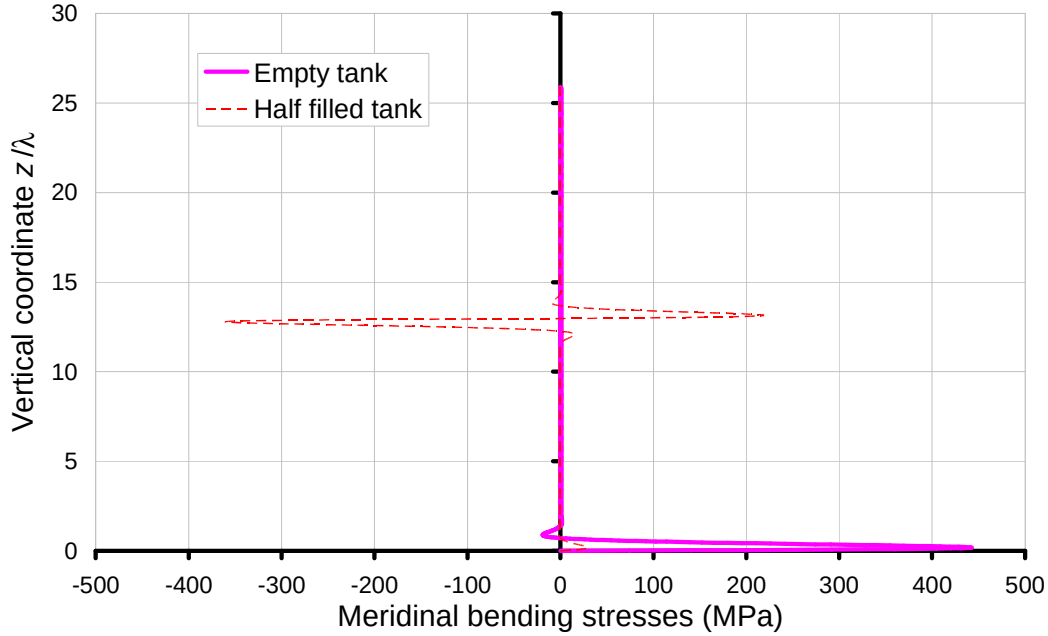

Figure 3-10 Meridional bending stresses in empty and half-filled tanks

3.5 Parametric study

3.5.1 Effect of radius to wall thickness *r*/*t* ratio (*r*/*t*)

The effect of radius to wall thickness ratio (*r/t*) was studied by varying the wall thickness *t* while the tank radius remains constant as *r*=10m.

Figures 3-11 a and b show that the radial deformation in the wall of half-filled tanks increases with an increase of *r/t* value in the region below the liquid surface. However, in the region above and away from the liquid surface, the radial deformations are identical for different *r*/*t* values. By examining Eqs 3-36 and 3-38, the radial displacement due to hydraulic pressure is inverse proportional to the thickness and the displacement due to temperature change does not relate to thickness.

The situation in an empty tank is consistent to that of the half-filled tank, except that the liquid level reduces to zero so that the radial deformation at the bottom boundary is restrained to zero (Figure 3-11c and d). It may be noticed that the peak deformation near the boundary or liquid surface is slightly larger in the empty tank (~32mm) than that in the half-filled tank (~31mm). This is because the restraint at the bottom boundary for the empty tank is stronger than that provided by the cool lower segment of the tank to the hot upper segment.

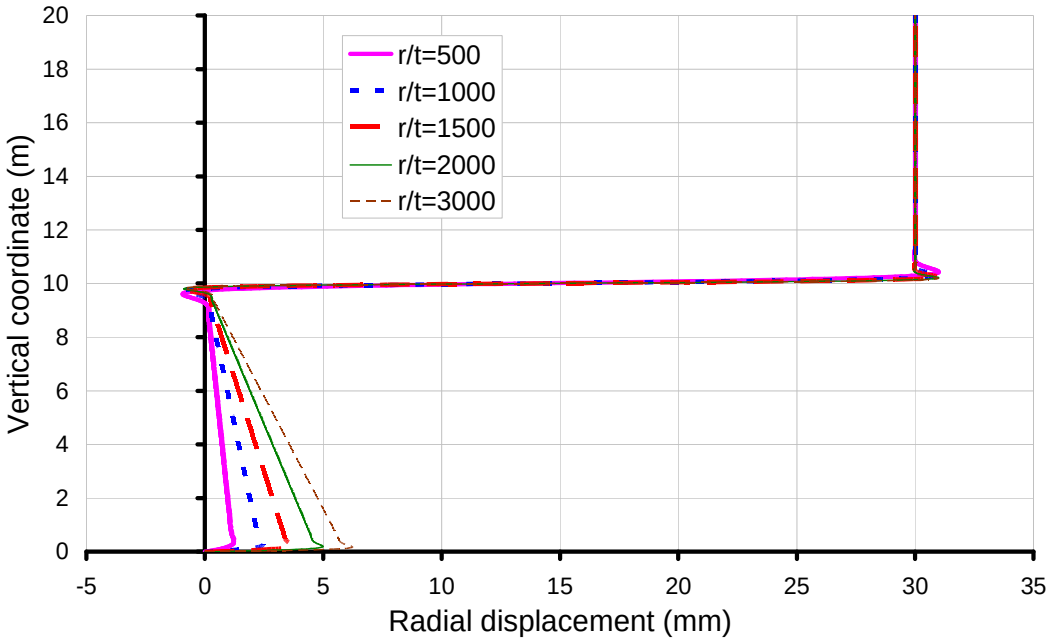

(a) Case 1: half-filled tank

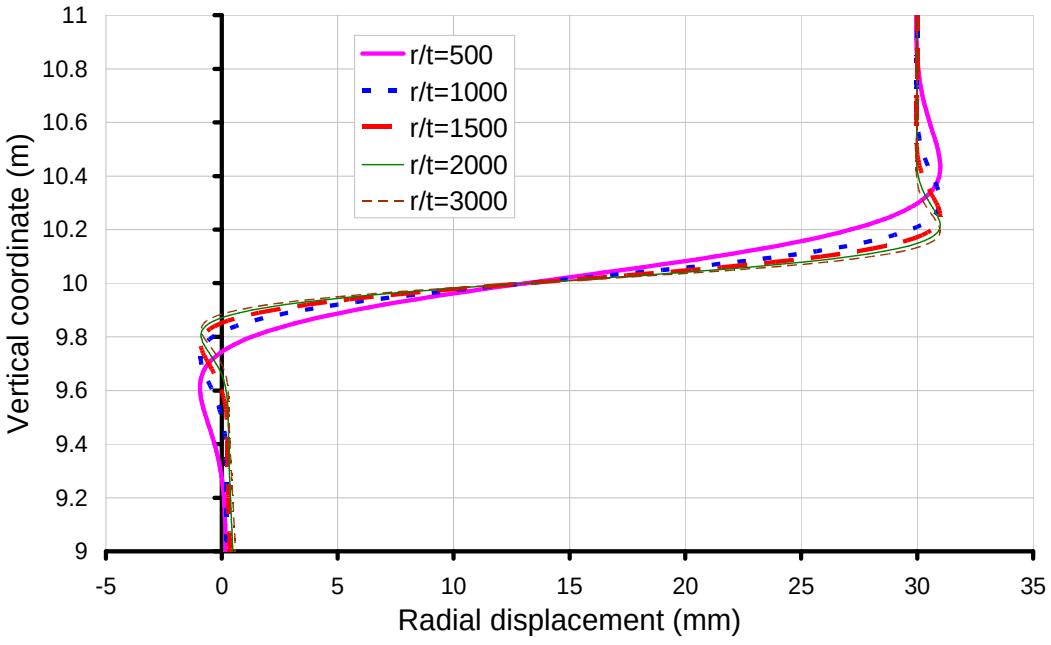

(b) Case 1: details near the thermal discontinuity

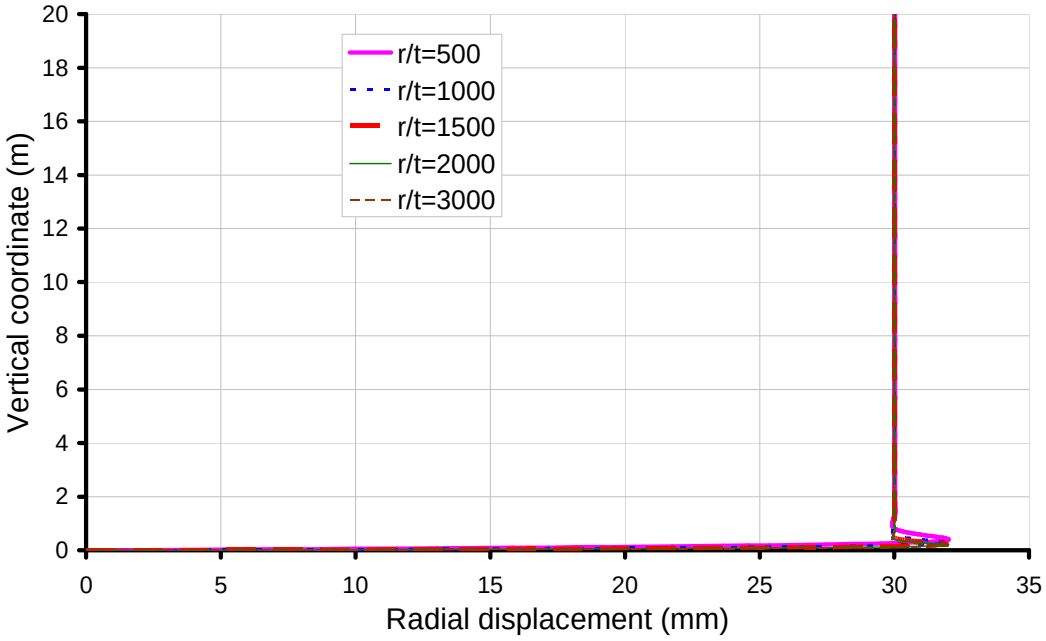

(c) Case 2: empty tank

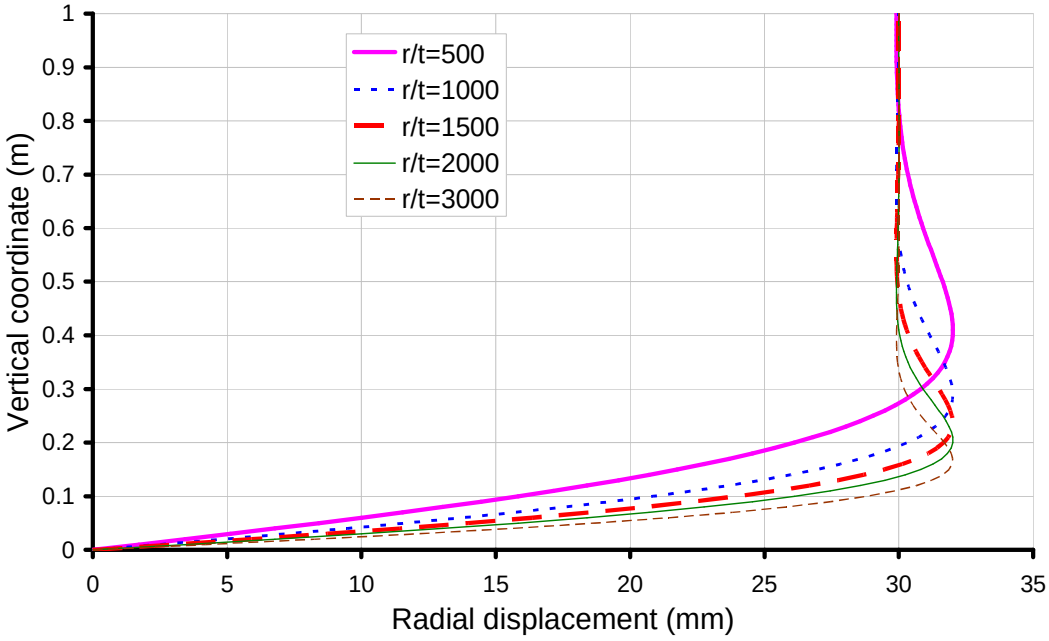

(d) Case 2: details near boundary

Figure 3-11 Effect of *r*/*t* ratio on radial deformation

The radial deformation is sensitive to the *r/t* value near the bottom boundary and liquid level where bending effect is significant (Figures 11b and d). This is because the half wavelength λ (Eq. 3-25b) relates to the *r*/*t* value. In contrast, the peak values are not (Figures 3-11b and d).

The effect of *r*/*t* ratio on the circumferential stress is shown in Figure 3-12. Similar to the situation of radial deformation, the circumferential stress is affected by the *r*/*t* value (i.e., the stresses due to hydrostatic pressure increase proportionally with *r/t*) in the region below the liquid surface but not in the region above. In the zones dominated by bending effect (i.e. near the bottom boundary and liquid surface), the stresses are affected by the *r*/*t* value.

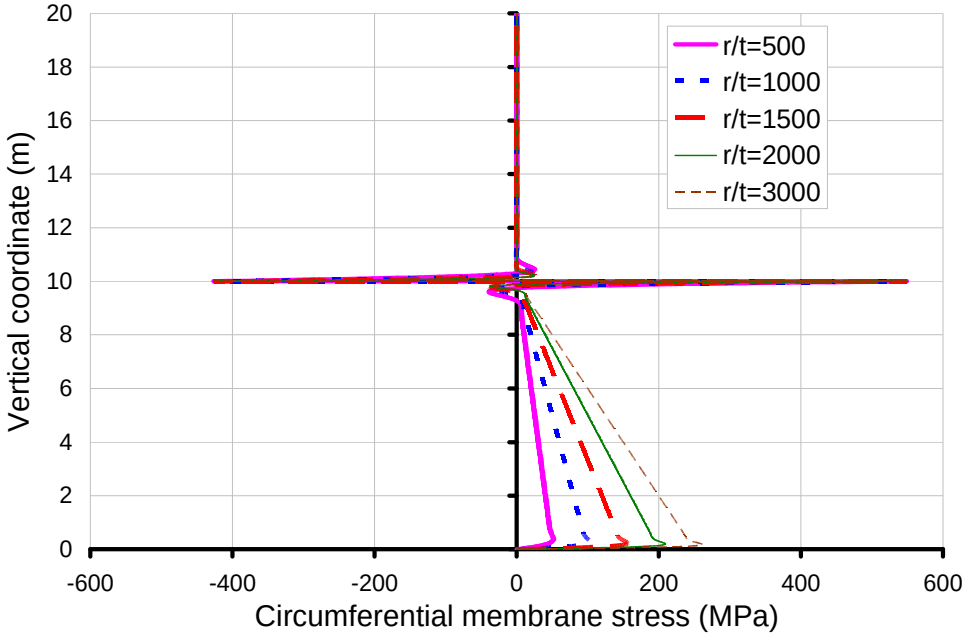

(a) Case 1: half filled tank

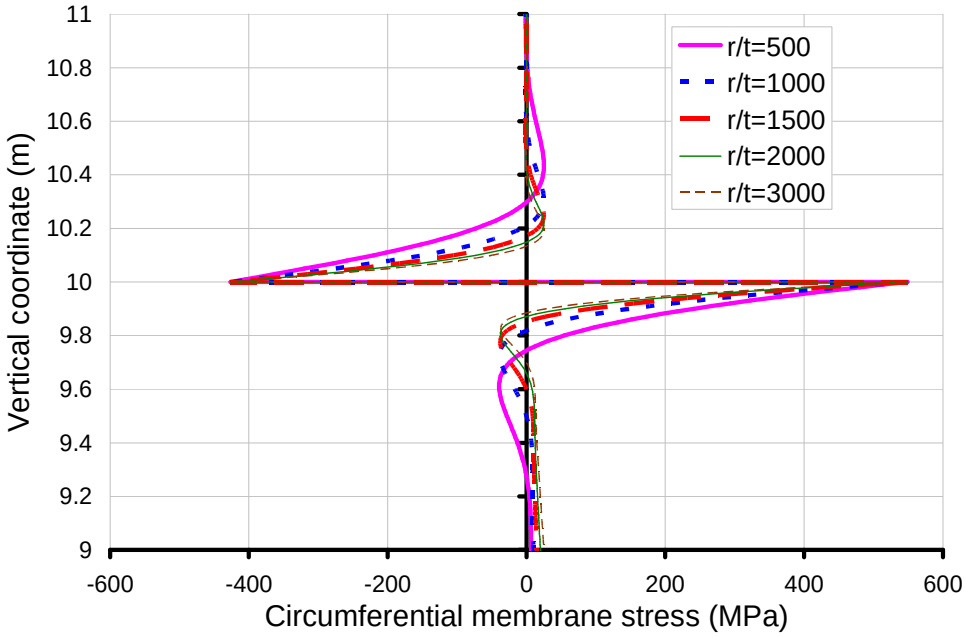

(b) Case 1: details near the thermal discontinuity

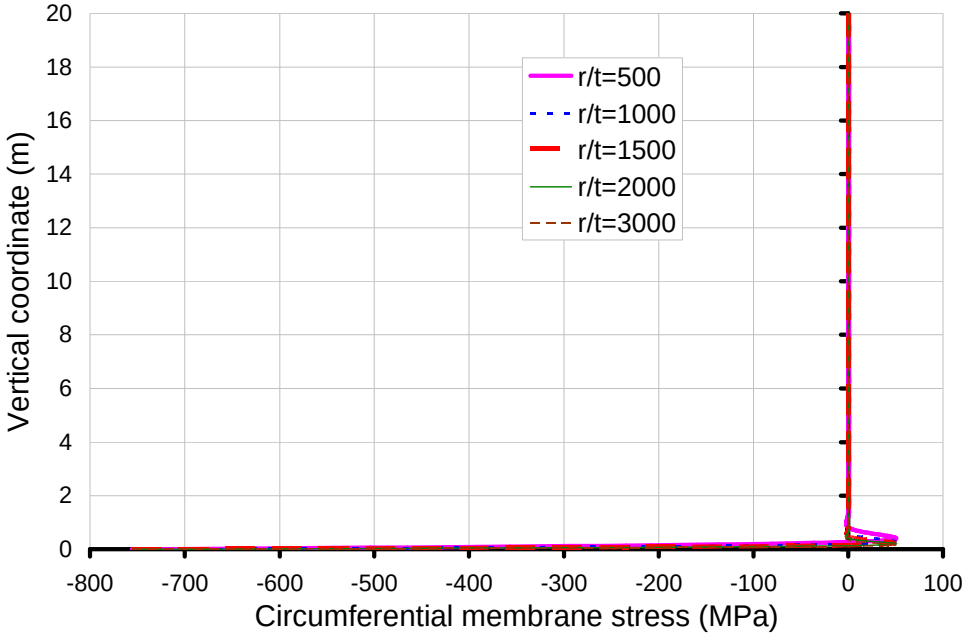

(c) Case 2: empty tank

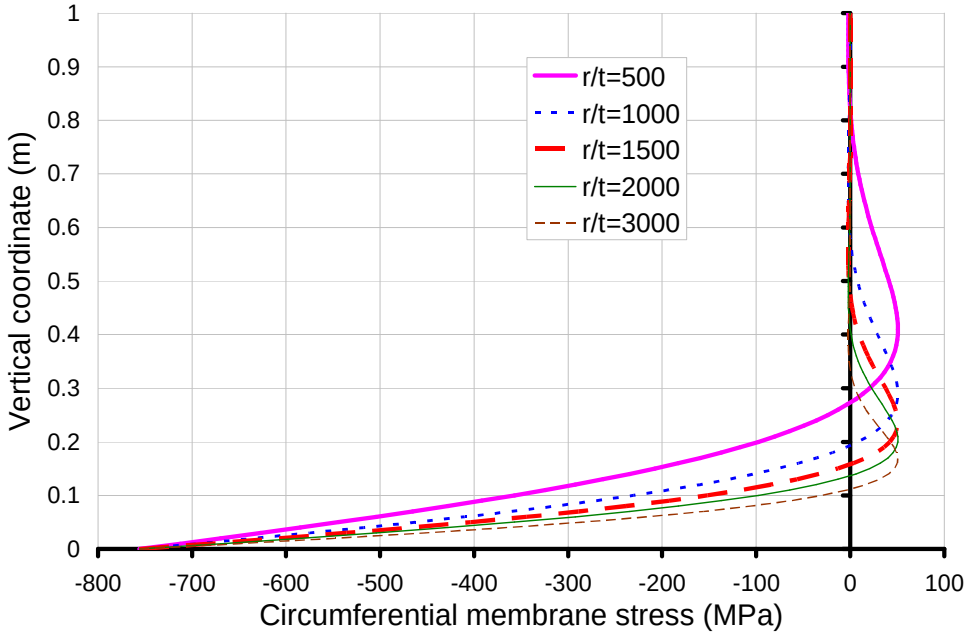

(d) Case 2: details near boundary

Figure 3-12 Effect of *r*/*t* ratio on circumferential membrane stress

3.5.2 The effect of temperature rise ΔT

The effect of temperature rise ΔT (difference between upper hot segment and the lower cold segment) on the wall stresses and deformation was investigated for both the half-filled tank and the empty tank where the *r/t* ratio was fixed at 500.

Figure 3-13 shows that the thermal expansion of the wall increases proportionally with the temperature rise in both cases. However, due to thermal softening of the material modulus, the circumferential membrane stress first increases but then decreases with increasing of temperature rise, as shown in Figure 3-14.

The maximum circumferential stresses occur when the temperature rise is about Δt =500°C, after which the stresses start decreasing because the adopted elastic modulus of steel decreases dramatically when temperature is above 500°C (Figure 3-5).

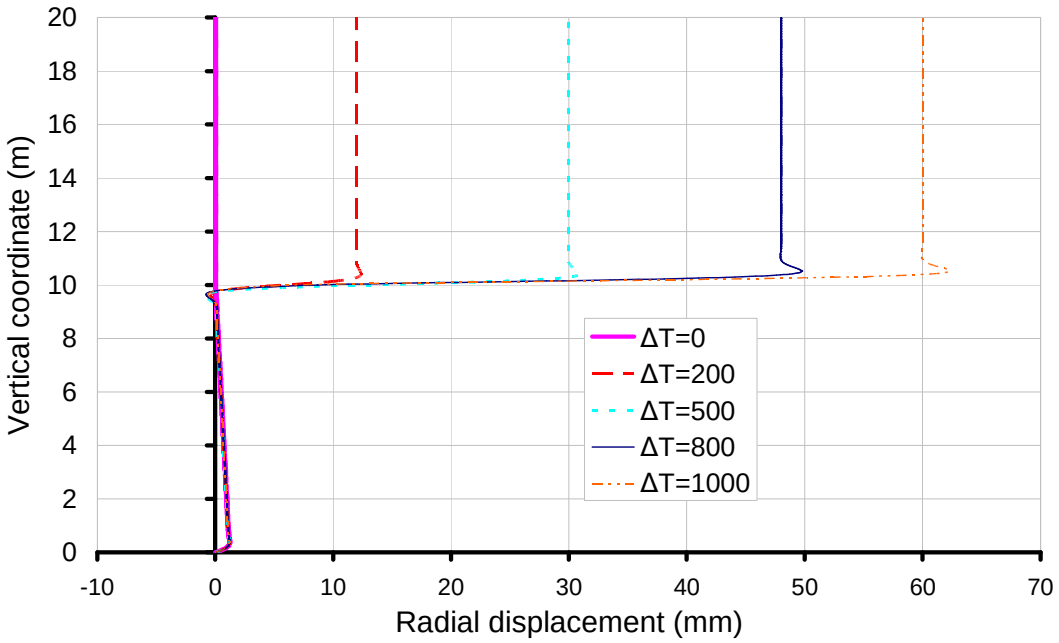

(a) Case 1: half filled tank

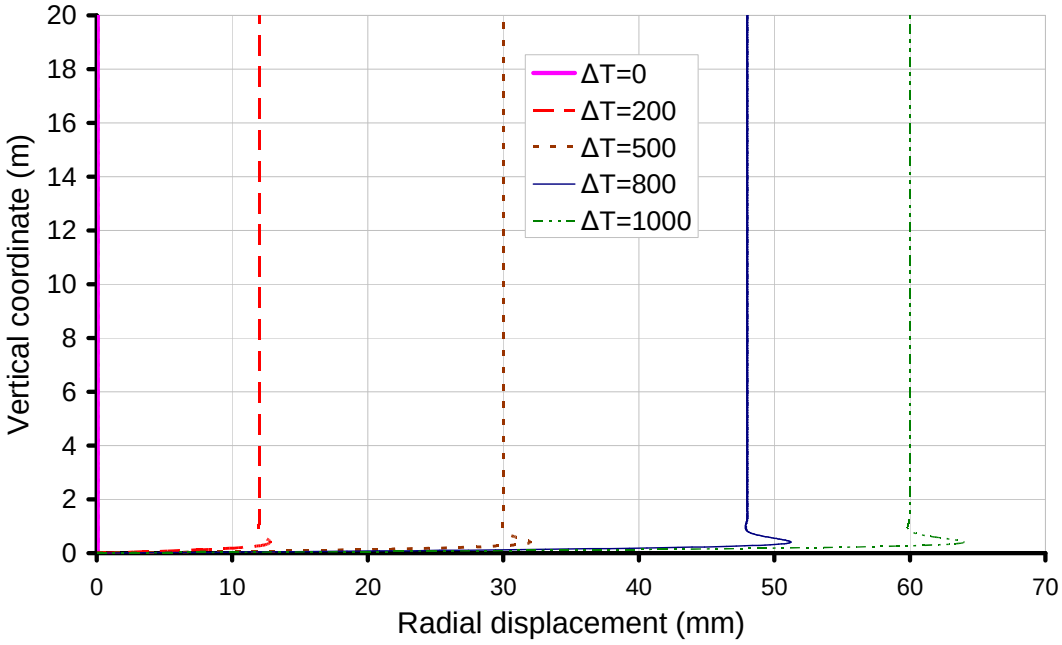

(b) Case 2: empty tank

Figure 3-13 Effect of temperature rise on radial deformation

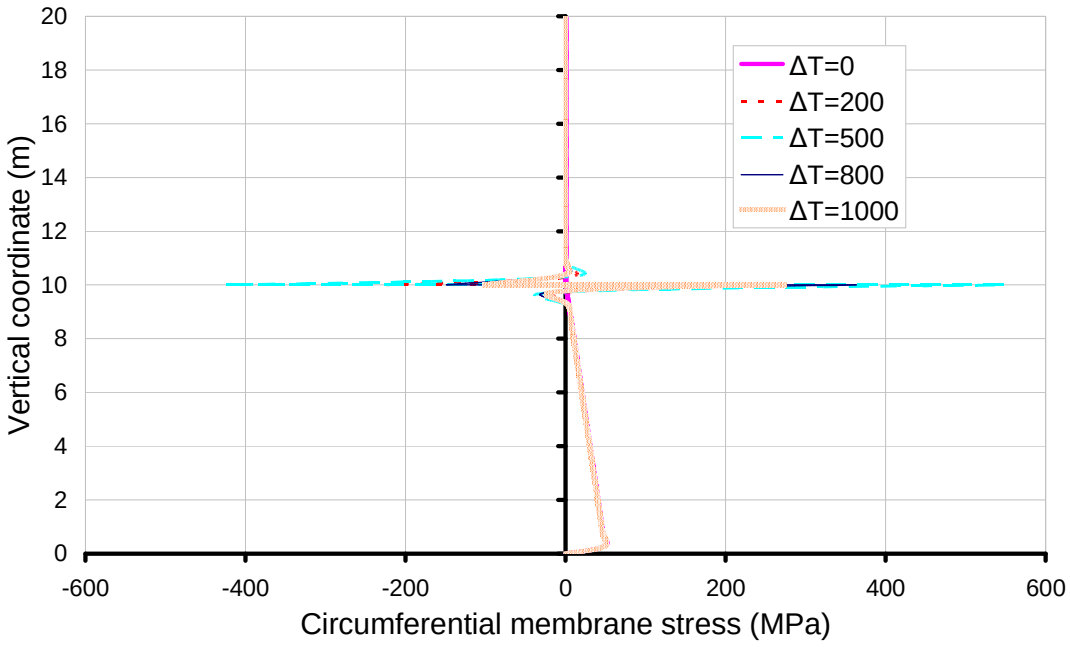

(a) Case 1: half –filled tank

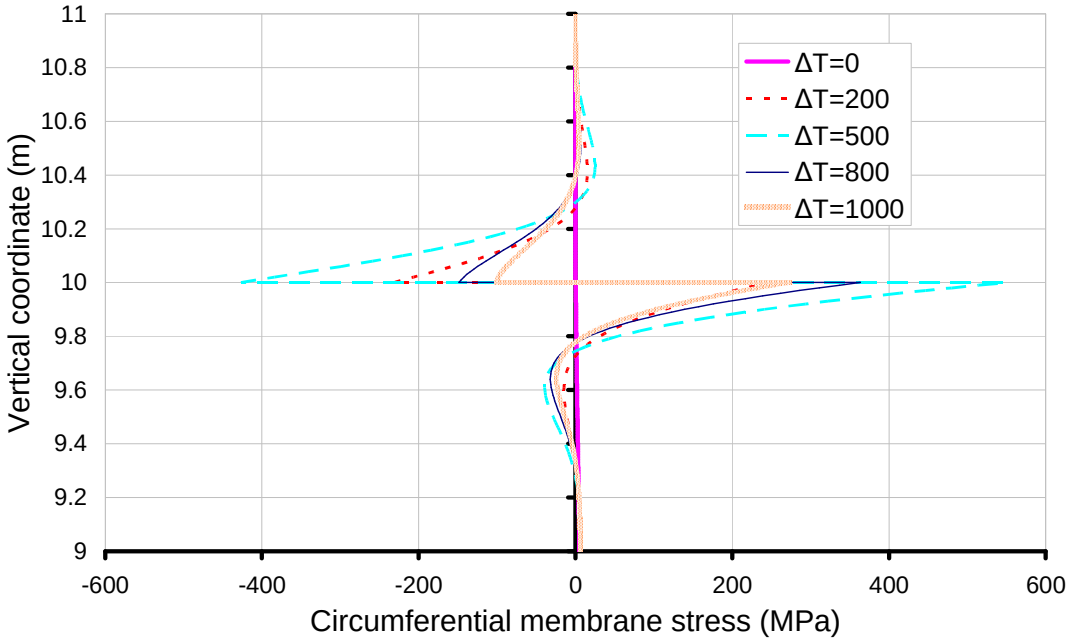

(b) Case 1: details near thermal discontinuity

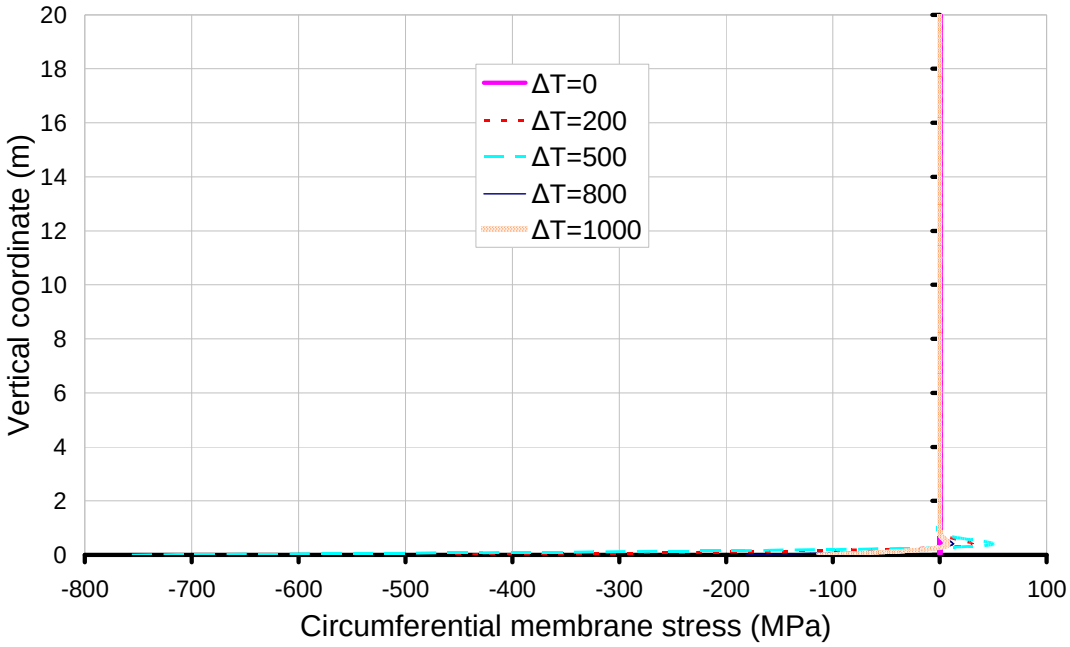

(c) Case 2: empty tank

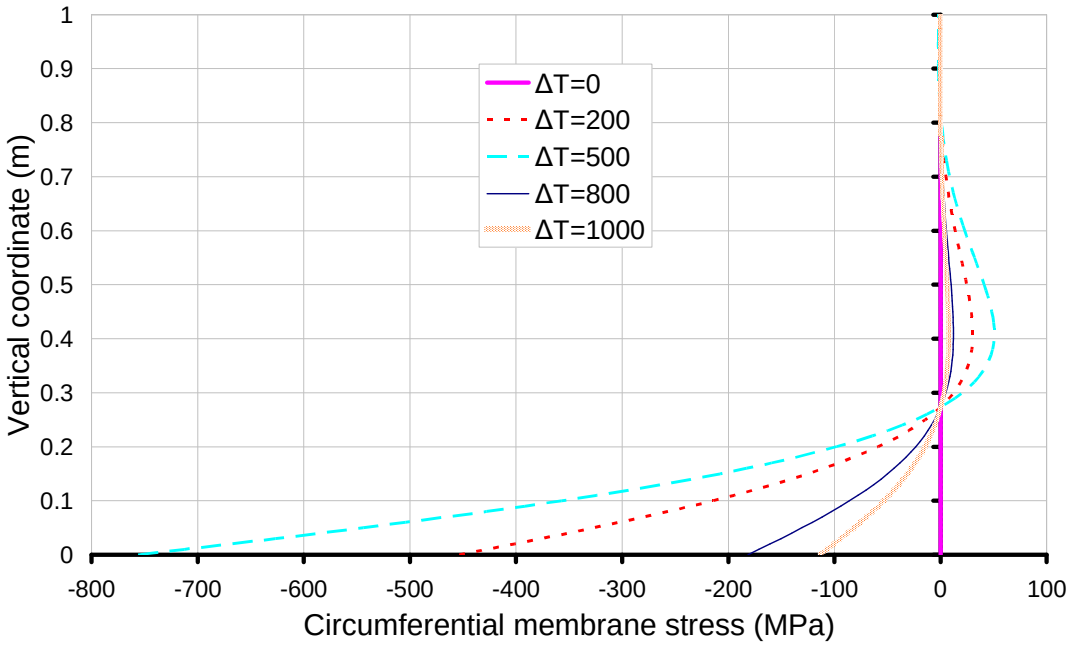

(d) Case 2: details near boundary

Figure 3-14 Effect of temperature rise on circumferential membrane stress

3.5.3 Deformation and stress envelops

The maximum values of the deformation and stress under different temperature rises and *r*/*t* values in the half-full tank are shown in Figures 3-15 to 3-17.

As shown in Figure 3-15, it is clear that the maximum radial deformation developed in the tank wall increases linearly with the temperature rise. In addition, the maximum value is independent of the *r*/*t* value, except when Δt<100°C where the maximum radial displacement occurs near the bottom boundary due to the hydraulic pressure.

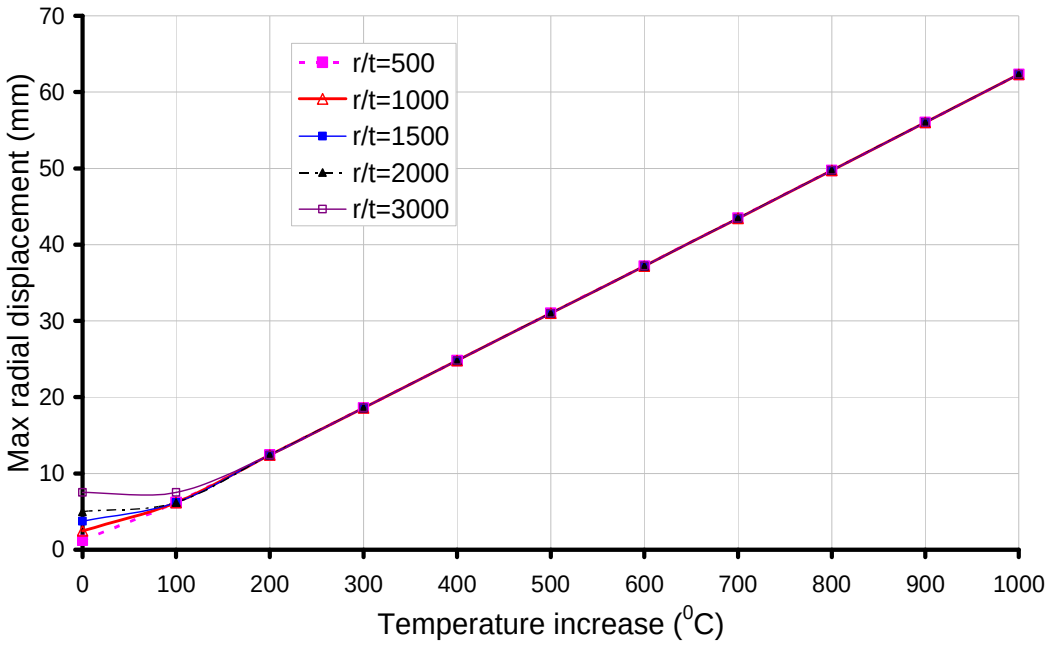

Figure 3-15 Maximum radial displacement in the tank wall with different temperature difference in the half-full tank

Figure 3-16 shows that the maximum value of circumferential stress in the heated region is independent of the *r/t* values. More importantly, the maximum value increases with temperature rise when temperature rise Δt<500°C but decreases afterwards due to the adopted temperature dependent elastic modulus.

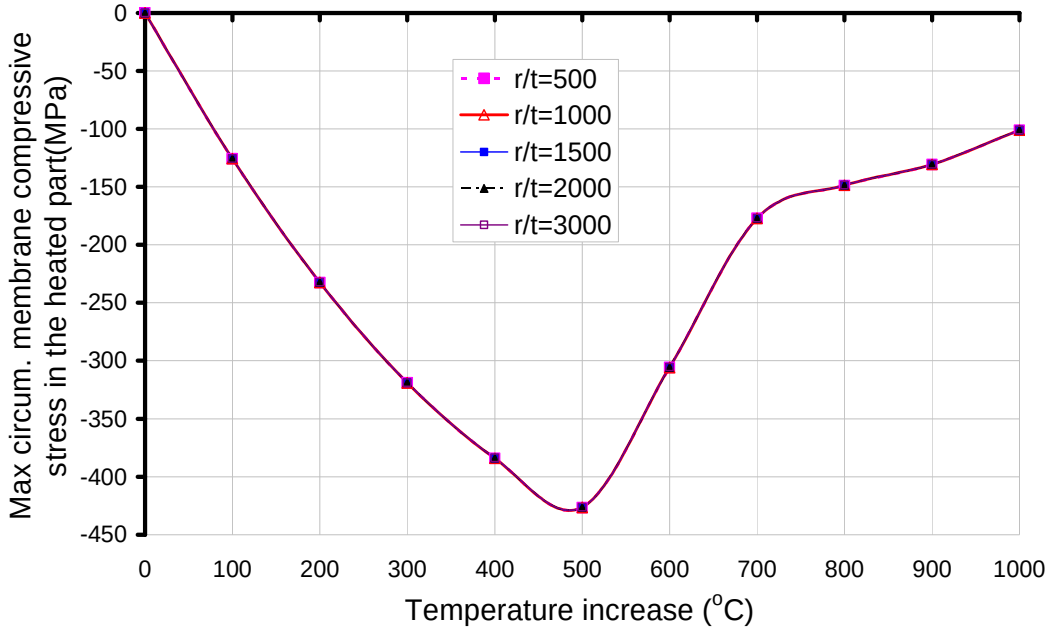

Figure 3-16 Effect of temperature rise on the maximum meridional bending stress in the half-full tank

If the circumferential stress is normalised by the classical elastic critical stress (Timoshenko 1910) $\sigma_{cr} = 0.605\,Et/r$, the value of the maximum compressive stress always increases with an increase of temperature rise as shown in Figure 3-17.

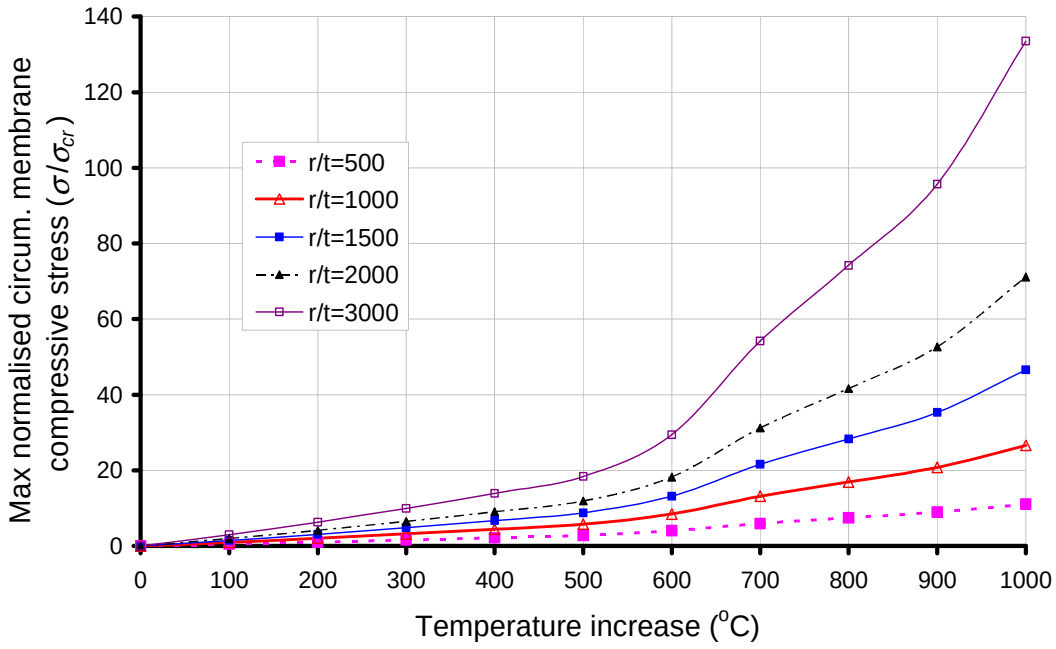

Figure 3-17 Effect of temperature rise on the maximum normalised membrane stress in the half-full tank

For the case of empty tank, since there is no hydrostatic pressure, the maximum values of radial displacement and circumferential stress are not affected by the *r*/*t* ratio.

Figures 3-18 and 3-19 compare the maximum values developed in the empty tank and the half-filled tank with an *r*/*t* value of 500. It can be seen from Figure 3-18 the maximum radial displacement developed in the empty tank is generally slightly larger than that in the half-filled tank except in the low temperature rise regime (Δt<100°C). However, the maximum circumferential stress in the empty tank is generally significantly larger than that in the half-filled tank (Figure 3-19).

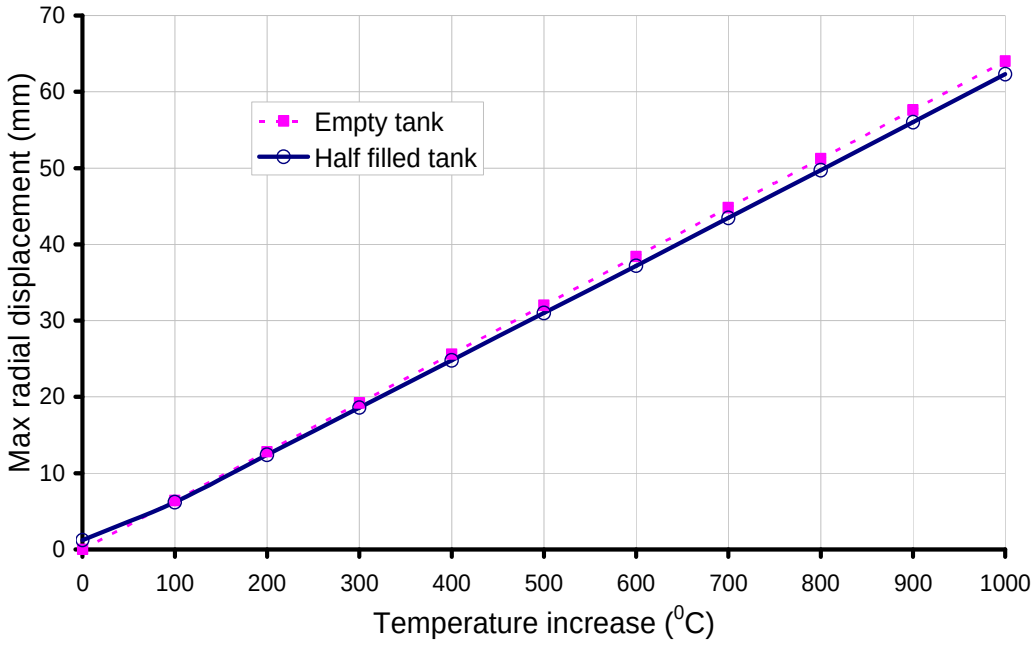

Figure 3-18 Maximum radial displacement in the empty and hall full tank (*r*/*t*=500)

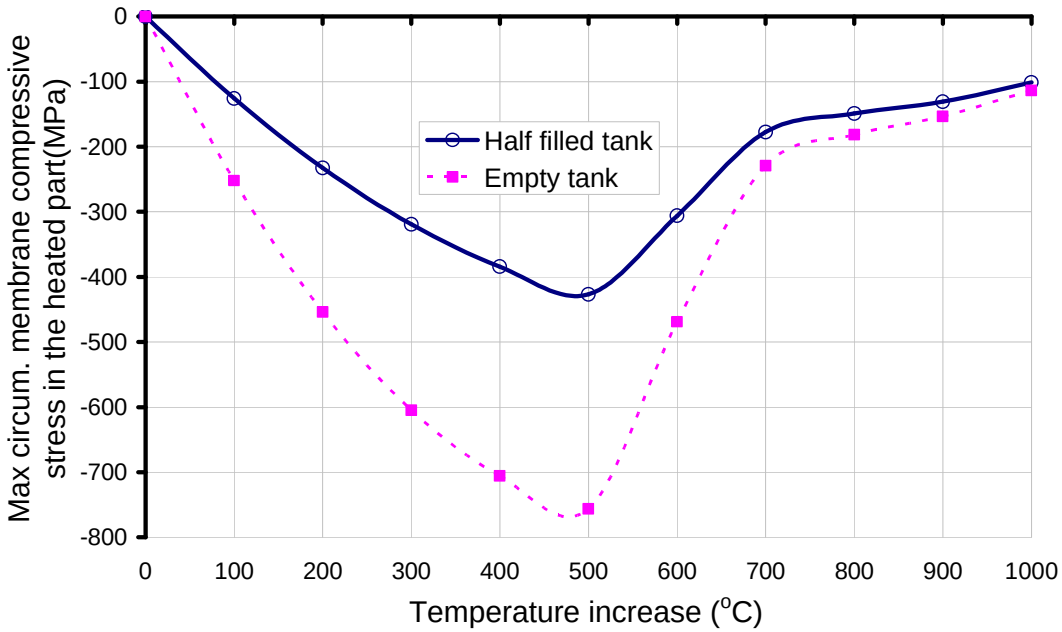

Figure 3-19 Maximum radial displacement in the empty and hall full tank (*r*/*t*=500)

3.6 Conclusions

This chapter has developed simple equations and procedures for determining the stresses and deformations in cylindrical tanks subjected to hydrostatic pressure, vertical loading and thermal expansions.

Equations for the stresses and displacements have been derived for a partially filled cylindrical tank subjected to axisymmetric temperature loading from an adjacent tank that is on fire. The tank was assumed to be simply supported at the bottom edge and free at the top. These equations have been numerically verified by comparison with the FE results.

The results of a partially filled tank and an empty tank exposed to fire have been analysed as two illustrative examples. The results have demonstrated that large compressive circumferential membrane stresses occur near the boundary for an empty tank and near the liquid level for a partially-filled tank when it is subjected to fire loading.

Both the radius to thickness ratio and the value of temperature rise have significant effects on the deflection and stresses in the tank walls. The maximum radial displacement developed in the empty tank and half-filled tank is very similar, while the maximum value of the circumferential stress developed in the empty tank can be significantly larger than that in the half-filled tank.

Chapter 4

4. A cylindrical tank under axisymmetric thermal loading with a transition zone near the liquid level

4.1 Introduction

The results presented in Chapter 3 have shown that large compressive circumferential membrane stresses occur near the liquid level, which may lead to tank material yielding or buckling in this narrow region. However, the thermal loading on the tank assumed in Chapter 3 contains an abrupt step change of temperature at the oil surface level, which is a simplification of the real temperature distribution. In reality, the temperature change between the hot upper part and the cold lower part must be smooth due to heat conduction through the tank wall. Thus the predicted wall stresses using the simplified temperature pattern in Chapter 3 are likely overestimated. In order to improve the solution, a tri-linear temperature

distribution is assumed in order to derive a more realistic solution for stresses and deflections in the tank wall. The difference between this tri-linear temperature rise pattern and the abrupt change of temperature in Chapter 3 is the inclusion of a transition zone along which the temperature varies linearly from a low value in the lower part of the tank to a high value in the upper part.

This chapter starts with the derivation of a new solution for a cylindrical shell under tri-linear temperature rise in heated part, followed by the validation of the solution against FE predictions. The effect of the height of the temperature transition zone is then studied and compared with solution from Chapter 3.

4.2 Analytical solution

4.2.1 Shell bending equations considering thermal effect and axisymmetric loading condition

The radial displacement w of an axisymmetrically loaded cylindrical shell under internal pressure q_n, axial stress resultant N_x and temperature rise T is governed by the differential equation (Gould 1999):

$$D\frac{d^4w}{dx^4}+\frac{Et}{r^2}w=q_n+\frac{(1-\nu)}{r}N_T-\frac{d^2M_T}{dx^2}-\frac{\nu}{r}N_x \tag{4-1}$$

The general solution to Eq. 4-1 is given by

$$w(x)=(C_1\cos\frac{\pi x}{\lambda}+C_2\sin\frac{\pi x}{\lambda})e^{-\pi x/\lambda}+\left(C_3\cos\frac{\pi x}{\lambda}+C_4\sin\frac{\pi x}{\lambda}\right)e^{+\pi x/\lambda}+w_m(x) \tag{4-2}$$

in which the membrane theory radial expansion is

$$w_m(x)=\frac{r^2q(x)}{Et}+\alpha T_m r-\frac{\nu r N_x(x)}{Et} \tag{4-3}$$

The half-wavelength for meridional bending of the shell λ is given by

$$\lambda = \frac{\pi\sqrt{rt}}{\left[3\left(1-\nu^2\right)\right]^{1/4}} = 2.444\sqrt{rt} \quad \text{for } \nu = 0.3 \tag{4-4}$$

If the shell is not short, i.e. $l > 4\lambda$, for the part close to the origin (x=0), the solution in Eq. 4-2 can be simplified to

$$w(x) = \left(C_1\cos(\pi x/\lambda) + C_2\sin(\pi x/\lambda)\right)e^{-\pi x/\lambda} + w_m(x) \tag{4-5a}$$

in which C_1 and C_2 can be determined from the boundary conditions at $x = 0$. Similarly, for the part close to x=l (the end away from the origin), the radial displacement can be expressed as

$$w(x) = (C_3\cos(\pi x/\lambda) + C_4\sin(\pi x/\lambda))e^{+\pi x/\lambda} + w_m(x) \tag{4-5b}$$

where C_3 and C_4 are constants of integration which can be determined from the boundary conditions at x=l.

The constants C_1 and C_2 can be expressed in terms of a transverse shear force Q_0 and bending moment M_0 applied uniformly around the circumference at $x = 0$ (Chen et al. 2006), as

$$\begin{Bmatrix} C_1 \\ C_2 \end{Bmatrix} = \begin{Bmatrix} -\dfrac{1}{2(\pi/\lambda)^3 D}\left(Q_0 + \dfrac{\pi}{\lambda}M_0\right) \\ \dfrac{M_0}{2(\pi/\lambda)^2 D} \end{Bmatrix} \tag{4-6}$$

Considering the fact that the temperature gradient through thickness of steel shells is very small and close to zero for normal thin steel tanks, M_T is neglected. Thus, the circumferential membrane stress resultant, meridional bending moment, circumferential moment and shear force per unit width of shell can be expressed in terms of radial displacements by

$$\begin{Bmatrix} N_\theta \\ M_x \\ M_\theta \\ Q \end{Bmatrix} = \begin{Bmatrix} \frac{Et}{r} w + \nu N_x - N_T(1-\nu) \\ -D\frac{d^2 w}{dx^2} \\ -\nu D\frac{d^2 w}{dx^2} \\ -D\frac{d^3 w}{dx^3} \end{Bmatrix} \tag{4-7}$$

4.2.2 Solution for a cylindrical shell under axisymmetric loading and with a tri-linear temperature rise

Consider a cylindrical shell under a loading condition analogous to that of an oil tank, as shown in Figure 4-1. The tank wall may be divided into three segments, which are the lower segment 1 which is in contact with the stored liquid, the upper segment 3 which is not in contact with the stored liquid and a small segment 2 between the two where rapid temperature change takes place. An axial force $N_x(x)$ is applied on the top edge of the shell. The lower segment 1 of the shell is subjected to an internal hydrostatic pressure $q_1(x)$ while the middle and upper segments are subjected to an internal pressure $q_2(x)$. The temperature rise varies up the tank wall. The lower segment 1 of the shell has a temperature rise T_1, while the upper segment 3 has a temperature rise T_3. The middle segment 2 that is next to the liquid surface level with a length of l_2 where the temperature $T_2(x)$ increases from T_1 linearly up to T_3. The elastic modulus of the shell is affected by the temperature and it is taken as E_1, E_2 and E_3 for the lower, middle and upper parts of the shell respectively. The whole shell has a radius r and uniform thickness t. The upper segment is associated

with vertical coordinate x_3. The middle and lower segments are associated with the meridional coordinates x_2 and x_1 respectively, as indicated in Figure 4-1. Consider the situation that $l_1>4\lambda_1$, $l_3>4\lambda_3$, so these two segments can be treated as long shell segments. It is noted that because the elastic modulus is different in each segment, λ_1 and λ_3 are different even if their thickness is the same. Considering the fact that temperature normally changes very quickly through a very short length in thin steel structures, so the middle segment is treated here as a short shell.

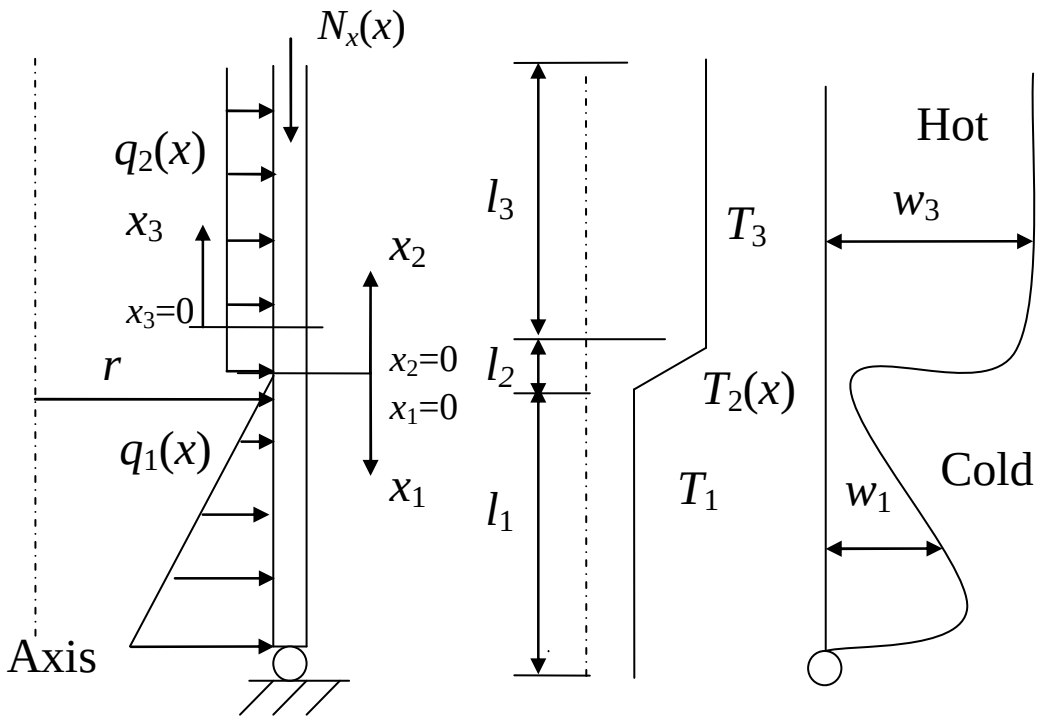

Figure 4-1 Sketch of load and temperature distribution in the shell and its deformed shape

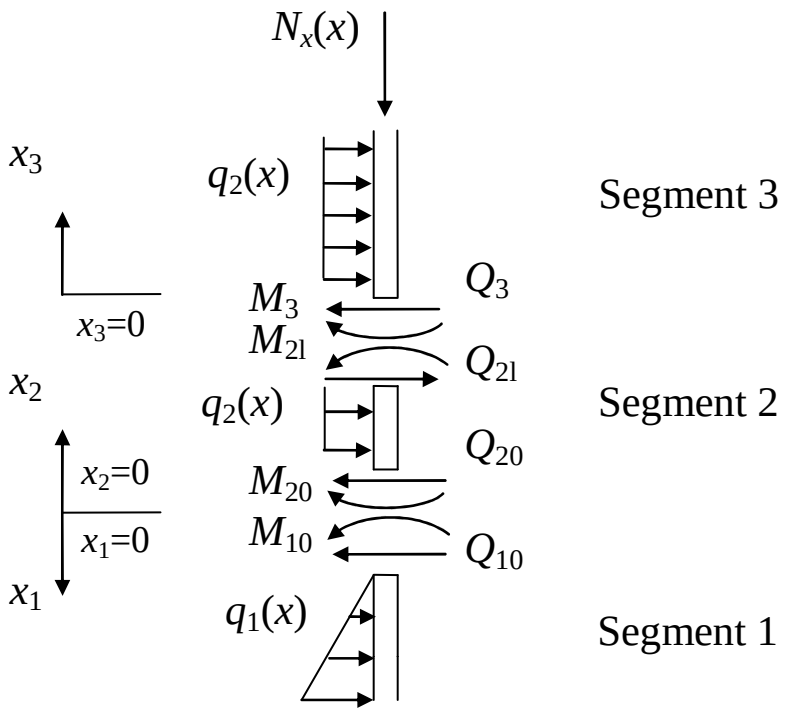

Figure 4-2 Equilibrium of the shell

The lower segment is under an internal hydrostatic pressure $q_1(x)$, a uniform temperature rise T_1, a vertical load $N_x(x)$ and is subjected to stress resultants M_{10} and Q_{10} at x_1=0, as shown in Figure 4-2.

According Eq. 4-3, the membrane radial expansion w_{1m} and its derivative under the internal hydrostatic pressure $q_1(x)=\gamma x$, temperature change T_1 and vertical load $N_x(x)$, at $x_1=0$ are

$$\begin{cases} w_{1m}\Big|_{x_1=0}=\dfrac{r^2 q_1(0)}{E_1 t}+\alpha T_{m1} r-\dfrac{\nu r N_x(0)}{E_1 t} \\ \dfrac{dw_{1m}}{dx_1}\Big|_{x_1=0}=\dfrac{r^2\gamma}{E_1 t} \end{cases} \tag{4-8}$$

Under the end actions M_{10} and Q_{10} alone, the bending radial expansion w_{1b} and its derivative at x_1=0 are

$$\begin{cases} w_{1b}\Big|_{x_1=0} = -\dfrac{1}{2(\pi/\lambda)^3 D_1}\left(\dfrac{\pi}{\lambda}M_{10} + Q_{10}\right) \\ \dfrac{dw_{1b}}{dx_1}\Big|_{x_1=0} = \dfrac{1}{2(\pi/\lambda)^2 D_1}\left(2\dfrac{\pi}{\lambda}M_{10} + Q_{10}\right) \end{cases} \tag{4-9}$$

By adding Eq. 4-8 and Eq. 4-9 together gives the displacement $w_1 = w_{1m} + w_{1b}$ and rotation $\dfrac{dw_1}{dx_1}$ at x_1=0 under all the considered mechanical and thermal loading:

$$\begin{cases} w_1(x)\Big|_{x_1=0} = \dfrac{r^2 q_1(0)}{E_1 t} + \alpha r T_{m1} - \dfrac{vrN_x(0)}{E_1 t} - \dfrac{1}{2(\pi/\lambda)^3 D_1}\left(\dfrac{\pi}{\lambda}M_{10} + Q_{10}\right) \\ \dfrac{dw_1}{dx_1}\Big|_{x_1=0} = \dfrac{1}{2(\pi/\lambda)^2 D_1}\left(2\dfrac{\pi}{\lambda}M_{10} + Q_{10}\right) + \dfrac{r^2\gamma}{E_1 t} \end{cases} \tag{4-10}$$

Following the same procedure, the deformations in the upper Segment 3 associated with coordinate system x_3 are

$$\begin{cases} w_3(x)\Big|_{x_3=0} = \dfrac{r^2 q_2(0)}{E_3 t} + \alpha r T_{m3} - \dfrac{vrN_x(0)}{E_3 t} - \dfrac{1}{2(\pi/\lambda)^3 D_3}\left(\dfrac{\pi}{\lambda}M_{30} + Q_{30}\right) \\ \dfrac{dw_{31}}{dx_3}\Big|_{x_3=0} = \dfrac{1}{2(\pi/\lambda)^2 D_3}\left(2\dfrac{\pi}{\lambda}M_{30} + Q_{30}\right) \end{cases} \tag{4-11}$$

Let $l_2 = ct$, where c is the normalised length of the transition zone height and t is the thickness of the shell, the temperature in segment 2 can be written as

$$T_2(x) = T_1 + \frac{(T_3 - T_1)}{ct} x \tag{4-12}$$

where T_3 is the temperature at $x_2=l$ and T_1 is the temperature at $x_2=0$.

Segment 2 is treated as short shell as the transition length l_2 is normally quiet short. According to Eq. 4-2, the displacements at $x_2=0$ and $x_2=l$ are expressed as

$$w_2\big|_{x2=0} = C_1 + C_3 + \frac{r^2 q_{20}}{E_2 t} + \alpha r T_{m1} - \frac{\nu r N_x}{E_2 t} \tag{4-17}$$

$$w_2\big|_{x2=l} = \left(C_1 \cos\frac{\pi l}{\lambda} + C_2 \sin\frac{\pi l}{\lambda}\right) e^{-\frac{\pi l}{\lambda}} + \left(C_3 \cos\frac{\pi l}{\lambda} + C_4 \sin\frac{\pi l}{\lambda}\right) e^{\frac{\pi l}{\lambda}} + \frac{r^2 q_{2l}}{E_2 t} + \alpha r T_{3m} - \frac{\nu r N_x}{E_2 t} \tag{4-18}$$

From Eq. 4-7, the internal forces at both ends are expressed as

$$\begin{aligned} M_x(0) &= M_{20} = -D_2 \frac{d^2 w}{dx^2}\Big|_{x_2=0} \\ Q_x(0) &= Q_{20} = -D_2 \frac{d^3 w}{dx^3}\Big|_{x_2=0} \\ M_x(l) &= M_{2l} = -D_2 \frac{d^2 w}{dx^2}\Big|_{x_2=l} \\ Q_x(l) &= Q_{2l} = -D_2 \frac{d^3 w}{dx^3}\Big|_{x_2=l} \end{aligned} \tag{4-19}$$

Substituting Eq. 4-2 into Eq. 4-19 gives

$$\begin{bmatrix} 0 & -1 & 0 & 1 \\ \frac{\pi}{\lambda} & \frac{\pi}{\lambda} & -\frac{\pi}{\lambda} & \frac{\pi}{\lambda} \\ e^{-\frac{\pi l}{\lambda}}\sin\frac{\pi l}{\lambda} & -e^{-\frac{\pi l}{\lambda}}\cos\frac{\pi l}{\lambda} & -e^{\frac{\pi l}{\lambda}}\sin\frac{\pi l}{\lambda} & e^{\frac{\pi l}{\lambda}}\cos\frac{\pi l}{\lambda} \\ ke^{-\frac{\pi l}{\lambda}}\left(\cos\frac{\pi l}{\lambda}-\sin\frac{\pi l}{\lambda}\right) & ke^{-\frac{\pi l}{\lambda}}\left(\cos\frac{\pi l}{\lambda}+\sin\frac{\pi l}{\lambda}\right) & -ke^{\frac{\pi l}{\lambda}}\left(\cos\frac{\pi l}{\lambda}+\sin\frac{\pi l}{\lambda}\right) & ke^{\frac{\pi l}{\lambda}}\left(\cos\frac{\pi l}{\lambda}-\sin\frac{\pi l}{\lambda}\right) \end{bmatrix} \begin{Bmatrix} C_1 \\ C_2 \\ C_3 \\ C_4 \end{Bmatrix}$$
$$= \frac{-1}{2\frac{\pi}{\lambda}^2 D_2} \begin{Bmatrix} M_{20} \\ Q_{20} \\ M_{2l} \\ Q_{2l} \end{Bmatrix} \tag{4-20}$$

Equilibrium between segments 1 and 2 requires

$$\begin{cases} M_1 = M_{20} \\ Q_1 = -Q_{20} \end{cases} \tag{4-21}$$

Compatibility between segment 1 and 2 requires

$$\begin{cases} w_1\big|_{x1=0} = w_2\big|_{x2=0} \\ \dfrac{dw_1}{dx}\Big|_{x1=0} = -\dfrac{dw_2}{dx}\Big|_{x2=0} \end{cases} \tag{4-22}$$

Similarly, considering equilibrium and compatibility conditions at $x_2=l$ and $x_3=0$, gives

$$\begin{cases} M_{2l} = M_3 \\ Q_{2l} = Q_3 \end{cases} \tag{4-23}$$

and

$$\begin{cases} w_2\big|_{x2=l} = w_3\big|_{x3=0} \\ \dfrac{dw_2}{dx}\big|_{x2=l} = \dfrac{dw_3}{dx}\big|_{x3=0} \end{cases} \tag{4-24}$$

The eight unknown parameters, M_1, M_3, Q_1, Q_3, C_1,C_2,C_3 and C_4 can be obtained by solving Eqs 4-21 to 4-24. Substituting them back into Eqs 4-3 and 4-5b, the deformation of the three segments can then be obtained. Because eight independent variables are involved, manual derivation is tedious. As a result, the mathematics software MATHEMATICA (Wolfram 1999) was used to solve above equations. The full set of expressions obtained is extremely complicated and lengthy, thus it is omitted here. For a special case where the elastic modulus does not change with temperature, the reduced expressions for the eight unknown parameters are significantly simplified, as given below.

Setting $\dfrac{(T_{2l} - T_{20})}{ct} = s_2$

$$M_1 = \frac{1}{2} D \frac{\pi}{\lambda} r s_2 \alpha e^{-\frac{\pi l}{\lambda}} \left(\cos\frac{\pi l}{\lambda} + \sin\frac{\pi l}{\lambda} \right) + \frac{-\gamma r\left(1+\dfrac{\pi}{\lambda}\right) + \dfrac{\pi}{\lambda} r\left(1-\dfrac{\pi}{\lambda}\right)(q_2 - q_1) - E s_2 t\alpha\left(1+\dfrac{\pi}{\lambda}\right) + E s_2 t\alpha \sin\dfrac{\pi l}{\lambda}\left(1-\dfrac{\pi}{\lambda}\right) e^{\frac{\pi l}{\lambda}}}{2E\left(1+\dfrac{\pi}{\lambda}\right) t} \tag{4-25}$$

$$Q_1 = \frac{2D\left(\dfrac{\pi}{\lambda}\right)^2 r\left[(q_1 - q_2)\dfrac{\pi r}{\lambda} - e^{-\frac{\pi l}{\lambda}} E s_2 t\alpha \sin\dfrac{\pi l}{\lambda} \right]}{E(1+\dfrac{\pi}{\lambda})t} \tag{4-26}$$

$$M_3=\frac{1}{2}D\frac{\pi}{\lambda}rs_2\alpha\left(\cos\frac{\pi l}{\lambda}-\sin\frac{\pi l}{\lambda}\right)\sin\frac{\pi l}{\lambda}$$
$$+\frac{D\frac{\pi}{\lambda}re^{-\frac{2\pi l}{\lambda}}\begin{Bmatrix}-e^{\frac{\pi l}{\lambda}}\gamma r\left(1+\frac{\pi}{\lambda}\right)\left(\sin\frac{\pi l}{\lambda}+\cos\frac{\pi l}{\lambda}\right)+e^{\frac{\pi l}{\lambda}}(q_2-q_1)r\left[\left(1-\frac{\pi}{\lambda}\right)\cos\frac{\pi l}{\lambda}+\left(1+\frac{3\pi}{\lambda}\right)\sin\frac{\pi l}{\lambda}\right]\\-e^{\frac{\pi l}{\lambda}}Es_2t\alpha\left(1+\frac{\pi}{\lambda}\right)\left(\sin\frac{\pi l}{\lambda}+\cos\frac{\pi l}{\lambda}\right)+Es_2t\alpha\sin\frac{\pi l}{\lambda}\left(1-\frac{\pi}{\lambda}\right)\left(\cos\frac{\pi l}{\lambda}-\sin\frac{\pi l}{\lambda}\right)\end{Bmatrix}}{2E\left(1+\frac{\pi}{\lambda}\right)t} \tag{4-27}$$

$$Q_3=\frac{\begin{array}{l}-4D\left(\frac{\pi}{\lambda}\right)^4e^{-\frac{\pi l}{\lambda}}(q_1-q_2)r^2\cos\frac{\pi l}{\lambda}\\+2D\left(\frac{\pi}{\lambda}\right)^2re^{-\frac{\pi l}{\lambda}}\left[\gamma r\left(1-\frac{\pi}{\lambda}\right)\sin\frac{\pi l}{\lambda}+\left(1+\frac{\pi}{\lambda}\right)\sin\frac{\pi l}{\lambda}\left(\frac{\pi}{\lambda}(rq_1-rq_2)+Et\alpha\sin\frac{\pi l}{\lambda}\right)\right]\end{array}}{2E\left(1+\frac{\pi}{\lambda}\right)t} \tag{4-28}$$

$$C_1=\frac{\gamma r^2\left(1+\frac{\pi}{\lambda}\right)+\frac{\pi}{\lambda}r^2\left(1+\frac{3\pi}{\lambda}\right)(q_1-q_2)+Es_2t\alpha r\left[\left(1+\frac{\pi}{\lambda}\right)+\left(1-\frac{\pi}{\lambda}\right)e^{-\frac{\pi l}{\lambda}}\sin\frac{\pi l}{\lambda}\right]}{4E\frac{\pi}{\lambda}\left(1+\frac{\pi}{\lambda}\right)t} \tag{4-29}$$

$$C_2=\frac{-\gamma r^2\left(1+\frac{\pi}{\lambda}\right)+\left(1-\frac{\pi}{\lambda}\right)\left[\frac{\pi}{\lambda}r^2(q_1-q_2)+Es_2t\alpha re^{-\frac{\pi l}{\lambda}}\sin\frac{\pi l}{\lambda}\right]-Es_2t\alpha r\left(1+\frac{\pi}{\lambda}\right)}{4E\frac{\pi}{\lambda}\left(1+\frac{\pi}{\lambda}\right)t} \tag{4-30}$$

$$C_3=\frac{e^{-\frac{\pi l}{\lambda}}rs_2\alpha\left(\sin\frac{\pi l}{\lambda}-\cos\frac{\pi l}{\lambda}\right)}{\frac{4\pi}{\lambda}} \tag{4-31}$$

$$C_4 = \frac{-e^{-\frac{\pi l}{\lambda}} r s_2 \alpha \left(\sin\frac{\pi l}{\lambda} + \cos\frac{\pi l}{\lambda} \right)}{\frac{4\pi}{\lambda}} \tag{4-32}$$

4.2.3 Internal forces and deformations near the bottom boundary

The boundary conditions of the shell at $x_1 = l_1$ are

$$\begin{cases} w_1(x)\big|_{x_1=l_1} = 0 \\ -D_1 \dfrac{d^2 w_1}{dx_1^2}\Big|_{x_1=l_1} - M_{T1} = 0 \end{cases} \tag{4-33}$$

Substituting Eq. 4-33 into Eq. 4-5b gives

$$\begin{cases} \left(C_5 \cos\dfrac{\pi l_1}{\lambda} + C_6 \sin\dfrac{\pi l_1}{\lambda} \right) e^{\frac{\pi l_1}{\lambda}} + w_{m1}(l_1) = 0 \\ -2k^2 e^{\frac{\pi l_1}{\lambda}} D \left(C_5 \cos\dfrac{\pi l_1}{\lambda} - C_6 \sin\dfrac{\pi l_1}{\lambda} \right) = 0 \end{cases} \tag{4-34}$$

So,

$$\begin{cases} C_5 = -w_{m1}(l_1) e^{-\frac{\pi l_1}{\lambda}} \cos\dfrac{\pi l_1}{\lambda} \\ C_6 = -\left(w_{m1}(l_1) e^{-\frac{\pi l_1}{\lambda}} \sin\dfrac{\pi l_1}{\lambda} \right) \end{cases} \tag{4-35}$$

The circumferential membrane stress, moment and shear force can be obtained from Eq.4-7.

4.3 Validation of analytical solutions against FE prediction

In this section, the analytical solutions are validated by comparing its predictions with FE analysis through an example. It is noted that in the analytical solution above, the elastic modulus was assumed to be constant in each segment, but in reality the elastic modulus changes continuously with temperature (Figure 3-4). In order to quantify the effect of this simplification, a comparison between the analytical solution incorporating uniform elastic modulus in the transition zone and the FE prediction considering accurately the temperature dependent elastic modulus is made.

4.3.1 An example problem

The tank model examined in this chapter is the same as that in Chapter 3 which is an open top cylindrical tank, 20*m* high and 10*m* in diameter with a uniform thickness 10*mm*, and has a Poisson's ratio 0.3 and coefficient of thermal expansion $\alpha = 12\times10^{-6}$ per °C. The tank is pinned at the bottom edge and free at the top. The density of the fluid stored in the tank is taken as γ = 1.0 tonne/m^3. The tank is assumed to be half-filled, thus the lower half shell is subjected to hydrostatic pressure. The self-weight of the shell is neglected in the calculation.

The temperature rise is assumed to rise by 0°C in the lower part of shell (below 10m) and 500°C in the upper part of the shell (above 10.5m). In the middle part of tank (temperature transition zone, between 10m and 10.5m), the temperature rise increases linearly from 0°C to 500°C. The value of elastic modulus is 2.1×10^{11} MP*a* below 10m and 1.26×10^{11} MPa above 10.5*m* according to Figure 3-4. The elastic modulus for the middle part (between 10m and 10.5m) is taken as the average of that of the lower and upper parts, which is 1.68×10^{11} MPa.

4.3.2 Finite element model

The FE analysis was conducted using Abaqus (Simulia 2008). A 2-node finite strain axisymmetric shell element shell208 was adopted to model the tank wall. Two different treatments of the elastic modulus *E* were examined: a) using constant value for each segment, the value of E in each segment is the same as what used in section 4.3.1; and b) using a temperature dependent modulus as shown in Figure 3-4.

4.3.3 Validation of the analytical solutions

The predictions of the above analytical solution for the radial defections of the tank wall are compared with the FE predictions in Figure 4-3. It shows that the analytical solution matches very well with the FE prediction. It appears that adopting a constant elastic modulus in the transition zone instead of a more precise variation (Figure 3-5) is already quite satisfactory for the displacement prediction.

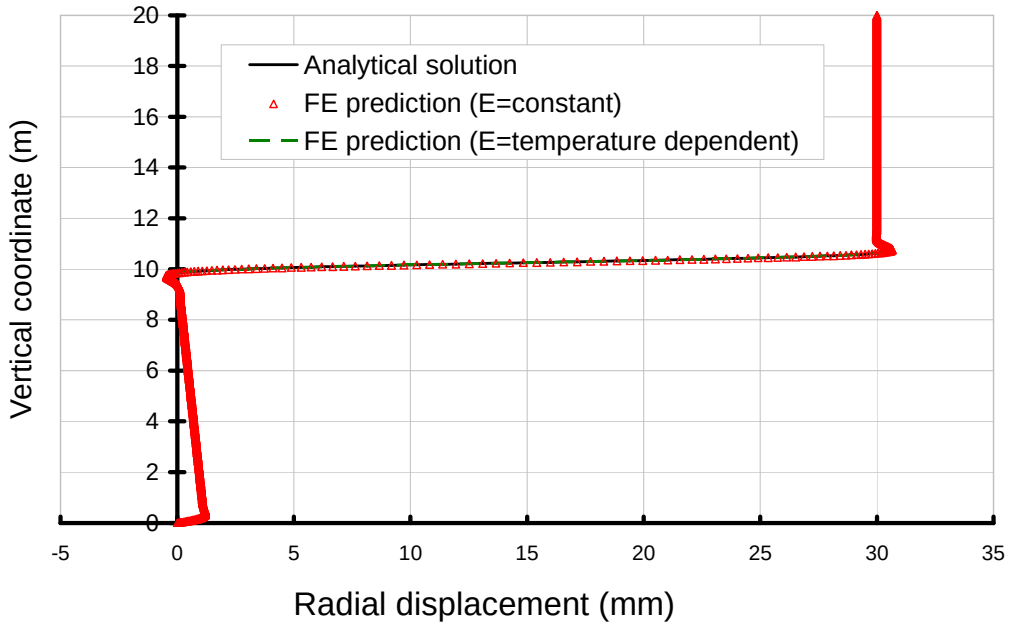

(a) Full range

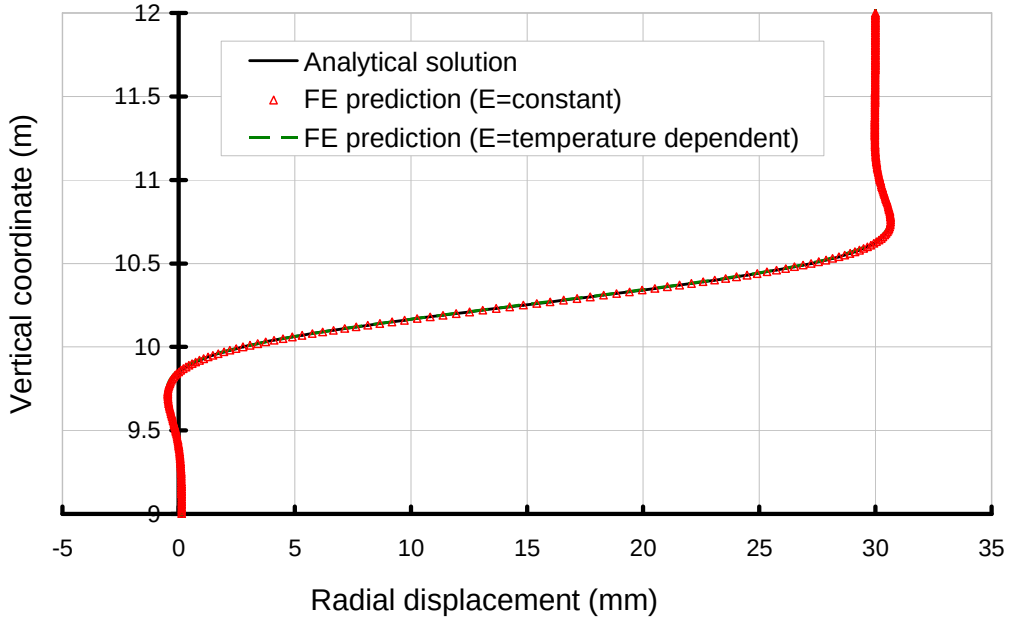

(b) Details in temperature transition zone

Figure 4-3 Verification: radial displacement

A further insight into the stresses and moment developed in the shell shown in Figures 4-4 to 4-6, also proved the correctness of analytical solution. The stresses induced in the shell changes continuously up vertical coordinate due to the fact of inclusion of a transition zone in the analytical solution. It predicts a more realistic state compared to that by the abrupt temperature change (zero transition) in Chapter 3. Although in the presented analytical solution the elastic modulus in the transition zone was not treated strictly following EN 1993-1-2 2007 but as a uniform value defined in Section 4.3.2, the results have shown that the analytical solutions provide sufficient accuracy for stress and deformation predictions.

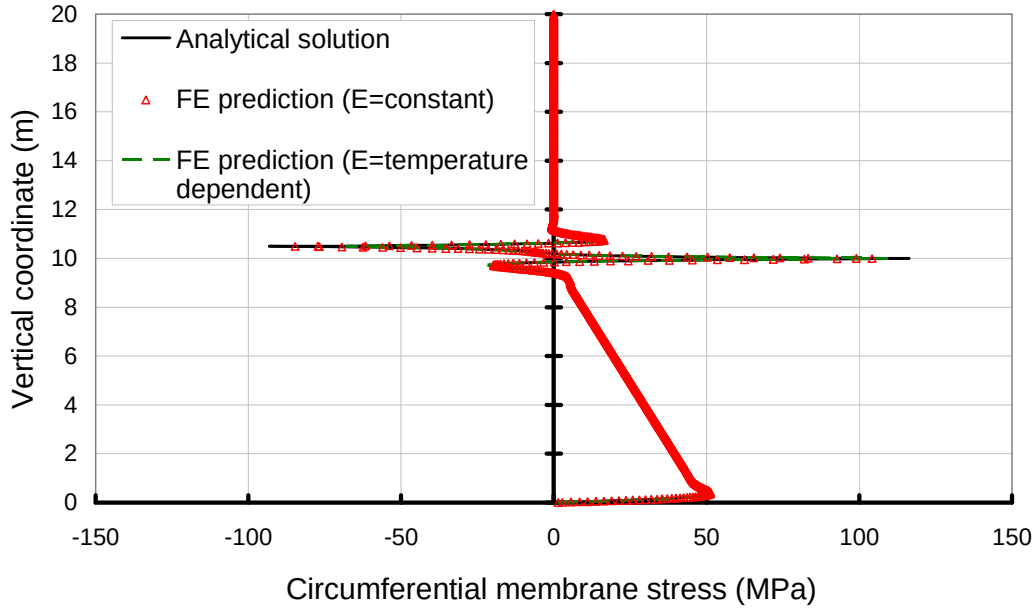

(b) Full range

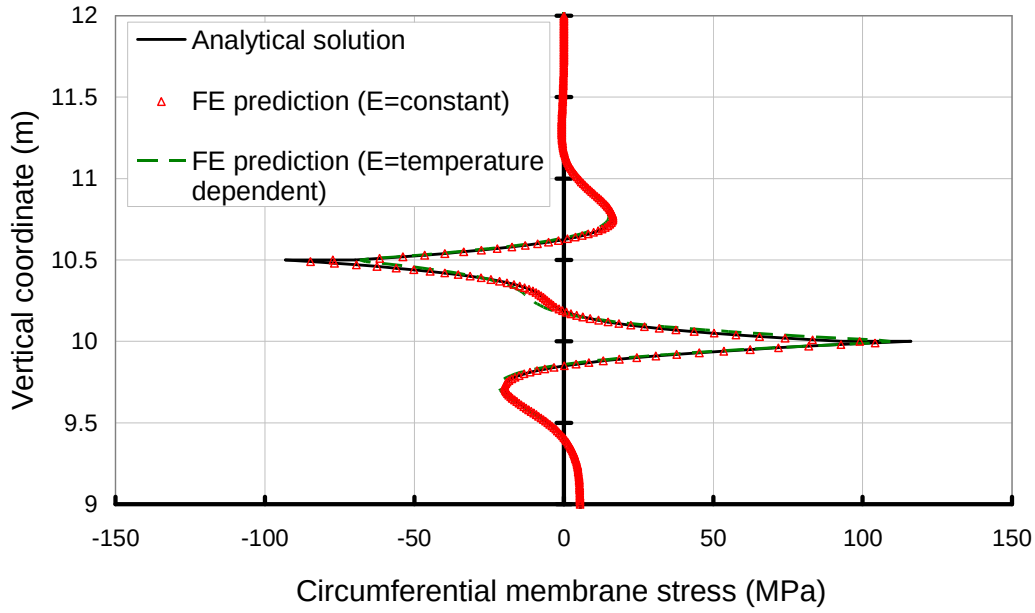

(b) Details in temperature transition zone

Figure 4-4 Verification: circumferential membrane stress

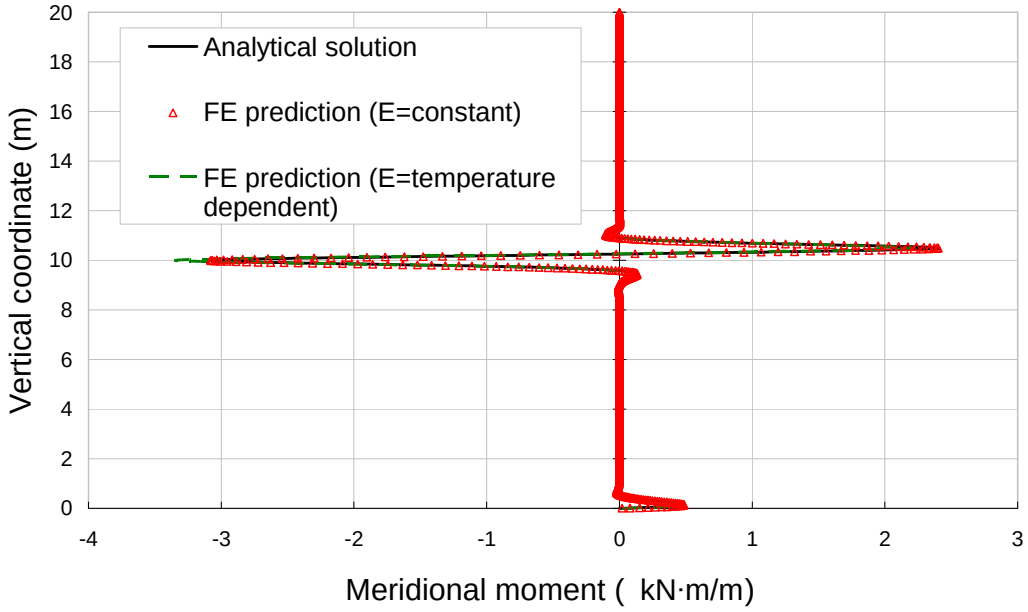

(a) Full range

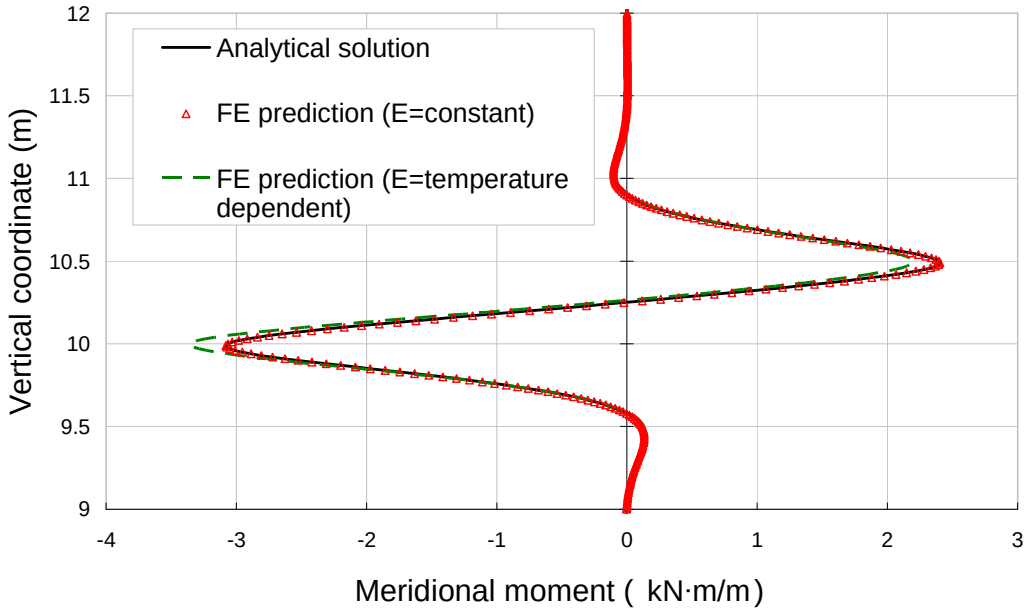

(b) Details in temperature transition zone

Figure 4-5 Verification: circumferential moment

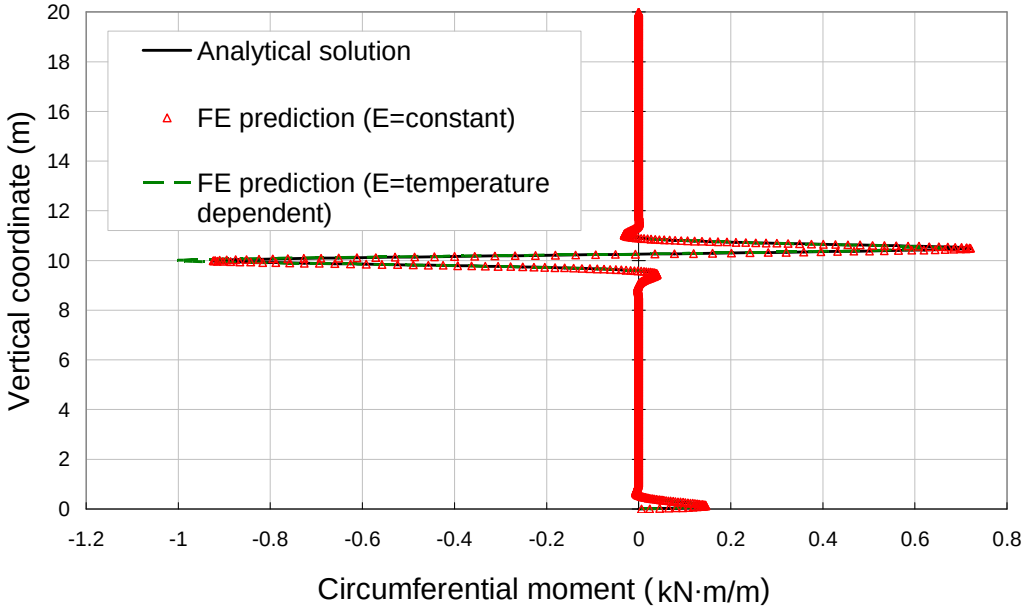

(a) Full range

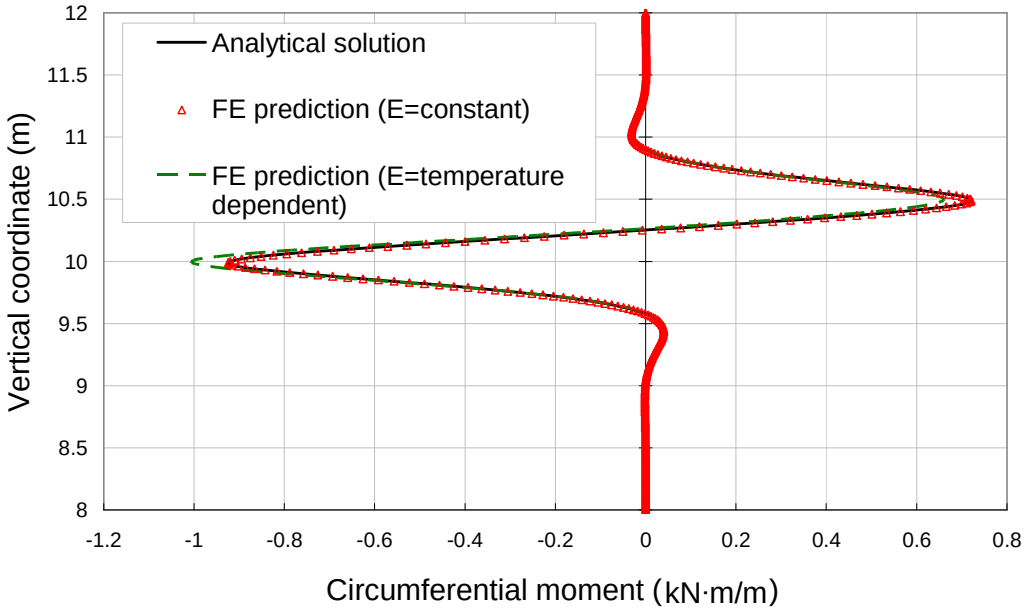

(b) Details in temperature transition zone

Figure 4-6 Verification: meridional moment

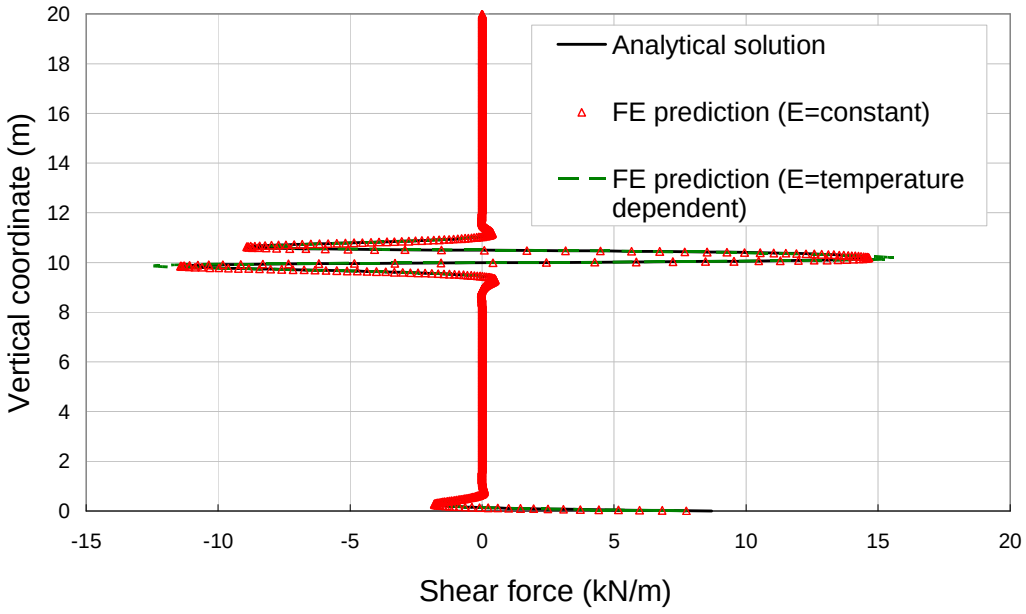

(a) Full range

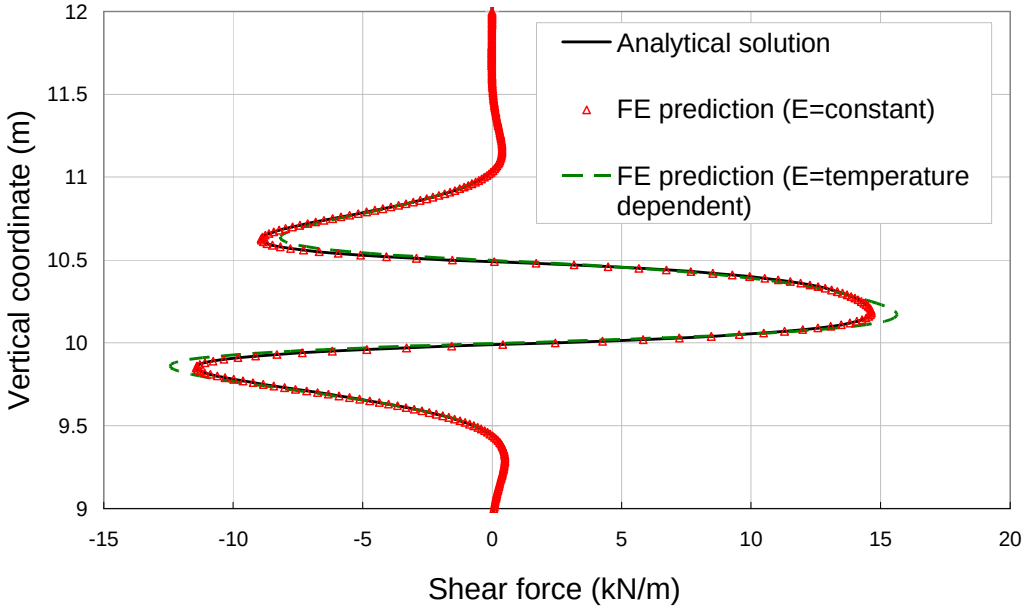

(b) Details in temperature transition zone

Figure 4-7 Verification: shear force

4.4 The effect of transition zone size

The effect of the transition zone size was examined by varying the length of the transition zone in the same model above. Figure 4-8 shows the radial displacement of the wall near the transition zone when the height of transition zone (l) increases from 0 to 100 times of the wall thickness t. It is seen that the amplitude of peak radial displacement due to the temperature change from the lower segment 1 to the upper segment 3 reduces with an increase of the transition zone size, indicating that a less abrupt change of the temperature along the wall can alleviate the local bending arisen from the thermal strain difference between the upper section 3 and the lower section 1. This is more clearly shown in Figure 4-9 where the maximum radial displacement is plotted against the transition height.

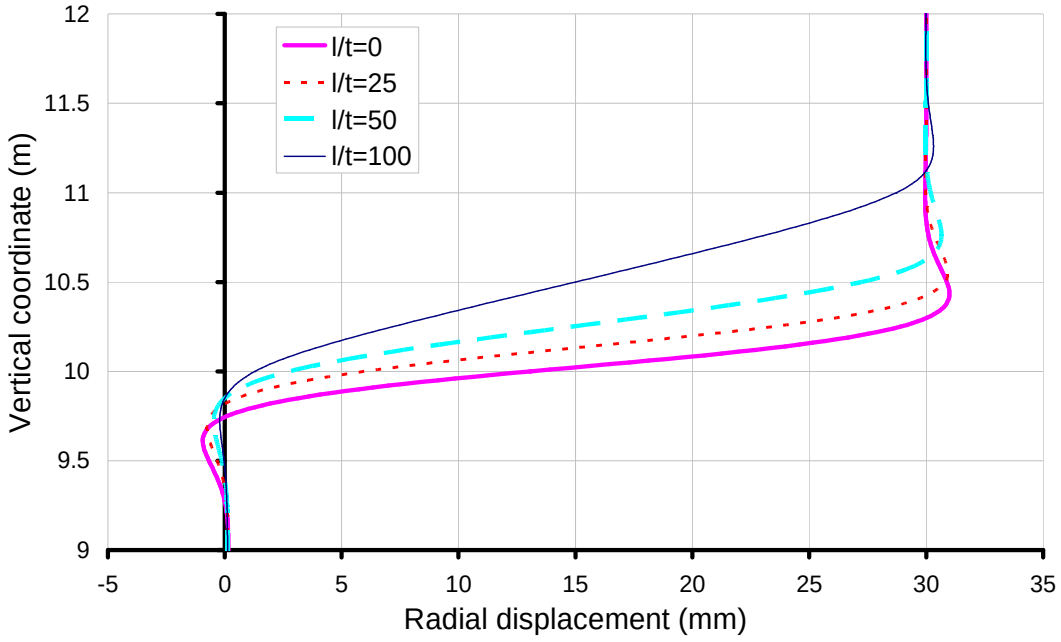

Figure 4-8 Radial displacement in the tank wall with transition zone heights

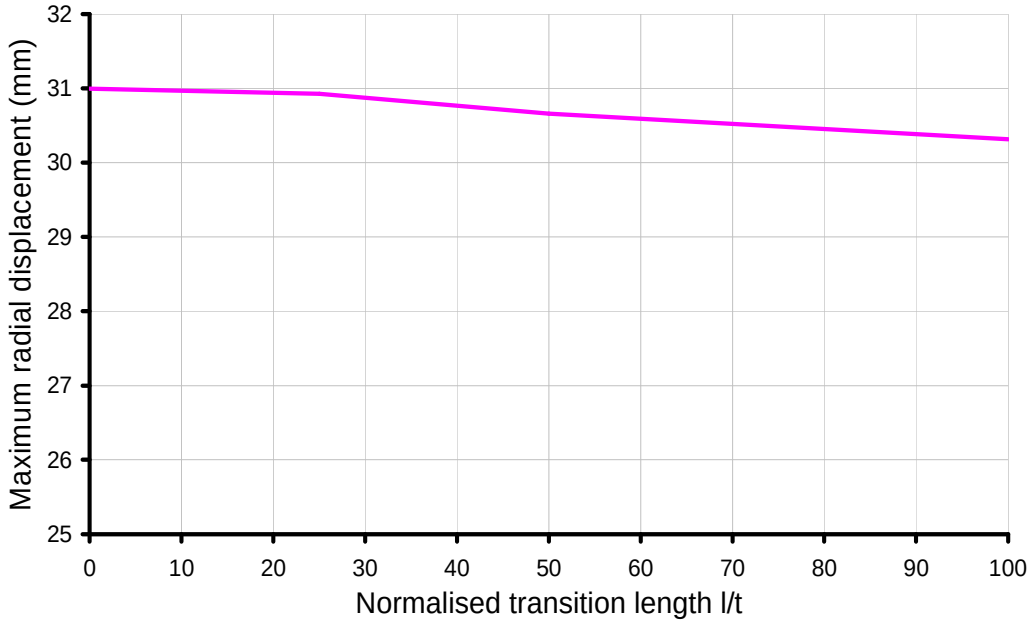

Figure 4-9 Maximum radial displacement versus normalise transition zone length *l*/*t*

Figures 4-10 to 12 show respectively the circumferential membrane stress, meridianal moment and shear force arisen due to the temperature change. Compared to the radial deformation, the effect of the transition zone size is more pronounced in these quantities. For example, when l increases from 0 to 100t, the maximum circumferential membrane stress is reduced by 90% (Figure 4-13).

From the above analysis, it may be concluded that size of the transition zone has a significant effect on local bending at the liquid surface level: an increase of the size leads to less local bending. This effect is more pronounced for the maximum meridional bending and circumferential membrane stresses than the radial displacement. This indicates that the accurate determination of the transition length is important for predicting the stresses in the tank wall.

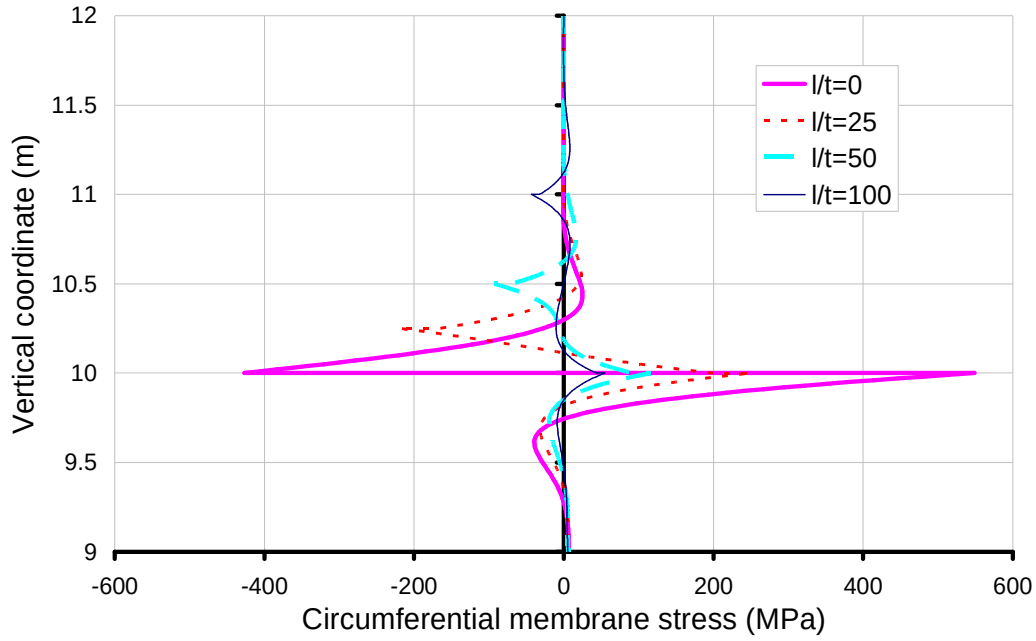

Figure 4-10 Circumferential membrane stress versus transition zone size *l*/*t*

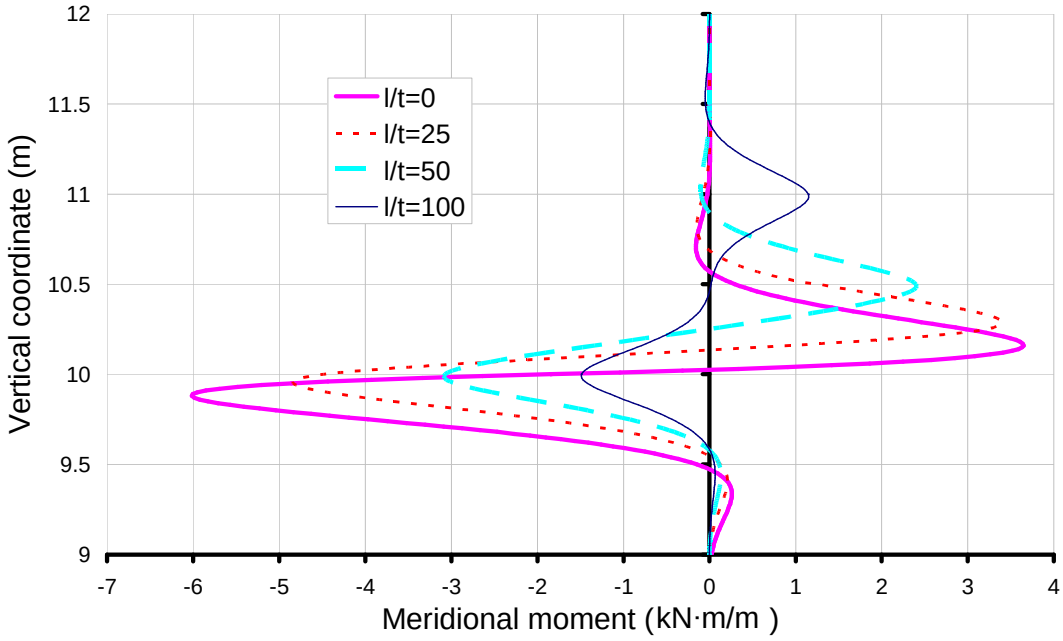

Figure 4-11 Meridional moment in the tank wall with different *l*/*t* values

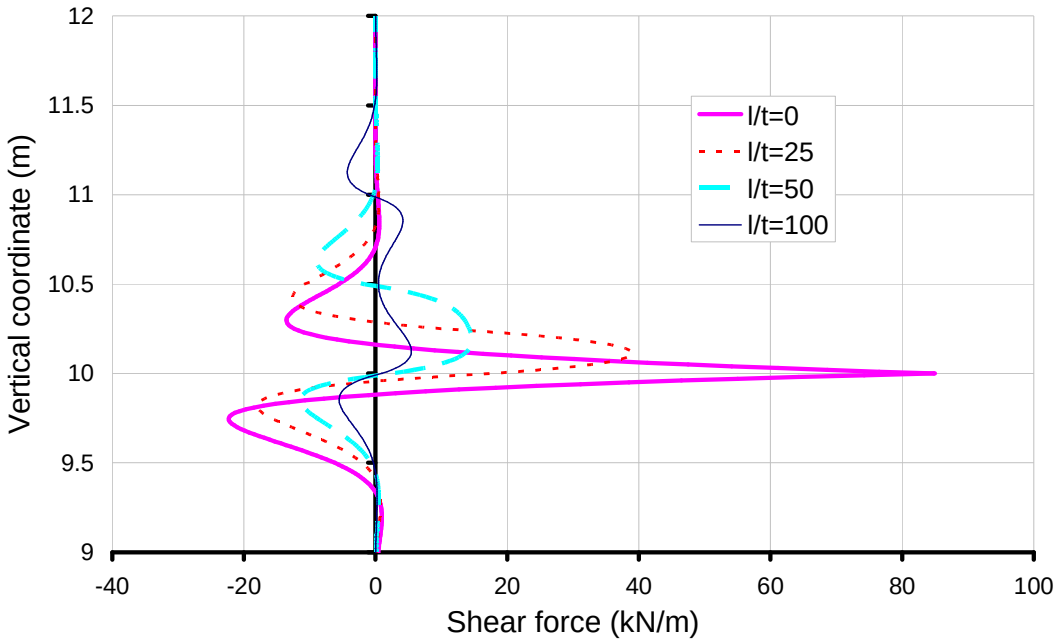

Figure 4-12 Shear force versus transition zone size *l*/*t*

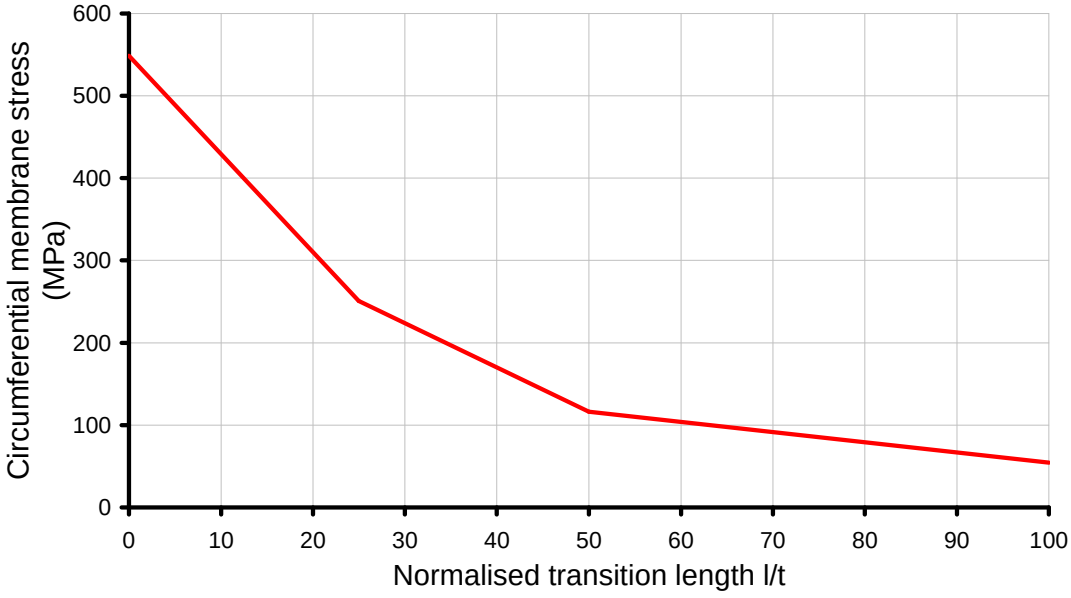

Figure 4-13 Maximum circumferential membrane stress versus transition zone size *l*/*t*

4.5 Conclusions

The thermal loading of the tank assumed in Chapter 3 contains an abrupt change of temperature at the oil surface level, which is a simplification of the real situation. A transition zone in which the temperature increases linearly from a low value at the lower segment of the tank wall to a high temperature of the upper segment is obviously more realistic to represent the temperature distribution in a partially-filled tank.

An analytical solution for the improved representation of temperature distribution on the partly-filled tank has been derived in this chapter. The solution for the stresses and displacements has been numerically validated by the finite element predictions. The results have shown that rather than adopting precisely the temperature dependent elastic modulus for the transition zone, using a constant average value in the transition zone appears to give satisfactory prediction of the stress and displacement with minimal errors.

The step change of temperature as adopted in Chapter 3 results in large local bending and circumferential membrane stresses at the liquid surface level. The introduction of the temperature transition zone in this chapter has led to a reduction of this local bending. The local bending is sensitive to the size of the transition zone: a larger transition zone leads to less local bending effect.

Chapter 5

5. Heat transfer modelling of a non-uniformly heated tank

5.1 Introduction

In the case of an oil tank fire, radiation can be sufficiently intense to threaten the integrity of adjacent structures, as well as the safety of nearby personnel and fire-fighters. In order to evaluate the hazards associated with such a scenario and predict the behaviour of adjacent structures, creditable modelling of the heat radiated by the flame is required. In Chapters 3 and 4, it was assumed that the temperature distribution was uniform around the circumference. However, the actual temperature distribution due to an adjacent fire should be uniformly: the side of the tank facing the fire has higher temperatures compared to the opposite side. As the stored liquid may absorb a significant amount of heat from the tank wall, the temperature distribution in the tank is also affected by the liquid level. In particular, the upper part of the tank wall which is not in contact with liquid would heat up much faster than the lower part that is in contact with liquid, because the heat transfer coefficient

of air is very low. Therefore the temperature of the steel tank wall shall vary both circumferentially and vertically. The existence of temperature gradients would lead to a complicated structural behaviour.

This chapter presents a numerical heat transfer analysis investigating the temperature distribution in a tank adjacent to a burning tank. The tank fire is treated as a problem of liquid hydrocarbon pool fire. The techniques adopted for modelling such pool fires will be introduced first. A finite element (FE) heat transfer analysis was conducted in Abaqus to obtain the temperature distribution in a steel cylindrical oil tank with conical roof. A parametric study was conducted to investigate the effect of possible fire scenarios having different fire size, location, tank geometry and filling level on the temperature pattern in the tank. In the next chapter, the predicted temperature distributions will be fitted by simple algebraic expressions which may serve as convenient guidance for future structural analysis.

5.2 Pool fire model

This section introduces the adopted pool fire model and its parameter selection. The oil tank fire scenario used in this study can be described as a fire burning in an open tank (Beyler 2004b). The premise is that an explosion has blown off the roof in a fixed roof tank with a weak roof-to-shell seam. This scenario does not preclude fire spread in fires involving massive overfilling or boilovers such that burning liquid flows around the adjacent tanks. Figure 5-1 shows the open tank fire scenario considered in this study. The flame height is assumed to have a height H_f, distance between the base of fire and the ground is denoted by H_{f0}. It is assumed that the base of the flame lies on the liquid surface in the burning tank and the flame radiation rate is constant over the entire flame surface irrespective of the possible wall obscuration.

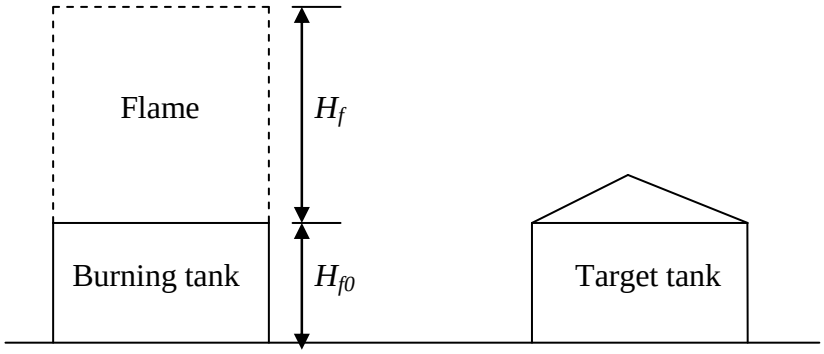

(a) Burning tank with full liquid inside

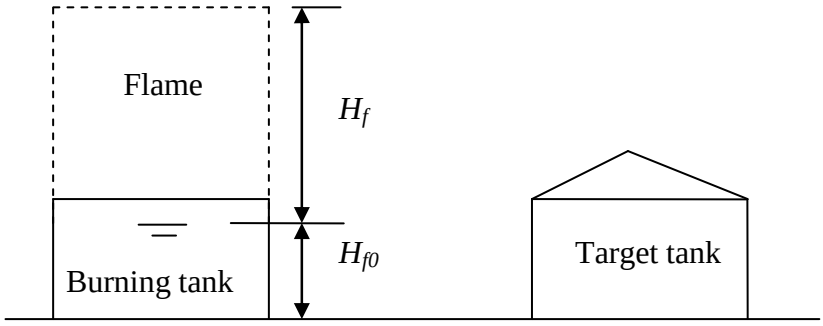

(b) Burning tank with partially filled liquid

Figure 5-1 Oil tank fire scenario

5.2.1 Heat transfer governing equation

In order to achieve an accurate prediction of the thermal radiation field around a pool fire, knowledge of three factors is required: the flame geometry and hence the view factor, the thermal radiative characteristics of the flame and the atmospheric transmissivity.

For a receiver adjacent to a liquid hydrocarbon pool fire, the incident thermal radiation can be generally determined by the following equation (Raj 2005; NFPA-58 2008):

$$E_t = \alpha_t \tau \varepsilon_f F E_f \tag{5-1}$$

where α_t is the absorptivity of the tank surface for fire radiation; τ is the atmospheric transmissivity; ε_f is the emissivity of the fire; F is the view factor; E_f is the emissive power of the fire and E_t is heat flux received by the target tank.

The atmospheric transmissivity is an important parameter in the model, as it takes account of the amount of radiation absorbed by the intervening atmosphere and the receiver. Atmospheric transmissivity is primarily dependent on the amount of water vapour in the atmosphere and the path length between the flame and the receiver. It's value is less than 1. For a conservative calculation in hazard assessment as in this research, the tansmissivity of the atmosphere may be taken to be 1.

The emissivity is the radiative property of a surface, with value in the range $0 \leq \varepsilon \leq 1$. This property provides a measure of how efficient the surface emits energy relative to a blackbody. In this study, the fire is considered to be optically thick at all locations along the visible height of the fire, that is to say that the fire can be considered as a "black body" emitter, thus emissivity is chosen as $\varepsilon_f = 1$.

The tank surface is assumed to be a grey surface, so that the absorptivity of the surface α_t is equal to the emissivity of the surface ε_s.

Substitute the above specific values into relevant parameters in Eq. 5-1, the received heat flux by the tank is expressed by

$$E_t = \varepsilon_t F E_f \tag{5-2}$$

5.2.2 Flame geometry

The radiation intensity at a given distance depends mainly on the radiative power and the flame's size and shape. The dimension of the flame area is characterized by the flame base diameter, visible flame height, and the flame tilt when considering wind effect. The flame diameter is dependent on the pool size. The flame height depends on the flame diameter and the burning rate. In this study upright circular cylinder

shape is chosen as the flame shape with its diameter equal to the tank diameter (Figure 5-2). The flame height depends on the flame diameter and the type of fuel characterised by the burning rate.

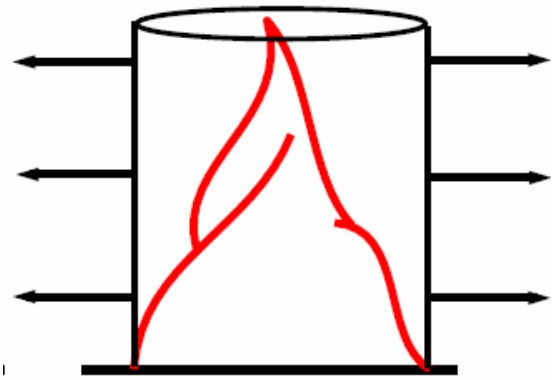

Figure 5-2 Cylindrical solid flame model

According to Eq. 2-6 (Thomas 1963) and Eq. 2-7 (Heskestad 1995), the flame height can be calculated for specific fuel and fire diameter. The parameters in these two correlations are the mass burning rate per unit surface area $\dot{m}''$, the rate of heat release $\dot{Q}$, the heat of combustion of the volatiles ΔH_c, an efficiency factor that takes into account incomplete combustion χ_{chem} and the pool fire diameter D_f.

The mass burning rate $\dot{m}''$ can be equal to the asymptotic burning rate when diameter of the fire D_f is approximately 2m or larger. Hydrocarbon liquids have values of $\dot{m}''$ in the range of 40-100g/sec-m^2 and heat of combustion ΔH_c in the range of 40-45kJ/g. Assume χ_{chem} = 1, their chemical heat release rate is in the range of 1.6-4.5 MW/m^2. There is evidence that the above value of $\dot{m}''$ overestimates the burning rate in very large pool fires in the order of tens of meters in diameter. According to Babrauskas (1986), the actual burning rate per unit area is no less than 80% of the above values.

For $\dot{m}''$ in the range of 40-80g/s·cm^2, ρ_o equal to 1.204kg/m^3 which corresponds to the density of air at 20°C, the minimum and maximum flame height for different liquid

can be calculated from Eqs 2-6 and 2-7. Figure 5-3 shows the flame height obtained for pool diameter in the range of 10m to 100m.

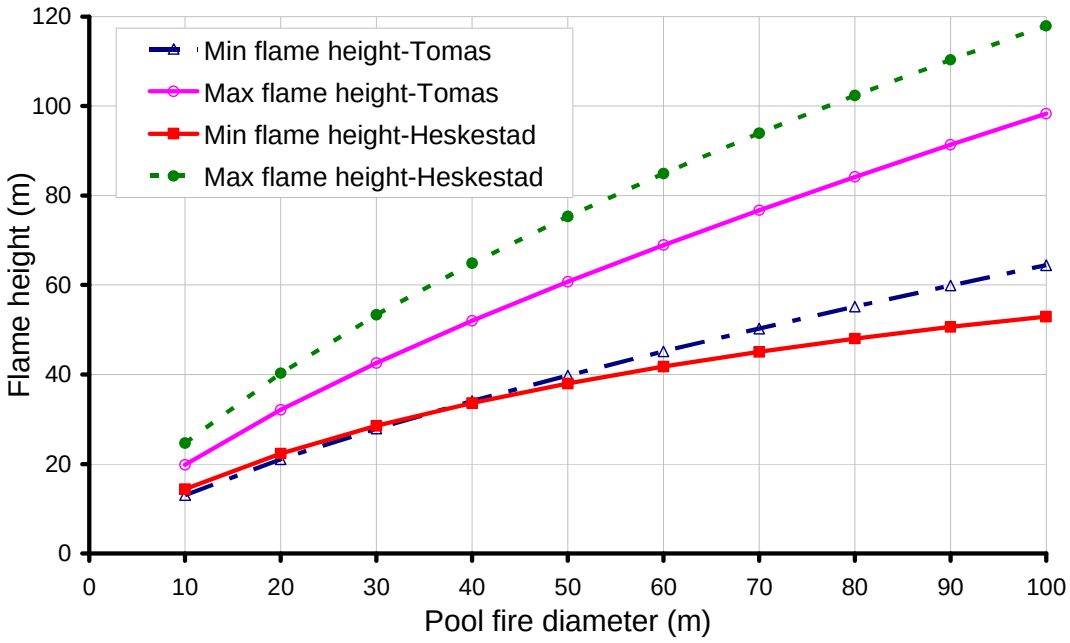

Figure 5-3 Variation of flame height with pool fire diameter

Winds can significantly increase the effective pool fire diameter and the mass burning rate. Wind tends to tilt and increase the flame diameter in the downwind direction which increases the heat flux reaching the exposed tank. Instead of modelling the flame with a tilt cylinder, the effect of wind may be taken into accounted by adopting a high emissive power for the flame so it is not explicitly modelled in this study.

5.2.3 Emissive power

The average surface emissive power (SEP) E_f is the energy radiated per unit nominal area of the visible fire plume, with radiation along the normal to this nominal surface of the fire. Values of flame emissive power for flammable liquid pool fires have been reviewed by Mudan and Croce (1988) and the diameter related correlation is shown in Figure 2-3 in Chapter 2. They explained that the emissive power depends on

whether or not the flame from the large pool fire is obscured by smoke on the outer periphery of the fire. This has been the case for large pool fires of gasoline, kerosene, and JP-4. From their study, the average surface emissive power is less than 40 kW/m^2 for pool diameters larger than 20m. However, liquid not prone to smoke obscuration of the flame surface would have emissive powers of 100-120kW/m^2 even at diameters in the order of 10m (Beyler 2004b), corresponding to a black body flame temperature of 880°C -935°C. Therefore, if the average surface emissive power is adopted for the whole flame, the radiation received by the surrounding structures near the luminous zone of the flame will be underestimated. In this study, a constant value corresponding to the luminous part of the fire is adopted for the whole flame height regardless of the diameter of the fire. This consideration also compensates the non-conservative consequence of adopting an upright cylinder for the flame shape. When wind is present, the flame is tilted, so the tank placed in the wind direction receives more heat flux due to a higher viewfactor F. In the reference case a flame temperature of 915°C is adopted, while the effect of the temperature value is evaluated in section 5.5.3.

5.2.4 Viewfactor

The viewfactor can be calculated internally in the Finite element software Abaqus according to Eq. 2-11.

5.3 Heat exchange between storage tank and environment

5.3.1 Heat exchange mechanisms

The heat exchange between the storage tank and environment occurs in three means: radiation, convection and conduction. Radiation is the dominant mechanism in case of fire. Tank surface receives radiation from adjacent tank fire and radiates out from its own surface to the environment. From all surfaces of the tank wall the dominating heat transmission mechanism to the contained liquid and air inside is convection.

Conduction is the heat transfer mechanism by which heat is transferred within the tank wall. Heat is transferred from the hotter tank walls to the colder parts of the tank by conduction. In the following analysis, all these heat transfer mechanisms are taken into consideration for the estimation of temperature of the tank wall.

Table 5-1 presents the heat transmission mechanisms considered for each part of the system. The conduction between liquid and tank wall was ignored, as it transfers very small magnitude of heat compared to that of convection.

In the scenario of a confined tank fire, the temperature rise of the ground would be limited. The radiation energy of a body is proportional to the forth power of its temperature. As a result, compared to the radiation energy released directly from the fire, the radiation energy released from the ground should be much smaller. Consequently the ground radiation was neglected from the numerical modelling.

Table 5-1 Heat transmission mechanisms in different parts of the system (thermal boundary conditions)

System parts		Heat transfer mechanisms
Target tank	External surface of the tank	Receive radiation from the fire and radiate out; convection to surrounding air
	Internal surface of the tank	Convection to air and liquid inside of the tank
	All tank wall	Conduction
Burning tank	External surface of the tank	Radiation to the target tank and convection to ambient air

5.3.2 Temperature of the burning liquid

Only the surface layers of a deep pool of pure liquid fuel is heated during steady burning (Drysdale 1999). The surface temperature of a freely-burning liquid is close to, but slightly below, its boiling point. Liquid mixtures, such as petrol, kerosene and

fuel oil, will form a hot zone which has a certain depth in steady-state. The precise mechanism of hot zone formation has not yet been established. In the following analysis, the temperature of the liquid in the tank on fire is assigned to a constant value of 100 °C.

5.3.3 Heat transfer coefficient of liquid

The convection heat transfer in the oil tank is natural convection. Fluid motion is induced by density differences resulting from temperature gradients in the fluid. The heat transfer coefficient for this regime is related to the buoyancy and the thermal properties of the fluid through dimensionless Rayleigh number R_a. When the Rayleigh number is below the critical value for that fluid, heat transfer is primarily in the form of conduction; otherwise is primarily in the form of convection. The Rayleigh number R_a is the product of the Grashof number Gr_L, and the Prandtl number Pr. The former describes the relationship between buoyancy and viscosity within a fluid and the latter describes the relationship between momentum diffusivity and thermal diffusivity (Incropera *et al.* 1996):

$$Ra_L = Gr_L \,\mathrm{Pr} = \frac{g\beta(T_s - T_\infty)L^3}{\nu\alpha} \tag{5-3}$$

where the fluid properties α , β and ν are evaluated at the film temperature $T_f \equiv (T_s + T_\infty)/2$, in which T_s is the surface temperature and T_∞ is the liquid temperature; β is the volumetric thermal expansion coefficient (K^{-1}); α is thermal diffusivity (m^2/s); and ν is the specific volume (m^3/kg).

The Nusselt number is defined as the ratio of convective to conductive heat transfer across the boundary. An empirical expression for the Nusselt number Nu_L is

$$Nu_L = \frac{\bar{h}L}{k} = CRa_L^n \tag{5-4}$$

in which $\bar{h}$ is the average convection coefficient for a surface of length L; k is the thermal conductivity; $n = \frac{1}{4}$ for laminar flows; C depends on fluid, the surface geometry, and the Rayleigh number. For common plate, cylinder, and sphere configurations, it is found to vary in a relatively narrow range of 0.45 to 0.65 for laminar flow and 0.11 to 0.15 for turbulent flow past the heated surface. The following expression for Nu_L has been developed for vertical plate

$$Nu_L = \left\{ 0.825 + \frac{0.387 Ra_L^{1/6}}{\left[1 + (0.492/\mathrm{Pr})^{9/16}\right]^{8/27}} \right\}^2 \tag{5-5}$$

in which $\mathrm{Pr} = \frac{\nu}{\alpha}$.

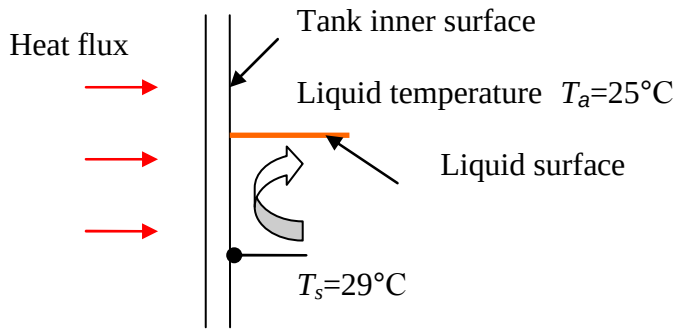

Figure 5-4 Convection in a tank

Although both circumferential and vertical temperature gradients may exist, for simplicity, the liquid temperature is assumed to be the same anywhere. Considering the large thermal inertial of liquids, the liquid temperature may be assumed to be equal to an ambient temperature $T_a = 25$ °C. For a typical material suitable for storage in an oil tank, say isopentane, its thermal property can be obtained from Bejan and Kraus (2003). Its thermo physical properties at T=300K are c_p=2.3239, k=95.472, μ=241.39, ρ=613.33, β=0.007. $\alpha = k/(\rho c_p)$=0.06698, $\nu = \mu/\rho$=0.88271, $P_r = \nu/\alpha$=13.1696. Here c_p is isobaric heat capacity (kJ/kg·K); k is thermal

conductivity (mW/m·K); μ is viscosity (μPa·s); ρ is density (kg/m^3). Assuming that the temperature of a steel tank constant at T_s=29°C (Figure 5-4) before heat transfer, substituting the above values together with liquid depth in the tank L=10m, the Rayleigh number $Ra_L=4.64\times10^{15}$, the Nusselt number Nu_L=23159.7 into Eqs 5-3 and 5-5 gives $\bar{h}=Nu_L\cdot k/L$=319.6. The $\bar{h}$ value for several liquid levels are evaluated and listed in Table 5-2 which shows that the heat transfer coefficient is dependent on the liquid depth but the dependency is weak for the studied case.

Table 5-2 Heat transfer coefficient change with liquid depth

Liquid level (m)	1	5	10	15
$\bar{h}$ ($W/m^2\cdot K$)	327.1	321.0	319.6	319.0

In the above analysis, the temperature of the tank surface was assumed to be known in advance. The accuracy of this simplification may be checked via a heat transfer analysis. Using $\bar{h}$=320 for the fluid in the tank, the mean value of the predicted temperature in the steel tank wall is 37.45°C. The film temperature is thus $T_f=(T_s+T_a)/2$=304.4K is only slightly different from the assumed 300K. This confirms that the assumed value of temperatures for the liquid is acceptable.

In cases where the calculated surface temperature is significantly different from the assumed value, iterations are required for determining the heat transfer coefficient. For the reference case in this study, $\bar{h}$=320 is adopted.

5.3.4 Emissivity of the target tank

The value of wall emissivity depends on the condition of the wall surface. According to the emissivity data in Holman (1990), mild steel has an emissivity in the range of 0.2-0.32 whereas sheet steel with a 'rough oxide layer' has an emissivity of 0.81 at T=300K. The emissivity may vary with temperature, but the variation is within 5% between T= 300K and T=800K (Madding 2002).

A value of ε=1 which is the upper bound of emissivity was adopted in the reference case for the tank wall. The effect of emissivity on the temperature distribution of the target tank will be investigated in section 5.5.3.

5.3.5 Tank spacing

Tanks are assumed to be spaced at a minimum distance specified by NFPA30(1996). The minimum tank spacing for different tanks is reproduced in Table 5-3. Table 5-4 summarizes the parameters used in the heat transfer analysis in this chapter.

Table 5-3 Minimum Tank Spacing (Shell-to-Shell) (NFPA 30 1996)

		Floating Roof Tanks	Fixed or Horizontal Tanks	
			Class I or II Liquids	Class IIIA Liquids
All tanks not over 150 ft in diameter		1/6 sum of adjacent tank diameters but not less than 3 ft	1/6 sum of adjacent tank diameters but not less than 3 ft	1/6 sum of adjacent tank diameters but not less than 3 ft
Tanks larger than 150 ft in diameter	If remote impounding is provided in accordance with 2.3.2.3.1	1/6 sum of adjacent tank diameters	1/4 sum of adjacent tank diameters	1/6 sum of adjacent tank diameters
	If diking is provided in accordance with 2.3.2.3.2	1/4 sum of adjacent tank diameters	1/3 sum of adjacent tank diameters	1/4 sum of adjacent tank diameters

For SI units, 1 ft = 0.3 m.

Table 5-4 Summary of parameters used in the reference case

Parameter	Symbol	Value
Emissivity	α	1
Absorptivity	ε	1
Atmospheric transmissivity	τ	1
Flame height	H	(1~2)D_f
Temperature of fire	T	915°C
Heat transfer coefficient of the liquid	$\bar{h}_{liquid}$	320 W/m^{2}K
Thermal conductivity of steel	k	45.8 W/m^{2}K
Heat transfer coefficient of air	$\bar{h}_{air}$	25 W/m^{2}K
Ambient temperature	T_{amb}	20°C
Temperature of the liquid inside of target tank	T_{tliq}	20°C
Temperature of the liquid inside of tank on fire	T_{fliq}	100°C

5.4 Test cases

In this thesis, the finite element software package Abaqus (Simulia 2008) was used to determine the temperature distribution in the oil tank. Steady-state heat transfer analysis was conducted. The heat transfer analysis in Abaqus can predict the temperature distribution in the oil tank surface from the convective and radiative effects at the boundaries. Before conducting the heat transfer analysis for the complicated models in Abaqus, a benchmark test for the 1-D model was performed first followed by a comparison of 2-D and 3-D model in Abaqus.

5.4.1 1D model

An example was taken from Beler (2004b) as a benchmark test here. A steel tank is exposed to a heat flux q'' at its outer surface. The heat transfer mechanisms are shown in Figure 5-5, in which radiation exchange is assumed to occur between the outer surface of the plate and the surrounding air and convection happens on both outside and inside of the plate. Conduction exists in the steel wall.

The thickness of this plate is *t*. The surrounding temperature of air is 20°C. The heat transfer coefficient of air h_{air} is 25W/m^{2}K. The emissivity of both inner and outer surfaces is assigned to 0.8. The upper and lower ends of the wall are insulated.

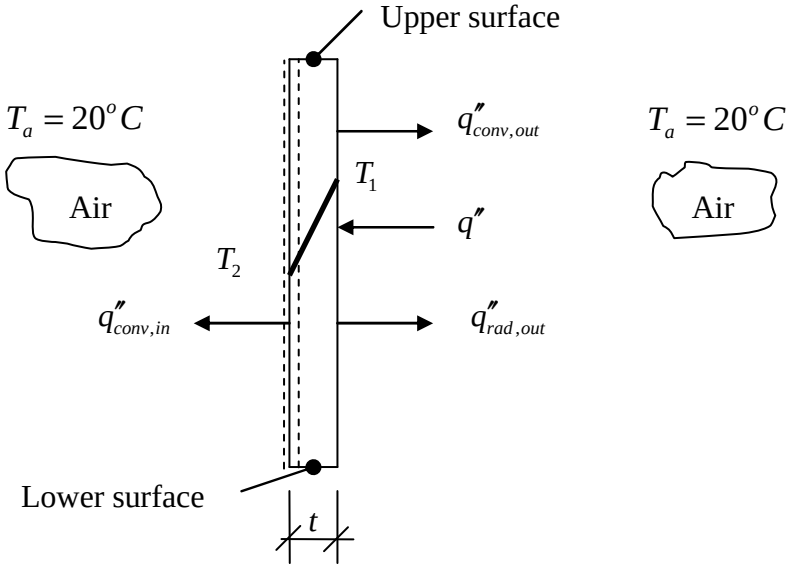

Figure 5-5 Conservation of energy for a plate

The general form of the energy conservation requirement is expressed on a rate basis for a given volume as

$$\dot{E}_{in} + \dot{E}_g - \dot{E}_{out} = \dot{E}_{st} \tag{5-6}$$

where $\dot{E}_{in}$ is the rate of energy entering into the system; $\dot{E}_{out}$ is the rate of energy exiting the system; $\dot{E}_g$ is the rate of energy generated in the system; $\dot{E}_{st}$ is the rate of energy stored in other forms (other than heat) into the system. As no heat is generated and no energy is stored in the plate, the energy conservation requirement may then be expressed as:

$$\dot{E}_{in} = \dot{E}_{out} \tag{5-7}$$

At a steady state, the energy balance takes the form of:

$$q''_{conv,in} = q'' - q''_{conv,out} - q''_{rad,out} \tag{5-8}$$

in which $q''_{rad,out}$ represents the net radiation exchange per unit area from the outer surface to the surroundings; $q''_{conv,out}$ and $q''_{conv,\mathrm{int}}$ are the convective heat flux at the outer surface and inner surface respectively. $q''_{rad,out}$, $q''_{conv,out}$ and $q''_{conv,\mathrm{int}}$ can be expressed as functions of the temperature of the surface, which are $q''_{rad,out} = \varepsilon_w \sigma\left(T_1^4 - T_a^4\right)$, $q''_{conv,out} = \bar{h}_{out}\left(T_1 - T_a\right)$, and $q''_{conv,in} = \bar{h}_{in}\left(T_2 - T_a\right)$. Substituting these terms into Eq. 5-8 gives:

$$\bar{h}_{in}\left(T_2 - T_a\right) = q'' - \bar{h}_{out}\left(T_1 - T_a\right) - \varepsilon_w \sigma\left(T_1^4 - T_a^4\right) \tag{5-9}$$

Conservation of energy requirement at the inner surface requires:

$$q''_{conv,in} = q''_{cond} \tag{5-10}$$

Substituting the expressions of $q''_{conv,in}$ and expressing the steady state conduction rate equation of $q''_{cond} = k\left(T_1 - T_2\right)/t$ into Equation 5-10 gives:

$$\bar{h}_{in}(T_2 - T_a) = k(T_1 - T_2)/t \tag{5-11}$$

Substituting q''=45493 W/m^2, $\bar{h}_{in} = \bar{h}_{out}$ =25W/m^{2}K, k=45.8W/m^{2}K, T_∞=20°C, ε_W=0.8, σ=5.669×10^{-8}W/m^{2}K^{4}s and t=0.001m into Eqs 5-9 and 5-11 and solving the resulting equations give T_1=540.0°C, T_2=539.8°C.

A simple model was created in Abaqus to compare the above analytical solution. Using the same properties and applying the same convective and radiative boundaries to the model in Abaqus, the predicted surface temperature are T_1=540.0°C and T_2=539.8°C, matching exactly with the analytical solutions.

5.4.2 2D model

In order to obtain the temperature distribution on the target tank, the viewfactor of each element needs to be accurately calculated. Abaqus accomplishes this task by conducting a 'cavity radiation' analysis. For a cavity radiation problem, the user needs to define all the surfaces in the cavity and the radiation properties of each surface. The cavity could be close or open. The open cavity is defined by specifying a value for the ambient temperature. Cavities are composed of surfaces which in turn are made up of finite element faces. For the purpose of viewfactor calculations, a cavity may be treated as a collection of element faces (or facets) corresponding to the finite element discretization around the cavity. Radiation within a cavity implies that every surface exchanges heat with every other surface. The sum of viewfactor at each element is equal to one as a result of the fact that all rays from surface *i* must strike some other surface *j* in an enclosed cavity. For an open cavity this sum is always less than one, indicating radiation to the ambient, which is the case of the current study.

To examine the temperature around the circumference of a tank, a model with two circular sections which represent the sections of two tanks separated from each other by a wall to wall distance of 20m was created in Abaqus (Figure 5-6). The diameter

of the target tank degignated as D is assumed to be 20m, the diameter of the heater (fire) is assumed to have the same diameter as the target tank (D_f=20m), and the thickness of the wall is t=0.01m. The distance between the fire and the tank is assumed to be 20m (d=20m). The tank on the right hand side is assumed to be on fire and produces uniform radiation. The temperature of the heater was set to 1000°C which corresponds to a heat flux of 120 kW/m^2.

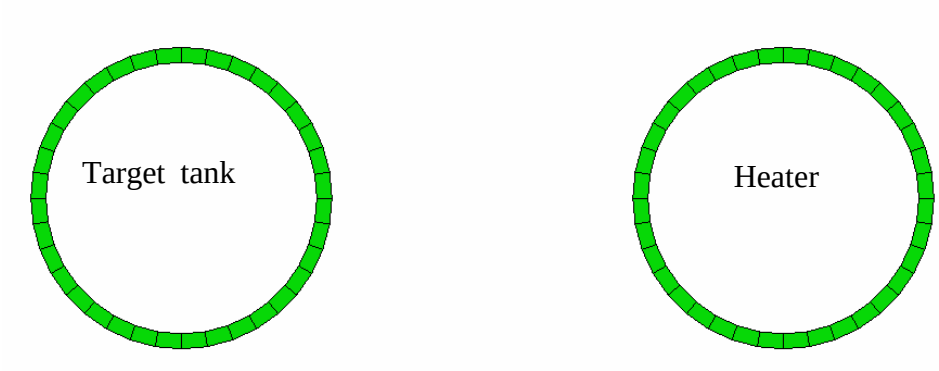

Figure 5-6 2-D FE model for calculating the view factor (D=D_f=20m, d=20m)

Radiation between the outer surfaces of these two tanks was considered by using CAVITY RADIATION in Abaqus. An emissivity of 1 was assigned to both surfaces.

Convection and conduction were also considered in this analysis. Both the inner and the outer surface of the tank on left hand side were assigned to SURFACE FILM interaction. Within this interaction a sink temperature is specified which represent the ambient temperature of 20°C. The same FE mesh was used for both sections. The 4-node linear diffusive heat transfer element DC2D4 was used for both sections.

The predicted steady state temperature of the outer surface around circumference of the target tank is shown in Figure 5-7, where θ=0° corresponds to the most heated meridian.

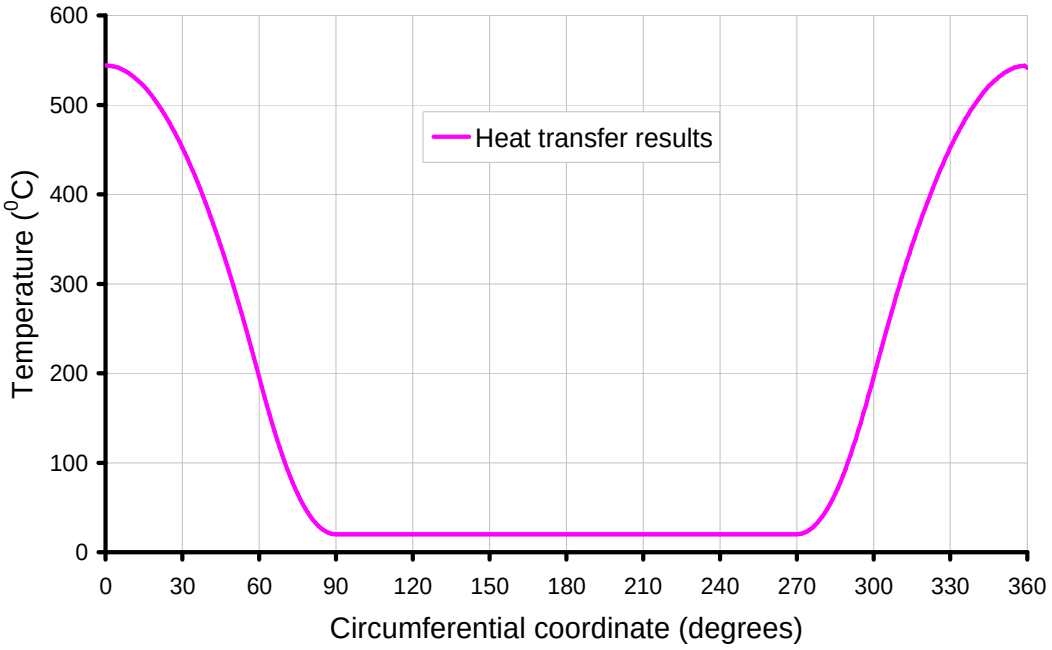

Figure 5-7 Temperature distribution on the outer surface of the tank (D=D_f=20m, d=20m)

It shows that when the tank is exposed to a heat flux from a radiator of the same size, nearly one half of the section is heated, and the other half away from the heater remains at the same temperature as the ambient air. The temperature of the heated part follows roughly a cosine function like distribution. The highest temperature is about 535°C occurring at 0 degree, reducing gradually along both sides.

5.4.3 3D Model

The 2-D model may represent the case of two infinite long cylinders radiating each other. Thus the temperature predicted from the 2-D model must be the highest temperature from which two cylinders with a finite length could reach under the same conditions. This 3D effect is considered in this section.

A model of two long cylinders of the same dimension was created as shown in Figure 5-8. The same boundary conditions as those in the 2-D model were applied. The 4-node quadrilateral shell element DS4 was adopted for modelling the tank and

fire. The adopted meshes were uniform in both the circumferential and vertical directions for both cylinders.

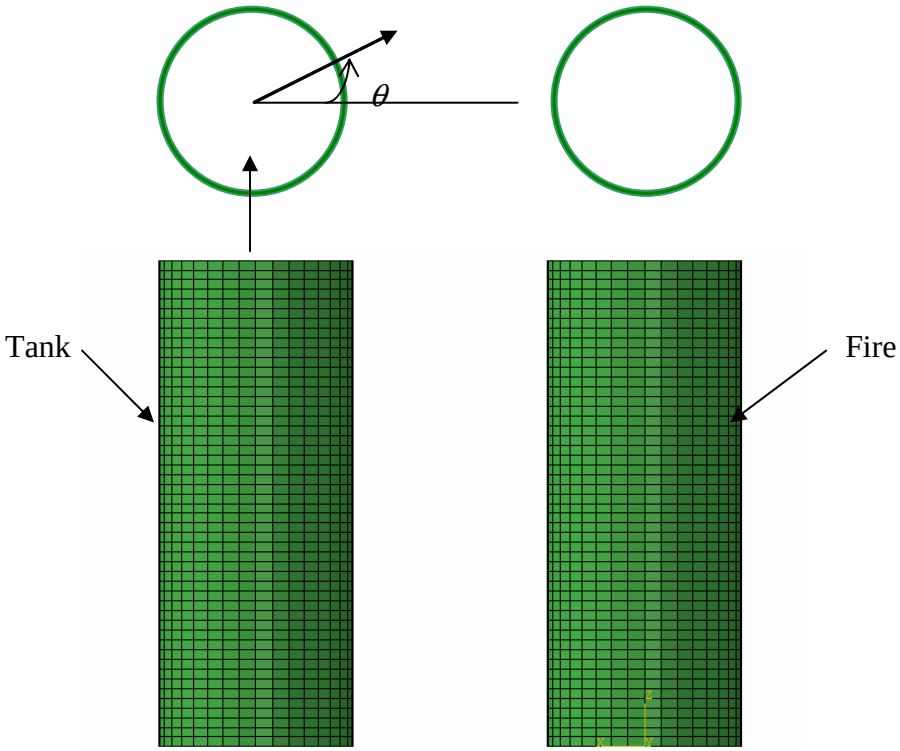

Figure 5-8 3D heat transfer analysis model (D=D_f=20m, d=20m, H_{f0}=0m, H_f=100m)

The predicted temperature distribution along the most heated meridian is shown in Figure 5-9 for two 100m long cylinders. The temperature varies along the height because viewfactor varies: it is higher where the elements can be seen more by the heater. As the energy of each element was assigned to be concentrated at the centre of each element in the simulation, the FE mesh size has some effect in the prediction as shown in Figure 5-9. It shows the temperature distribution prediction converges when the mesh is refined. A very coarse mesh may significantly over predict the temperature but the prediction converges quickly when the mesh is refined.

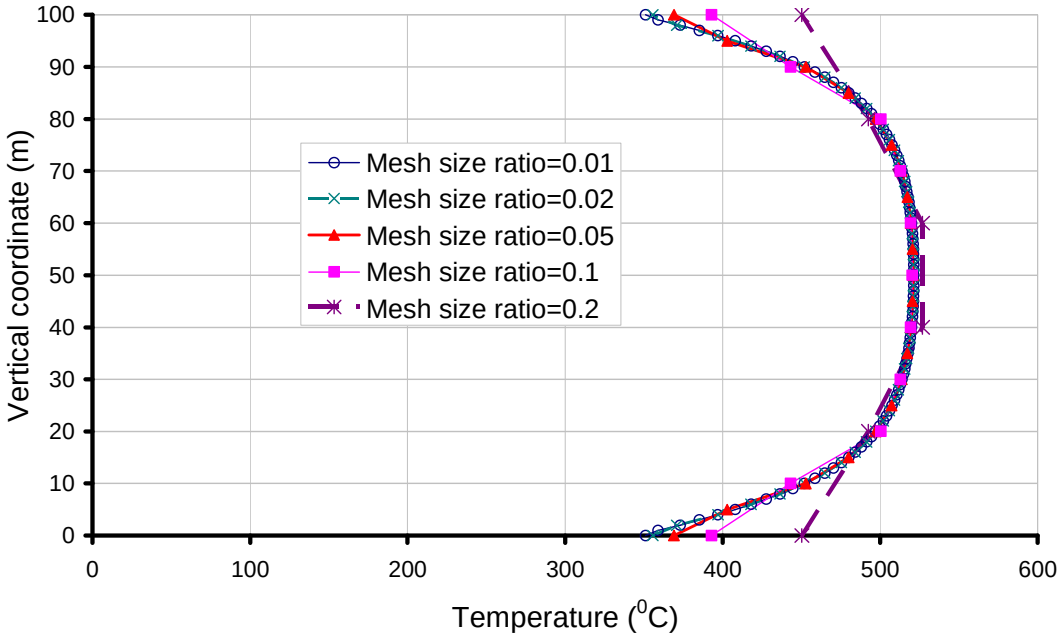

Figure 5-9 Effect of vertical mesh size on the temperature along the most heated meridian (D=D_f=20m, d=20m, H_{f0}=0m, H_f=100m)

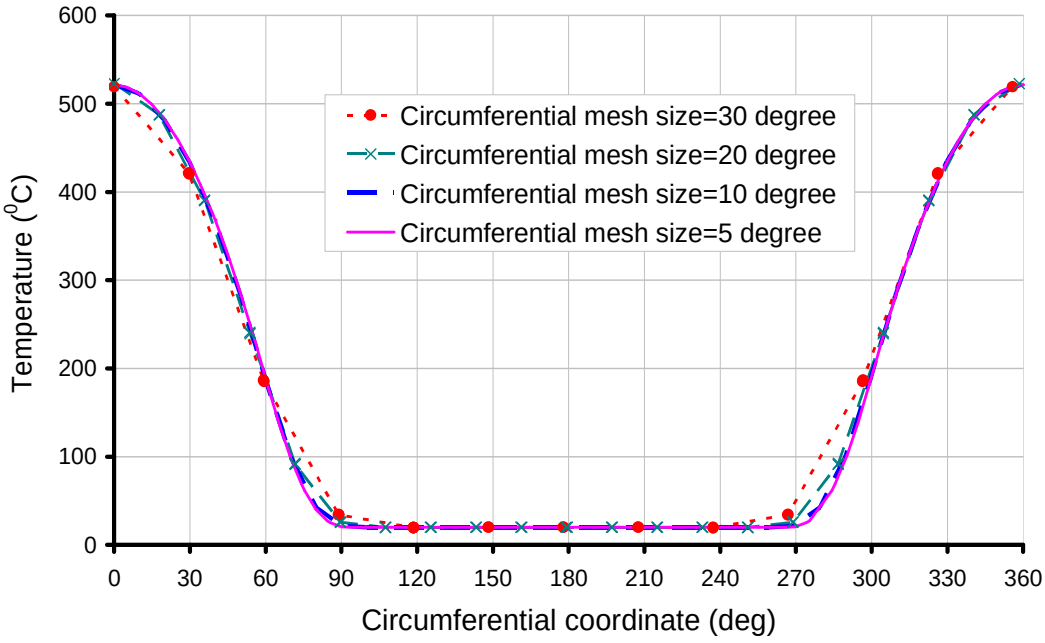

Figure 5-10 Effect of circumferential mesh size on the temperature distribution around the circumference at z=50m (D=D_f=20m, d=20m, H_{f0}=0m, H_f=100m)

Figure 5-10 shows the effect of mesh size around the circumference on the predicted temperature distribution, which suggests a mesh size of 10-degree for each element is sufficient small in predicting the converged temperature distribution. As a result in all the following analyses, the adopted element mesh was 5 degrees around the circumference and 0.5m in the vertical direction.

For tanks with different heights, the predicted temperature distributions along the most heated meridian and that around the circumference at the mid-height of the tank are shown in Figure 5-11 and Figure 5-12 respectively. Figure 5-13 shows the maximum temperature on the outer surface of the tank, which indicates that as the length of both cylinders increase, the highest temperature on the outer surface of the cylinder approaches that of the 2-D model (Figure 5-7).

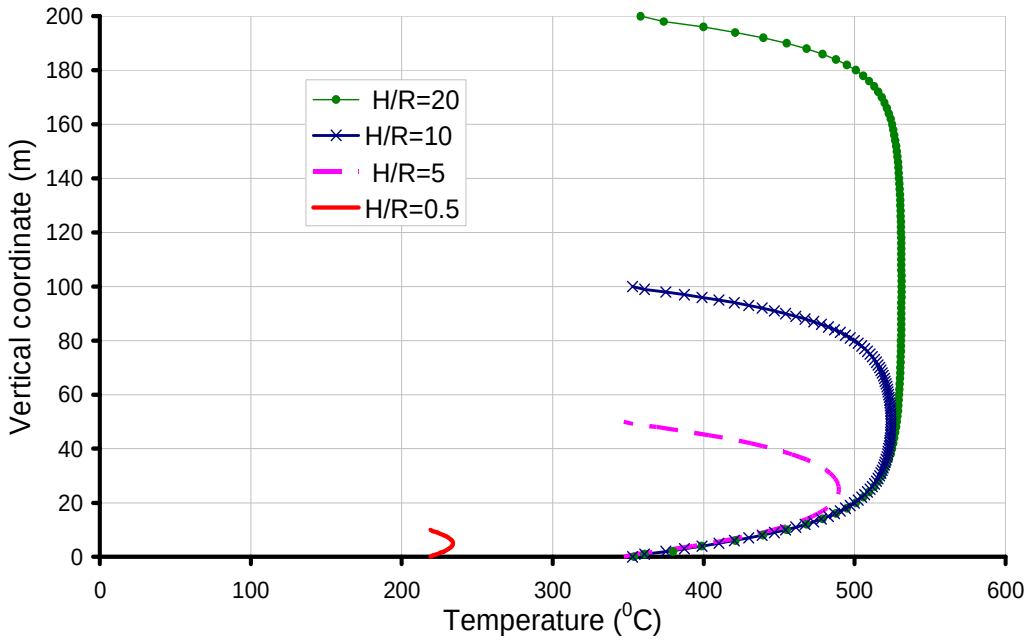

Figure 5-11 Temperature distribution along the most heated meridian (D=D_f=20m, d=20m)

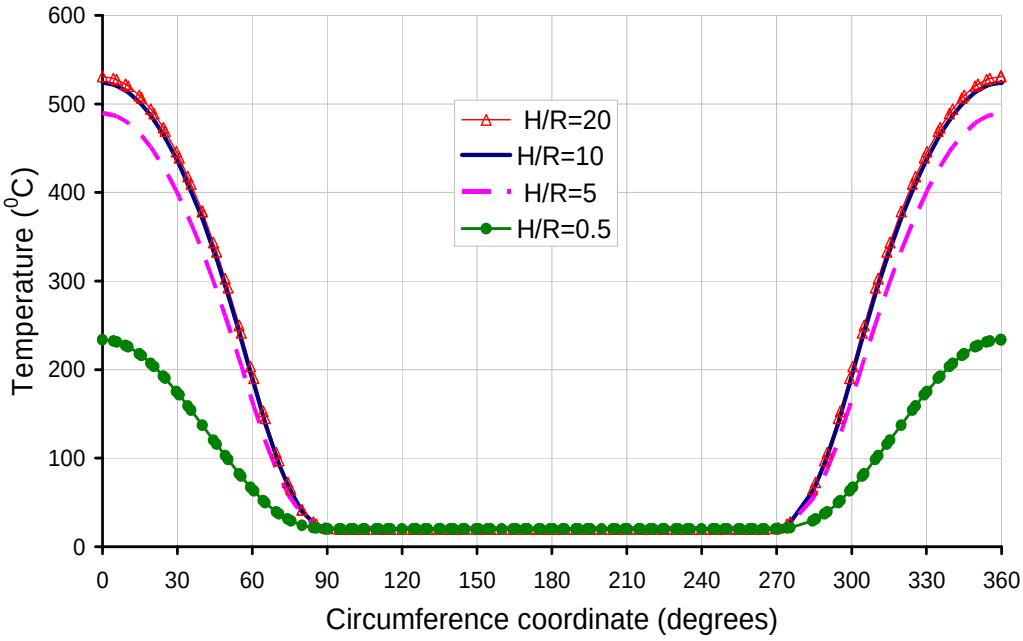

Figure 5-12 Temperature distribution around circumference at mid-height of the tank (D=D_f=20m, d=20m)

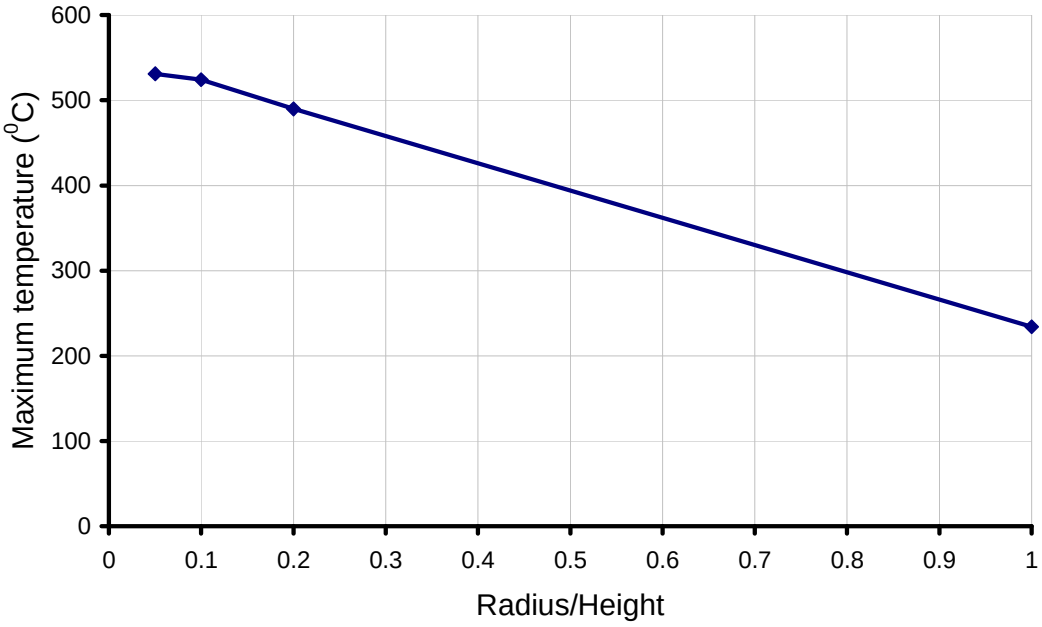

Figure 5-13 Highest temperature on the outer surface of the tank (°C); D=D_f=20m, d=20m

5.5 Temperature distribution in tanks

5.5.1 Model setup

Figure 5-14 shows the Abaqus FE model for the reference case. The target tank has a dimension of 20m in diameter and 20m in height. The tank is assumed to have a uniform wall thickness of 10mm for both the cylinder wall and roof. The adjacent tank fire is assumed to have the same base diameter of the target tank. Fire may occur at different heights relative to the target tank but a ground level tank fire is assumed here (H_{f0}=0m represents the vertical location of the base of fire is 0m). Two flame heights, 1 and 2 times of the fire diameter are considered, corresponding to the possible minimum and maximum flame height in a tank fire according to Figure 5-3. The target tank is assumed to be empty.

The thermal boundary conditions considered in the analysis can be found in Table 5-1. The parameters for heat transfer coefficient, tank separation distance, and other relevant information are given in Tables 5-2, 5-3 and 5-4.

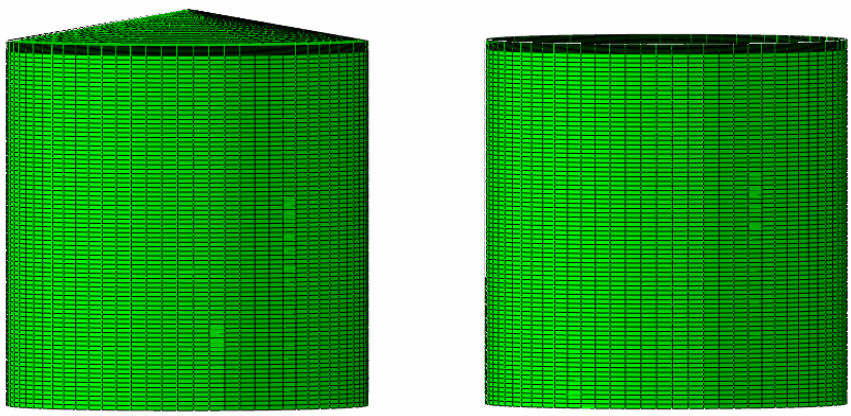

Target tank Fire

Figure 5-14 The numerical model in Abaqus for heat transfer analysis

The mesh adopted in circumference and vertical direction of the tank wall and roof is uniform except near the cylinder-to-roof joint where a refined mesh of 1/10 of the

global element size is adopted (Figure 5-15). The refinement is necessary because temperature changes rapidly in this zone due to a sudden change of viewfactor. The corresponding height of the fire used the same mesh size as that of the target tank.

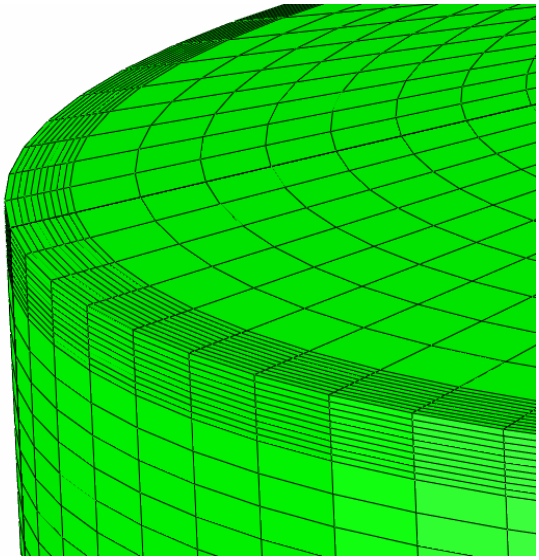

Figure 5-15 A close-up look of the mesh pattern at the cylinder-to-roof joint

5.5.2 Temperature distribution in the reference case

The predicted temperature distribution in the target tank is shown in Figure 5-16. For both flame heights (i.e., H_f=20m and H_f=40m), the circumferential temperature gradient in the cylindrical wall is pronounced, while the vertical temperature gradient is smaller, as shown in Figures 5-17~5-19. From the temperature distribution at different heights around the circumference (Figures 5-18 and 5-19) can be seen that nearly half of the tank facing the fire is heated following a cosine-like distribution around the circumference.

The flame height mainly influences the vertical temperature distribution, especially on the roof. When the flame is higher than the tank, the roof is significantly heated, including the part of the roof away from the fire (Figure 5-20). In contrast, when flame does not reach the roof level, the whole roof remains cool and large temperature gradient exists at the cylinder-to-roof joint, especially at the most heated region. Figure 5-21 shows the temperature distribution around the circumference at

21m, which also follows closely a cosine function, although it spread to a wider range (compared with that in the cylinder section), for this case, the whole roof.

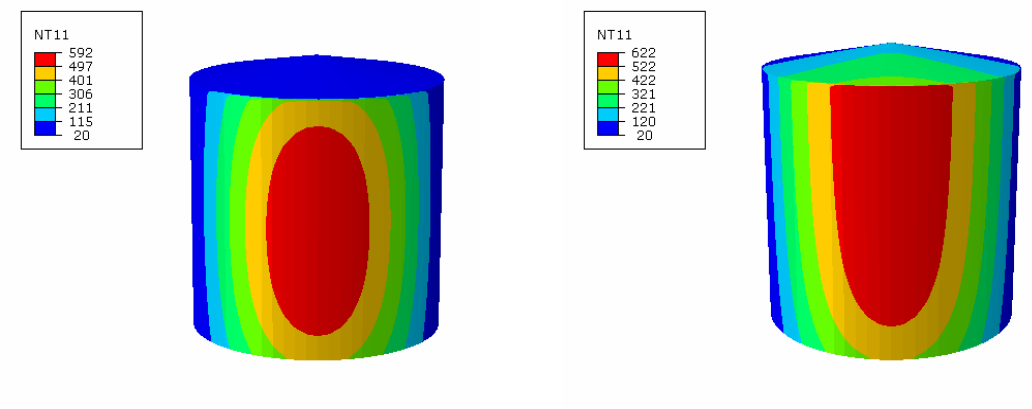

(a) Flame height=20m (b) Flame height=40m

Figure 5-16 Temperature distribution in the target tank (°C)

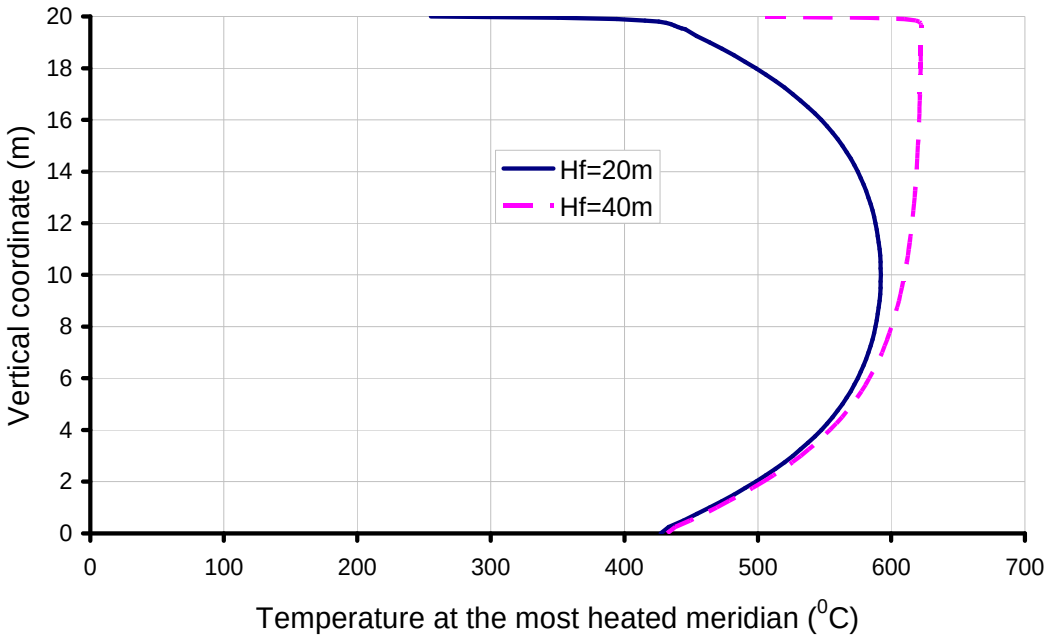

Figure 5-17 Effect of flame height on temperature distribution along the meridian of θ=0° of an empty tank (D=D_f=20m, d=6.67m, H_{f0}=0m)

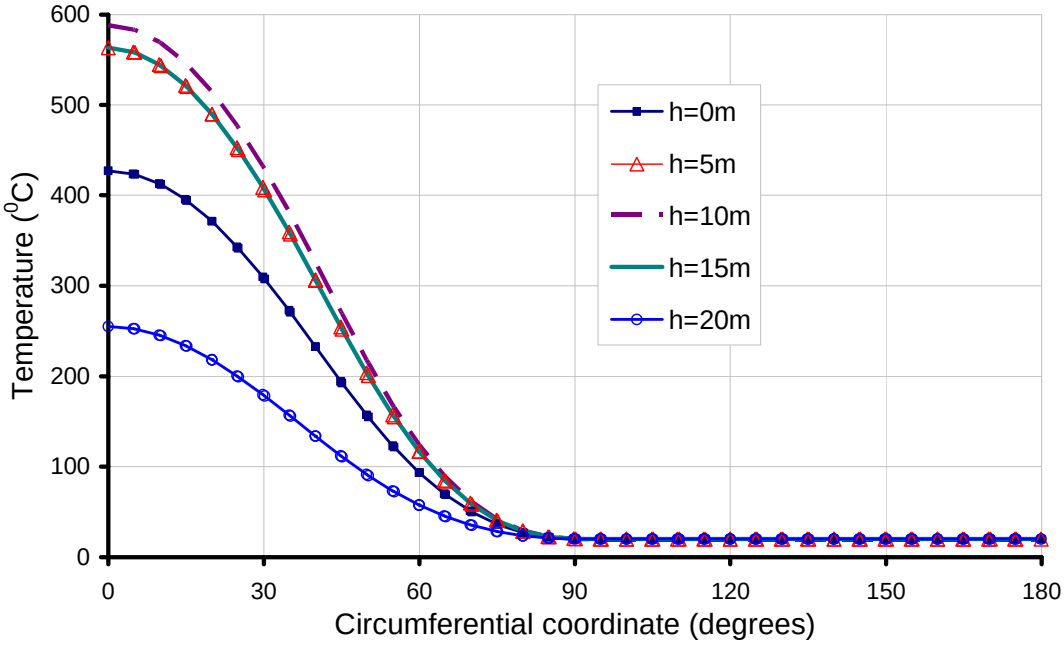

Figure 5-18 Temperature distribution around the circumference of an empty tank at different heights (D=D_f=20m, d=6.67m, H_{f0}=0m, H_f=20m)

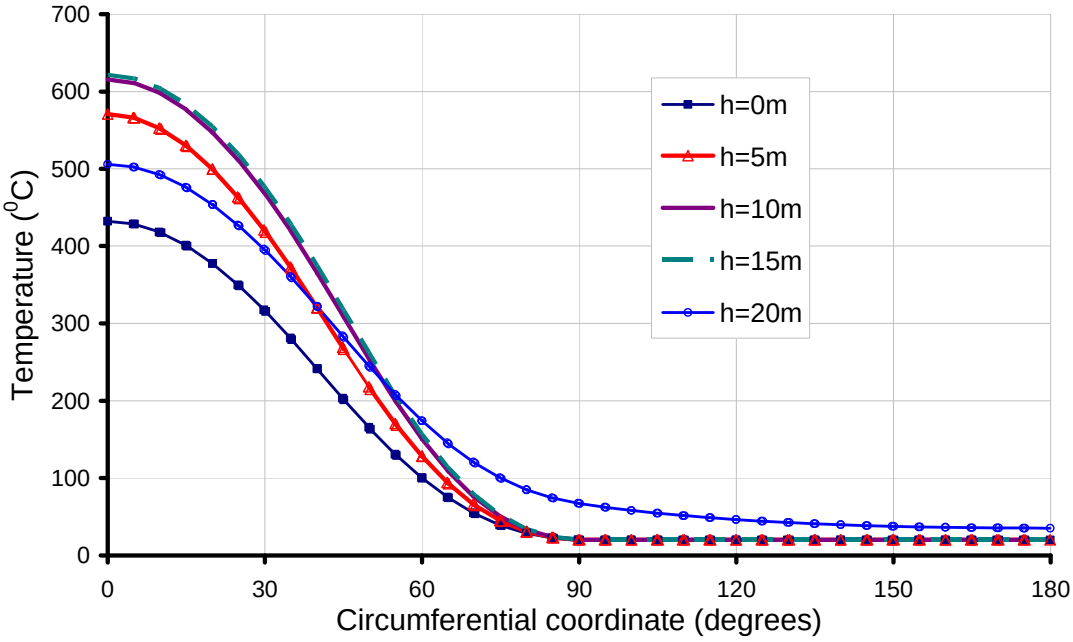

Figure 5-19 Temperature distribution around the circumference of an empty tank at different heights (D=D_f=20m, d=6.67m, H_{f0}=0m, H_f=40m)

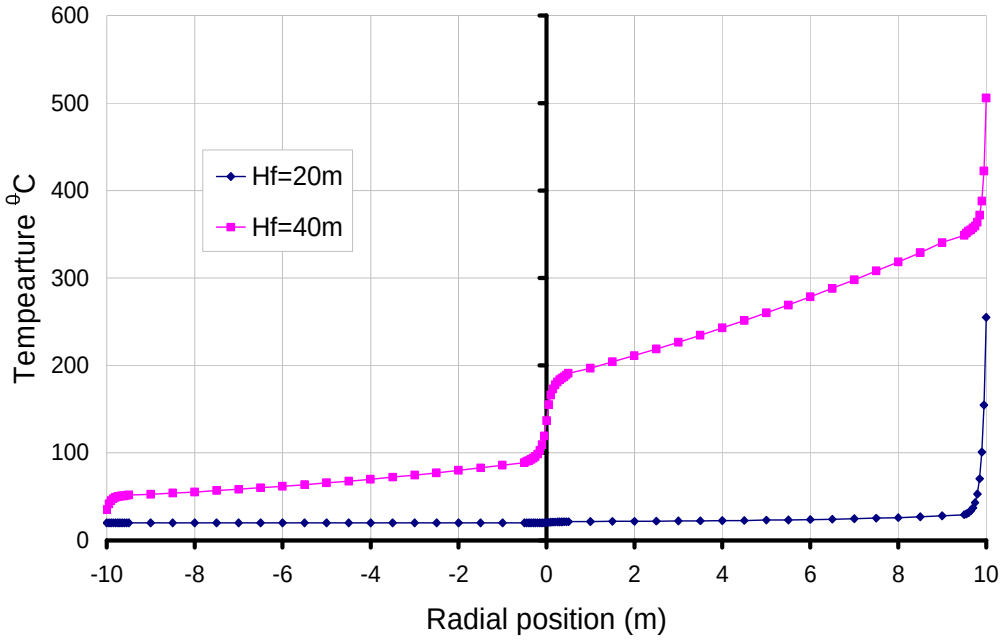

Figure 5-20 Temperature distribution on the conical roof at θ=0° (D=D_f=20m, d=6.67m, H_{f0}=0m)

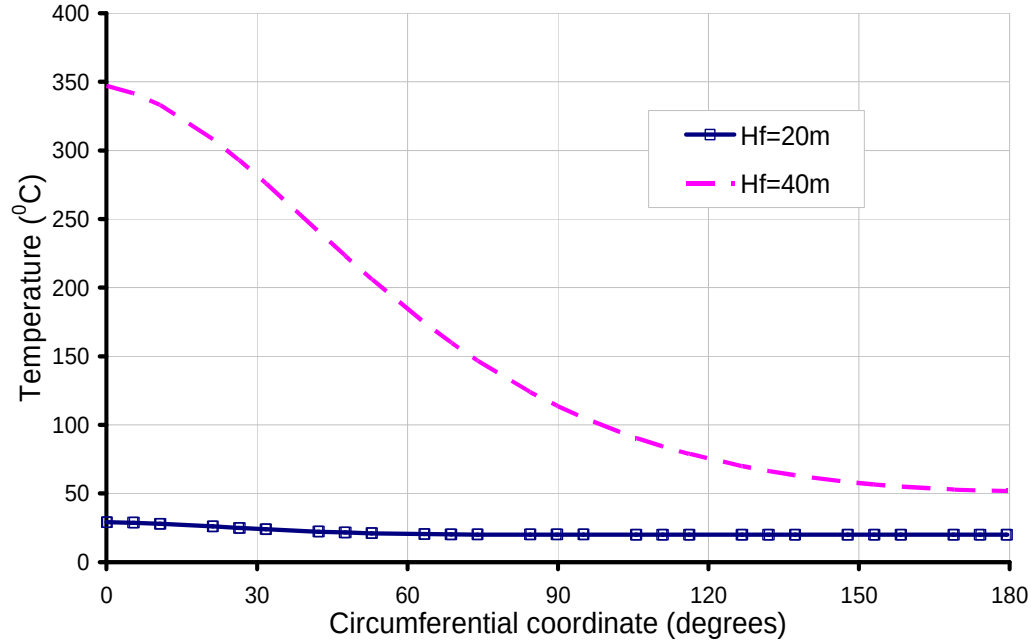

Figure 5-21 Temperature distribution around the circumference at roof (h=21m, D=D_f=20m, d=6.67m, H_{f0}=0m)

The results shown above are the temperature at the outer surface of the tank. The change of maximum temperature at both inner and outer surface under two different thermal boundary conditions with change of wall thickness is shown in Figure 5-22. It can be seen the through-thickness temperature gradient increases with increase of thickness. When both sides of the surface are in contact with air which is the case of an empty tank, the temperature gradient through thickness is negligible (Figure 5-22a), while for tanks with liquid inside, temperature gradient changes in range of 3%-35% for thickness between 5mm to 100mm. As for commonly used steel oil tanks that typically have a thickness of 8mm-12mm, or less, the temperature gradient is less than 5%. Therefore, it is deemed the through-thickness thermal gradient within the tank wall may be neglected.

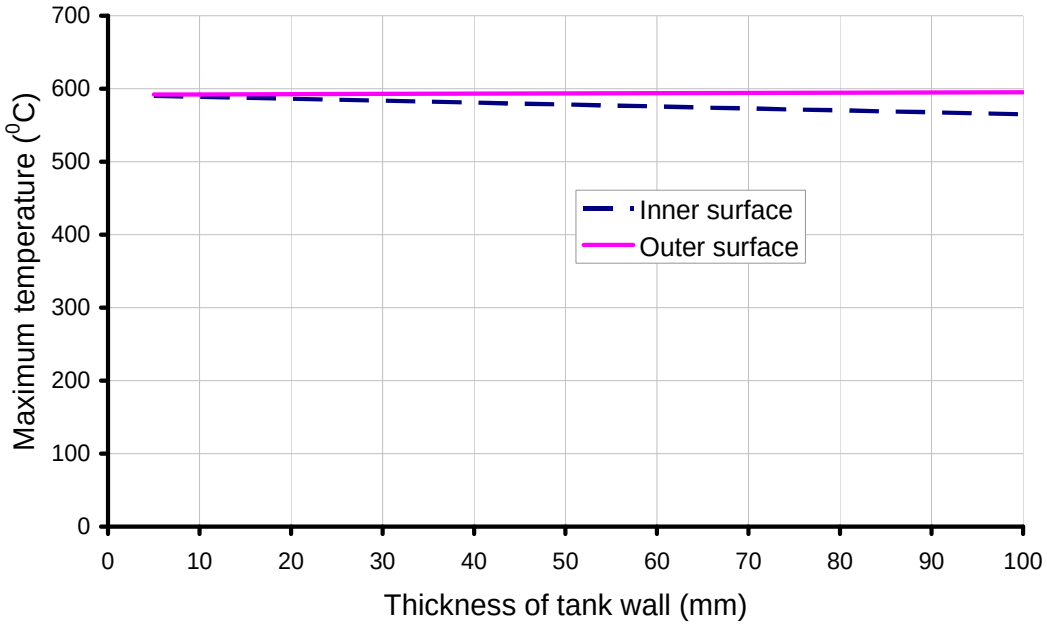

(a) Empty tank

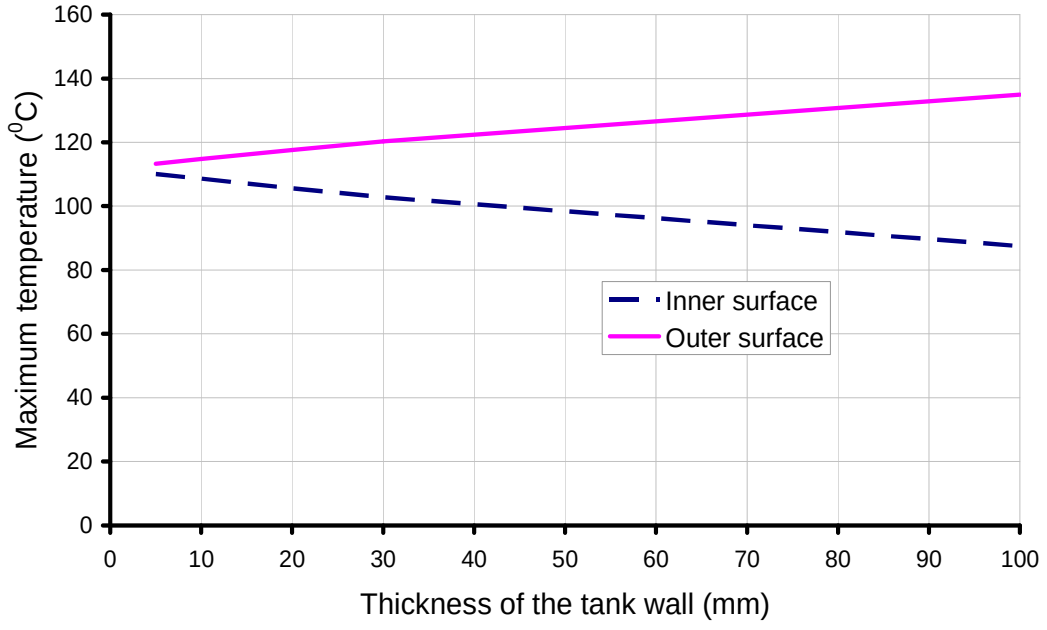

(b) Tanks with liquid inside

Figure 5-22 Effect of wall thickness on the maximum temperature at tank surfaces (D=D_f=20m, d=6.67m, H_f=20m, H_{f0}=0m)

To further investigate the influence of parameters related to fire model and the tank itself, a parametric study was performed. The size of target tank in the following analysis is fixed as 20m in diameter and 20m in height, with uniform wall thickness and roof thickness of t_c=t_f =0.01m.

5.5.3 Sensitivity of input parameters in the fire model

This section presents a sensitivity study of the fire variables on the temperature distribution in the target tank. The investigated parameters include the heat transfer coefficient of the liquid, the radiative emissivity, the fire emissive power, the convective heat transfer coefficient and the conductivity of the tank.

Convective heat transfer coefficient

The convection heat transfer coefficient $\bar{h}$ depends on the type of fluid or gas and their properties. The determination of $\bar{h}$ is often tedious and needs data not yet available in the preliminary stage of simulation. Therefore, typical values and the range of $\bar{h}$ are useful. Typical values of the convection heat transfer coefficient are between 50 and 1000 W/m^{2}K for liquids, between 2 to 25 W/m^{2}K for air (Incropera *et al.* 1996).

Figure 5-23 compares the temperature distribution at the most heated meridian predicted with different values of the liquid heat transfer coefficient for a half filled tank. It shows that this parameter can significantly affect the temperature below the liquid level. A larger heat transfer coefficient of the stored liquid leads to a cooler tank wall approaching the ambient temperature.

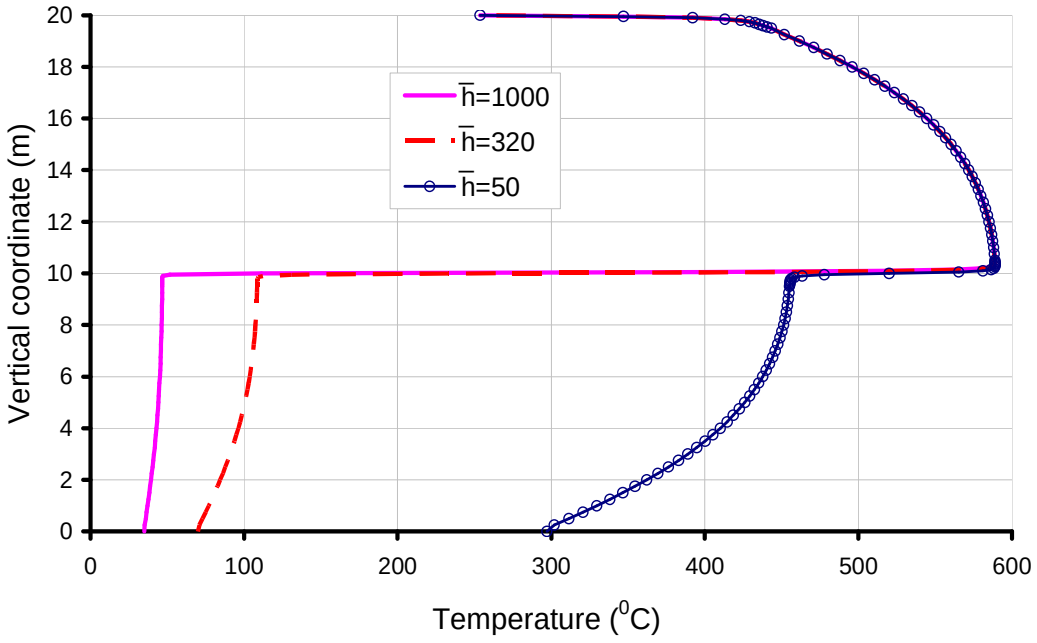

Figure 5-23 Effect of heat transfer coefficient of the liquid inside of the tank on the temperature distribution along the most heated meridian in a half filled tank (D=D_f=20m, d=6.67m, H_f=20m, H_{f0}=0m)

The predicted maximum temperature in an empty tank with different values of the heat transfer coefficient for air ($\bar{h}_{air}$) is shown in Figure 5-24. The predicted maximum temperature reduces linearly as $\bar{h}$ increases: a larger value of the heat transfer coefficient leads to a lower tank wall temperature. A value of $\bar{h}_{air}$ =25 W/m^{2}K was adopted in the reference case.

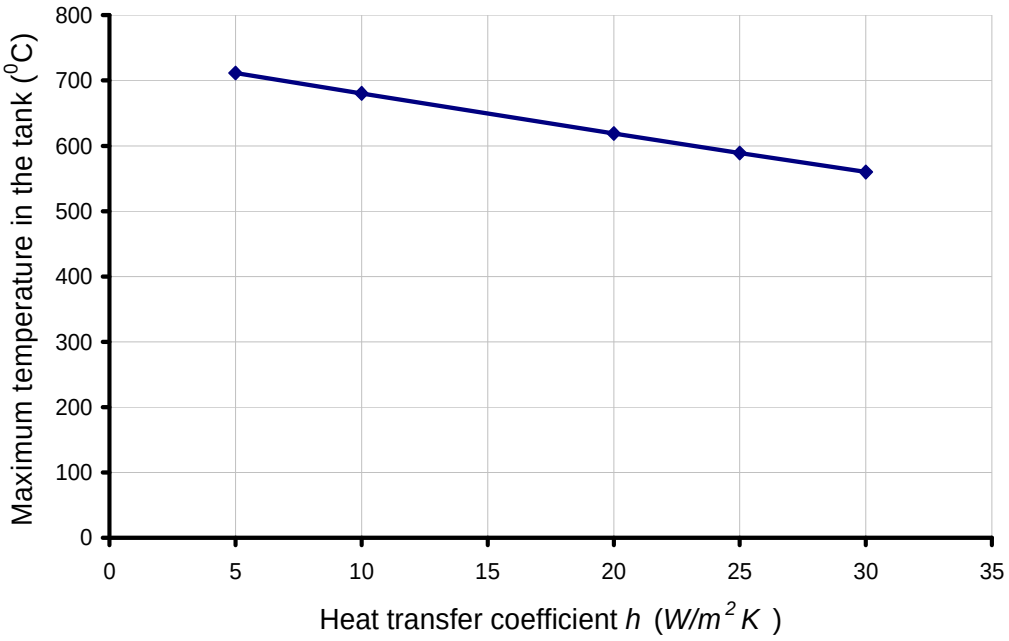

Figure 5-24 Effect of the heat transfer coefficient on the maximum temperature in an empty tank (D=D_f=20m, d=6.67m, H_f=20m, H_{f0}=0m)

Emissivity of the tank surface

Apart from the radiation received by external tank surface from fire, there is also radiation between inner tank surfaces. The internal radiation mainly transfers heat from the hot part of the tank to the cold part. For steel without oxide layer, which is usually the case for the inner surface of oil tanks, the emissivity has a low value of around 0.2-0.32. In the reference case, this radiation between the inner tank surfaces is neglected, while its effects are investigated below.

Figures 5-25 and 26 show variation of normalised temperature $(T\text{-}T_{0a})/(T_{0m}\text{-}T_{0a})$ distribution when the external surface emissivity ε_{out} varies from 0.2 to 1.0, while the inner surface emissivity is neglected (ε_{in}=0), around the circumference and along the meridian respectively, where, T is the temperature in the tank wall, T_{0a} is the ambient temperature, and T_{0m} is the maximum temperature developed in the tank wall. A

lower value of emissivity leads to a slightly more concentrated temperature distribution in both the circumference and meridianal directions.

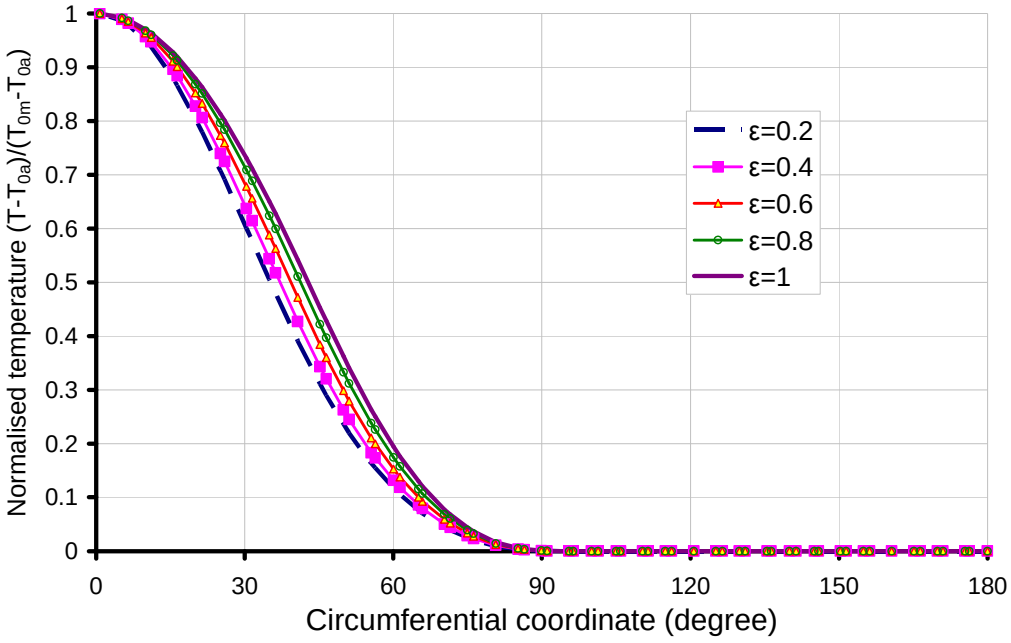

Figure 5-25 Effect of external tank surface emissivity on temperature distribution around the circumference at z=10m (inner surface radiation neglected; D=D_f=20m, d=6.67m, H_f=20m, H_{f0}=0m)

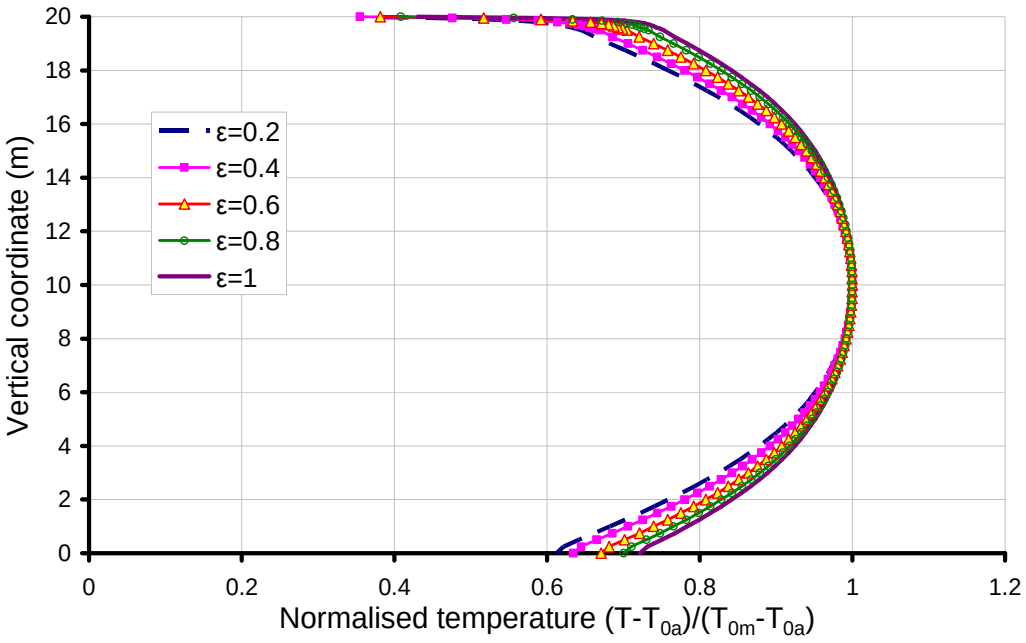

Figure 5-26 Effect of external tank surface emissivity on temperature distribution along the meridian at θ=0° (inner surface radiation neglected; D=D_f=20m, d=6.67m, H_f=20m, H_{f0}=0m)

Figure 5-27 shows the influence of inner surface radiation on the predicted temperature in the tank. The effect of the inner surface radiation depends on the value of external surface emissivity. For external surface with low values of emissivity, the predicted temperature distributions are not sensitive to the inner surface radiation. For external surface with high emissivity, neglecting the inner surface radiation may lead to higher temperatures in the hotter part and lower temperatures in the cooler part.

Figure 5-28 shows the effect of emissivity on the predicted maximum temperature. The maximum temperature in the tank increases significantly with an increase of emissivity, with differences exceeding 350°C within the shown range. In Figure 5-8 the dotted line represents the case where both inner and outer surfaces have equal value of emissivity. The two solid lines provide envelops where the inner surface emissivity is either fixed as 0 or 1 repetitively. All other cases with other values of emissivity should lie in between the two solid curves in Figure 5-28. As a result a

tank constructed with high emissivity materials such as the sheet steel with a rough oxide layer on the outer surface can develop high temperature when it is subject to an adjacent fire.

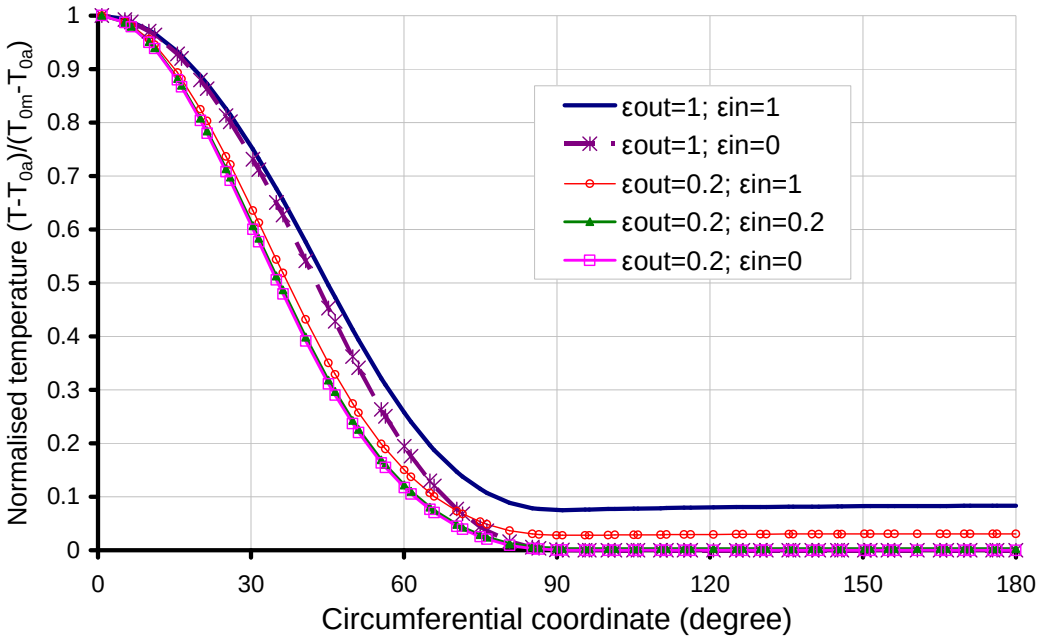

Figure 5-27 Effect of inner surface emissivity on the temperature distribution around the circumference (D=D_f=20m, d=6.67m, H_f=20m, H_{f0}=0m)

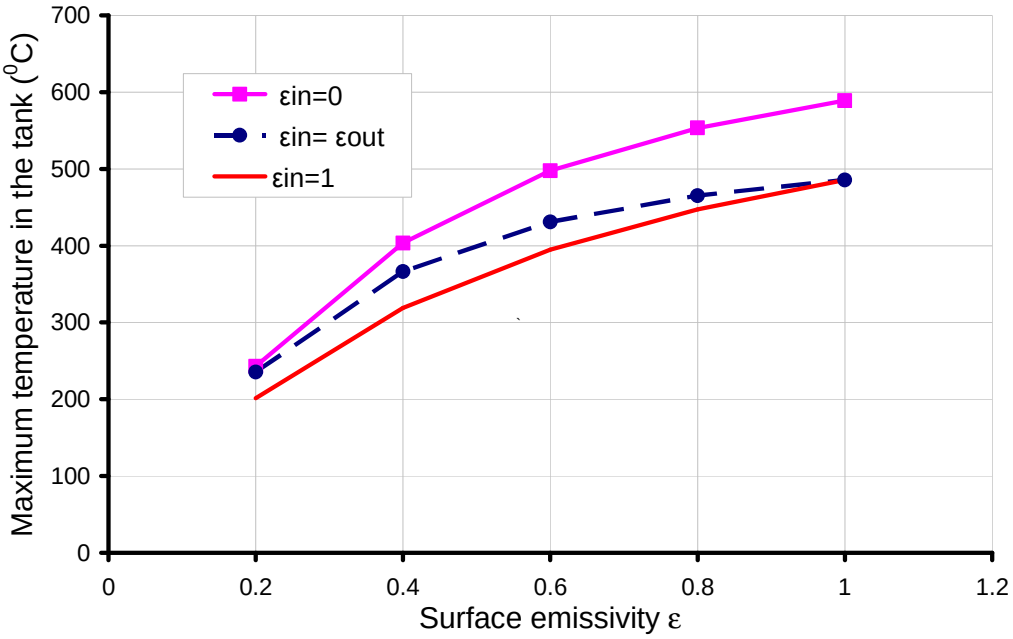

Figure 5-28 Effect of surface emissivity on the maximum wall temperature (D=D_f=20m, d=6.67m, H_f=20m, H_{f0}=0m)

Emissive power of the fire

The emissive power of fire depends on the type of fuel burning in the tank. Figure 5-29 shows the predicted maximum temperature in the adjacent tank versus the emissive power of the fire which is represented by the fire temperature. The maximum target tank temperature increases almost linearly with the increase of the emissive power of fire. It may be noted that the value of the emissive power does not change the temperature distribution in any significant way, which is hence not shown here.

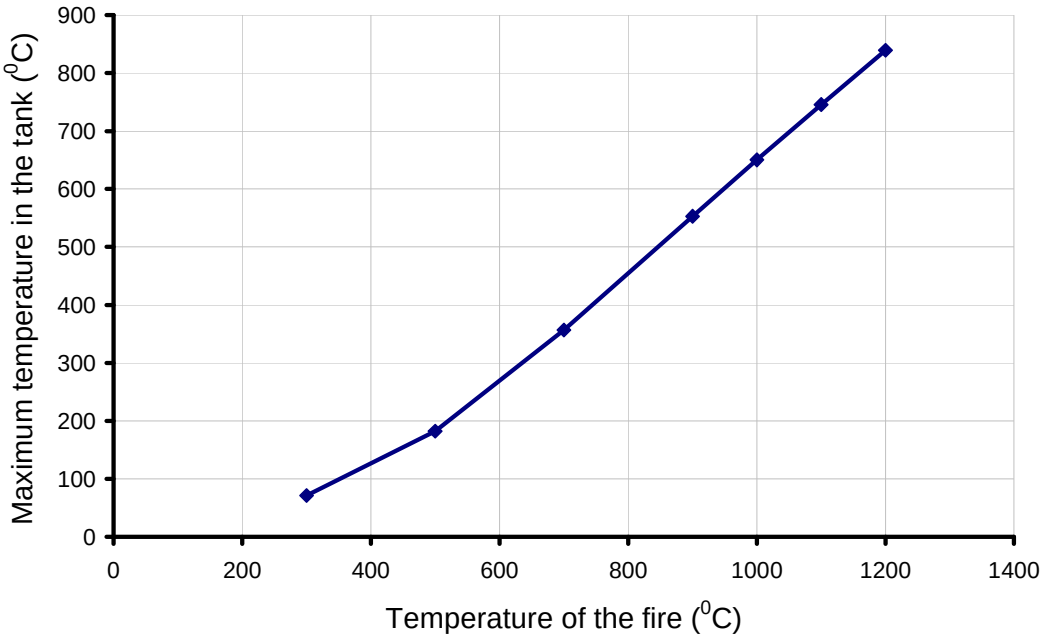

Figure 5-29 Effect of fire emissive power on the predicted maximum temperature in the tank (D=D_f=20m, d=6.67m, H_f=20m, H_{f0}=0m)

Thermal conductivity

The thermal conductivity of steel is around 50, and aluminium around 250. Although the interest of this thesis mainly lies on steel tanks, the effect of thermal conductivity of the tank material is also investigated. Figure 5-30 shows that the value of thermal conductivity for common metals has negligible influence on the predicted tank temperature.

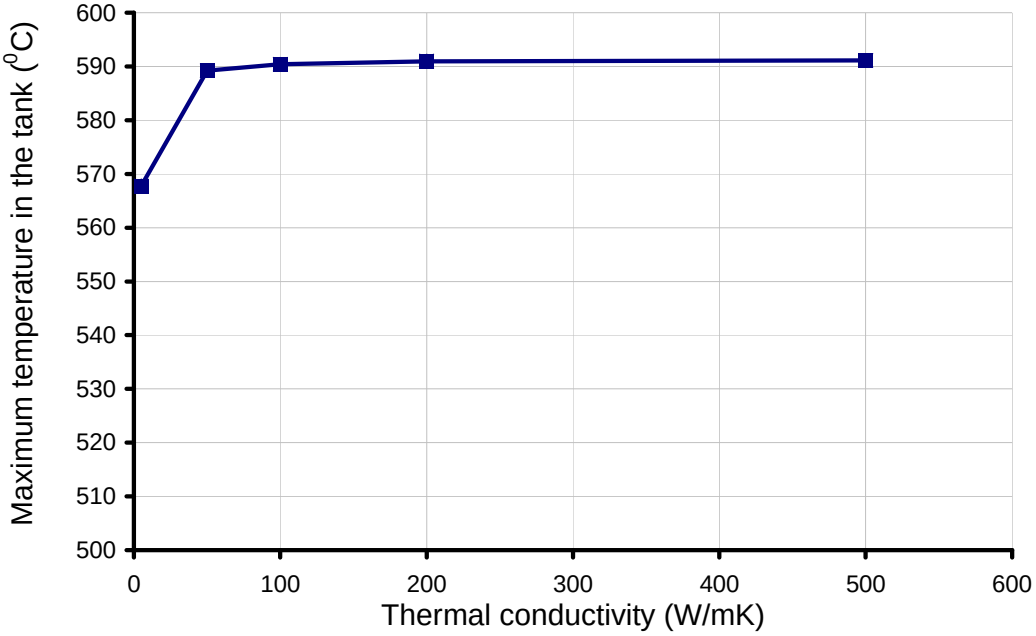

Figure 5-30 Effect of thermal conductivity on the predicted maximum temperature in the tank (D=D_f=20m, d=6.67m, H_f=20m, H_{f0}=0m)

5.5.4 Effect of liquid filling height

The effect of the filling height in the target tank was examined for the reference fire (starting from the ground with a diameter 20m and flame height of 20m). Fig 5-31 shows the predicted temperature distribution along the most heated meridian.

The temperature distribution in the wall followed the same pattern as that in an empty tank when the wall is in contact with air or is the same as that of a fully filled tank when the wall is in contact with liquid. Near the liquid surface there is a sudden change of temperature within a very short distance. The detailed temperature distribution near the liquid level for H_{liq}=5m, 10m and 15m are shown in Figure 5-32. It is seen that no matter where the liquid level is, the transition zone is almost the same. Therefore, it is possible to obtain the temperature distribution in a partially filled tank by examining two extreme cases (i.e., empty and fully filled tank), and

then adding the sharp temperature change into this temperature curves at the transition zone.

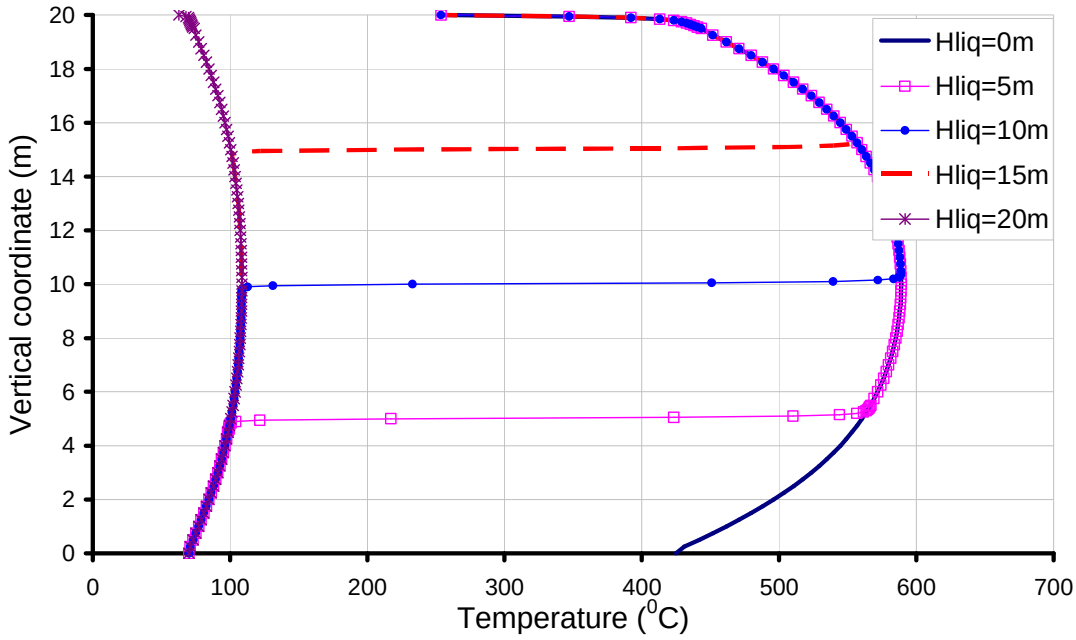

Figure 5-31 Temperature distribution along the most heated meridian in a partially filled tank (D=D_f=20m, d=6.67m, H_f=20m, H_{f0}=0m)

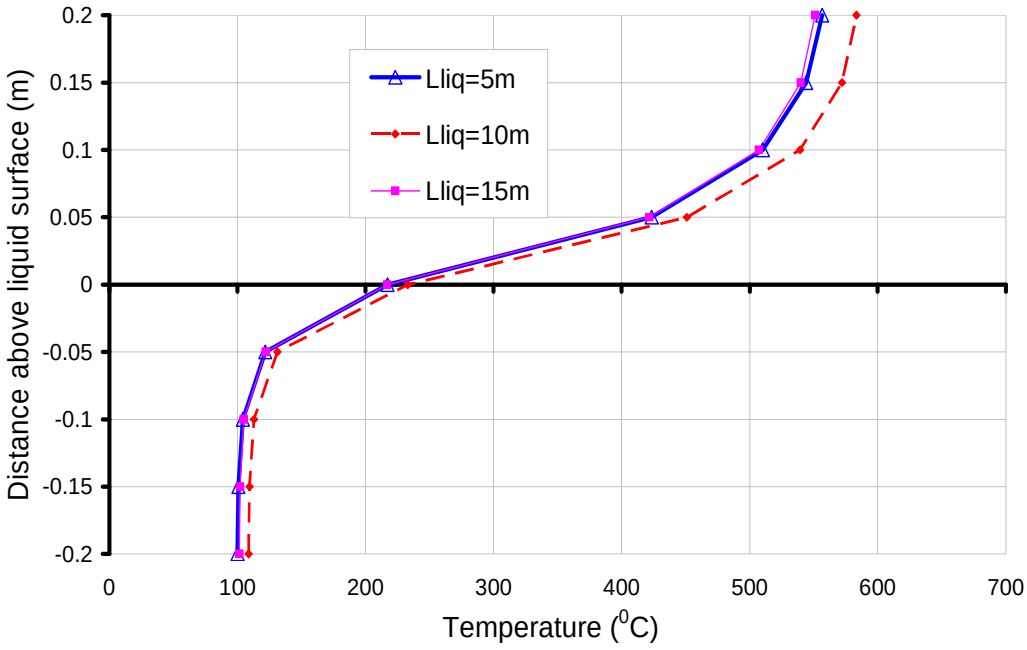

Figure 5-32 Temperature distribution near the liquid level along the most heated meridian (D=D_f=20m, d=6.67m, H_f=20m, H_{f0}=0m)

Figure 5-33 shows the temperature distribution around the cylinder-to-roof junction, where the temperature decreases rapidly within a short distance.

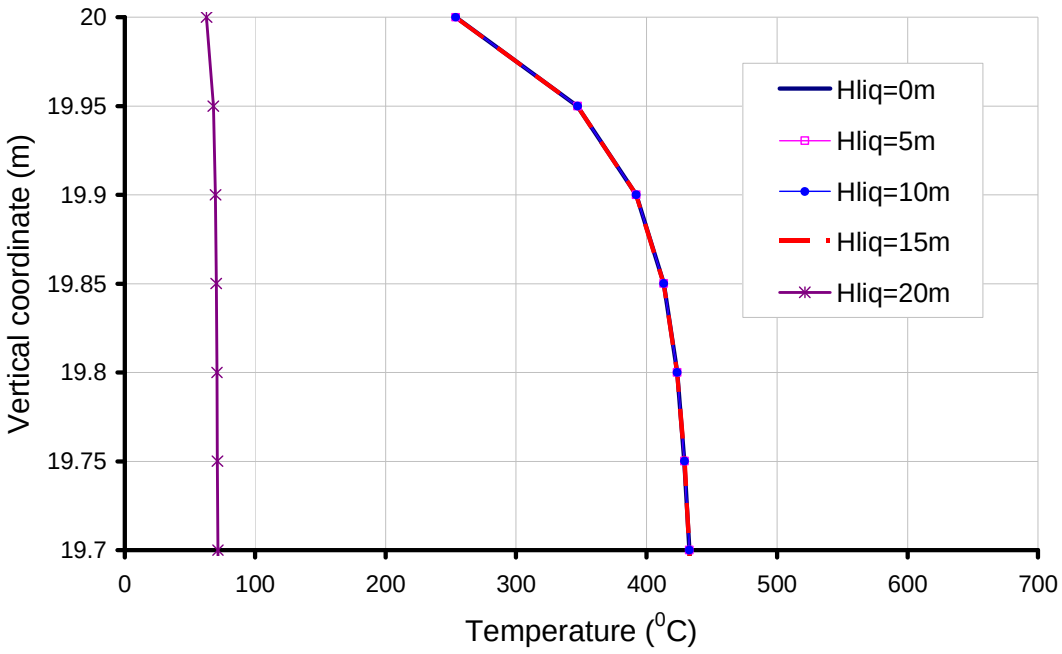

Figure 5-33 Temperature distribution near the roof along the most heated meridian (D=D_f=20m, d=6.67m, H_f=20m, H_{f0}=0m)

5.5.5 Effect of vertical fire location and flame height

Eight different vertical fire locations with different flame heights were examined in this analysis. The fire was assumed to start at 0, 2, 5, 8, 10, 12, 15 and 20m above the ground level. The flame heights of 1 and 2 times of diameter of the fire were examined. The temperature distribution along the most heated meridian for the empty tank and fully filled tank are shown in Figures 5-34 and 5-35 respectively. The temperature distribution is shown to be very sensitive to the vertical fire location. For an empty tank, the temperature rise in the cylindrical tank wall is approximately uniform if the fire starts from a very low height and the flame height is no lower than the height of target tank. If these conditions are not satisfied, the maximum temperature in the tank wall can be significantly different. For the case of fire starting from a higher level, the flame height has almost no effect on the temperature distribution of the cylindrical wall. For a fully filled tank, the temperature rise is less than 100 °C in all cases.

Figures 5-36 to 5-38 further examine the temperature distribution around the circumference in an empty tank at h=2m, h=10m and h=18m respectively. The results show that the circumferential temperature distribution also varies significantly with the vertical fire location, especially in the lower part of the tank (Figures 5-36 and 37), while temperature in the upper part of the tank does not show any significant difference (Figures 5-38).

It is noticed that in Figure 5-36 there is a dip around θ=0° when the base of the fire is high (e.g. H_{f0}=15 and 20m). This is mainly caused by the view factor (see Equation 2-9), which can be larger around θ=0° on the target tank than that at θ=0° near the ground when the fire is very high so that the angle between the fire and the target is very small (leading to large ϕ_i and ϕ_j values (close to 90°)). As an extreme case, when the cylindrical fire is directly next to the target tank (i.e. the distance between them is zero) and the fire is above the roof level of the target tank, the target tank at θ=0° receives zero radiation from the meridian of the fire directly above, but a small amount from the sides of the fire. In contrast, the target at sides with $\theta \neq 0$ receives more radiation from the side of the fire.

The temperature distribution on the roof is very sensitive to flame height, as shown in Figures 5-39 and 5-40.

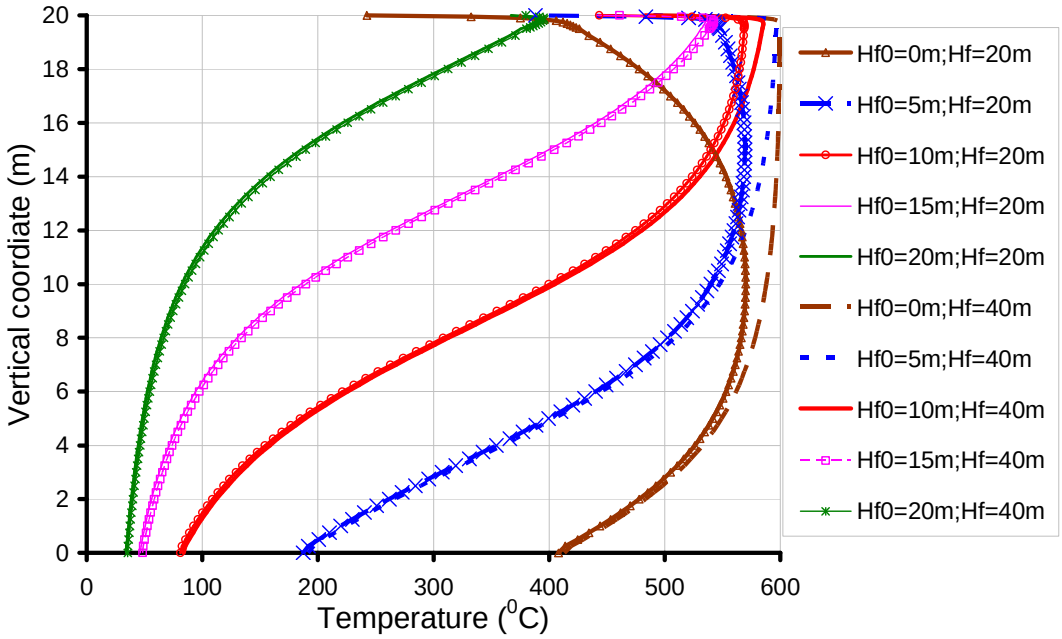

Figure 5-34 Temperature distribution at the most heated meridian of an empty tank: effects of vertical fire location and flame height (D=D_f=20m, d=6.67m)

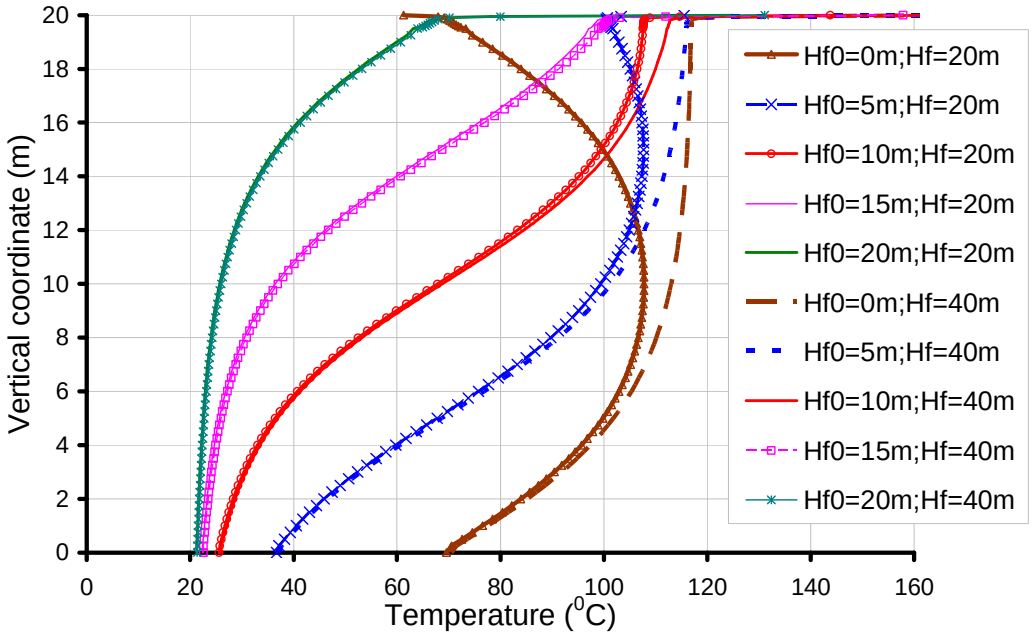

Figure 5-35 Temperature distribution at the most heated meridian of a fully filled tank: effects of vertical fire location and flame height (D=D_f=20m, d=6.67m)

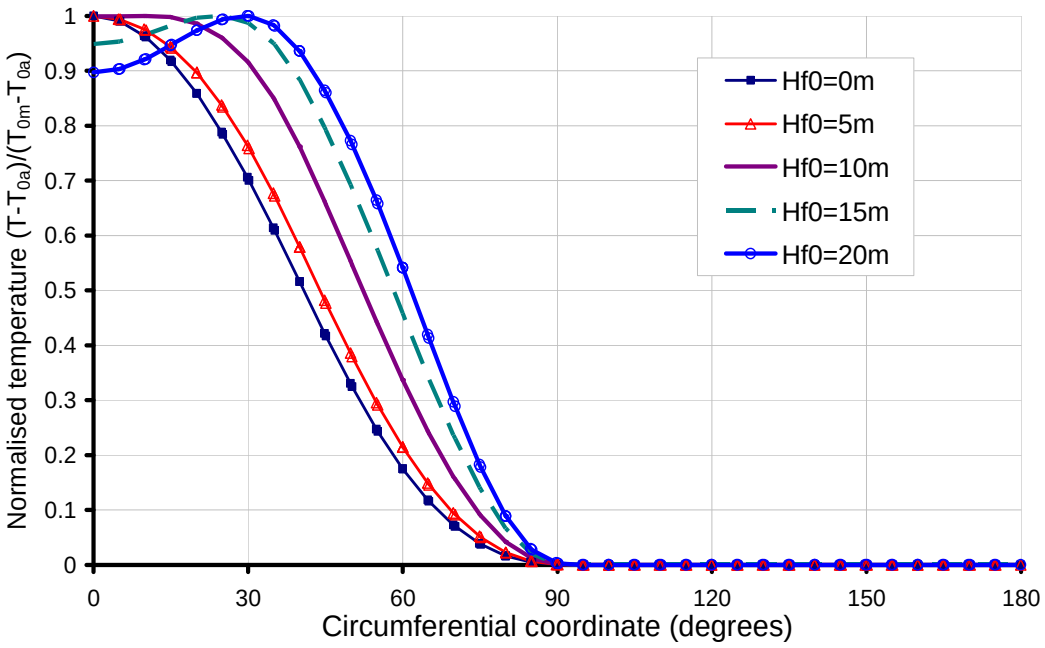

Figure 5-36 Temperature distribution around the circumference of an empty tank at h=2m: effect of vertical fire location (D=D_f=20m, d=6.67m, H_f=20m)

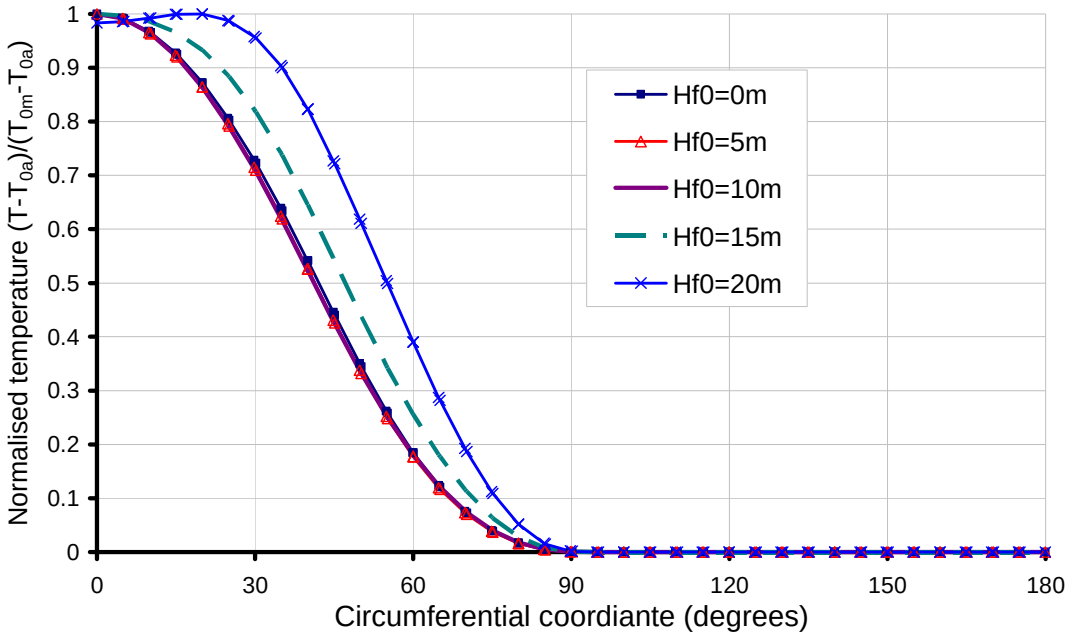

Figure 5-37 Temperature distribution around the circumference of an empty tank at *h*=10m: effect of vertical fire location (*D*=*D*$_f$=20m, *d*=6.67m, *H*$_f$=20m)

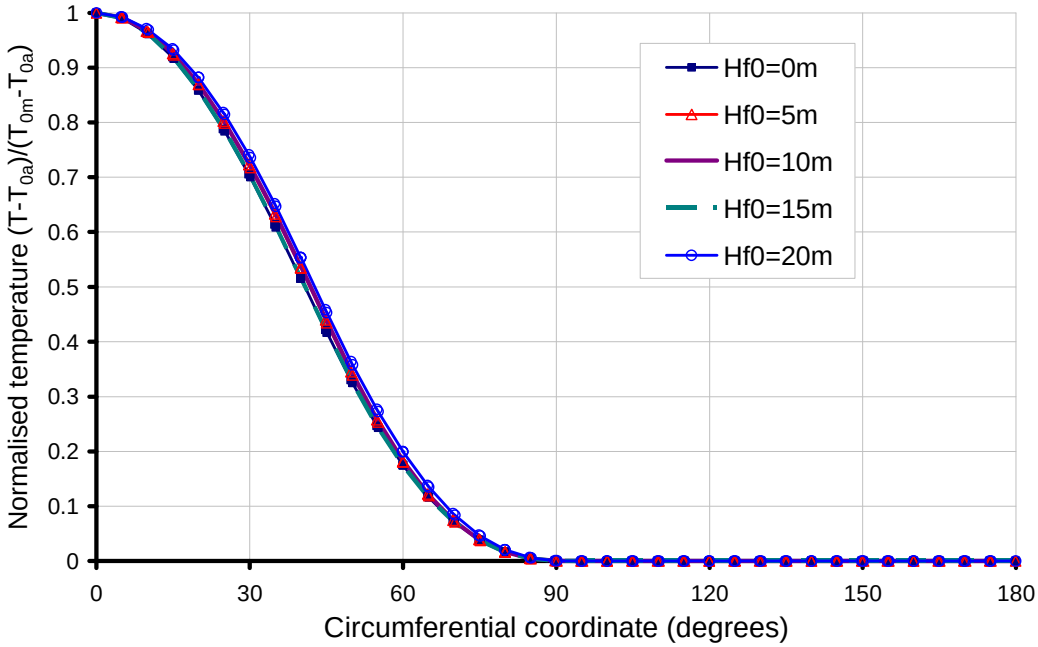

Figure 5-38 Temperature distribution around the circumference of an empty tank at *h*=18m: effect of vertical fire location (*D*=*D*$_f$=20m, *d*=6.67m, *H*$_f$=20m)

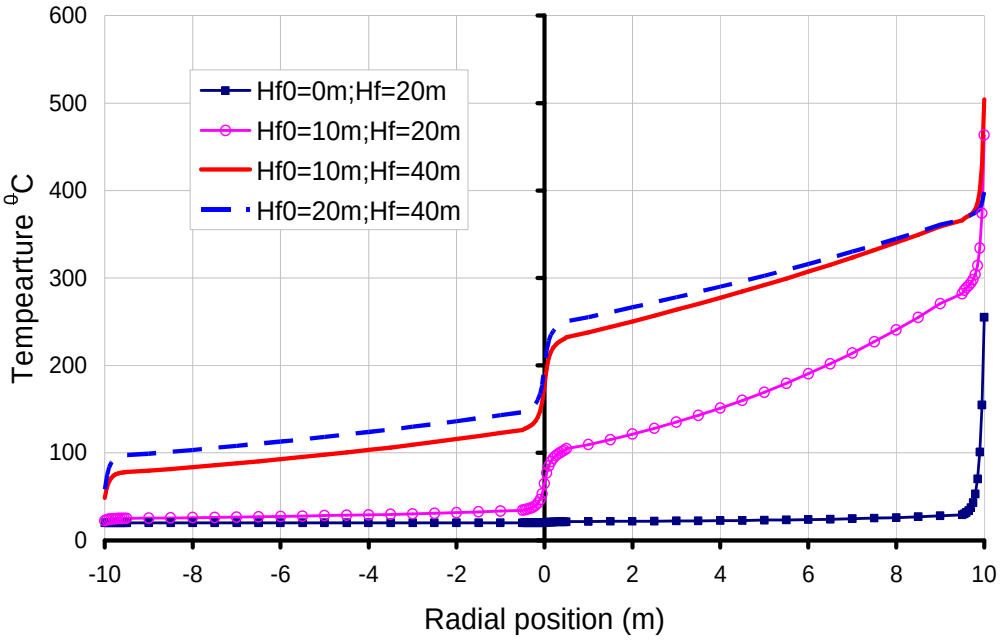

Figure 5-39 Temperature distribution in the diametric section through θ=0° on the conical roof (D=D_f=20m, d=6.67m)

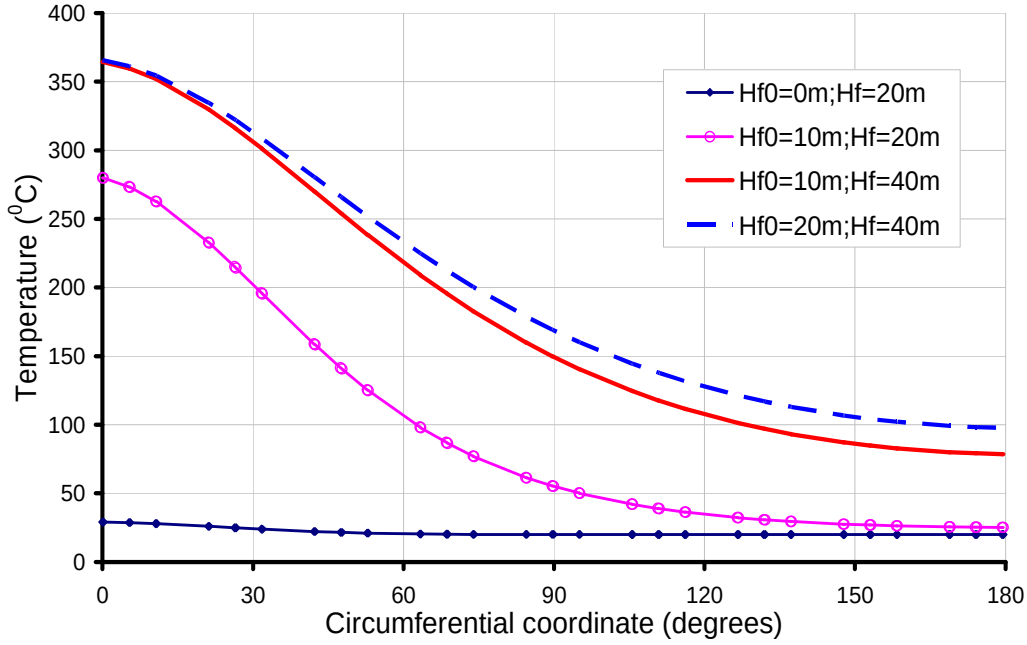

Figure 5-40 Temperature distribution around the circumference at r=6.27m (h=21m) on the roof (D=D_f=20m, d=6.67m)

5.5.6 Effect of horizontal fire location

The effect of horizontal distance between the fire and target tank on the temperature distribution in the target tank is investigated in this section. The distance *d* here refers to the distance between the facing walls of the fire and target tanks. It is varied from 3m to 30m in the simulations.

The horizontal distance has a negligible small effect on the temperature distribution around the circumference (Figure 5-41a&b), but a small effect on the distribution along the meridian (Figure 5-41c).

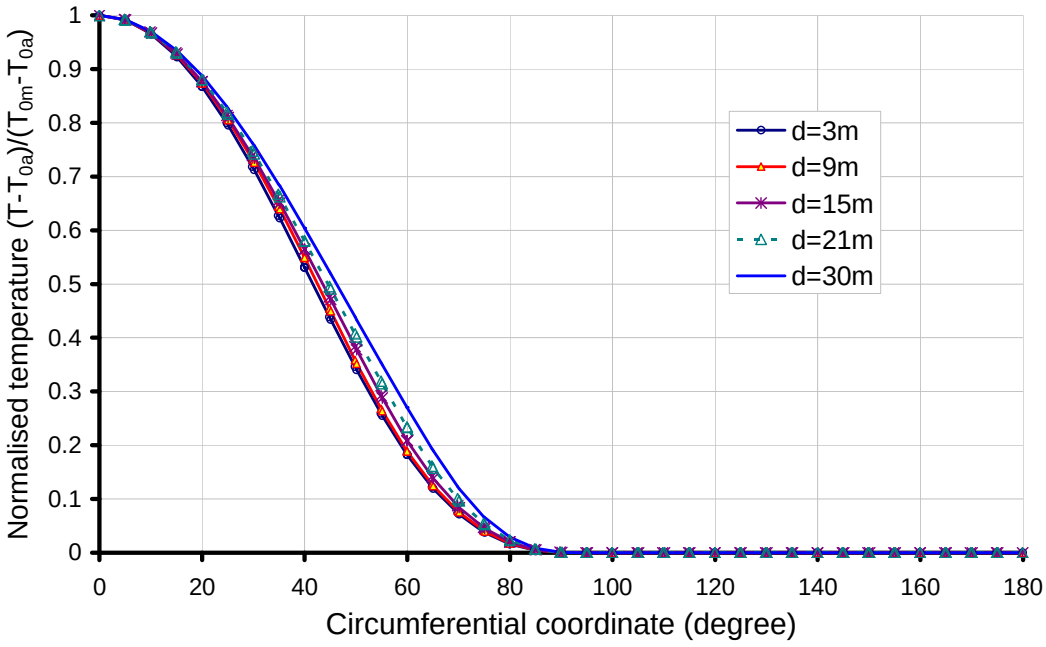

(a) Normalised temperature distribution around the circumference at *h*=10m

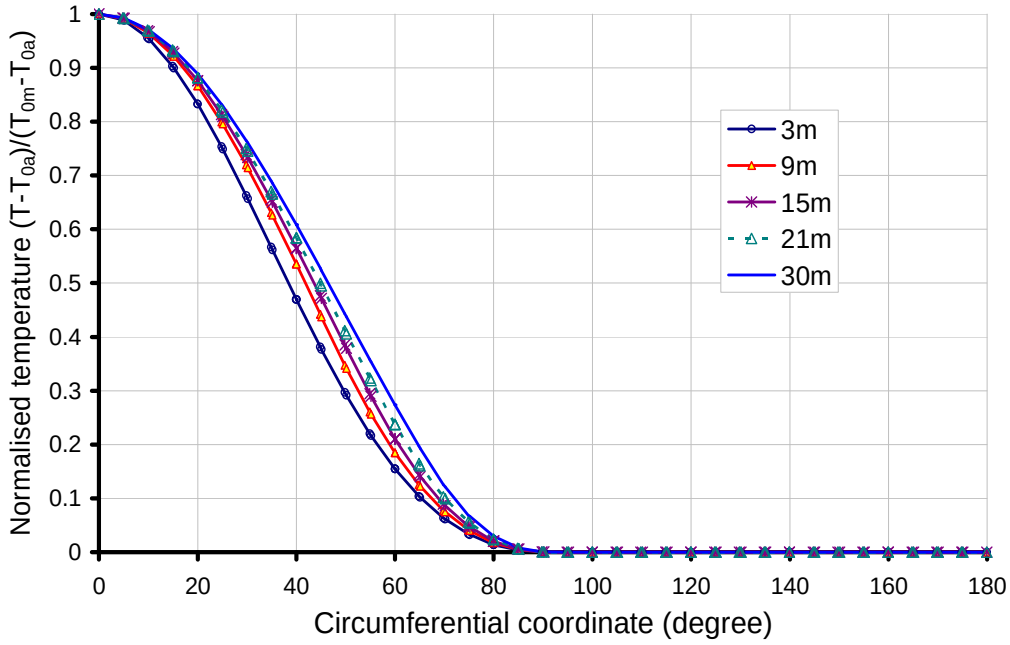

(b) Normalised temperature distribution around the circumference at *h*=2m

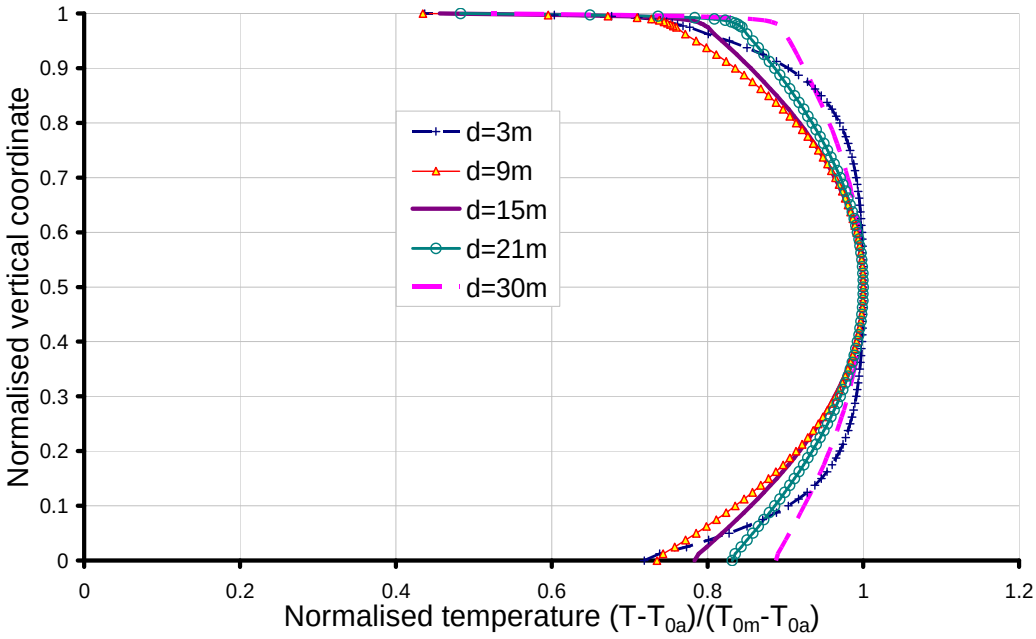

(c) Normalised temperature distribution along the most heated meridian

Figure 5-41 Effect of horizontal fire location on temperature distribution in an empty tank (D=D_f=20m, H_f=20m;H_{f0}=0m)

The above observation is based on the case that the value of the flame height is the same as the tank height. In order to examine whether these observed features are influenced by the flame height, additional simulations with a flame height H_f=40m were conducted.

It can be seen that the features of temperature distribution around the circumference observed in cases with H_f=20m are still valid in cases with H_f=40m (Figure 5-42 b): the temperature pattern around circumference doesn't change much with horizontal fire locations and the temperature distribution up vertical coordinate displays more variation than that in circumferential direction (Figure 5-42 b). By comparing Figure 5-41 with Figure 5-42, it may be seen that the flame height mainly affects the temperature along the vertical direction but not around the circumference, irrespective of the distance between the tank and the fire.

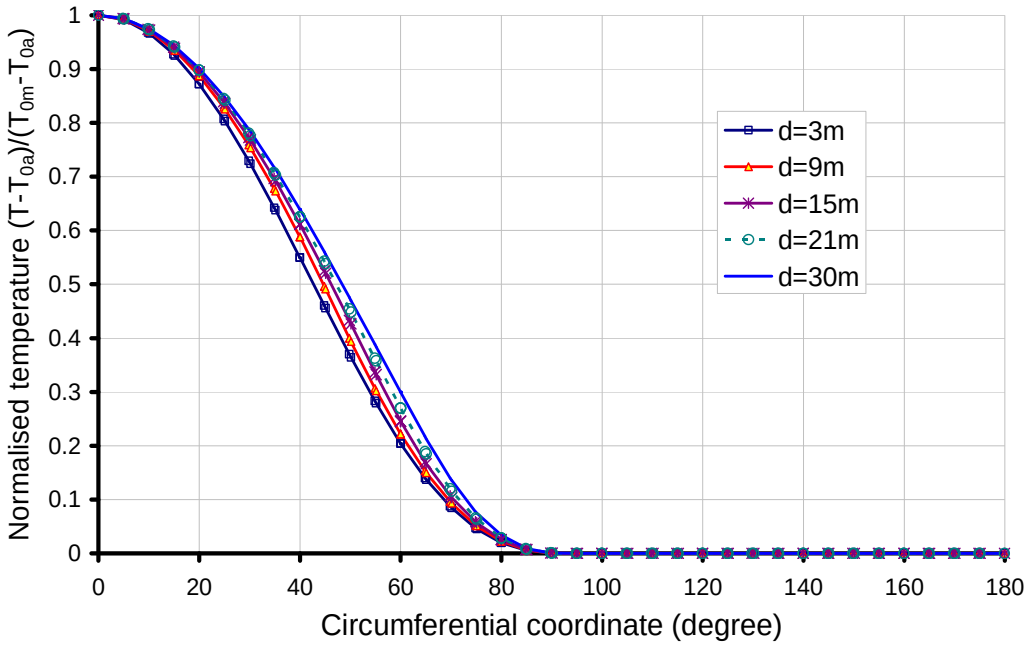

(b) Normalised temperature distribution around the circumference at h=10m

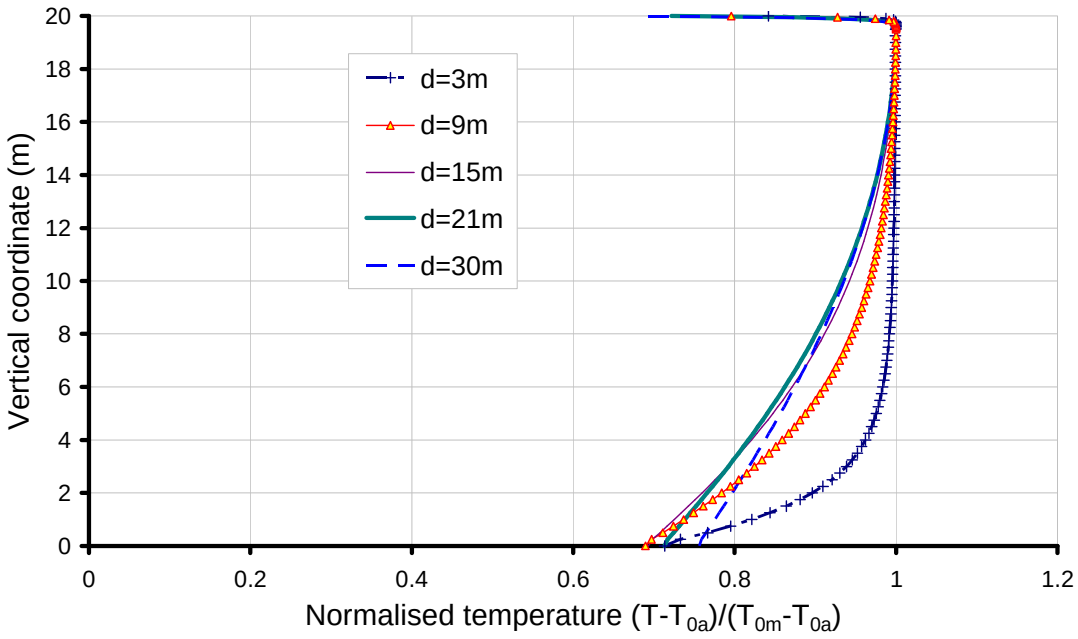

(d) Normalised temperature distribution at the most heated meridian

Figure 5-42 Effect of horizontal fire location on the temperature distribution of an empty tank (D=D_f=20m, H_f=40m, H_{f0}=0m)

The effect of the tank to fire distance on the maximum temperature is shown in Figure 5-43. It can be seen the maximum temperature increases almost linearly when the fire distance reduces.

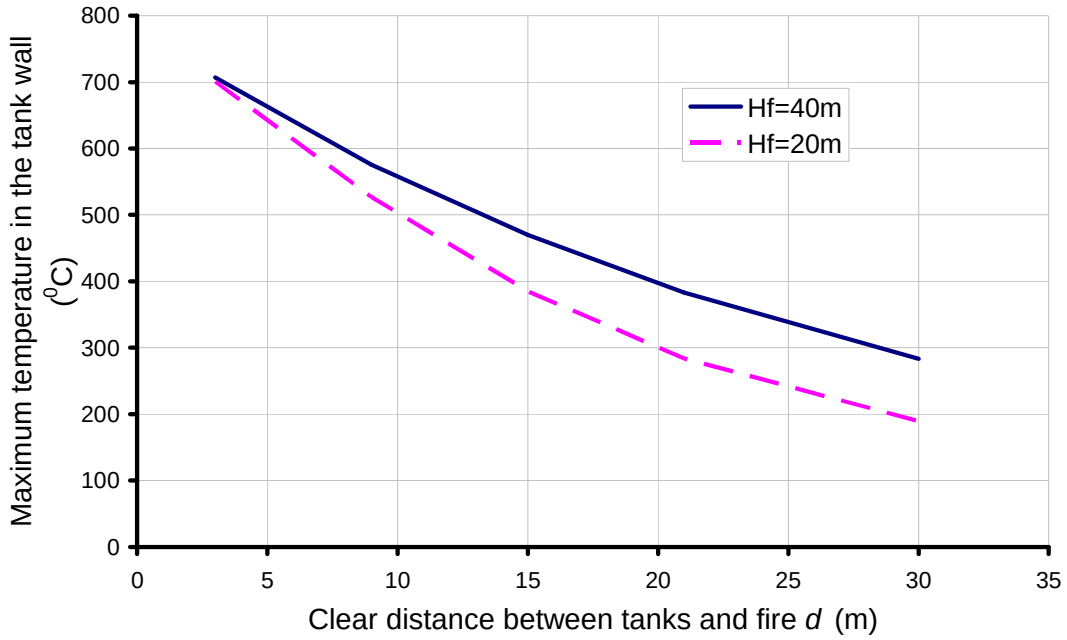

Figure 5-43 Effect of fire-to-tank distance on the maximum temperature in an empty tank (D=D_f=20m, H_{f0}=0m)

5.5.7 Effect of fire diameter

For all the results presented above, both the burning tank and the target tank were assumed to have the same diameter. The influence of the fire size on the target tank temperature distribution is investigated in this section for the reference target tank with a diameter of 20m as used earlier. The fire is assumed to start from the ground level. The separation distance between tanks is dependent on the fire size according to NFPA30, shown in Table 5-3. Two cases of separation are considered in this study. For case 1, the separation is fixed. For case 2, the tank separation varies with fire diameter D_f according to NFPA30 (1996). In order to compare results with the earlier predictions, the separation between tanks is chosen as the same as that of the

reference case, which is 6.67m. In Case 2 the separation between the target tank and fire varies. The flame height of the fire for both cases is assumed to be 20m.

The predictions in Case 1 show that the heating range around the circumference is significantly affected by the fire diameter (Figure 5-44a), but the vertical temperature distribution is not (Figure 5-44b).

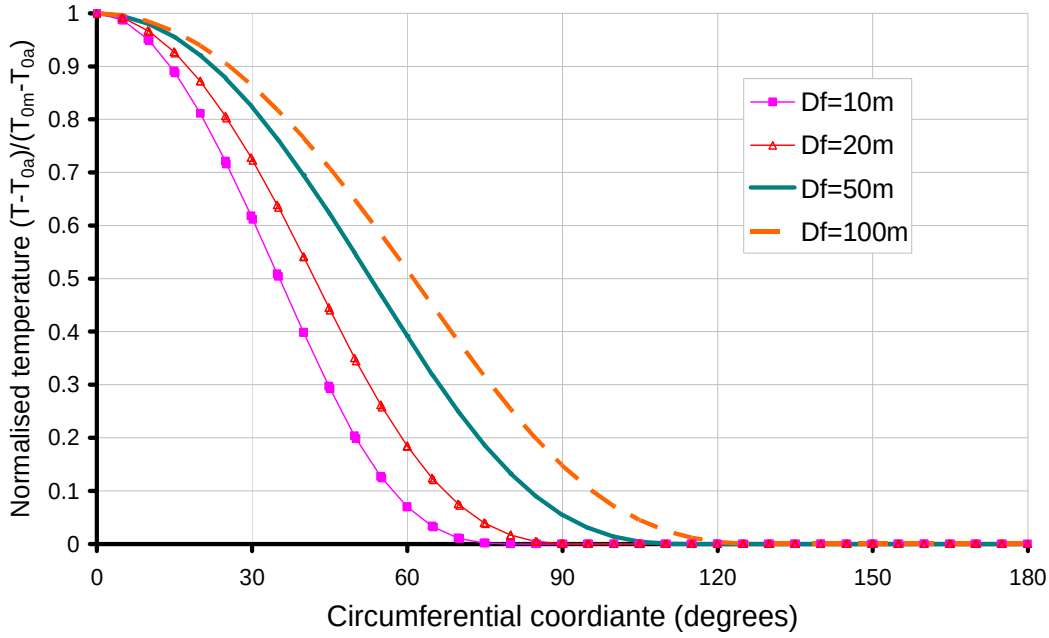

(a) Normalised temperature distribution around the circumference at h=10m

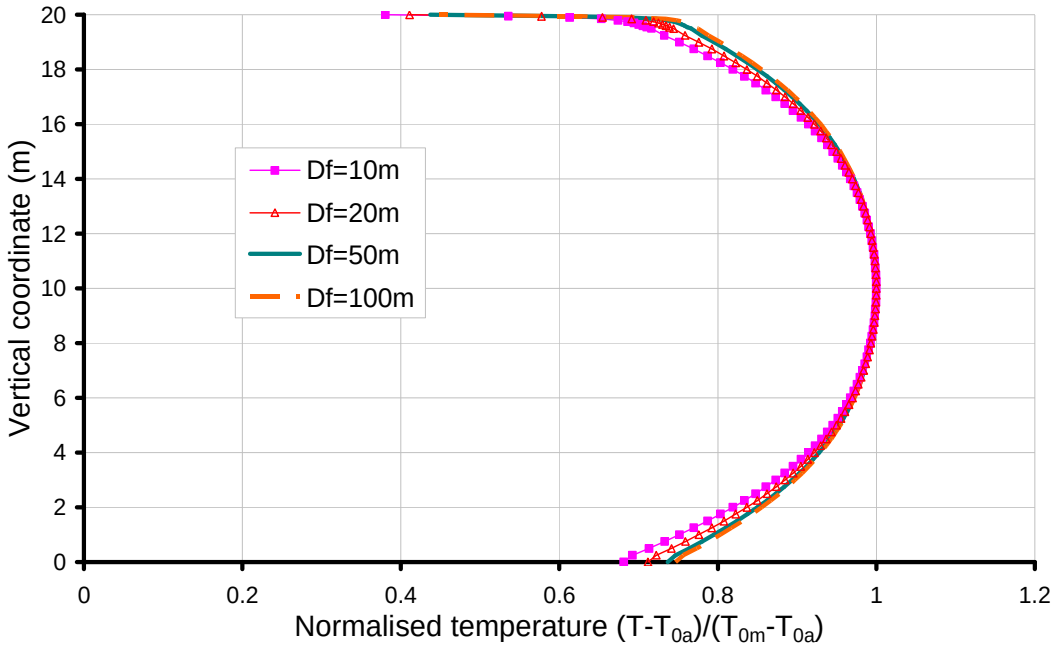

(b) Normalised temperature distribution along the most heated meridian

Figure 5-44 Effect of fire diameter on temperature distribution of an empty tank (H_{f0}=0m, Case 1)

When the tanks are placed following NFPA 30 requirements (Case 2), the circumferential heating range still increases with the fire size (Figure 5-45a). However, the vertical temperature distribution is only slightly affected by the fire size, which is mainly due to the change of the fire-tank distance, the fire diameter.

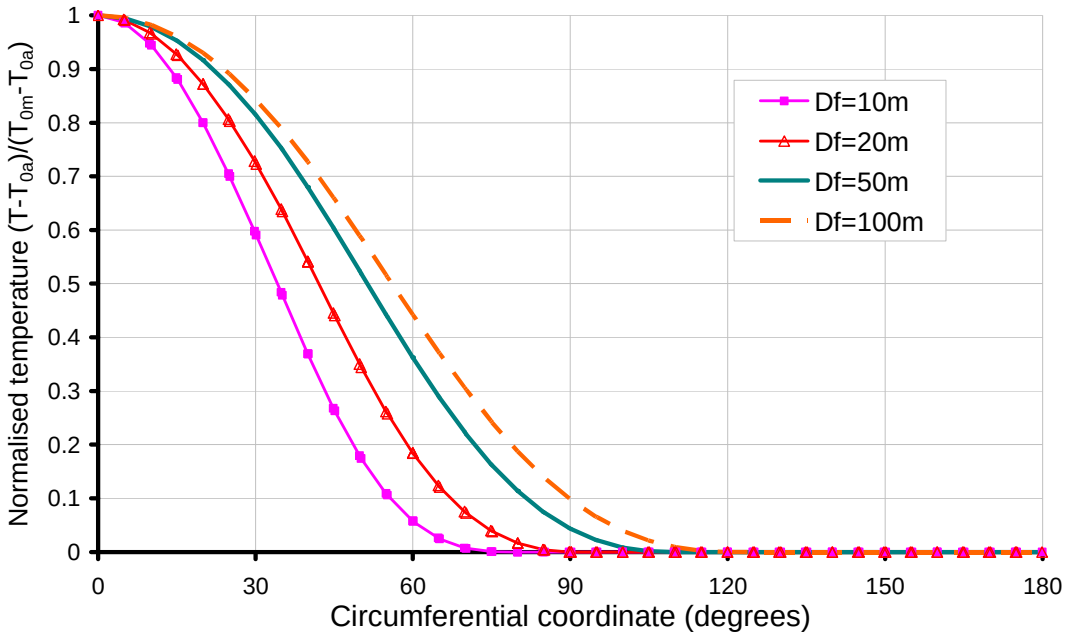

(a) Normalised temperature distribution around the circumference at *h*=10m

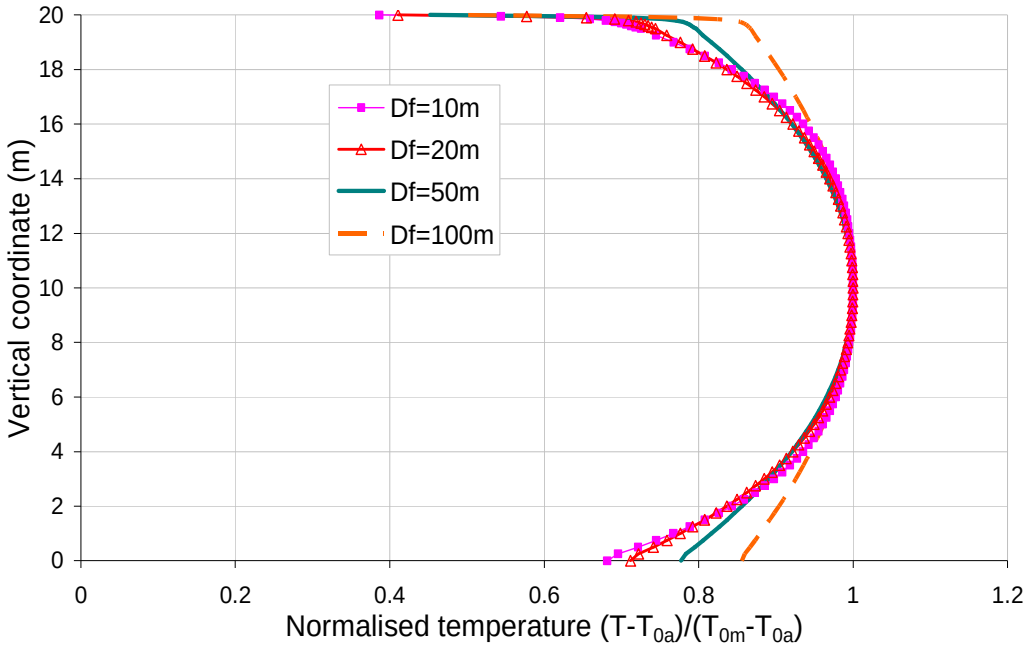

(b) Normalised temperature distribution along the most heated meridian

Figure 5-45 Effect of fire size on temperature distribution of an empty tank (H_{f0}=0m, Case 2)

Figure 5-56 shows the effect of the fire diameter on the predicted maximum temperature for both cases. If the tank separation is fixed (Case 1), the maximum temperature increases with the fire size all the time but the rate of increase is not linear and reduces with an increased fire size. When a variable separation is employed (Case 2), the predicted maximum temperature rise increases initially with the fire diameter. It reaches a peak at an intermediate fire diameter and then reduces as the fire diameter further increases.

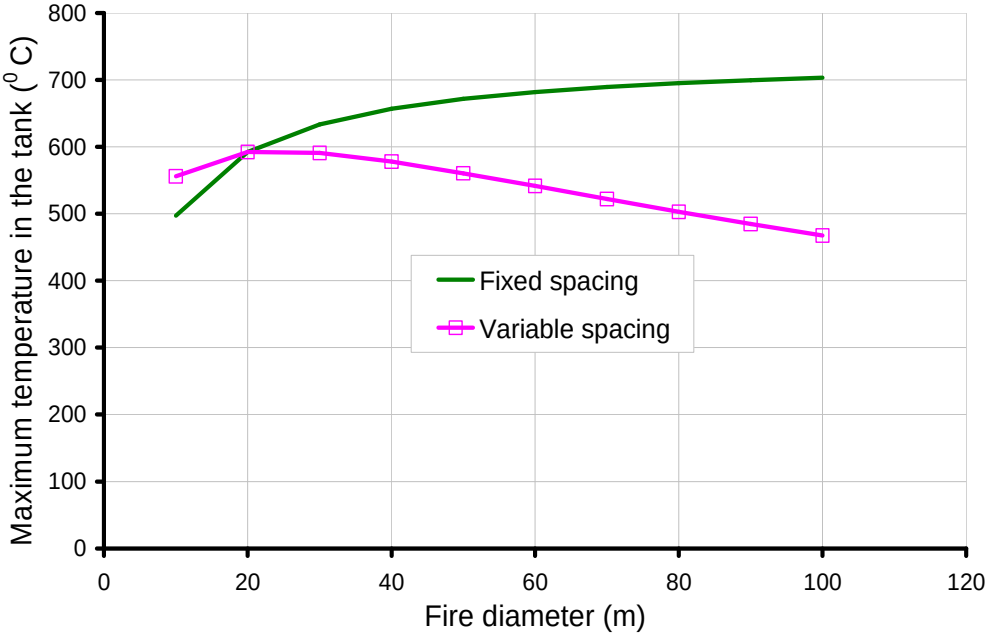

Figure 5-46 Effect of fire size on the maximum temperature in the cylindrical tank wall (H_{f0}=0m)

5.6 Conclusions

This chapter has presented the detailed techniques for modelling liquid hydrocarbon pool fires. A semi-empirical model, i.e. the solid flame model was adopted for this study. An upright cylinder was chosen to represent the shape of a tank fire. Typical values of parameters for defining the fire model were given. 1D and 2D steady state heat transfer analyses were conducted using Abaqus. The results were further validated against theoretical solution and 3D model.

The results of a reference case which involves an empty tank exposed to an adjacent fire of the same diameter show that the predicted temperature in the target tank has large spatial gradient around the circumference. Only about one half of the tank is heated and the temperature around the circumference has a cosine-like distribution. The temperature gradient in the meridian direction is not significant especially when

a larger flame height is adopted. There is negligible temperature difference between the inner and outer surfaces of the tank wall, due to good conductivity of steel and thin thickness of the wall. Temperature on the roof of the tank is mainly dependent on how high the flame reaches. The tank roof remains cool if the fire does not reach the roof height, otherwise it is heated. The temperature distribution in the circumferential direction on the roof is similar to that of the cylindrical wall.

A sensitivity study has been carried out for the fire parameters on the prediction of temperature distribution. Among those variables studied, the heat transfer coefficient of the liquid has a significant effect. The temperature of tanks containing liquid with a high heat transfer coefficient only increases a little above the ambient temperature, but it is not the case for liquids with a low heat transfer coefficient. The inclusion of radiation inside of the tank is essential in heat transfer analysis only when the emissivity of the inner surface is large. The peak value of temperature rise in the tank increases with the emissivity. The fire emissive power is another important parameter in this analysis. The predicted temperature shows a linear relationship with the emissive power of fire. The value of the thermal conductivity of common metals has negligible influence on the temperature prediction.

Various fire scenarios and tank conditions on the temperature distribution in the tank have been studied. Firstly, the filling level inside of the tank was investigated. For a partially filled tank, there exists a sudden temperature change near the liquid surface. Temperature elevates along the tank wall in a very short distance from a low value below the liquid level to a high value above. The length of such transition zone is almost independent on the liquid level. It has also been discovered that the temperature distribution along the meridian of a partially filled tank can be obtained by first examining two extreme cases: when the tank is empty or fully filled, and then adding the temperature change near the transition part to joint the two temperature distribution curves.

The vertical fire location and the flame height have been shown to mainly influence the temperature distribution pattern along the meridian direction of the cylindrical tank wall. For an empty tank, the cylindrical tank wall has an approximately uniform

temperature rise only if fire starts from a very low height and the flame height is no lower than the height of the target tank. For other situations, the maximum temperature occurs in the tank wall along a meridian can have a difference as large as 400 °C. For the case of a fire starting from at high level, the flame height has little effect on the temperature distribution along the meridian in the cylindrical wall. For a fully filled tank, the temperature rise is within 100 °C in all the cases.

The horizontal distance between tank and the fire can significantly influence the maximum temperature induced in the tank, but it does not affect the temperature distribution pattern around the circumference. The temperature distribution along the vertical coordinate also only affected slightly and it tends to be more uniform when the fire is placed farther away from the tank.

The fire diameter affects both the circumferential range of temperature increase and the highest temperature in the tank. It is shown if the separation between tanks is fixed, the larger the fire diameter is, the higher the temperature is developed in the tank and the wider the tank is heated. However, if the separation distance follows the requirement of NFPA30, in which the separation is a linear function of the diameter of both the tank and the fire, the highest temperature is not produced by the largest diameter fire scenario but the heated region still increase in size with an increase in the fire diameter.

Chapter 6

6. Simple temperature distribution models for heated tanks

6.1 Introduction

This chapter deals with the generalisation of the predicted temperature distributions in Chapter 5, aiming to develop simple models with algebraic expressions for the convenience of structural analysis. A generalised algebraic expression is useful to people who have no knowledge of heat transfer analysis but need to do some quick structural assessment. A generalised expression for such purpose is normally expected to possess two properties: first, it is able to capture the salient characteristics of the temperature distribution; second, the form of the expression should be preferably as simple as possible.

It should be pointed out that, the second feature above is not only due to the concern of convenience in practical usage, but also based on the fact that some idealisations and assumptions have been made in the solid flame model for heat transfer analysis

which usually may have significantly reduced the overall accuracy already. Therefore the effectiveness of a precise fitting of the numerical predictions cannot be well justified. In other words, an over-refined fitting simply loses its practical meaningfulness if the accuracy of the heat transfer analysis is limited. As a result, the emphasis in this chapter is on seeking a simple expression which can largely represent the most important features without employing many fitting coefficients whose physical meanings are obscure and values sensitive to idealisations and assumptions made in the heat transfer analysis.

6.2 Proposed simple mode of temperature distribution

As investigated in Section 5.5.3, the liquid level inside the tank only noticeably alters the temperature distribution pattern along the vertical coordinate; it has little effect on the pattern around the circumference. Specifically, for a liquid with a high heat transfer coefficient, the temperature remains close to the ambient temperature below liquid level, and rises upward in the transition zone of about 0.2m, reaching the temperature that develops in an empty tank. Thus it is feasible to focus on the temperature distribution in an empty tank and then modify the resultant pattern to the cases of partially filled tank by including a lower ambient temperature zone and a transition zone.

Considering an empty tank exposed to a fire with the same diameter, the predicted temperature contours in the tank wall have been shown in Figures 5-19 to 21. As described in Section 5.5.2, the temperature distribution follows a cosine like function around the circumference. As further examined in section 5.5.5, when the relative size of the tank diameter to the fire diameter varies, the heated region around the circumference changes accordingly but the shape of the temperature distribution remains almost the same as in the reference case. Based on these observations, the following temperature pattern is proposed to fit the temperature distribution around the circumference:

$$T(\theta)=\begin{cases}(T_{0m}-T_{0a})\cos^2\left(\dfrac{\theta}{\theta_0}\cdot\dfrac{\pi}{2}\right) & if\ |\theta|\le\theta_0\\ 0 & if\ |\theta|>\theta_0\end{cases} \tag{6-1}$$

where θ is the circumferential coordinate, originating from the meridian facing the fire; θ_0 is the critical angle which represents the limit of the heated zone; T_{0a} is the ambient temperature; and T_{0m} is the maximum temperature reached in the tank wall when fire reaches the steady state and this temperature is on the most heated generator (θ=0°).

The temperature distribution along the vertical coordinate is more complex, as it changes significantly under different fire scenarios, for example, where the flame height or tank-fire distance varies. A straightforward algebraic expression as that for circumferential temperature distribution is not available. However, it may be noticed that the variation of the temperature along the vertical coordinate is mainly due to the effect of viewfactor. Thus an approximate expression may be constructed by modifying the calculated equations for the viewfactor along the vertical coordinate. In such way, the parameters used here also possess the same practical meanings as that of the viewfactor, such as the tank-fire distance, vertical fire location and flame height. The development of the expression is presented below.

For simplicity, the calculation of the viewfactor is simplified as a 2-D problem, by neglecting the finite size of the fire and tank in the horizontal plane. This is acceptable as the purpose of this calculation is only seeking a useful expression instead of an accurate value. In Figure 6-1, the left and right bars represent the tank and the fire respectively. The clear distance between the tank and fire, the flame height, the height of the target tank and the height of starting level of the fire are respectively denoted as d, H_f, H and H_{f0}.

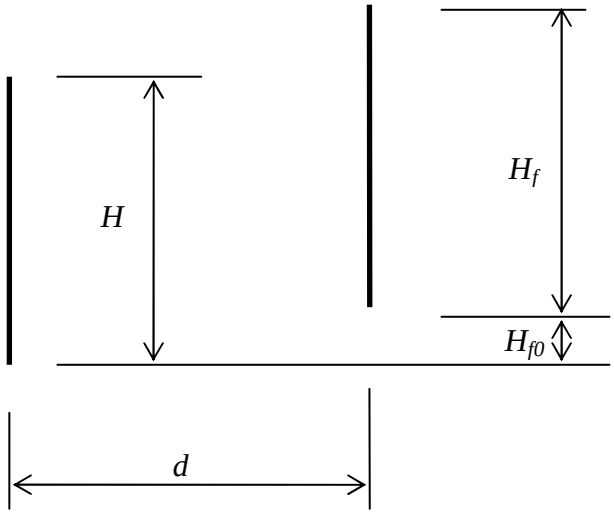

Figure 6-1 A Simplified 2D model of tank-fire viewfactor

As introduced in Chapter 2, the viewfacor can in general be expressed as

$$F_{ij} = \frac{1}{A_i}\int_{A_i}\int_{A_j}\frac{\cos\phi_i \cos\phi_j}{\pi R_{ij}^2} dA_i dA_j , \tag{6-2}$$

The 2-D viewfactor F_{ij} can then be derived by using geometrical parameters in Figure 6-1 as

$$F_{ij} = \int_{H_{f0}}^{H_f+H_{f0}} \frac{d^2}{\pi\left(d^2+(x-z)^2\right)^2} dx = \frac{d^2}{\pi}\int_{H_{f0}}^{H_f+H_{f0}} \frac{1}{\left(d^2+(x-z)^2\right)^2} dx \tag{6-3}$$

Simplifying the integration by replacing *x*-*z* by *y*, gives

$$
\begin{aligned}
F_{ij} &= \int_{H_{f0}-z}^{H_f+H_{f0}-z} \frac{d^2}{\pi\left(d^2+y^2\right)^2} dy \\
&= \frac{d^2 y}{2\pi d^2\left(d^2+y^2\right)}\Bigg|_{H_{f0}-z}^{H_f+H_{f0}-z} + \frac{1}{2\pi} arctg\, \frac{y}{d}\Bigg|_{H_{f0}-z}^{H_f+H_{f0}-z} \\
&= \frac{H_f+H_{f0}-z}{2\pi\left(d^2+\left(H_f-z\right)^2\right)} - \frac{H_{f0}-z}{2\pi\left(d^2+\left(H_{f_0}-z\right)^2\right)} \\
&\quad + \frac{1}{2\pi} arctg\, \frac{H_f+H_{f0}-z}{d} - \frac{1}{2\pi} arctg\, \frac{H_{f0}-z}{d}
\end{aligned}
\tag{6-4}
$$

Expression in Eq. 6-4 is very complicated and contains four terms: A= $\frac{H_f+H_{f0}-z}{2\pi\left(d^2+\left(H_{f0}-z\right)^2\right)}$, B= $\frac{z-H_{f0}}{2\pi\left(d^2+\left(H_{f_0}-z\right)^2\right)}$, C= $\frac{1}{2\pi} arctg\, \frac{H_f+H_{f0}-z}{d}$, D= $\frac{1}{2\pi} arctg\, \frac{z-H_{f0}}{d}$. It is desirable to examine the significance of each term so that further simplification may be achieved.

Taking the reference tank case in Section 5.5.2 as an example, the quantities of the four parts are plotted in Figure 6-2.

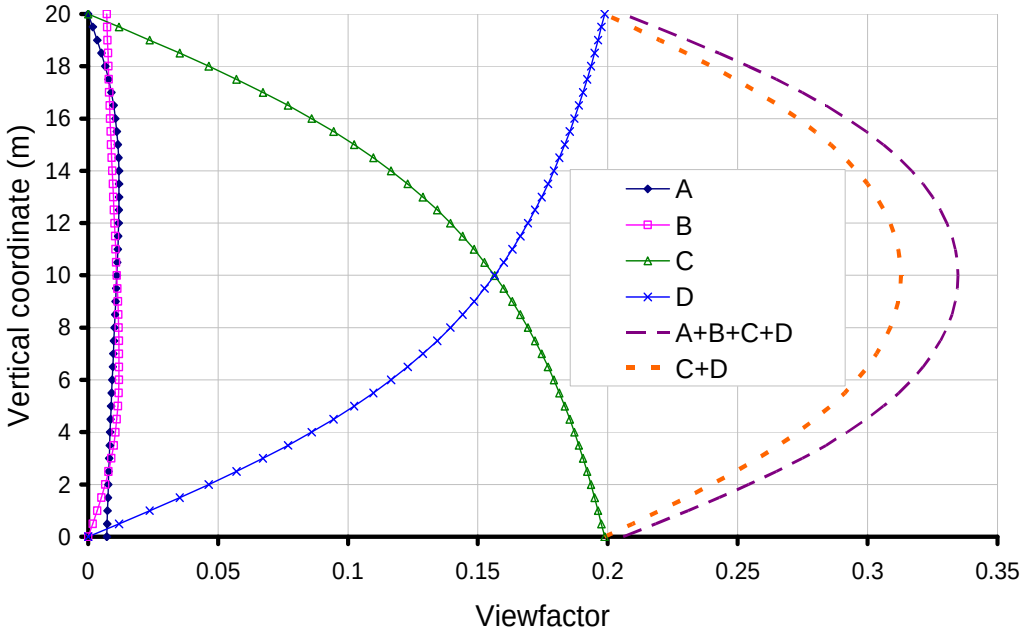

Figure 6-2 Quantities of the four terms in Eq.6-4 for the reference case (d=20/3m; H_f=20m, H_{f0}=0m)

It can be seen the relative weightings of terms A and B are rather small compared to that of terms C and D. Hence, terms A and B may be neglected so that Eq. 6.4 is reduced to

$$F = C + D = \frac{1}{2\pi}\left(arctg\frac{H_f + H_{f0} - z}{d} - arctg\frac{H_{f0} - z}{d} \right) \tag{6-5}$$

Expression F is then normalised below to provide the final expression used for describing the temperature distribution in vertical direction.

Letting $$\frac{dF}{dz} = \frac{1}{2\pi}\left(-\frac{1}{d}\frac{1}{1+\left(\frac{H_f + H_{f0} - z}{d}\right)^2} + \frac{1}{d}\frac{1}{1+\left(\frac{H_{f0} - z}{d}\right)^2} \right) = 0$$

gives $z = \frac{H_f}{2} + H_{f0}$ where the maximum F occurs. Substituting it into Eq. 6-5 gives

$$F\Big|_{z=\frac{H_f}{2}+H_{f0}} = \frac{1}{\pi} arctg \frac{H_f}{2d} \tag{6-6}$$

If $\frac{H_f}{2} + H_{f0}$ <H, the normalised expression *F* then can be written as

$$F(z) = \frac{arctg \frac{H_f + H_{f0} - z}{d} - arctg \frac{H_{f0} - z}{d}}{2 arctg \frac{H_f}{2d}} \tag{6-7}$$

If $\frac{H_f}{2} + H_{f0}$ >H, the normalised expression *F* then can be written as

$$F(z) = \frac{arctg \frac{H_f - z}{d} + arctg \frac{z}{d}}{arctg \frac{H_f - H}{d} + arctg \frac{H}{d}} \tag{6-8}$$

It is shown in Figure 6-3 that neglecting terms A and B in Eq. 6-4 has only negligible influence on the final normalised expression.

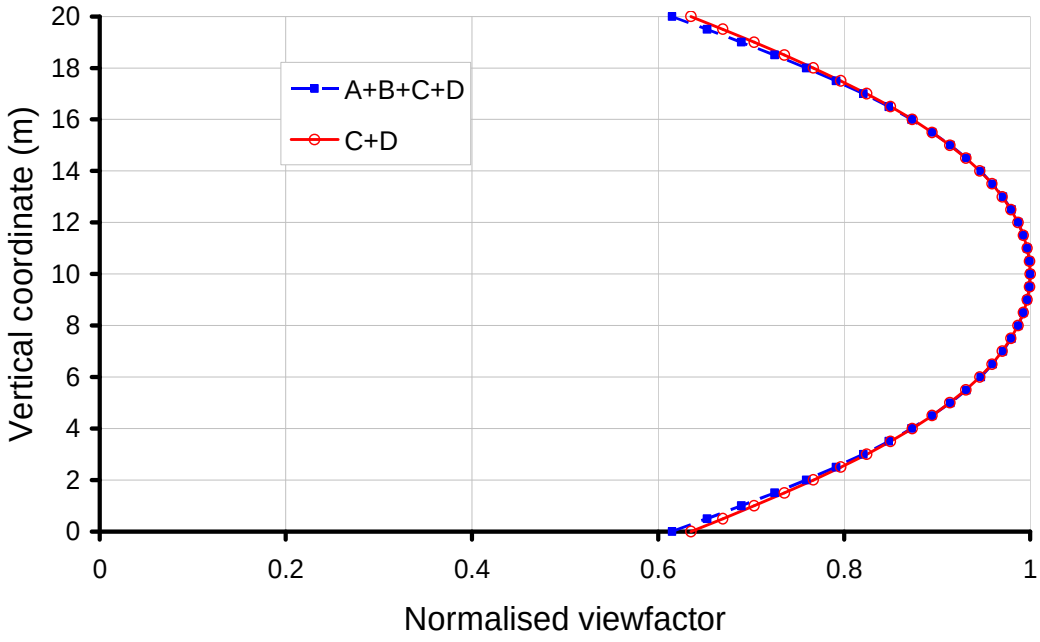

Figure 6-3 Normalised viewfactor *F* (*d*=20/3m H_f=20m)

Equation 6-7 and 6-8 is the proposed expression for temperature distribution along the vertical coordinate for an empty tank. For partially filled tanks, as explained earlier, to account for the effect of liquid level this expression is modified to

$$F(z)=\begin{cases}\chi F(z)_{empty} & if\ z<H_{liq}\\ (1-\chi)F(z)_{empty}\dfrac{z-H_{liq}}{l_t}+\chi F(H_{liq})_{empty} & if\ H_{liq}<z<H_{liq}+l_t\\ F(z)_{empty} & if\ z>H_{liq}+l_t\end{cases} \quad (6\text{-}9)$$

where H_{liq} is the liquid level in the tank; l_t is the transition length above the liquid level, $F(z)_{empty}$ is the temperature in the empty tank expressed in Eqs 6-7 and 8, χ is a fraction of the maximum temperature developed in the empty tank. The value of χ is dependent on the properties of the liquid inside the tank. For liquid having a large heat transfer coefficient, χ=0, which means the temperature of tank wall in contact with liquid is the same as the ambient temperature. For a typical material stored in oil

tanks, such as what considered in the reference case in Chapter 5, χ has a value in the range of 0 to 0. 8. χ = 0.19 was adopted in the reference case with liquid inside.

Finally the temperature distribution for the whole tank wall is proposed as follows

$$T(\theta, z) = T_{0a} + F(z) \times T(\theta) \tag{6-10}$$

where T_{oa} is the ambient temperature. Based on temperature distribution in a partially-filled tank as shown in Figure 5-31 to Figure 5-33, a value of 0.2m for the transition length l_t is suggested. The value is dependent on the thickness of the tank wall, but as the conductivity of the metal is very large, this number is not sensitive to practical wall thickness.

Temperature distribution in the roof is highly dependent on the flame height. In cases where flame is not high enough to heat the whole roof surface, the back side of the roof remains cool. In this case the heating range (θ_0) on the roof is nearly the same as that in tank wall. The temperature along vertical coordinate can be reasonably taken as linearly decreasing above the cylinder-roof junction. The reducing rate depends on the slope of the roof. The following function is proposed to represent the temperature distribution on the roof:

$$T_{roof} = \begin{cases} (T_0 - T_{0a})[\xi_0 + (1-\xi_0)\sin\phi]\cos^2\left(\frac{\theta}{\theta_0}\cdot\frac{\pi}{2}\right)\frac{r}{R} + T_{0a} & if\ |\theta| \le \theta_0 \\ T_{0a} & if\ |\theta| > \theta_0 \end{cases} \tag{6-11}$$

where ϕ is the roof slope, r is the radial coordinate on the roof, R is the radius of the tank, and T_0 is the temperature of the hottest point on the roof edge. The maximum temperature in the roof is defined as $\xi_0 T_0$, with $0 \le \xi_0 < 1$. If ξ_0 =0, T_{roof} = 0 for a flat roof and 1 for a vertical roof. $\xi_0 = 0.5$ may be suggested for normal oil tanks.

For cases where the fire starts near the roof level, or the flame is high enough to heat the whole roof surface, Eq. 6-11 remains applicable, if a larger θ_0 is used (similar to the case of the tank wall subjected to a large diameter fire).

It should be pointed out that, the circumferential temperature distribution pattern along the whole tank height in above proposed expressions is kept to the same. This is a good approximation for tanks exposed to fire from near ground level. However, for fire starts at a very high position above the ground, the circumferential temperature distribution varies along the height as studied in Section 5.5.5. The effect of adoption of a constant value for θ_0 will be further evaluated in Chapter 9.

6.3 Determination of parameters in the proposed model

There are only two coefficients in the proposed model which need to be determined: the maximum temperature developed in the tank T_{max} and the heating range θ_0. This section aims to determine these two coefficients and compares the temperature distribution calculated from the proposed model with that predicted by the heat transfer analysis in Chapter 5.

The reference case in Section 5.5.2 is studied here. Only two unknown parameters in the proposed temperature pattern need to be determined for each particular case: the maximum temperature developed in the tank wall T_{0m} and the heated range around circumference θ_0.

The temperature around circumference at different locations can be fitted by the Eq. 6-1 and the results are shown in Figure 6-4.

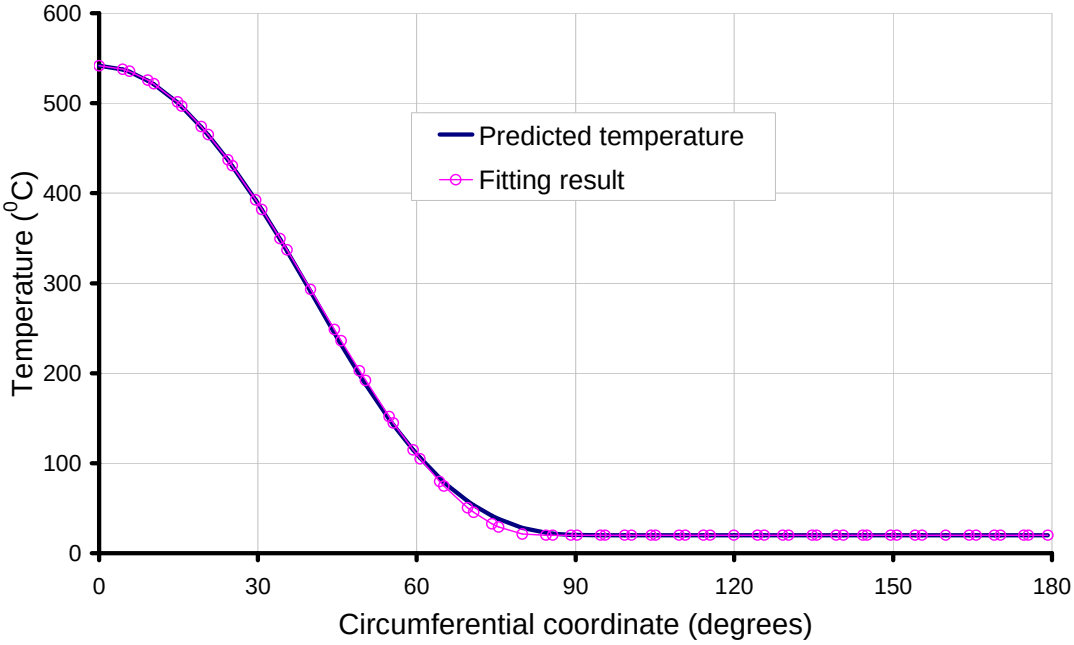
600
500
400
300
200
100
0
Temperature (^{0}C)
Predicted temperature
Fitting result
0
30
60
90
120
150
180
Circumferential coordinate (degrees)

(a) h=5m

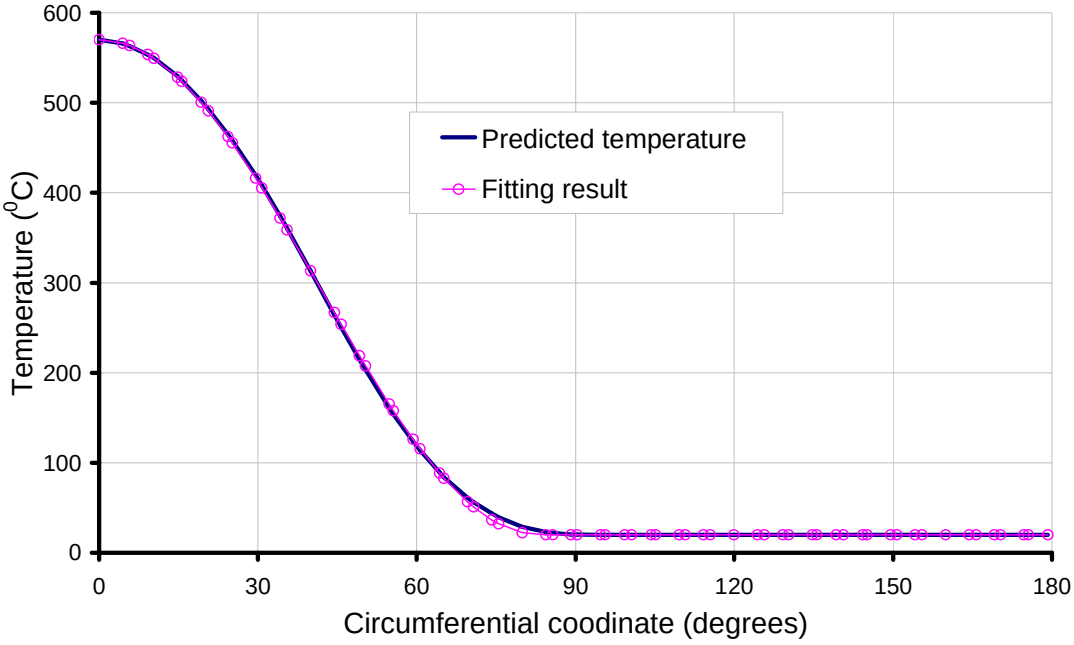
600
500
400
300
200
100
0
Temperature (^{0}C)
Predicted temperature
Fitting result
0
30
60
90
120
150
180
Circumferential coodinate (degrees)

(b) h=10m

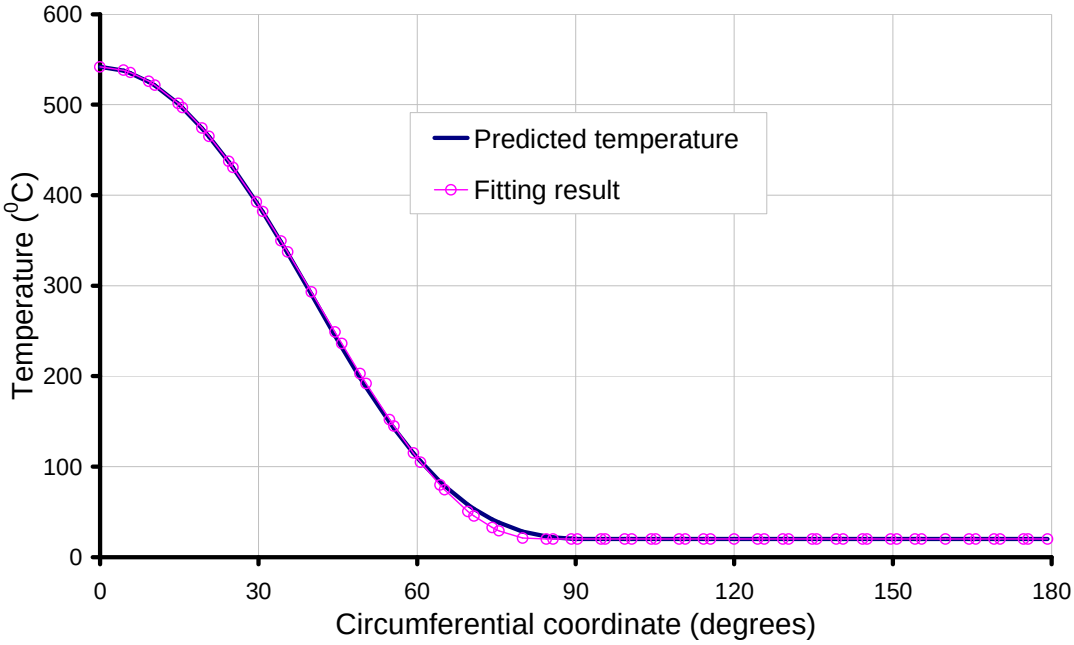

(c) h=15m

Figure 6-4 Comparison of predicted temperature distribution around the circumference and fitted temperature at different vertical locations (d=20/3m; H_f=20m; H_{f0}=0m)

It can be seen that the proposed temperature pattern fits the predicted temperature around circumference very well at various heights. The fitting results shown in Figure 6-4 are for cases with a flame height H_f=20m. It is noted that the proposed equation can also well fit that of cases with different flame heights. For example, a different flame height H_f=40m has also been examined, but the results are omitted here.

The fitted values of the critical angle θ_0 at different vertical locations are shown in Figure 6-5 for two cases with different flame heights. Clearly there is only a small variation of the value θ_0 along the vertical coordinate for the majority of the wall. Thus it is acceptable to adopt a constant value of heating range θ_0 for the whole height (e.g., a mean value of these θ_0 along vertical coordinate).

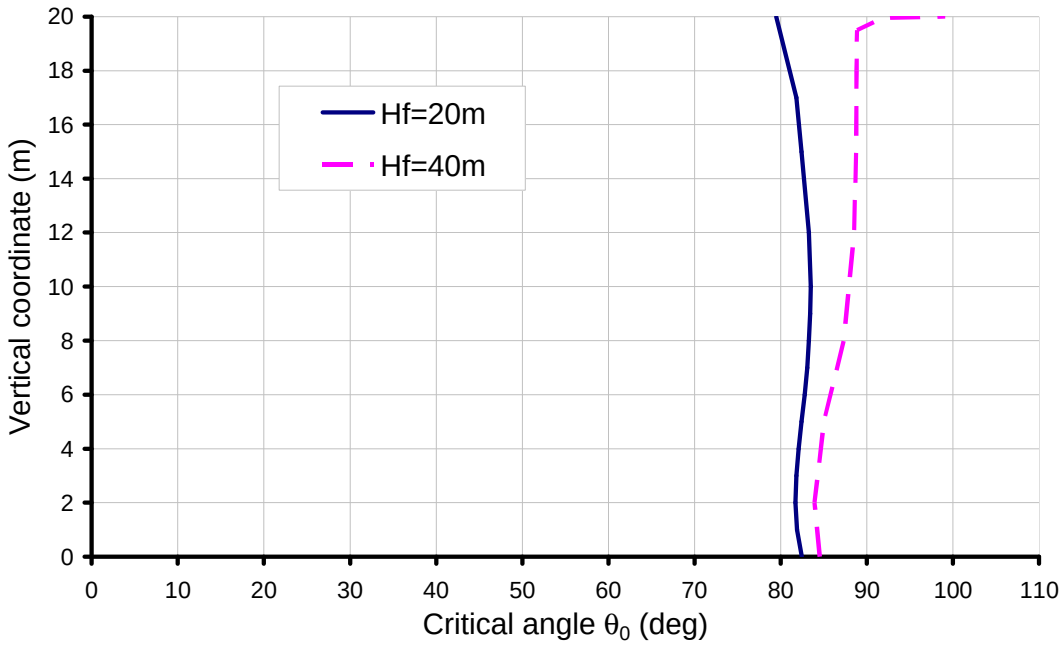

Figure 6-5 Variation of fitted θ_0 along the vertical coordinate

The proposed temperature distribution along the vertical coordinate at different circumferential coordinate is shown in Figure 6-6. It can be seen that the proposed expression can closely describe the shape of the predicted temperature distribution with small discrepancies near the top and bottom boundaries. The effect of this discrepancy on the structural behaviour will be further investigated in Chapter 9.

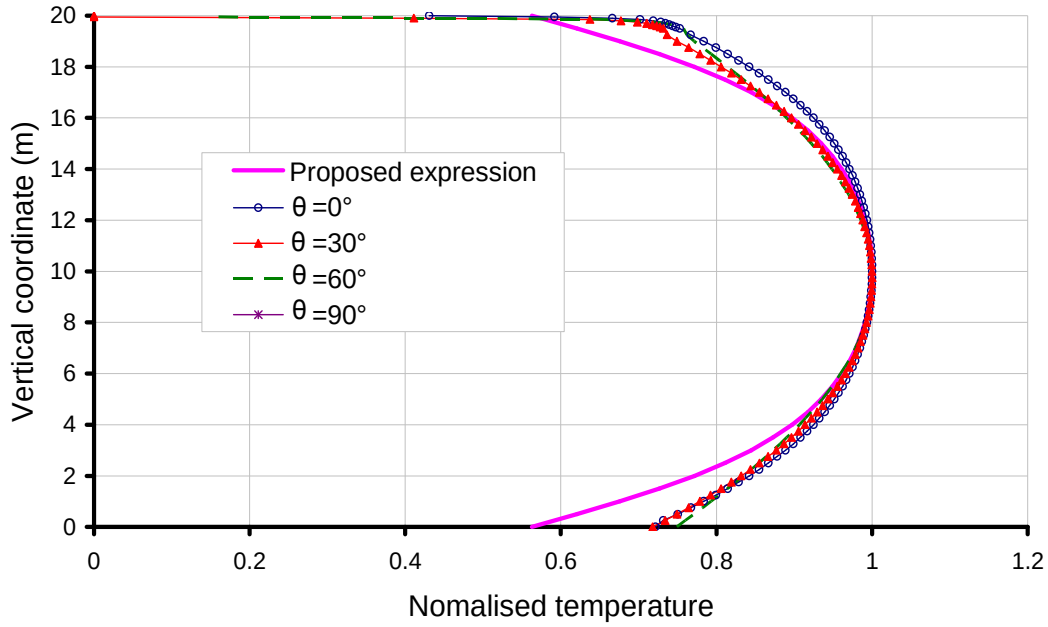

Figure 6-6 Temperature distribution along the vertical coordinate: proposed expression vs. numerical heat transfer analysis (d=20/3m; H_f=20m; H_{f0}=0m)

The value of θ_0 for each fire scenario will be examined in the next section.

The second unknown parameter in the proposed model is the maximum temperature developed in the tank wall T_{0m}. This can be obtained from basic heat transfer equations constructed upon a 1-D scenario (Figure 6-7).

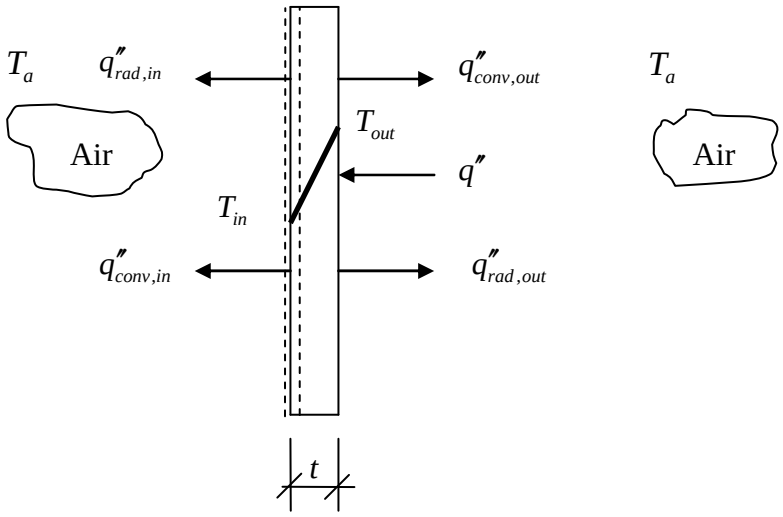

Figure 6-7 Conservation of energy for a plate

In this 1-D situation, the plate may be regarded as the most heated meridian of the tank wall. The wall receives heat flux due to fire radiation $q'' = F_{\max} q''_f$, where F_{max} is the maximum viewfactor in the tank, and q''_f is the heat flux of the fire. Radiation heat transfer on the outer and inner surfaces of the tank are $q''_{rad,out} = \varepsilon_w \sigma\left(T_{out}^4 - T_a^4\right)$ and $q''_{rad,in} = \varepsilon_w \sigma\left(T_{in}^4 - T_a^4\right)$ respectively. Convection heat transfer inside and outside of the tank are $q''_{conv,out} = \bar{h}_{out}\left(T_{out} - T_a\right)$ and $q''_{conv,in} = \bar{h}_{in}\left(T_{in} - T_a\right)$ respectively.

For the steady state, the energy balance takes the form:

$$\varepsilon_{in}\sigma\left(T_{in}^4 - T_a^4\right) + \bar{h}_{in}\left(T_{in} - T_a\right) = F_{\max} q''_f - \bar{h}_{out}\left(T_{out} - T_a\right) - \varepsilon_{out}\sigma\left(T_{out}^4 - T_a^4\right) \quad (6\text{-}12)$$

As has been studied in Section 5.4.1, for thin steel tank walls, the temperature in the inner surface (T_{in}) and outer surface (T_{out}) is almost the same. Let $T_{in} = T_{out} = T_s$, Eq. 6-12 is simplified to

$$F_{\max} q''_f - \bar{h}_c\left(T_s - T_a\right) - \varepsilon\sigma\left(T_s^4 - T_a^4\right) = 0 \quad (6\text{-}13)$$

where $\bar{h}_c = \bar{h}_{in} + \bar{h}_{out}$ and $\varepsilon = \varepsilon_{in} + \varepsilon_{out}$.

The wall temperature can then be obtained by solving Eq. 6-13. As Eq. 6-13 is a quartic equation, solving it may be not straightforward. An alternative iterative solution is proposed as follows.

Eq. 6-13 can be further written as

$$F_{\max} q''_f - h_c (T_s - T_a) - \varepsilon_w \sigma \left(T_s^2 + T_a^2\right)\left(T_s + T_a\right)\left(T_s - T_a\right) = 0 \qquad (6\text{-}14)$$

Set

$$\bar{h}_T = \bar{h}_c + \varepsilon\sigma \left(T_s^2 + T_a^2\right)\left(T_s + T_a\right) \qquad (6\text{-}15)$$

Eq. 6-14 becomes

$$F_{\max} q''_f = \bar{h}_T (T_s - T_a) \qquad (6\text{-}16)$$

So,

$$T_s = \frac{F_{\max} q''_f}{\bar{h}_T} + T_a \qquad (6\text{-}17)$$

As the viewfactor F_{max} is within the range of 0 to 1, the most conservative value for F_{max} is 1. The accurate calculation of the maximum view factor for tanks exposed to specific fire scenario can be found in Shokri and Beyler (1989).

The equivalent heat transfer coefficient $\bar{h}_T$ with surface temperature is shown in Figure 6-8 for different values of surface emissivity. It can be seen that $\bar{h}_T$ increases with the surface temperature. Its variation is rather small for a low surface emissivity, but large for a high surface emissivity. The maximum temperature in the oil tank due

to fire radiation can be obtained through an iterative process using Eqs 6-15 and 6-17: a) use an estimated T_s to calculate $\bar{h}_T$ from Eq. 6-15; b) a new T_s is calculated from Eq. 6-17. This new T_s is then used in Eq. 6-15 to repeat the process until a convergence is reached.

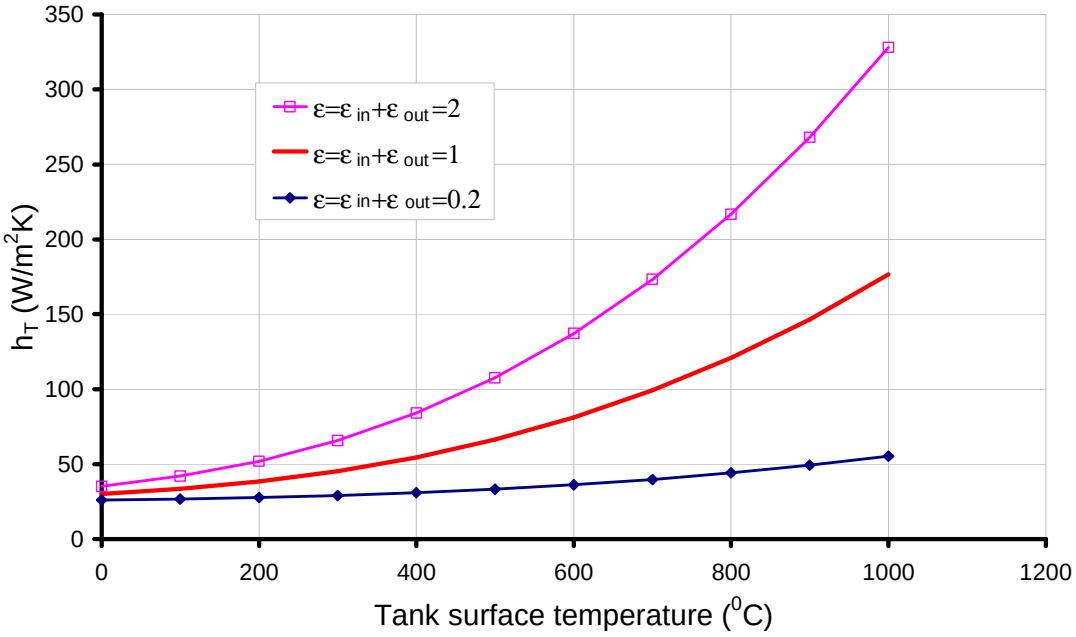

Figure 6-8 Effect of material emissivity on the equivalent heat transfer coefficient - tank surface temperature

6.4 Examination of the proposed temperature model in various fire scenarios

The accuracy of the proposed temperature distribution model is further compared below with that resulted from heat transfer analysis under different fire scenarios.

6.4.1 Fire diameter

The effect of fire diameter investigated in Section 5.5.7 shows that the diameter of the fire mainly affects the heating range around the circumference. The temperature

around the circumference at mid height of the tank can be fitted by the Eq. 6-1. The heating range (θ_0) for a target tank of 20m diameter exposed to fire with diameter ranging from 2m to 200m is shown in Figure 6-9. It can be seen that θ_0 lies in the range of 40 degrees to 130 degrees. When the spacing between the tank and fire is fixed, the critical angle θ_0 is slightly larger than that in the case where tanks are spaced according to NPFA30. Figure 6-9 shows that the critical angle θ_0 changes with the ratio of diameter of tank on fire and the target tank. The change of θ_0 with the normalised fire size is shown in Figure 6-10, which may be used for estimating this angle.

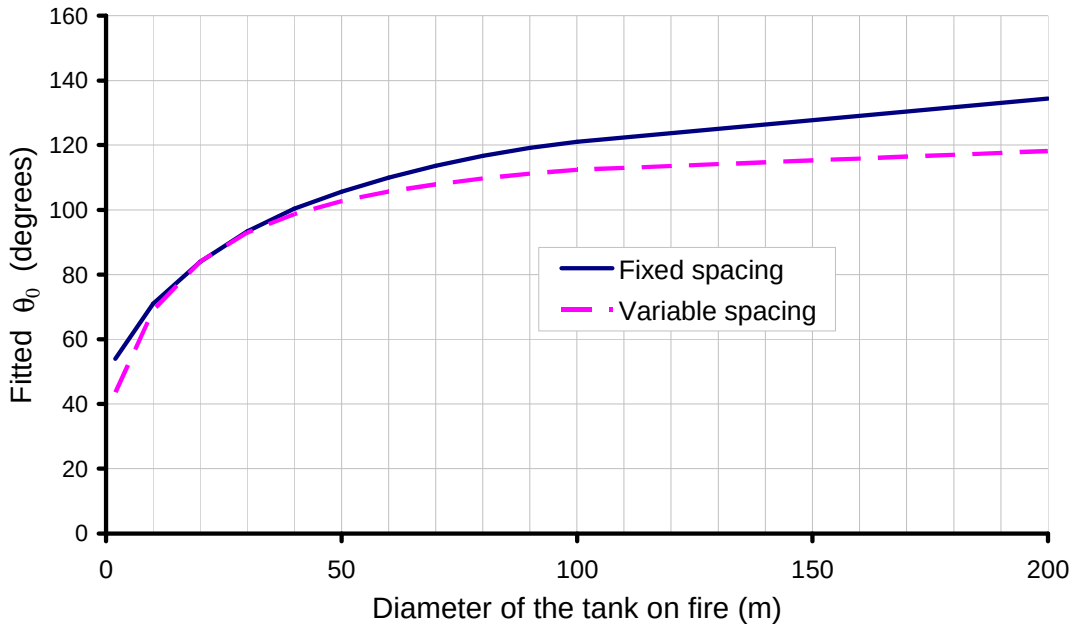

Figure 6-9 Effect of fire size on θ_0

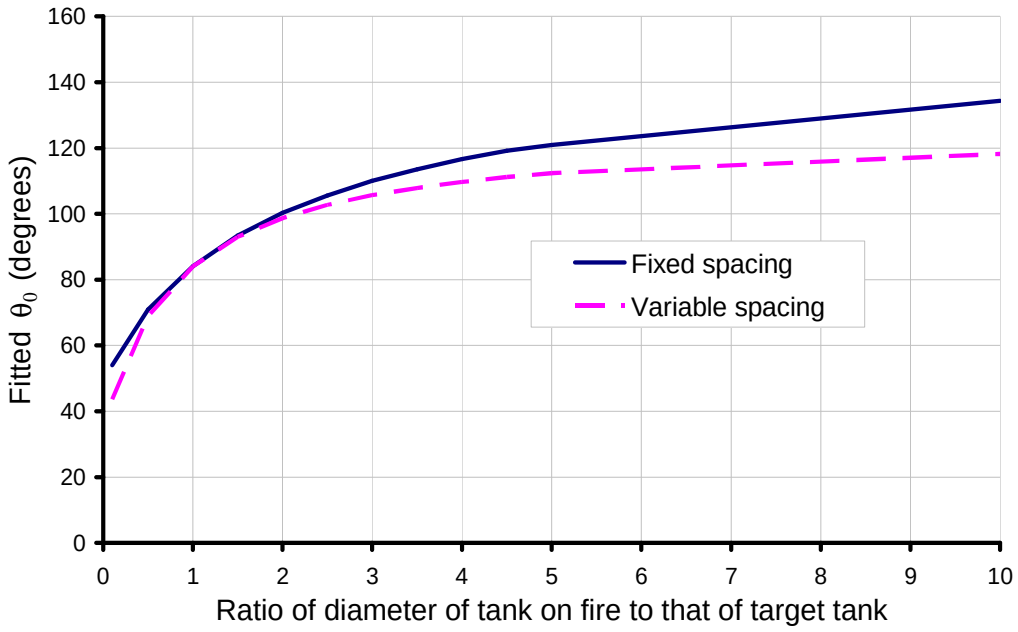

Figure 6-10 Variation of θ_0 with the normalised fire size

6.4.2 Fire locations

The effect of the fire location is mainly influencing the temperature distribution along the vertical coordinate. The temperature at the most heated meridian ($\theta=\theta_0$) is extracted for comparison. It can be seen from Figs 6-11 to 6-13 that the proposed temperature distribution model may describe various fire cases reasonably well, such as when the fire is placed at various horizontal and vertical locations and with different flame heights..

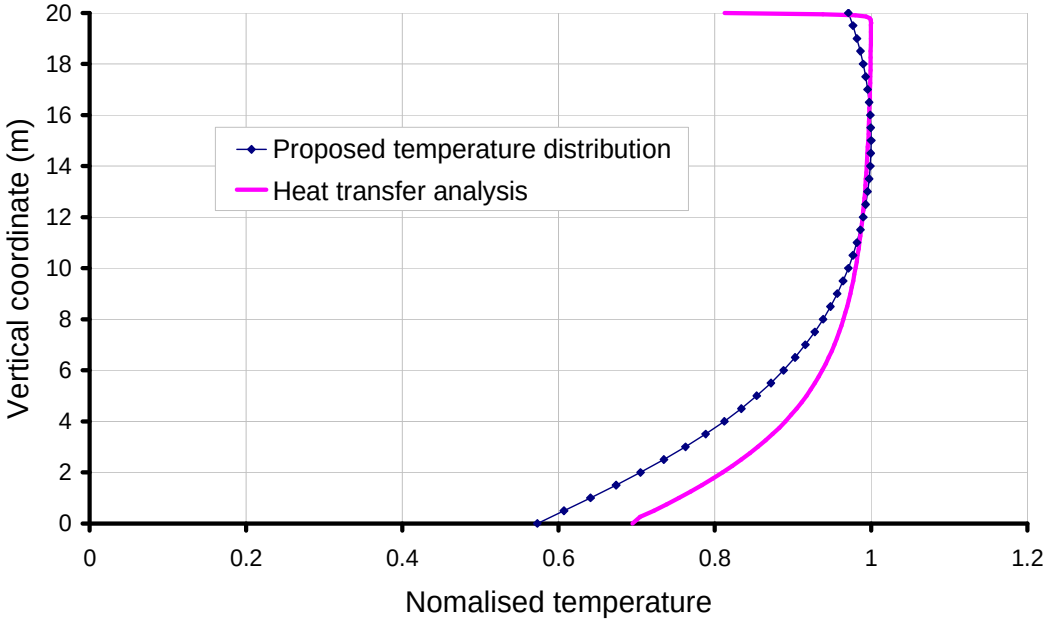

Figure 6-11 Normalised temperature distribution along the vertical coordinate (d=6.67m; H_f=40m; H_{f0}=0m)

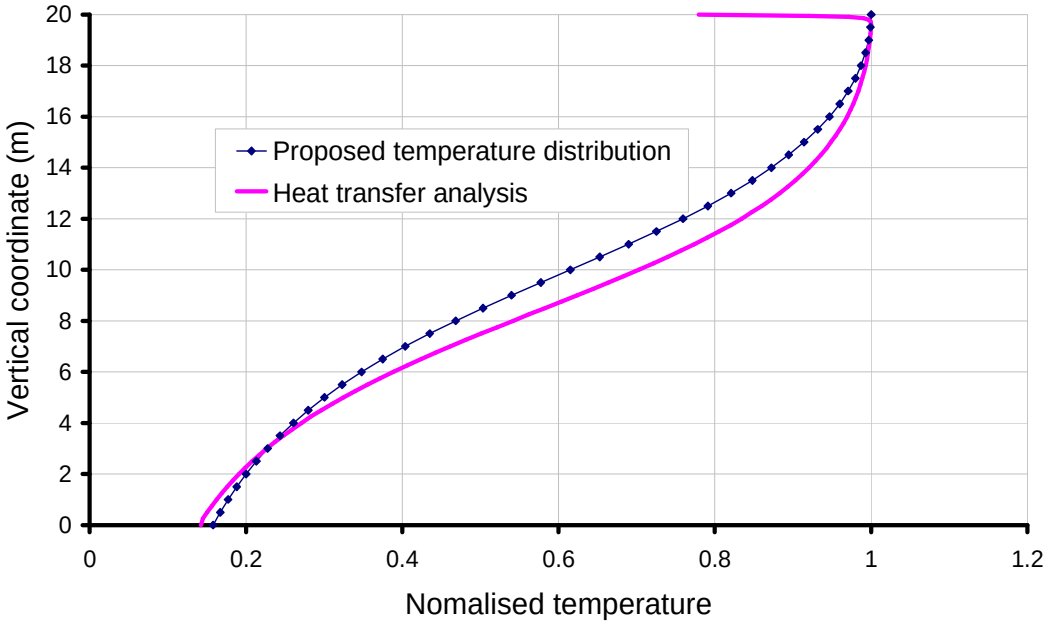

Figure 6-12 Normalised temperature distribution along the vertical coordinate (d=6.67m; H_f=20m; H_{f0}=10m)

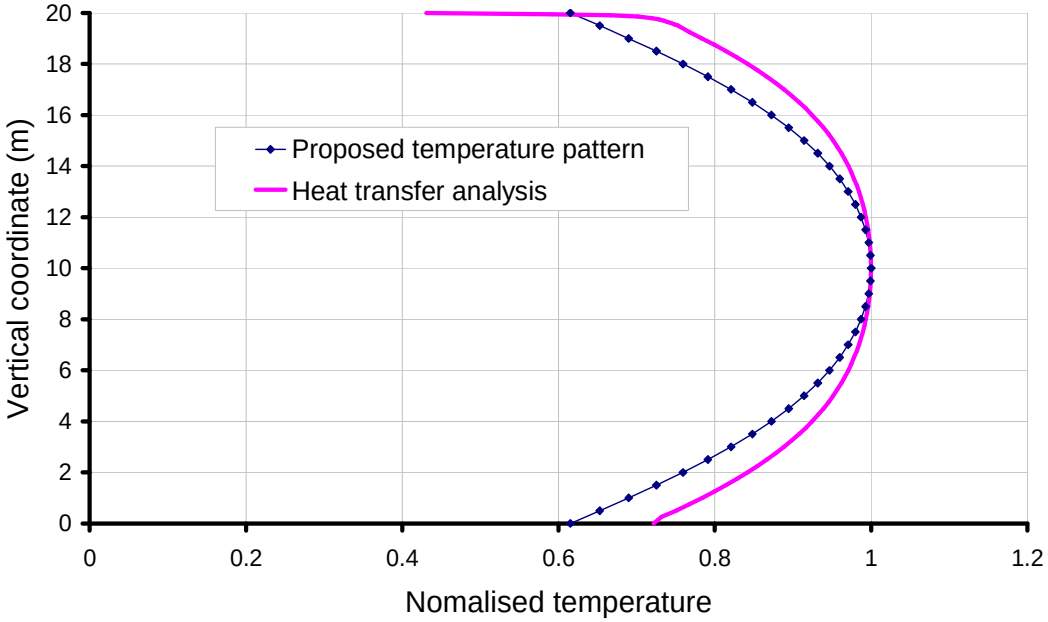

Figure 6-13 Normalised temperature distribution along the vertical coordinate (d=15m; H_f=20m; H_{f0}=0m)

6.4.3 Liquid level

For partly filled tank, the temperature distribution developed in the tank only differs in the vertical direction compared to that of an empty tank. In addition, the adopted heat transfer coefficient $\bar{h}$ has an effect on the temperature below the liquid level, as studied in Section 5.5.4 and shown in Figure 5-31. This variation is considered by adopting a different value of χ in Eq. 6-9.

Figures 6-14 a, b & c compare the proposed temperature rise along the vertical coordinate at θ=0 with predictions from the heat transfer analysis by using different heat transfer coefficients. They show that the proposed temperature distribution model gives a very good approximation to the heat transfer predictions for liquid with all convective heat transfer coefficients. The factor χ is between 0.07 and 0.78, which determines the temperature below the liquid level.

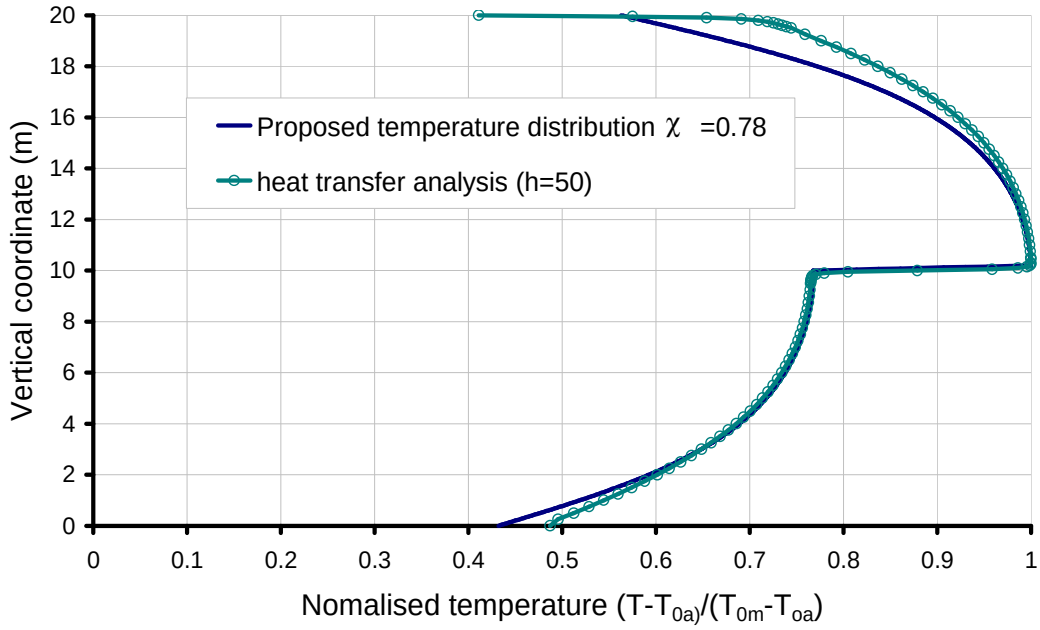

(a) $\bar{h}$ =50 W/m^{2}K

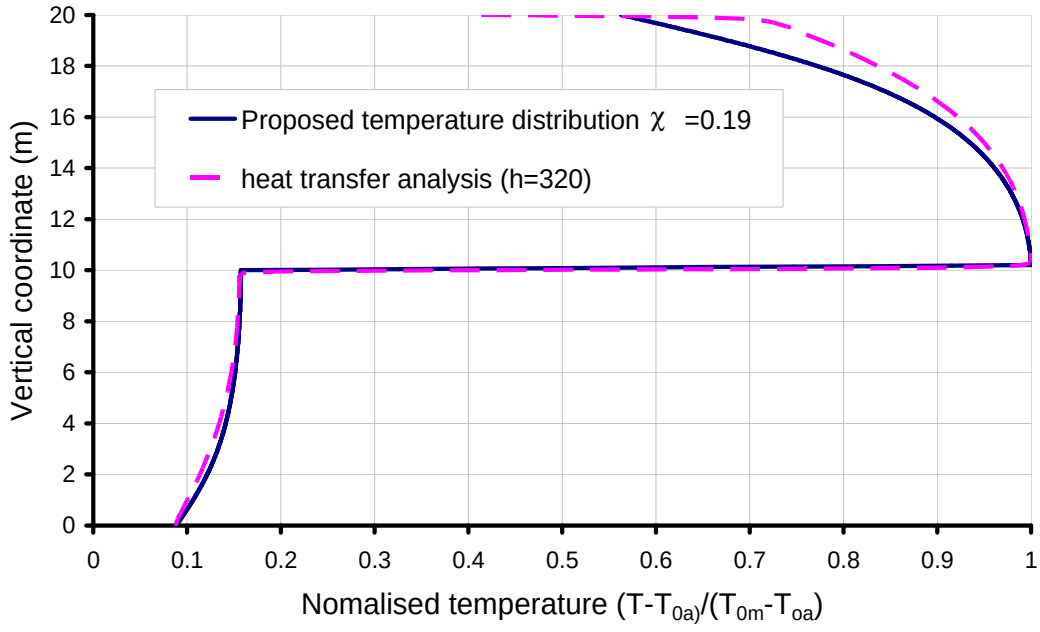

(b) $\bar{h}$ =320 W/m^{2}K

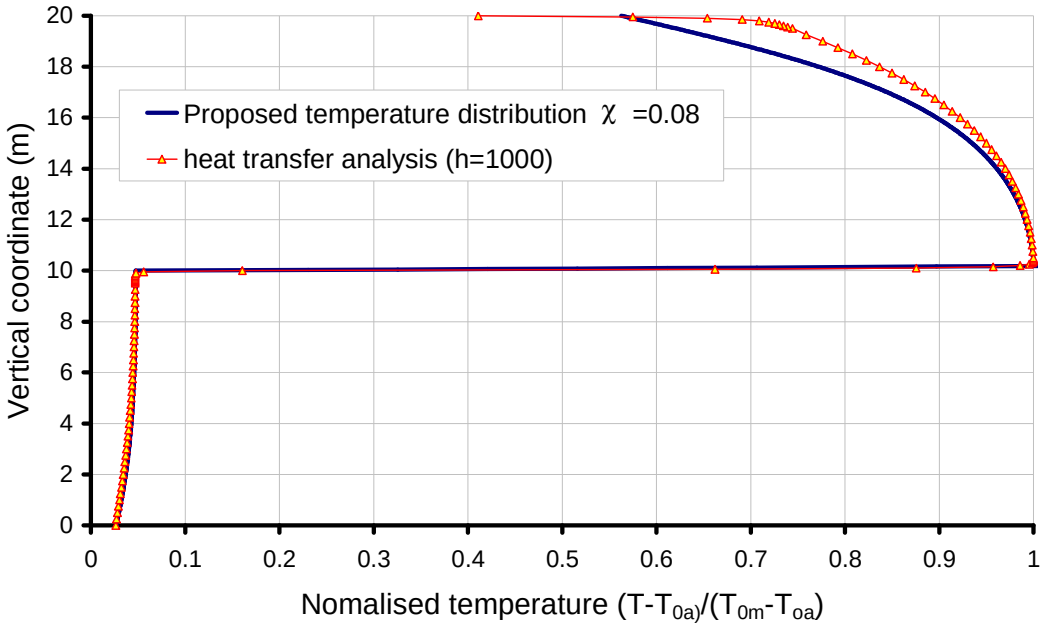

(c) $\bar{h}$ =1000 W/m^{2}K

Figure 6-14 Normalised temperature distribution along the vertical coordinate (d=6.67m; H_f=20m; H_{f0}=0m)

6.5 A further simplified model

The above proposed algebraic temperature distribution model has been shown to be able to closely describe the salient features of the numerically predicted temperature distribution in the target tank. However, the form of it may still be regarded as complex, mainly in the vertical direction. It is therefore in this section, a further simplification is considered in order to provide an even simpler model for future structural analysis such as in Chapter 7.

Considering the heat transfer analysis results in Figure 5-17, a uniform temperature change is conceived to be acceptable to approximate the temperature rise along the vertical coordinate for cases where the fire starts from ground level. For fires that locate at different horizontal distances, the critical angle and the temperature variation along the vertical coordinate change slightly, and only the maximum

temperature in the tank varies significantly as investigated in Section 5.5.6 (Figure 5-42). Therefore, it may be assumed that both the circumferential size of the heating zone remains constant and the temperature distribution in the vertical direction is uniform. Following these assumptions, the temperature distribution is expressed by:

$$F(z)=\begin{cases} 1 & if \quad z > H_{f0} \\ \dfrac{z}{h_{f0}} & if \quad h_l < z < H_{f0} \\ 0 & if \quad z > H_{liq} \end{cases} \qquad \text{for } h_l<H_{f0} \qquad \text{(6-11a)}$$

$$F(z)=\begin{cases} 1 & if \quad z > H_{liq}+l_t \\ \dfrac{z-h_{l0}}{l_t} & if \quad H_{liq} < z < H_{liq}+l_t \\ 0 & if \quad z < H_{liq} \end{cases} \qquad \text{for } h_l>H_{f0} \qquad \text{(6-11b)}$$

where H_{f0} is the height of the starting point of the fire; H_{liq} is the liquid level inside of the target tank; l_t is the transition length above the liquid level and z is the vertical coordinate.

Figure 6-15 compares the temperature rise between the simple model and the numerical predictions along the vertical coordinate for the reference case. It shows that the simple model fits roughly the numerically predicted temperature with some discrepancies. The simple model may give conservative temperature estimation as the full height is assigned to the maximum temperature. As for the partially-filled tank, the temperature below the liquid level is assumed to be the same as the ambient temperature which approximates the case where the liquid has a large heat transfer coefficient (Figure 6-15b).

Figure 6-16 shows the temperature distribution along the vertical coordinate in an empty tank under a fire starting from different vertical locations.

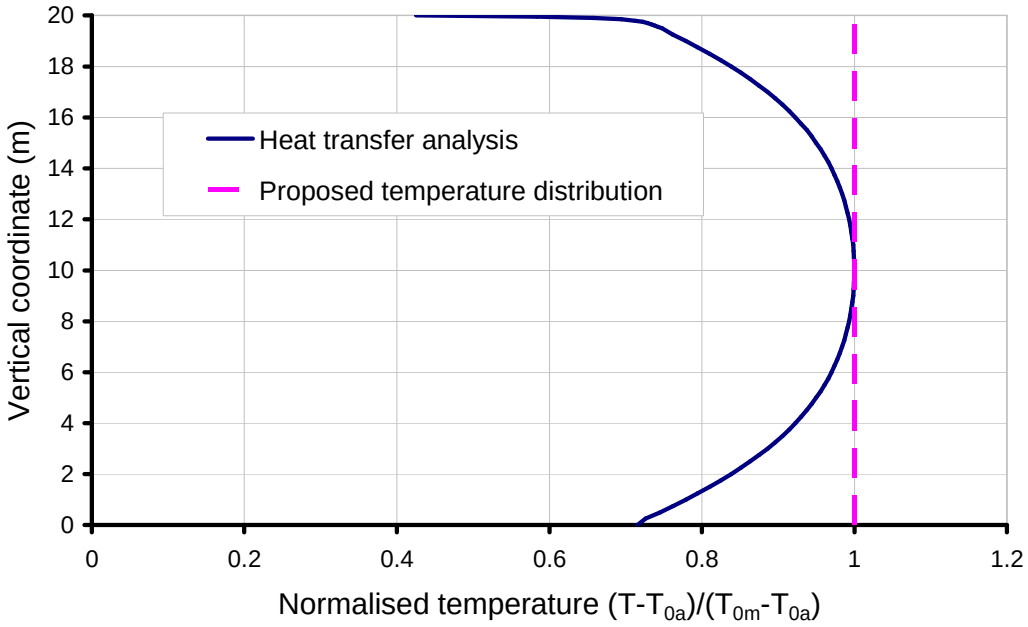

(a) An empty tank

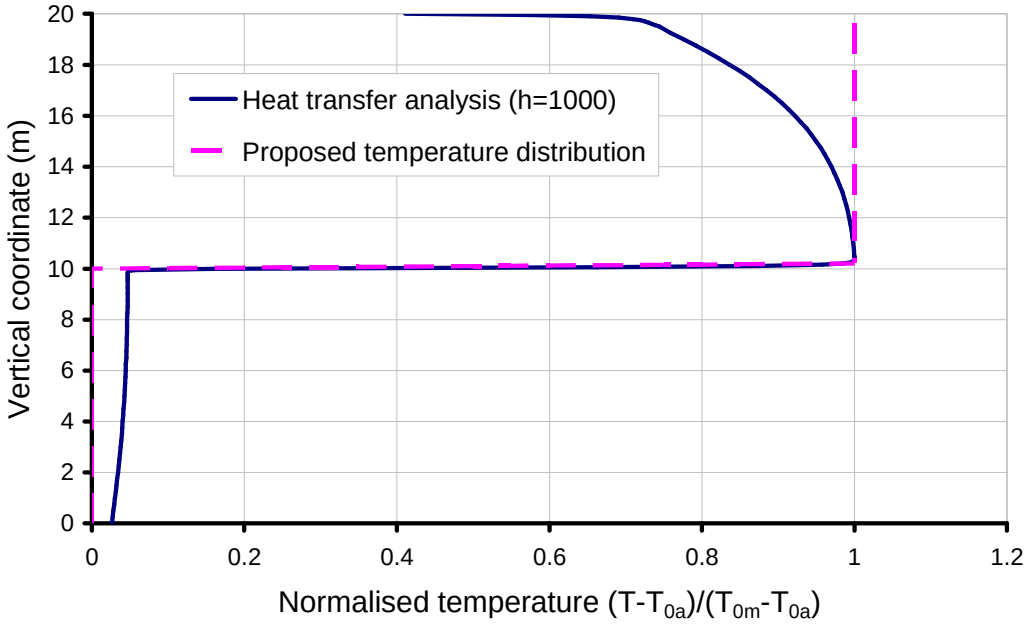

(b) A half-filled tank

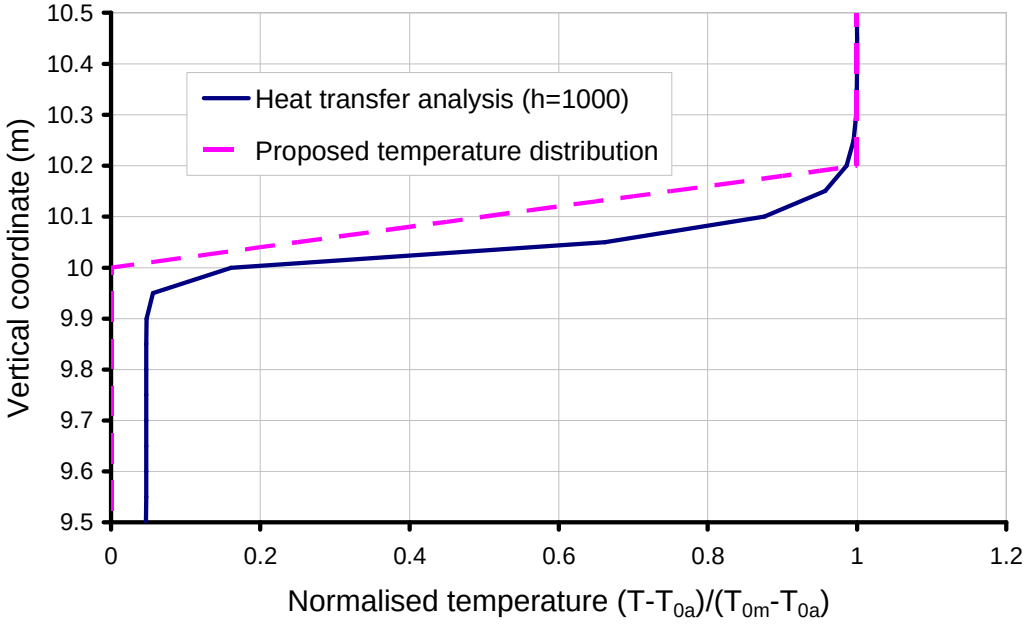

(c) Detailed temperature variation near the liquid level

Figure 6-15 Temperature distribution along the vertical coordinate: proposed further simplified model vs. heat transfer analysis (d=6.67m; H_f=20m; H_{f0}=0m)

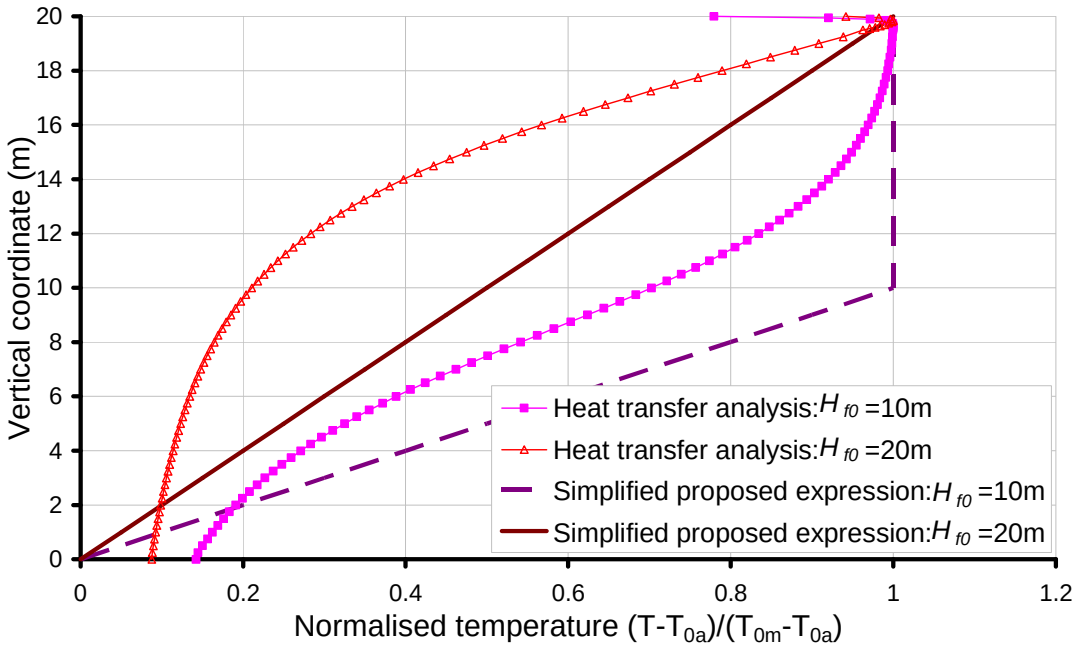

Figure 6-16 Normalised temperature distribution along the vertical coordinate: further simplified model vs. heat transfer analysis (d=6.67m; H_f=20m)

6.6 Conclusions

This chapter has presented two temperature distribution models for the target tanks: a rigorous model based on semi-analytical solution and a simple model simplified from it. These models may serve as convenient models for analyzing the behaviour of the tank structure under the thermal loading. The rigorous model has only a few parameters which all possess physical meanings such as the diameter of the fire, location of fire and liquid level inside of the target tank. It has been shown that this model is able to accurately describe the numerically predicted temperature rise in the tank under all kinds of fire scenarios considered.

A further simplified model has also been proposed for those cases where the rigorous model is still considered as cumbersome. In this model the temperature pattern around circumference remains the same as that in the rigorous model while the simplified temperature rise along vertical coordinate is introduced. It is shown that this expression can also largely capture the most silent feature of the temperature rise pattern and has an advantage of its simplicity yet providing a conservative temperature distribution for structural analysis. This model may be used in preliminary structural analysis.

Chapter 7

7. Buckling behaviour of a tank under a simplified temperature distribution

7.1 Introduction

This chapter conducts non-linear buckling analysis of a typical tank exposed to an adjacent tank fire. The simplified temperature distribution model in Chapter 6 Section 6.5 was adopted here to establish the character of the problem and to determine whether buckling failures might be expected under this fire loading.

The objectives of this chapter are to describe the potential buckling failure modes of oil tanks exposed to an adjacent tank fire and to explore the influences of relevant parameters on such failures. The reasons for such buckling failures in oil tanks under fire may be found in the reduced modulus of steel at elevated temperatures, coupled with thermally-induced stresses due to the restraint of thermal expansion. Since the temperatures reached in such structures can be several hundred degrees Centigrade, any restraint to thermal expansion leads to the development of compressive stresses,

and the high susceptibility of thin shell structures to elastic buckling under very low stresses means that this type of failure is easily provoked.

The Chapter starts with introduction of the finite element model and mesh convergence study. Various analysis procedures were then conducted, including linear bifurcation analysis (LBA), geometrically non-linear analysis (GNA), and geometrically and materially non-linear analysis (GMNA), geometrically nonlinear elastic analysis with imperfections (GMNIA). Finally, the effects of several different parameters were investigated.

7.2 Finite element modelling

7.2.1 An example problem

To explore the potential for buckling in a typical cylindrical oil storage tank, a finite element study was undertaken for an example problem, following the requirements of the European Standard for Shell Strength and Stability (EN1993 1-6 2007). The goal of this study was to investigate the temperature rise required to cause a failure condition in the tank wall when the tank is heated from one side, using credible temperature distributions for the thermal field arising from a fire in an adjacent tank sited at one side of the target tank.

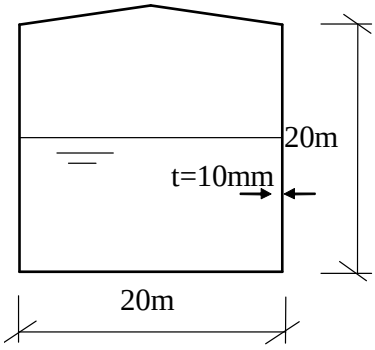

Figure 7-1 Example tank

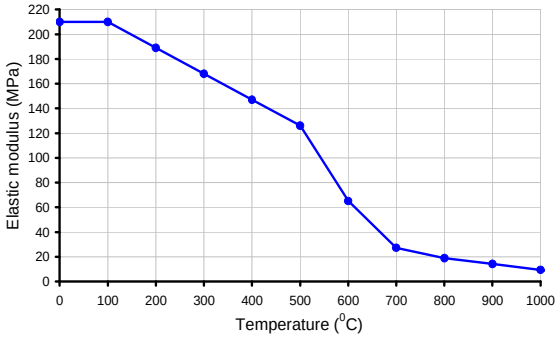

Figure 7-2 Reduction of elastic modulus with temperature (EN 1993-1-2, 2007)

As a suitable example structure, a tank of 20m high and 20m in diameter with a uniform cylindrical wall thickness of 10mm was chosen. A conical roof with a slope of 10° to the horizontal was assumed. The tank was assumed to be constructed from mild steel with an ambient temperature elastic modulus of $E = 2.1\times10^5$ MPa and a Poisson's ratio $\nu = 0.3$. The coefficient of thermal expansion and the elastic modulus were assumed to decline with temperature according to EN 1993 1-2 (2007). The shell was treated as pinned at the bottom edge and connected only to the shell roof at the eaves, with no ring. The effect of the boundary conditions on the buckling behaviour will be investigated in Section 7.3.2. The density of the stored liquid was taken as $\gamma = 0.74$ tonne/m^3. The tank geometry was assumed to be perfect.

A smaller diameter tank would have a thin roof without any internal support structure, while larger diameter tanks often have internal trusses and/or columns to support the roof structure which enhance the stiffness of the roof. As a simple model, a roof shell with uniform thickness was adopted while the support structure to roof was omitted. The effect of the support structure to the roof stiffness, however, was investigated by adopting different values of roof thickness which varies between 1 to 1000 times that of the cylindrical wall thickness. Although the upper bound of this range is clearly purely idealised, it shows how the roof stiffness influences the buckling temperature of an oil tank. It is noted that when the thickness was changed, the gravity of the roof was changing too. In order to keep the mass of the roof unchanged and equals to that of the mass when t_f=t_c, the density of roof material was scaled.

7.2.2 Thermal loading

When an adjacent tank of the same diameter is on fire, only half of the heated tank experiences temperature rises, as shown in Figure 7-3. If the burning tank has a larger diameter, it produces a slightly wider spread of heated zone in the target tank. By contrast, a burning tank of smaller diameter produces a concentrated heated zone in the target tank.

(a) Smooth-edge (θ_0=90°) (b) Half-cosine (θ_0=90°)

Figure 7-3 Temperature distribution patterns

Two alternative circumferential temperature distributions (Figure 7-3) will be used in this chapter. One is the simplified temperature model obtained by fitting functions to the results of the heat transfer analysis (Chapter 6 Section 6.5), which is here denoted as "Smooth-edge" pattern; the other one is a cosine function distribution, denoted "Half-cosine" pattern. The functional forms are given by

"Smooth-edge" temperature distribution:

$$T_\theta = \begin{cases} (T_{0m} - T_{0a}) \cos^2\left(\dfrac{\theta}{\theta_0} \cdot \dfrac{\pi}{2}\right) & if\ |\theta| \le \theta_0 \\ 0 & if\ |\theta| > \theta_0 \end{cases} \tag{7-1}$$

"Half-cosine" temperature distribution:

$$T_\theta = \begin{cases} (T_{0m} - T_{0a}) \cos\left(\dfrac{\theta}{\theta_0}\right) & if\ |\theta| \le \theta_0 \\ 0 & if\ |\theta| > \theta_0 \end{cases} \tag{7-2}$$

where θ is the circumferential coordinate, θ_0 is the critical angle which represents the limit of the heated zone and T_{0m} is the temperature on the most heated generator (θ=0°). The temperature rise T_{0m}- T_{0a} is used to characterise the temperature rise in

what follows. Figure 7-3 shows these two temperature distribution patterns with $\theta_0 = 90^0$.

The reason of choosing a Half-cosine function distribution temperature pattern for the temperature distribution around circumference is to investigate how sensitive the structural behaviour is to the circumferential temperature distribution, as a cosine distribution pattern is only slightly different from the other temperature pattern.

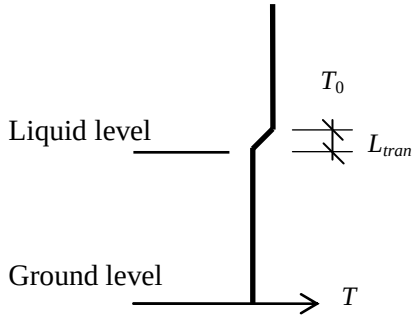

Figure 7-4 Temperature variation with vertical coordinate

As proposed in Chapter 6 Section 6.5, the temperature distribution up the vertical coordinate was simplified into a uniform temperature rise for an empty tank. A trilinear temperature distribution was used for a partially filled tank, as shown in Figure 7-4. Because the liquid inside the tank has a large thermal inertial, the tank wall in contact with the liquid remains quite cool during the fire, but the upper empty part of the tank wall can be rapidly heated and was here taken to experience a uniform temperature rise throughout its height. Between the cool and hot parts, a linear temperature variation was assumed to make some allowance for heat conduction between the hot and cool parts of the wall. The transition length used in this study is 0.2m.

Two thermal treatments of the roof were studied: it was either deemed to be heated (termed here “hot roof”) or to remain cool (termed here “cool roof). These two conditions correspond to the effects due to different flame heights in the adjacent burning tank. For the hot roof case, the variation of the temperature in the roof

around circumference was assumed to have the same pattern as the cylindrical wall. In the radial direction, it was assumed to vary linearly with radial coordinate at all circumferential coordinates. The maximum temperature in the roof was defined as $\xi_0 T_0$, with the parameter ξ_0 lying in the range $0 \leq \xi_0 \leq 1$, giving 0 for a flat roof and 1 for a vertical wall. Equation 3 gives the temperature function in the roof:

$$T = T_\theta \frac{r}{R}[\xi_0 + (1 - \xi_0)\sin\phi] \tag{7-3}$$

where ϕ is the roof slope, r is the radial coordinate of a point on the roof, R is the radius of the tank, and T_θ is the temperature of the hottest point on the cylindrical wall. In the following calculations, the temperature distribution was characterised by $\xi_0 = 0.5$.

The two treatments of the roof as “hot” and “cold” were used to explore whether the roof temperature is important in determining when the shell may collapse or buckle under this thermal regime.

In this Chapter, an ambient temperature of 0°C was assumed.

7.3 Analysis procedure

Structural failure of the tank was studied using the commercial finite-element (FE) package Abaqus (Simulia 2008). Four different types of analysis were adopted, namely linear buckling analysis (LBA), geometrically nonlinear buckling analysis (GNA), geometrically and materially nonlinear buckling analysis (GMNA) and geometrically nonlinear elastic analysis with imperfections (GNIA). The results are described as below.

7.3.1 Linear buckling analysis (LBA)

Eigenvalue buckling analysis is generally used to estimate the critical buckling loads of stiff structures. However, even when the response of a structure is nonlinear before collapse, a general eigenvalue buckling analysis can provide useful estimates of collapse mode shapes and it may be a good estimate for the limit load in the nonlinear buckling analysis. The buckling loads are calculated relative to the base state of the structure. The base state can include preloads, such as the gravitational load of the tank structure in this study.

In the analysis presented below, a general analysis step prior to the eigenvalue buckling analysis was conducted first, with the preload being the gravity loads. As geometric nonlinearity was omitted in LBA, the base state geometry remains the original configuration of the body. In the eigenvalue analysis step, the incremental loading pattern was the thermal loading patterns defined in Eqs 7-1 and 7-2, in which T_0=100°C. The whole tank was modelled using the 4-node general purpose element S4.

Mesh convergence

Before conducting extensive simulations, a mesh convergence study was performed to make sure that converged accurate results were being obtained. The classical elastic square wave buckling half-wavelength λ_{clsq} is given (Rotter 2004) by $\lambda_{clsq} \approx 3.46\sqrt{Rt} = 3.46\sqrt{10\times 0.01} = 1.09m$, whilst an axisymmetric buckle has half this wavelength. This classical square-wave buckling half-wavelength corresponds to a circumferential angle of 6.3°. The mesh sizes around the circumference and up the height must both be chosen to capture buckles as small as this. Near the boundary and liquid surface, large circumferential stresses gradients develop, so a fine mesh is needed there.

The vertical mesh scheme is shown in Figure 7-5 for partially filled tank. A fine mesh was used near the base, the liquid surface and the eaves. A mesh size of

L_1=1.5m was used in the final model. In other zones, a coarser mesh was adopted. When the tank was empty, the fine mesh was only used near the base and eaves. The mesh spacing around the circumference was uniform.

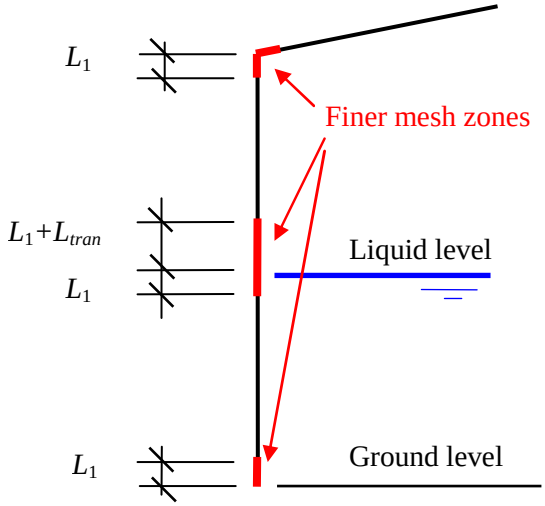

Figure 7-5 Mesh scheme along vertical coordinate

In Figure 7-6, the variation of the temperature at which buckling is predicted by a linear elastic eigenvalue analysis is plotted against the size of the critical elements first in the circumferential direction and then in the vertical direction. Unlike buckling under static mechanical loading, where a buckling load or stress can be compared with that for a simpler case (e.g. uniform axial compression), there is no corresponding reference condition for a tank (tanks do not buckle at all under uniform temperature rise). As a result, the predicted temperatures at buckling T_0 have been normalised relative to the value found for the chosen mesh $T_{0refe.}$, and provided that $T_{0refe.}$ is reasonably close to the correct answer, this should be an adequate method of normalisation. The problem chosen for this mesh convergence (Figure 7-1) was assessed as sufficiently typical for this mesh convergence process to be relevant to all the tank geometries used in this thesis. It is possible that tanks that buckle at very much higher temperatures would have different mesh convergence characteristics, but such tanks are not typical of current design.

As indicated in Figure 7-6, the circumferential mesh spacing has a more significant influence on the linear eigenvalue buckling temperature prediction than the vertical mesh spacing. To determine what might be a mesh of adequate accuracy, the linear eigenvalue temperature, which is the target parameter of this calculation, was plotted against the size of the critical elements in the buckling zone in each mesh, so that the correct solution might be expected to be found when the size of these elements tends towards zero. To obtain an estimate of the correct solution, the lines in Figures 7-6a and b were projected to reach the temperature axis, giving an estimate of the error in each of the different meshes used. A criterion of being within 3% of the correct answer was adopted, and practically useful meshes were chosen for the remainder of the study that met this criterion.

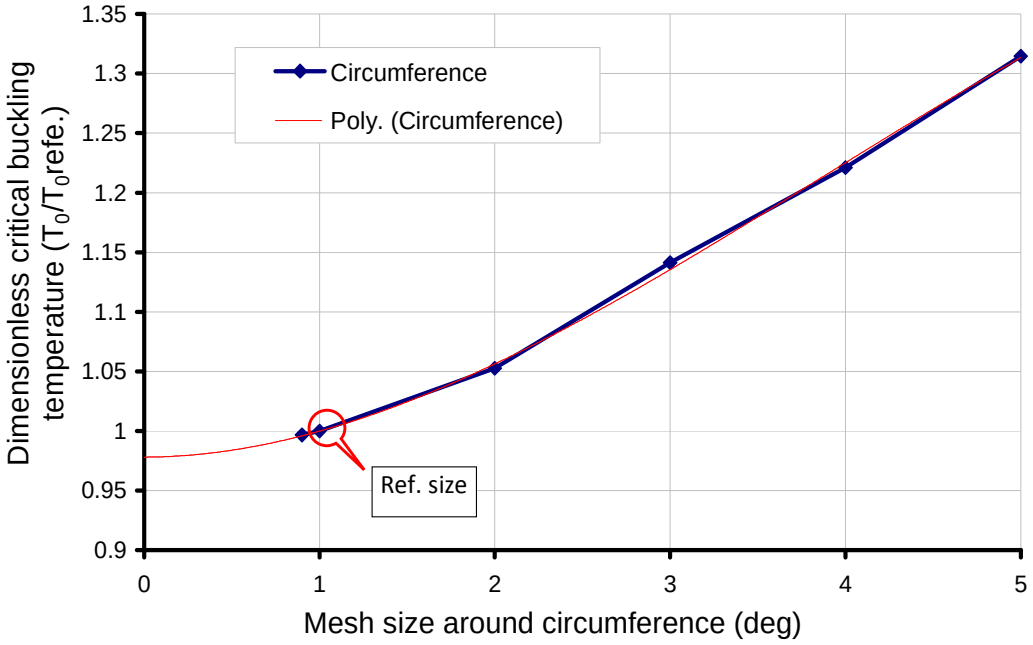

(a) Mesh convergence study around circumference

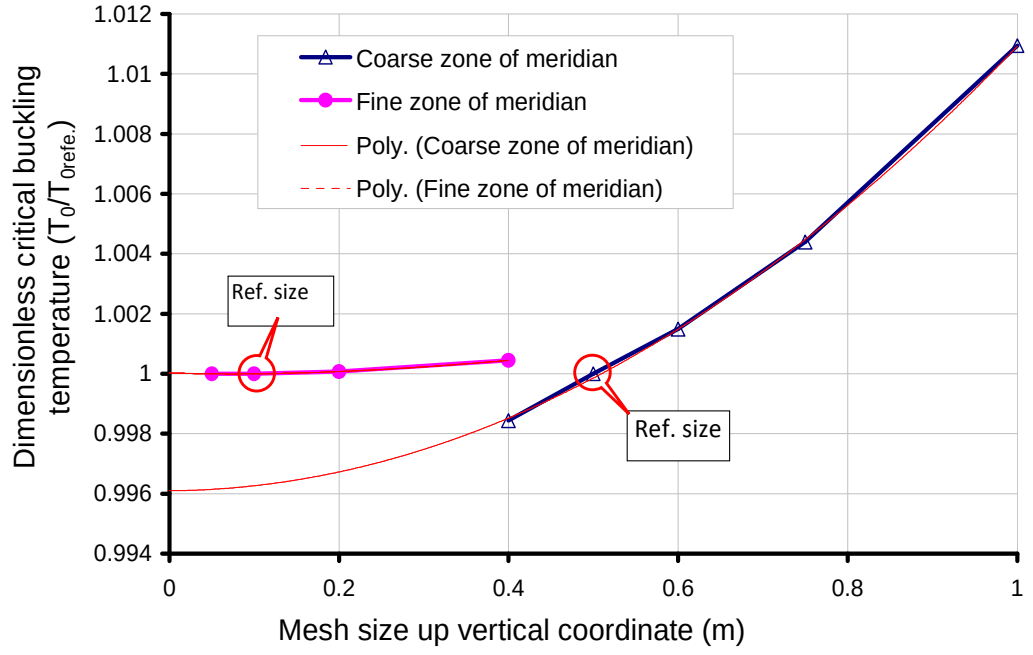

(b) Mesh convergence study up vertical coordinate

Figure 7-6 Mesh convergence study for an empty tank under smooth-edge temperature distribution with a cool roof (t_f=2t_c). The dashed curves are 3rd order polynomial fittings of the data lines.

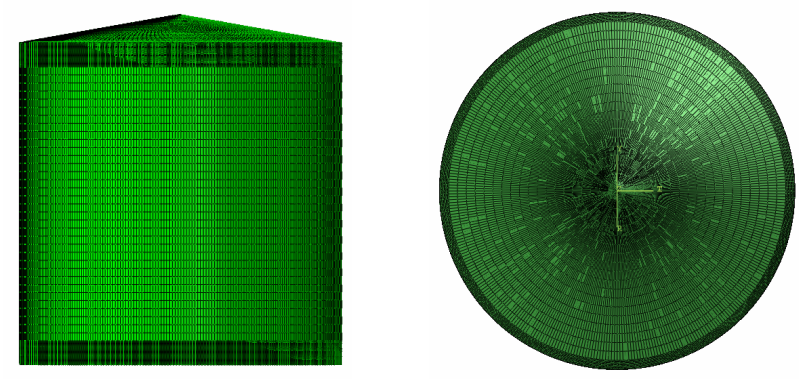

(a) Side view (b) Overhead view

Figure 7-7 FE model of an empty tank in Abaqus

Predicted buckling modes and buckling temperature

The results presented below adopted a roof thickness t_f=2t_c. The calculated first 20 buckling loads are listed in Table 7-1 for two types of temperature distributions and two types of roof thermal conditions. Negative eigenvalues are reported in all these four analyses. These negative eigenvalues indicate that the structure would also buckle if the tank experiences temperature decrease in the given thermal patterns. For the interest of fire loading studied here, only a positive temperature rise is realistic and thus buckling modes associated with a negative temperature rise will be ignored in the following discussion.

The predicted buckling temperature for the four loading cases listed in Table 7-1 are 138°C, 202°C, 135°C and 198°C respectively. It shows the Smooth-edge temperature pattern results in an easier buckling failure compared to the Half-cosine pattern. The buckling temperature of the tank wall was predicted to be not sensitive to the question of whether the roof is heated or not.

Table 7-1 Buckling temperature in LBA (t_f=2t_c, °C)

	Hot roof		Cold roof	
	Smooth edge	Half cosine	Smooth edge	Half cosine
1	137.9	-174.2	135.2	-171.5
2	137.9	-174.2	135.2	-171.5
3	-139.1	-188.4	-136.4	-185.4
4	-139.1	-188.4	-136.4	-185.4
5	-139.2	-189.5	-136.5	-186.4
6	-139.2	-189.5	-136.5	-186.4
7	140.2	-197.8	137.4	-193.7
8	140.2	-197.8	137.4	-193.7
9	158.0	-198.1	155.5	-194.0
10	158.1	-198.1	155.5	-194.0
11	159.3	-198.8	156.2	-195.7
12	159.3	-198.8	156.2	-195.7
13	-159.9	201.9	-156.8	197.7
14	-159.9	201.9	-156.8	197.7
15	-160.0	202.1	-156.8	198.0
16	-160.0	202.1	-156.8	198.0
17	160.1	202.7	157.0	198.5
18	160.1	202.7	157.0	198.5
19	167.7	-202.8	164.8	-198.6
20	168.4	-202.9	165.5	-198.6

It is interesting to note that many eigenvalues come in pairs: e.g., first two ranks share the same eigenvalue and 7th and 8th ranks share the same value. By observing the eigen-vectors, it is shown that such an eigenvalue corresponds to a pair of buckling modes: a symmetrical mode and an anti-symmetrical one. Figures 7-8 to 7-9 show the first two buckling modes that are with positive buckling temperature rise for two cool roof cases. It is noted that the buckling modes for hot roof cases are qualitatively same as that of cool roof cases, thus not shown here. Figure 7-8a and Figure 7-9a show symmetrical buckling modes and Figure 7-8b and Figure 7-9b show antisymmetric buckling modes. It may also be noticed that the eigenvalues distribute slightly more closely in Smooth-edge cases than in half-cosine cases.

The wave length of the buckles in the wall is shown to be much smaller along the circumference than the meridian, which explains the different sensitivity of the buckling temperature on the mesh sizes of circumferential direction and vertical direction. By comparing the buckling modes of tank wall under the two thermal

patterns in Figure 7-8 and Figure 7-9, it is clear that the Smooth-edge thermal pattern leads to a shell buckling in a narrower band. Buckling occurred in heated zone under Smooth-edge thermal pattern, while appeared in both heated side and cold side under Half-cosine thermal pattern.

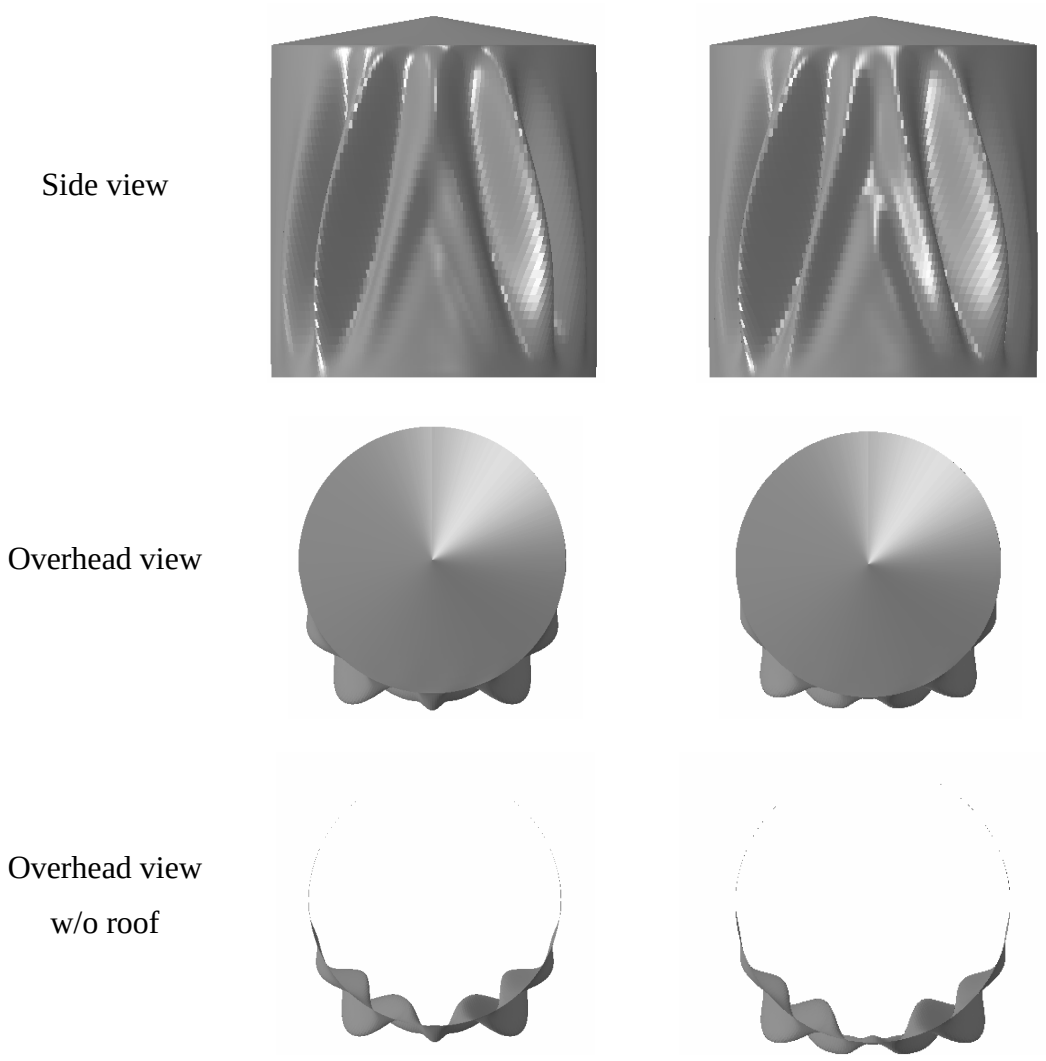

(a) Mode 1 (b) Mode 2

Figure 7-8 Bucking mode shape of an empty tank (Smooth-edge; cool roof; t_f=2t_c)

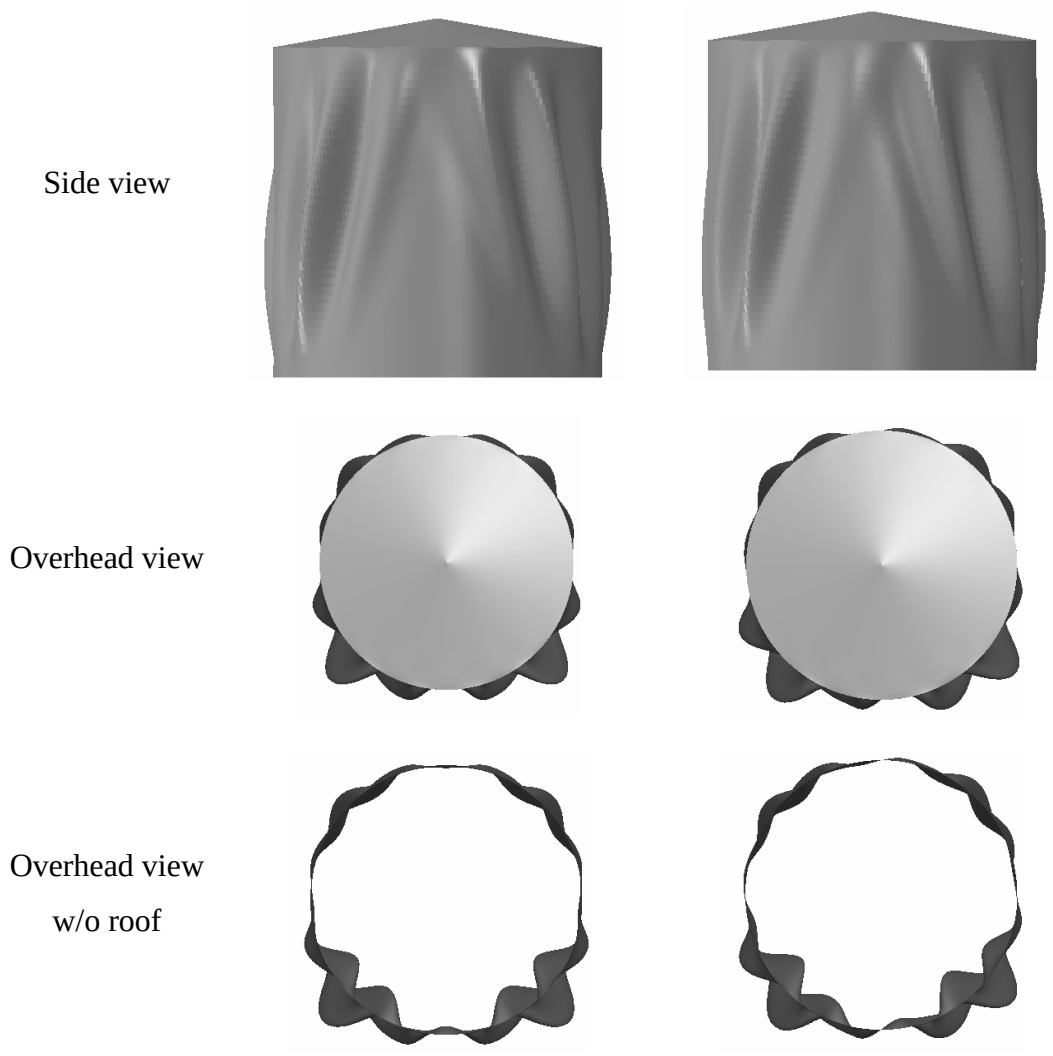

Figure 7-9 Bucking mode shape of an empty tank (Half-cosine; cool roof; t_f=2t_c)

Summary

In previous study the first predicted buckling modes in all the four cases were symmetry buckling, which suggests only half of the model with symmetry boundary condition would be accurate enough in modelling the current problem.

7.3.2 Geometrically non-linear elastic analysis (GNA)

In a LBA analysis, the specified temperature does not affect temperature-dependent material properties during an eigenvalue buckling prediction step. The material properties are based on the temperature in the base state. Furthermore, the tank undergoes geometric nonlinearity prior to buckling. Therefore, it is more realistic to perform a geometrically nonlinear load-displacement analysis (Riks analysis) according to EN 1993 1-6 (2007) to determine the collapse loads for the current problem. Exploiting the plane of symmetry, half of the tank (0°-180°) was modelled using the 4-node general purpose element S4 with symmetric boundary conditions at 0° and 180°. The dependence of both the elastic modulus and the thermal expansion coefficient on temperature were included in this analysis.

Mesh convergence

The mesh convergence study was also conducted for GNA analysis. As shown in Figure 7-10, the size of circumferential mesh has a significant effect on the prediction, which is consistent to the case in above LBA analysis.

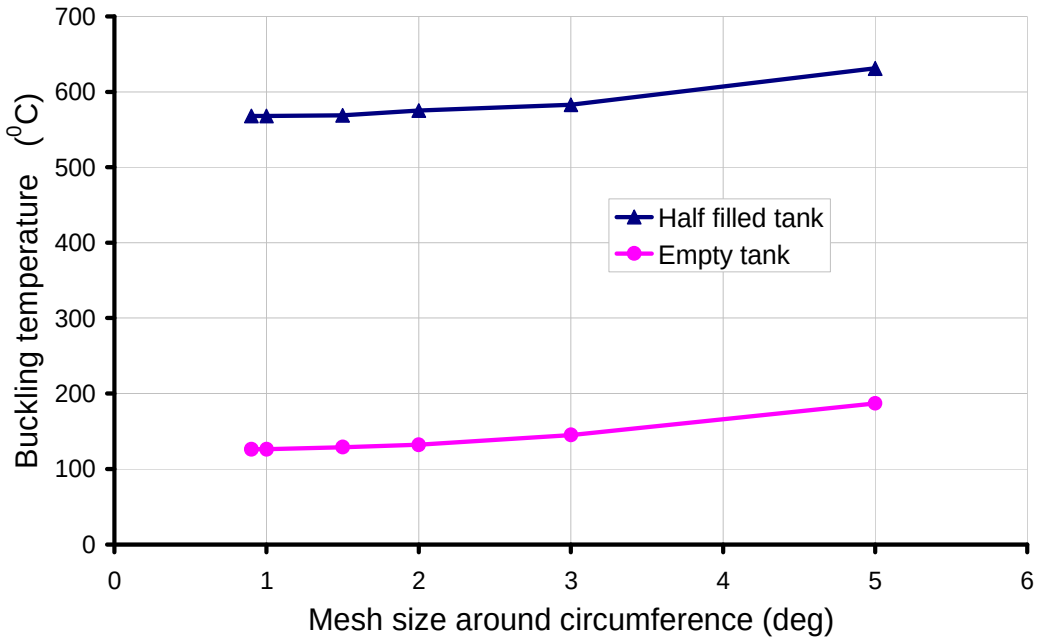

Figure 7-10 Mesh scheme 1: uniform mesh around circumference with non-uniform mesh along meridian

Table 7-2 lists the buckling temperatures for some different mesh schemes. It shows that the sensitivity of the buckling temperature on the size of vertical mesh is not as high as that of the circumference mesh to the buckling temperature prediction. Nevertheless, by comparing the buckling modes prediction (Figure 7-11), it was found that a fine mesh near the boundary along vertical coordinate is still necessary for accurately capturing the buckling mode. Mesh scheme 2 was adopted for the following analyses, because it predicted accurate buckling temperature and buckling mode and computational cost effective.

Table 7-2 Comparisons of different mesh schemes for empty tank

Case	Circumferential mesh (degree)	Vertical mesh			Buckling temperature increase(°C)
		L_1 (m)	Fine mesh size (m)	Coarse mesh size (m)	
Mesh 1	0.9	1.5	0.05	0.5	128
Mesh 2	1	1.5	0.05	0.5	128
Mesh 3	1	1.5	0.05	1	128
Mesh 4	1	1.5	0.05	0.25	128
Mesh 5	1	2	0.05	0.5	128
Mesh 6	1	1	0.05	0.5	128
Mesh 7	1	0.5	0.05	0.5	128
Mesh 8	1	1	0.025	0.5	128
Mesh 9	1	0	0.5	0.5	128
Mesh 10	1.5	1.5	0.05	0.5	130
Mesh 11	2	1.5	0.05	0.5	133
Mesh 12	3	1.5	0.05	0.5	146
Mesh 13	5	1.5	0.05	0.5	189

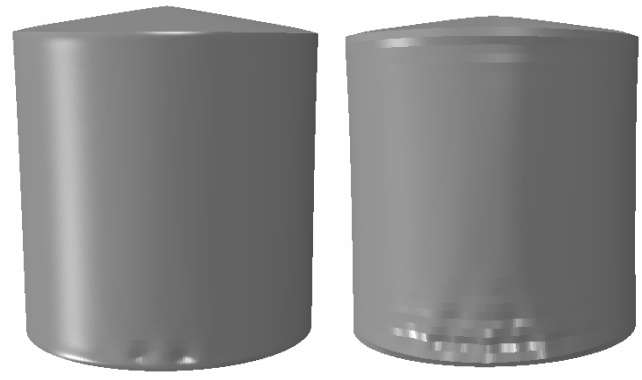

(a) Mesh 2 (b) Mesh 9

Figure 7-11 Comparison of post-buckling modes between two mesh schemes

Predicted behaviour of the tank

Figure 7-12 shows the temperature increase against the radial displacement of the node at crest of the buckle for the cases of tank under smooth-edge temperature

distribution for both hot-roof and cool-roof situations. "Load-deflection" curve is often used to illustrate the evolution of the deformation against the variation of the applied action, for example, the load applied upon the edge of a cylindrical shell. In the current model, the applied load variable is the temperature instead of the conventional mechanical load. Therefore the temperature change is adopted for the longitudinal coordinate in the load-deflection curve.

The buckling shown in Figure 7-12 is of bifurcation type instead of limit point in nature. This is because there exists an unstable primary path (denoted as dash line in Fig. 7-12) above the buckling point. The corresponding maximum temperature at the most heated meridian for the two cases are both T_0 = 128°C, which are slightly lower than the predicted value by eigenvalue analysis. The temperature increase is very easily attained in a fire of this kind.

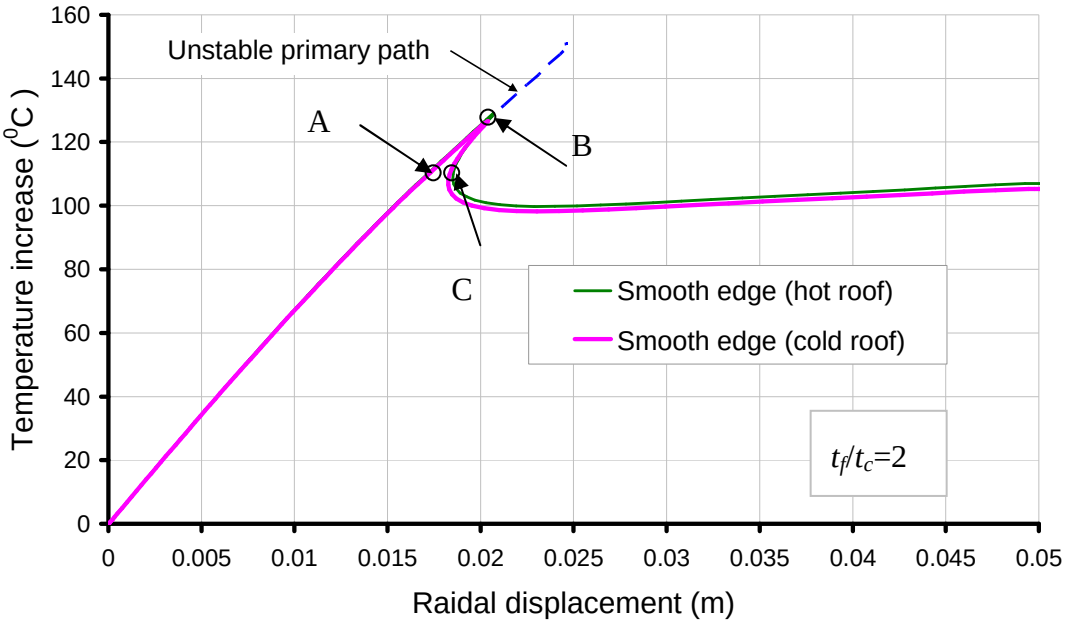

Figure 7-12 Temperature-radial displacement curves of the node at θ=0, h=2.5m

(a) Buckling mode (b) Post buckling mode

Figure 7-13 Buckling and post-buckling modes of an empty tank under smooth-edge pattern with hot roof (t_f=2t_c)

The buckling modes of the hot-roof and cool-roof cases are similar. Figure 7-13 shows the deformed shape of the cylinder well into the post-buckling response for the hot roof case. Figure 7-13 a and b corresponding to the deformation at Point B and C in Figure 7-12 respectively. Buckling occurs near the base and spreads to the tank wall on the heated zone. Further insight into the buckling modes can be gained by examining the axial compressive stresses that develop in the shell. For the hot roof condition the axial membrane stress distributions down the most heated meridian and around the circumference at h=2m are illustrated in Figure 7-14 and Figure 7-15. The circumferential membrane stresses are shown in Figure 7-16 and Figure 7-17. The pre-buckling, bucking and pot-buckling in the following figures refer to the results of point A, B and C in Figure 7-12 respectively.

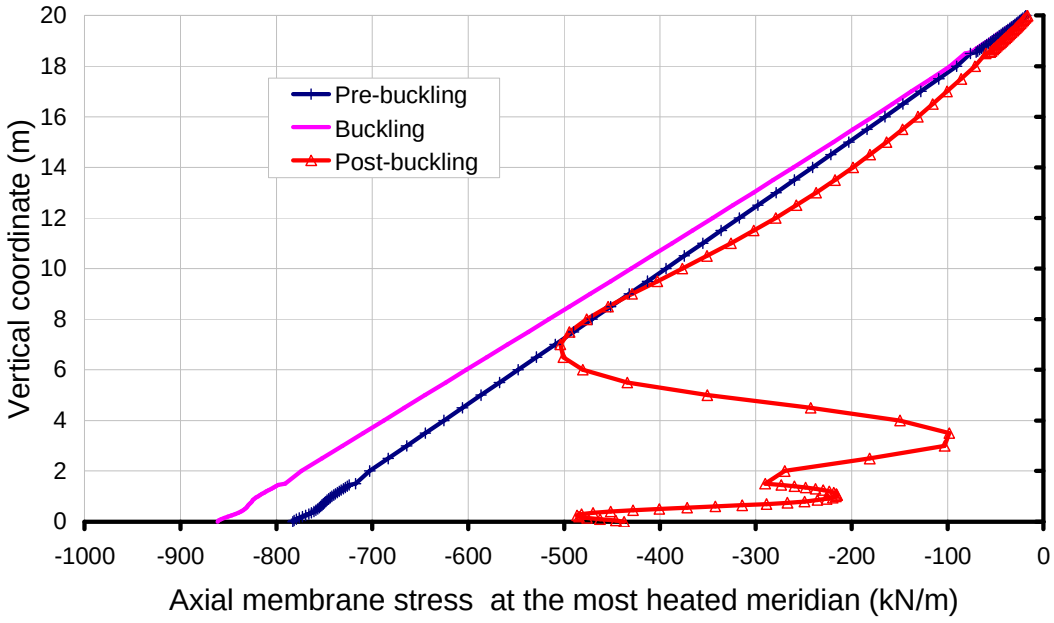

Figure 7-14 Axial membrane stresses down most heated meridian (smooth-edge: hot roof)

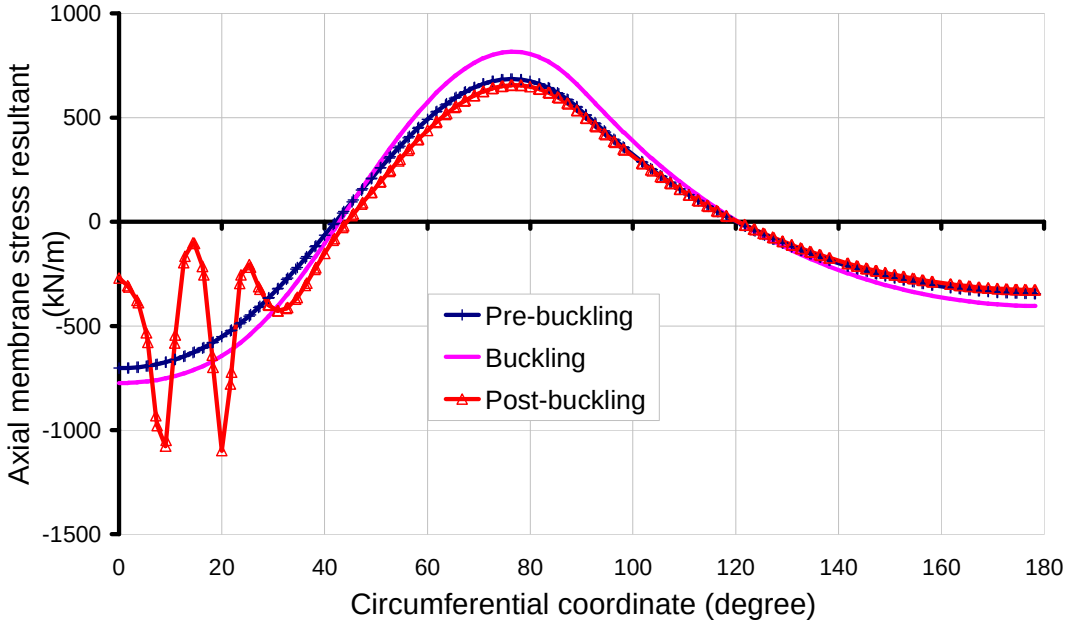

Figure 7-15 Axial membrane stresses around circumference at *h*=2m (smooth-edge: hot roof)

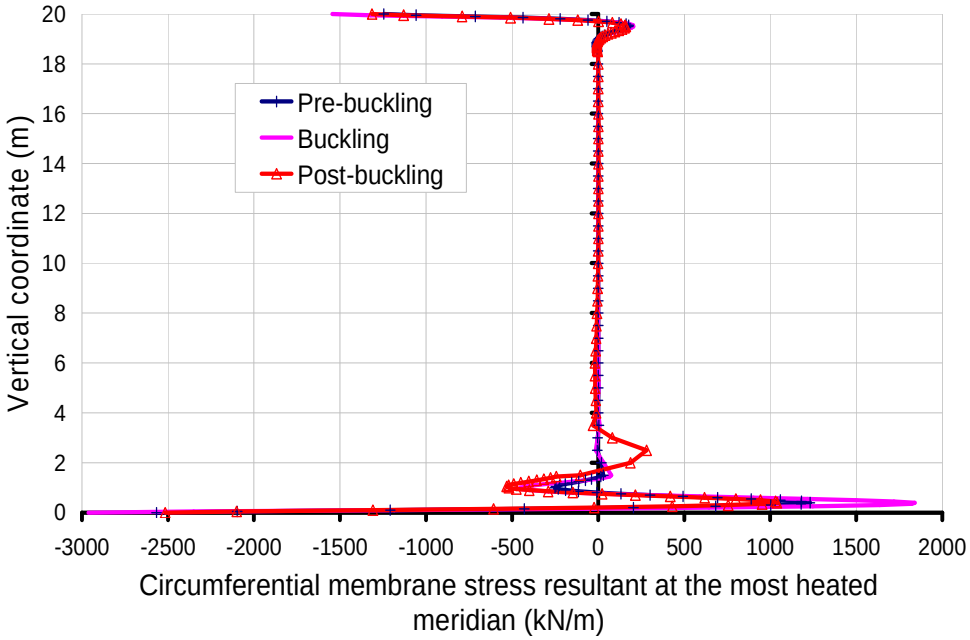

Figure 7-16 Circumferential membrane stress down most heated meridian (smooth-edge: hot roof)

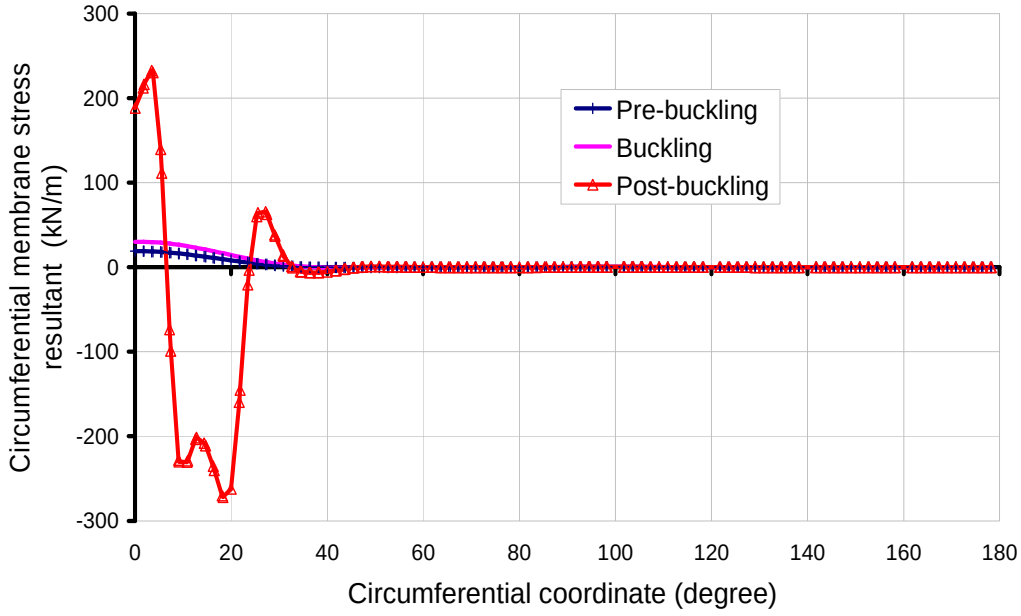

Figure 7-17 Circumferential membrane stresses around circumference at *h*=2m (smooth-edge: hot roof)

The most heated meridian (Figure 7-14) displays pre-buckling axial compressive stresses that increase from zero at the eaves to a maximum at the base. The position of buckling is where the maximum compressive stresses developed in the pre-buckling regime.

The pattern around the circumference (Figure 7-15) shows compression due to restrained expansion over the heated face ($-40° < \theta < +40°$), with a corresponding axial tension (to satisfy axial equilibrium) in the side zone ($+40° < \theta < +120°$), followed by axial compression again on the cold back face (to satisfy global moment equilibrium). Buckling occurs on the heated side (Figure 7-13) because of the large compressive stress accompanied with a reduced modulus of the steel there. On the cool side, the compressive stress is slightly smaller and the modulus is not reduced so it is not critical there.

The membrane axial stress distribution shapes in the pre-buckling and buckling states are very similar, which presents a linear response. In the post-buckling state, the compression stress redistributes circumferentially and vertically. The shape of post-buckling stress is consistent with the observation of the post-buckling mode.

Figure 7-16 and Figure 7-17 show the circumferential stress state in the tank wall. The circumferential stresses only occur at the place which thermal expansions of the wall are been restricted. Thus, they are developed near the boundary at the vertical direction and on the hot side where thermal expansion exists. In the current problem, the axial stress is the main reason for buckling. However, the existing of large compressive circumferential stresses near the base also contributes to the occurrence of buckling.

The structure of a real oil tank usually includes a bottom plate. In the above simulations, the bottom plate was ignored and the bottom edge of the wall shell treated as simply supported, i.e., translational degrees of freedom were fixed while rotational ones were relaxed. As practically a bottom plate can provide certain extent of rotational rigidity, it is necessary to evaluate the effect of such extra rotational rigidity on the buckling behaviour. Consequently additional calculations with fully

fixed bottom boundary were conducted. The predicted buckling temperature for the fully fixed bottom boundary was 129 °C, which shows negligible difference from that of a simply supported bottom boundary. The predicted buckling mode was also identical under these two boundary conditions. As a result, it is completely valid to adopt simply supported bottom boundary for all the rest of calculations.

7.3.3 Geometrically nonlinear analysis with materially nonlinear analysis (GMNA)

Geometrically and materially elastic-plastic non-linear analysis (GMNA) according to EN 1993 1-6 (2007) was conducted to trace the failure behaviour of the oil tank under the above loading scenario. The Riks routine was employed for the following analyses. The only difference between GNA and GMNA analysis is the inclusion of temperature-dependent plasticity in the steel. The dependence of both the elastic modulus and the thermal expansion coefficient on temperature were included in both analyses. The material plasticity was assumed to obey a von Mises yielding surface with on hardening (Figure 7-18). The following calculations refer to a cold roof tank with a reference roof thickness of 2 times that of the cylinder wall under a smooth-edge temperature rise with critical angle equal to 90°.

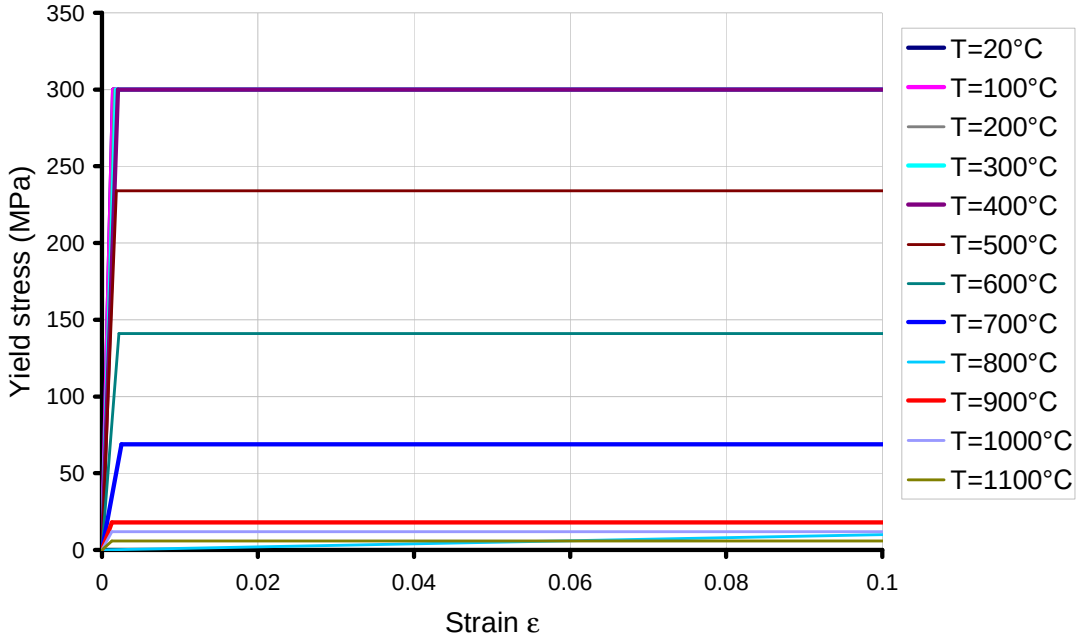

Figure 7-18 Stress-strain relationship for steel at elevated temperatures with a yield stress of 300MPa at *T*=20°C

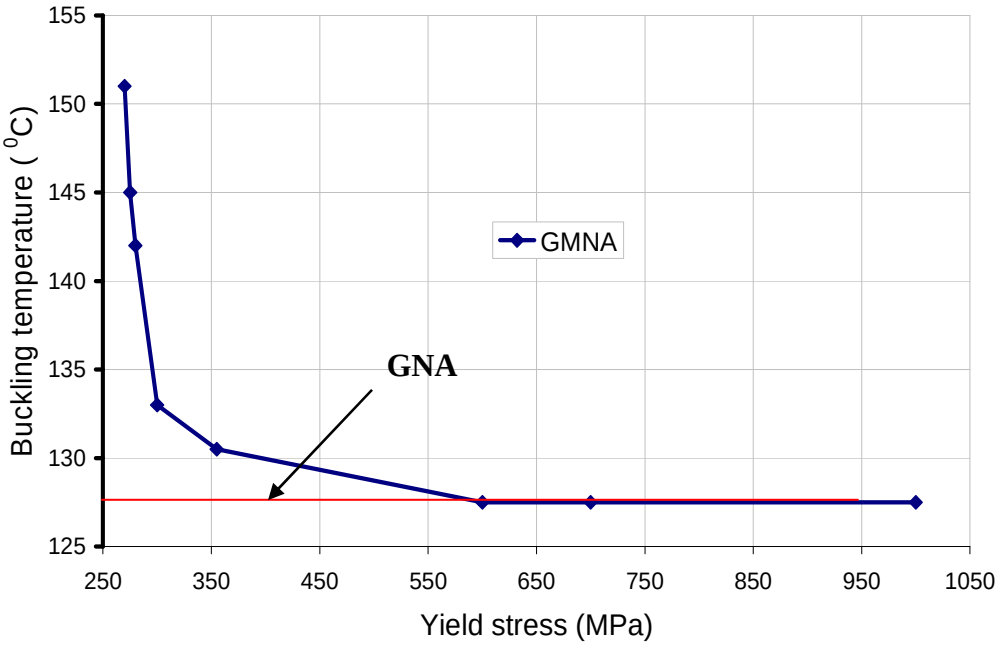

Figure 7-19 Effect of yield stress on the buckling temperature

It was found that the tank buckles at temperatures that are not very high. The change in the peak temperature from ambient to T_0 is used here to define the condition at buckling. If the tank is treated as always elastic, the buckling temperature rise was found to be 128ºC, but inclusion of yielding in 255MPa yield stress steel led to a reduction in the stresses and a rise in the buckling temperature rise to 151ºC. The variation of the buckling temperature rise with specified yield stress is shown in Figure 7-19, where this change can be seen to be progressive.

Usually plasticity is disadvantageous to the stability of a structure, manifested by a reduced modulus that leads to lower bifurcation limit. However, above tank model sees a contrary trend where GMNA gave higher buckling temperatures than GNA. Such a phenomenon may be understood as follows.

Figure 7-13 to Figure 7-17 have shown that the buckling occurs near the bottom boundary and the large membrane stresses in this area. The buckling limit should be controlled by the stresses and configuration in this area. Figure 7-20 plots the development of the plastic strain before the buckling. It is shown that plastic strain localised in a circumferential strip just above the bottom edge that is also the lower border of the buckles. This zone is the critical one for the stresses induced by restraint of thermal expansion, and yielding permits the highest stress in this location to be dissipated, making buckling less likely. Because the stresses causing the buckle are caused by incompatibility, not by static loads, yielding relieves the stress concentration and permits higher temperatures to be reached. As the temperature rises further, even more yielding occurs, so this yielding tends to have a very marked beneficial effect on the buckling temperature, as is seen in Figure 7-19.

This plasticity can be seen as similar to a geometrical imperfection located at the same point. The imperfection permits a local softening of the membrane stiffness of the structure and so reduces the development of stresses caused by restrained thermal expansion. It is well known that geometric imperfections can be either beneficial or disadvantageous to the stability behaviour of a structure. In this case it is clear that both imperfections and plastic deformation can be beneficial.

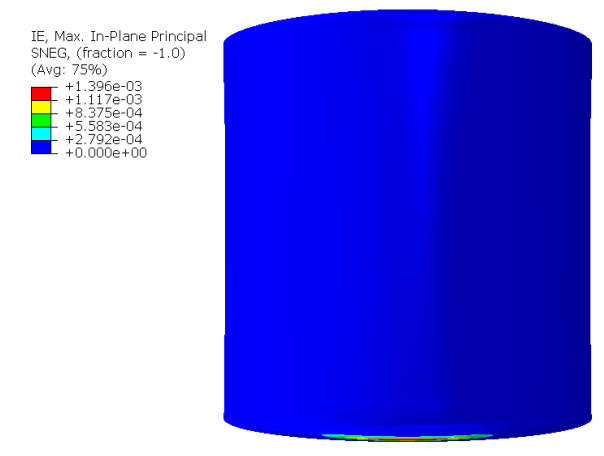

(a) Pre-buckling

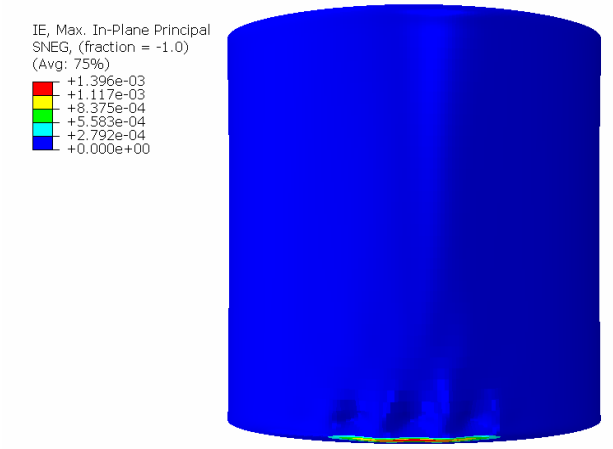

(a) Post-buckling

Figure 7-20 The equivalent plastic strain contour in an empty tank from a GMNA analysis ($\sigma_y = 275$ MPa)

The effect of roof stiffness is shown in Figure 7-21, where a yield stress of 275MPa has been adopted. The elastic GNA analysis always predicts a lower buckling temperature but the difference between the two analyses is not very significant for this yield stress. Because GNA analyses always gave lower buckling temperature rises, it was adopted for all the remaining calculations described here.

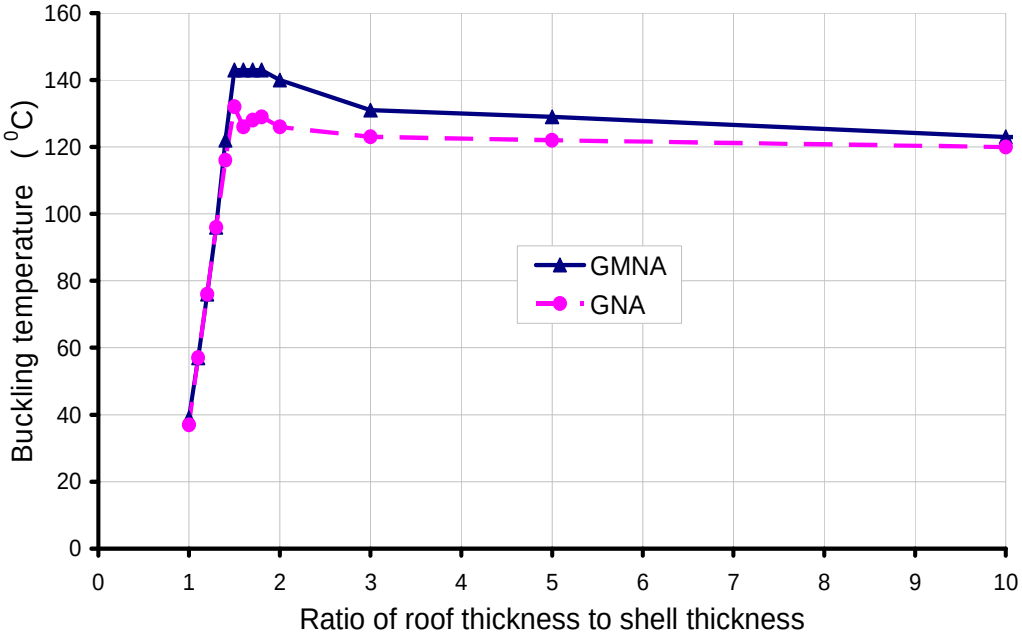

Figure 7-21 Effect of material nonlinearity on the prediction

7.3.4 Geometrically nonlinear elastic analysis with imperfections (GNIA)

Thin shell structures often show considerable sensitivity to geometric imperfections under certain loading patterns. Due to the thin thickness of the tank wall, the elastic buckling governs many of the failure type. Therefore, the imperfection sensitivity is mainly explored here using a geometrically nonlinear elastic analysis.

The study of geometrical imperfections normally comprises two different categories of imperfection modes: fabric imperfection and stochastic imperfection. The former arises in the construction and fabrication and is measurable in practice (Teng and Rotter 1992; Ding *et al.* 1996; Rotter 1997; Holst *et al.* 2000). The latter is difficult to measure in reality but has been shown to be critical in some structures, though a most critical stochastic mode for a structure is never known (Rotter 2004). Usually the stochastic imperfection mode can be chosen as certain combination of eigenmodes from linear buckling analysis and the critical mode is studied by trial and error (Simitses 1986; Greiner and Guggenberger 2004; Song *et al.* 2004).

Due to the lack of real measurement data, the study of the effect of fabric imperfection is omitted in the current study. For the study of stochastic imperfection, only the first eigenmode of the linear eigenvalue analysis is studied to probe the sensitivity of the studied tank structure on the typical imperfection pattern. The mesh is, therefore, perturbed in the radial direction by that eigenmode, scaled so that the largest perturbation is a fraction of the shell thickness. The studies reported here use perturbations of 0.1%, 20%, 40%, 60%, 80% and 100% of the thickness. The imperfection was introduced by the *IMPERFECTION option in Abaqus.

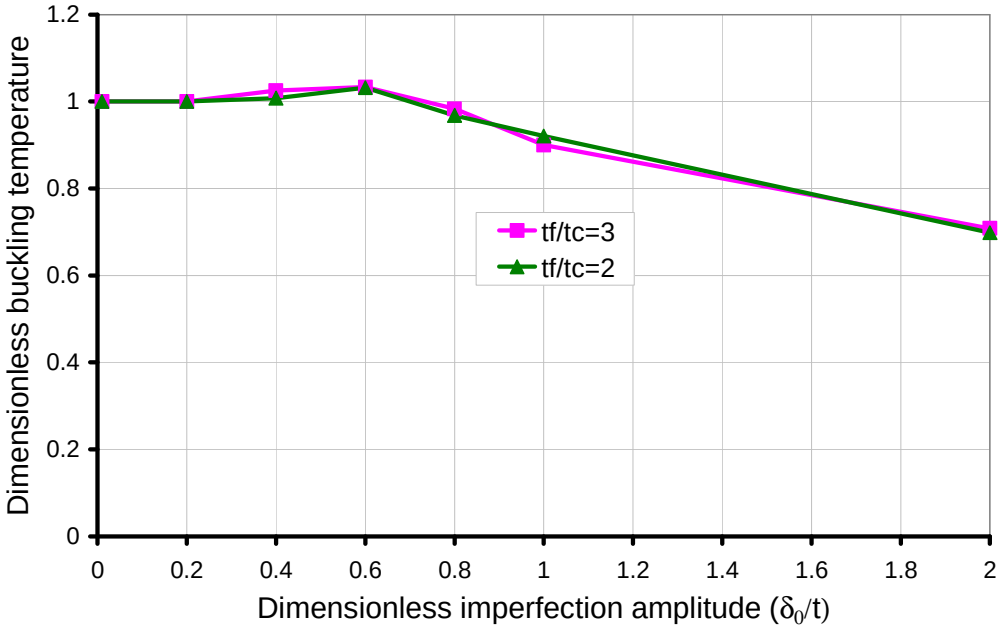

Figure 7-22 Imperfection sensitivity of empty tank under smooth-edge temperature distribution with cool roof

Figure 7-22 shows the variation of the ratio of critical buckling temperature in cases considering imperfection to that of a perfect shell. It can be seen the imperfection can be beneficial when the imperfection amplitude is in the range of 0-0.6 times of shell thickness. But when the imperfection gets larger, the critical buckling temperature decreases and it drops dramatically after the imperfection amplitude reaching one thickness of shell thickness. When the imperfection amplitude is within 0.8 times of shell thickness, the variation of buckling temperature is in range of 10% of that of the

perfection shell, which indicates that 0.8 times of shell thickness of imperfection amplitude does not influence most the strength reduction from the geometric imperfection influence.

It should be noted the trend shown in the above curve is based on the first eigenmode-affine imperfections. Using other types of imperfection mode such as the weld imperfection would very probably give a different trend even contrary to the above prediction. The imperfection sensitivity study is not the main interest of this study thus has not being elaborated further.

7.4 Parametric study

7.4.1 Effect of roof stiffness

Two different types of buckling modes are observed as shown in Figure 7-23, depending on the stiffness of the roof. In the first mode, a large buckle develops first in the roof (Figure 7-23 a). This situation occurs when the thickness of the roof t_f is less than 1.6 times of the thickness of the cylindrical wall t_c. The second mode is the buckling of the cylindrical wall (Figure 7-23c to n), which occurs in all thicker roofs. Because cylindrical wall buckling is expected to result in more serious consequences, this Chapter is focussed on this mode. A choice of t_f/t_c=2 was therefore adopted in the following work, which is hereafter termed a slender roof, and t_f/t_c=1000 was adopted to represent an ideally stiff roof.

For buckling occurring in the tank wall, the buckling mode is still very sensitive to the roof to tank wall stiffness ratio. It may be either shear buckling which occurs in whole tank wall (e.g. Figure 7-23c) or local buckling which occurs near the boundaries where large vertical and circumferential compressive membrane stresses are present (e.g. Figure 7-23f).

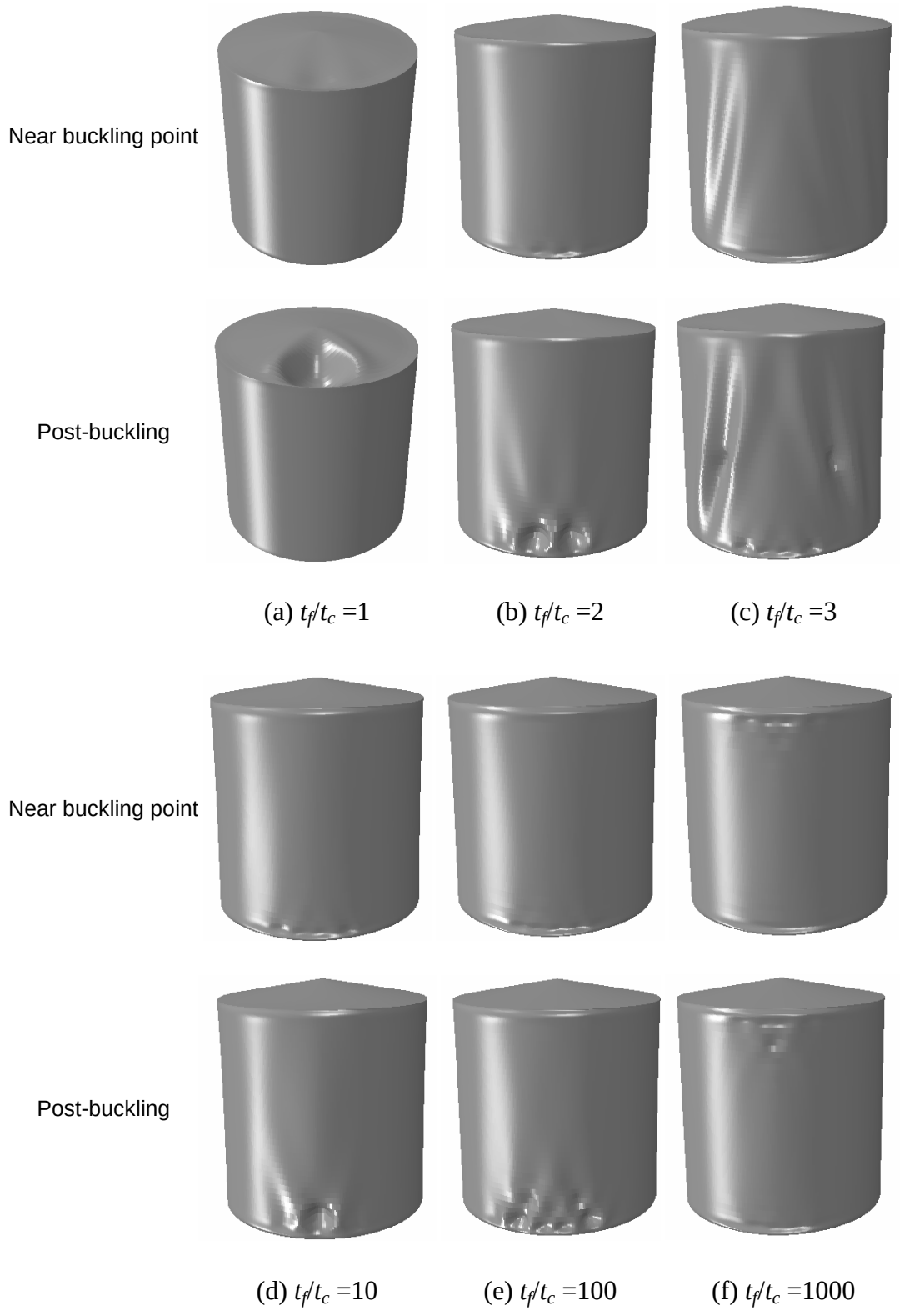

Figure 7-23 Buckling and post-buckling modes in an empty tank under smooth-edge temperature distribution (deformation scale factor=20)

The cause of buckling in the wall is the axial membrane stress induced in the cylindrical wall by restraint to differential thermal expansion. The pattern of these stresses in the wall is shown in Figure 7-24, where a linear variation with height (Figure 7-24a), coupled with a strong variation around the circumference (Figure 7-24b), can be seen. For credible roof stiffness, the stress at the top of the wall is close to zero, but very stiff roofs have a significant effect and the idealised rigid roof moves the highest stress from the base to the top of the wall. The circumferential pattern shown in Figure 7-24b indicates a peak compression at the base whose maximum lies at the most heated location, but declining to zero by about 40º and followed by a zone of axial tension.

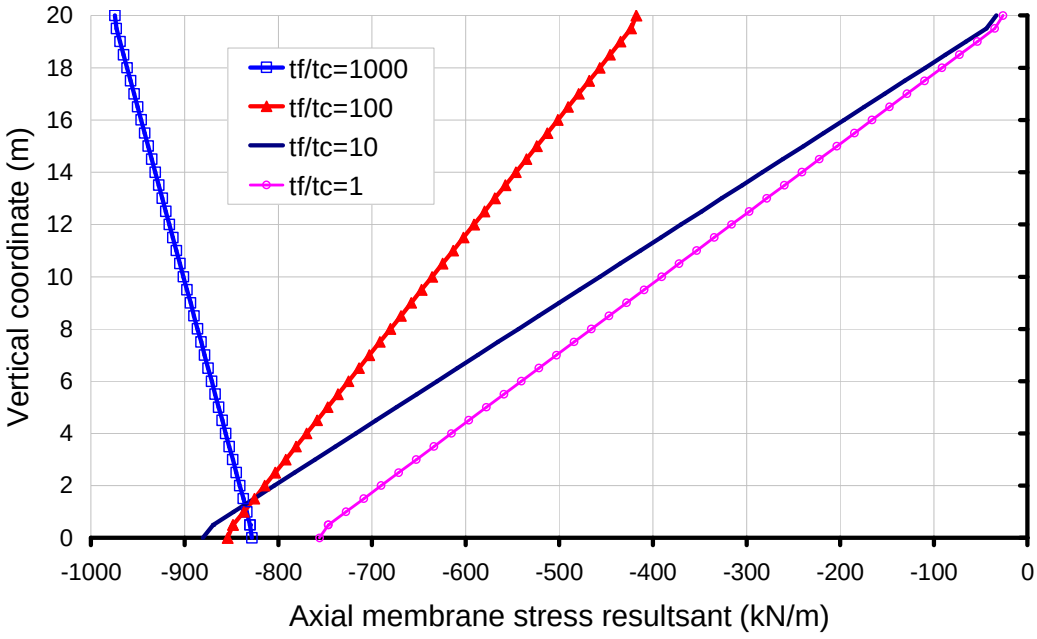

a) Axial membrane stress up vertical coordinate at the most heated meridian (T_0=100ºC)

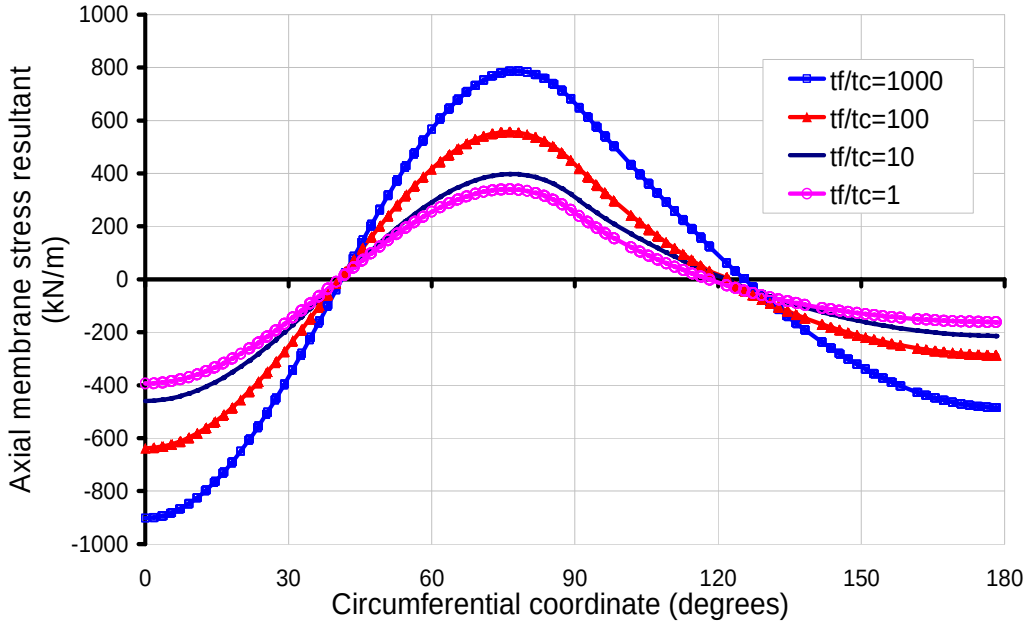

b) Axial membrane stress around circumference at mid-height of the tank (T_0=100ºC)

Figure 7-24 Axial membrane stress distribution of empty tanks with various roof stiffness

The stresses developing in the tank wall can be divided into two parts. The dominant part is caused by differential thermal expansion between the heated and unheated zones, whilst a second part arises from restraint of thermal expansion by the roof. The component of stress due to the latter part depends on the roof slope, stiffness and temperature condition. In particular, the roof restricts the top edge of the cylinder from translating radially and rotating about the circumferential axes. The extent of this restriction depends on the stiffness of the roof. Where the roof stiffness is realistic, most of the axial membrane stress in the wall arises from the first cause. When the roof stiffness is very large, the roof retains its original shape under thermal loading but may globally tilt, leading to redistributed stresses in the cylindrical wall.

The different conditions of empty and half-filled tanks were studied, each with either "hot" or "cold" roofs. For each, several different roof stiffness were examined. The buckling temperature for each is shown in Figure 7-25. The empty tank is insensitive to the roof stiffness, and buckles at very low temperature irrespective of whether the roof is heated or not. A partially filled tank, by contrast, buckles at very much higher temperature rises, and the result is slightly sensitive to the heated condition of the roof. A cool roof was found to buckle at slightly lower temperature rises than the hot roof, but both were far above the empty tank temperatures. Buckling temperature decreases with increasing of roof stiffness for half filled tanks.

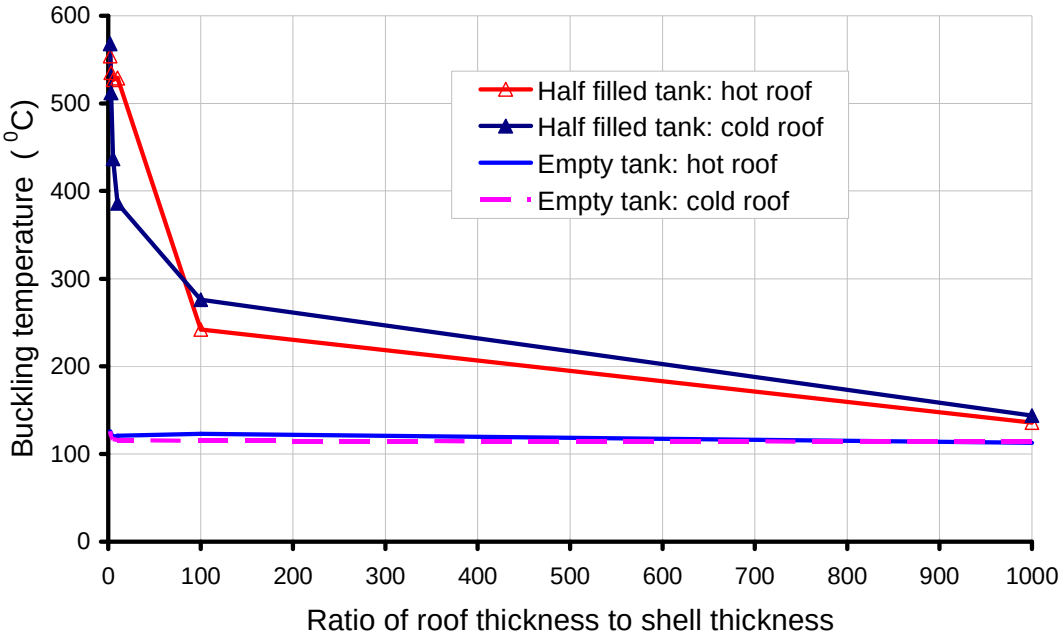

a) Full range

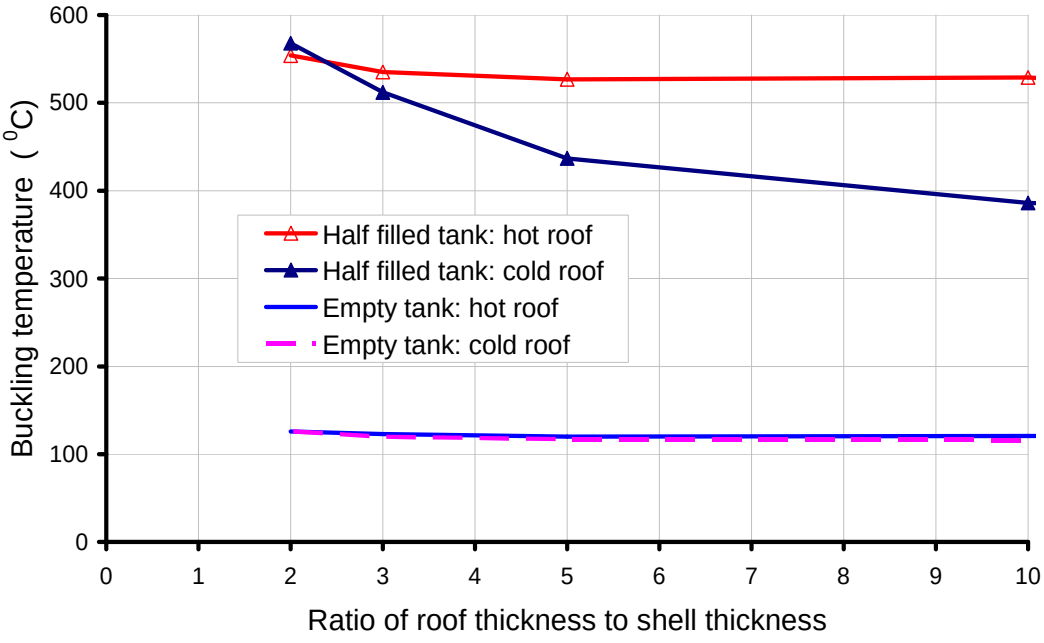

b) In range of t_f/t_c<10

Figure 7-25 Buckling temperature rises in empty and half-filled tanks

7.4.2 Effect of temperature pattern around circumference

This section explores the temperature distribution variation around circumference on the buckling behaviour of the tank. The same critical angle of 90° for the two temperature patterns were adopted in the calculations. The temperatures at bifurcation reached in each of the four cases displayed above are shown in Table 7-3. It is clear that the smooth-edge pattern of temperature rise leads to bifurcation at lower temperatures, indicating that a narrower band of high temperature induces buckling earlier than a more uniform temperature rise over a wider zone. The bifurcation temperatures are not sensitive to the question whether the roof is heated.

Table 7-3 Buckling temperatures for different cases (t_f=2t_c)

Temperature pattern	Roof temperature	Bifurcation temperature T_0 °C
Half-cosine	Hot roof	212
Half-cosine	Cool roof	210
Smooth-edge	Hot roof	126
Smooth-edge	Cool roof	126

The buckling modes of the cool-roof cases under Half-cosine temperature pattern are shown in Figure 7-26a and Figure 7-26b for t_f=2t_c and t_f=3t_c respectively. The buckling modes are an elephant's foot at the base, coupled with a shear buckle around the shell in the heated zone. By contrast, buckling mode under Smooth–edge temperature pattern (Figure 7-23) chiefly concentrates at the base within the heated zone when t_f=2t_c .When t_f=3t_c, the buckling mode is similar to that under half cosine temperature distribution, but is in a relatively narrower band.

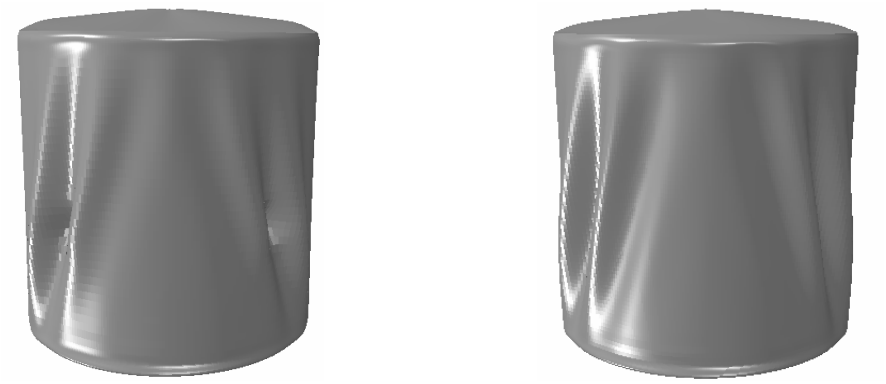

(a) $t_f=2t_c$ (b) $t_f=3t_c$

Figure 7-26 Post-buckling mode of an empty tank under half-cosine temperature distribution pattern (cool roof)

Further insight into these buckling modes can be gained by examining the axial compressive stresses that develop in the shell. Figure 7-27 and Figure 7-28 show the axial membrane stresses developed in the tank under smooth-edge temperature pattern are much higher than that under Half-cosine pattern. Consequently, the buckling temperature is lower under smooth-edge temperature rise.

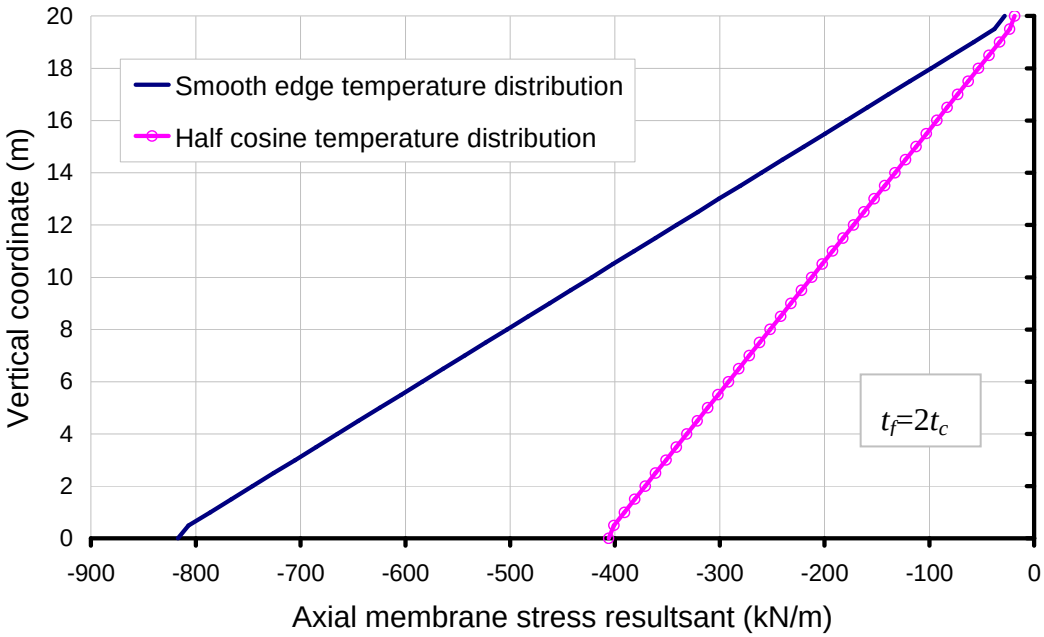

Figure 7-27 Axial membrane stresses down most heated meridian (cool roof)

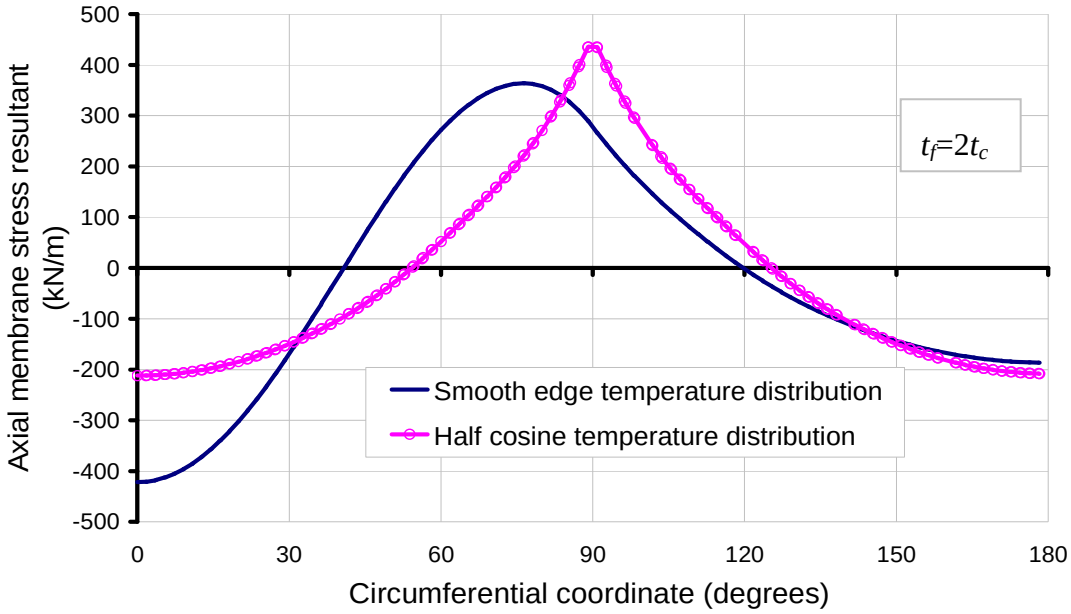

Figure 7-28 Axial membrane stresses around circumference at mid-height of tank (cool roof)

7.4.3 Effect of roof slope

The British Code (BS EN14015:2004) states that the slope of the roof should comply with the requirements specified by the purchaser or shall be 1 in 5. The American Code (API 650 2007) is more specific and says that slope shall be within the range of 9.5° to 37°. As the slope angle isn't a fixed value in practice, it is useful to investigate its effect on the buckling behaviour of the whole structure. Figure 7-29 and Figure 7-30 show the effect of roof slope in the range of 10° to 30°on the buckling temperatures of empty tanks and half-filled tanks respectively. It appears that the roof slope has only small influence on the bucking temperature when the tank has a relatively stiff roof but has significant effect when the tank roof is slender. The global trend of the curves remains same for both empty tank and half-filled tank.

Generally the increase of roof slope results in an increased buckling temperature.

When the roof stiffness is very small (t_f=t_c), the tank has a roof buckling mode. The increase of roof slope strengthens the stiffness of the roof and therefore postpones the

initial of buckling. By contrast, for the stiffer roof tank ($t_f \geq 2t_c$), buckling happens in the tank wall, in which case the resistance of buckling ability for the roof is stronger than the cylindrical wall that lead the wall to buckle ahead of the roof. As stated in section 7.3.6, the stresses developing in the tank wall consist of two parts, one of which is the dominant part caused by differential thermal expansion between the heated and unheated zones, whilst the other part arises from restraint of thermal expansion by the roof.

When the roof thickness is relatively small ($t_f=2t_c$), the contribution of the roof slope to the roof stiffness may be relatively large. Apparently a steeper roof provides a stronger restraint for the thermal expansion thus introduce larger compression in the wall, which results in a lower buckling temperature.

When the roof thickness is very large ($t_f=10t_c$), the roof stiffness is very large, in which case, the top of the cylinder will always tend to retain a circle in a plane, no matter how steep the roof is. Consequently the roof angle has relatively no effect on the buckling temperature.

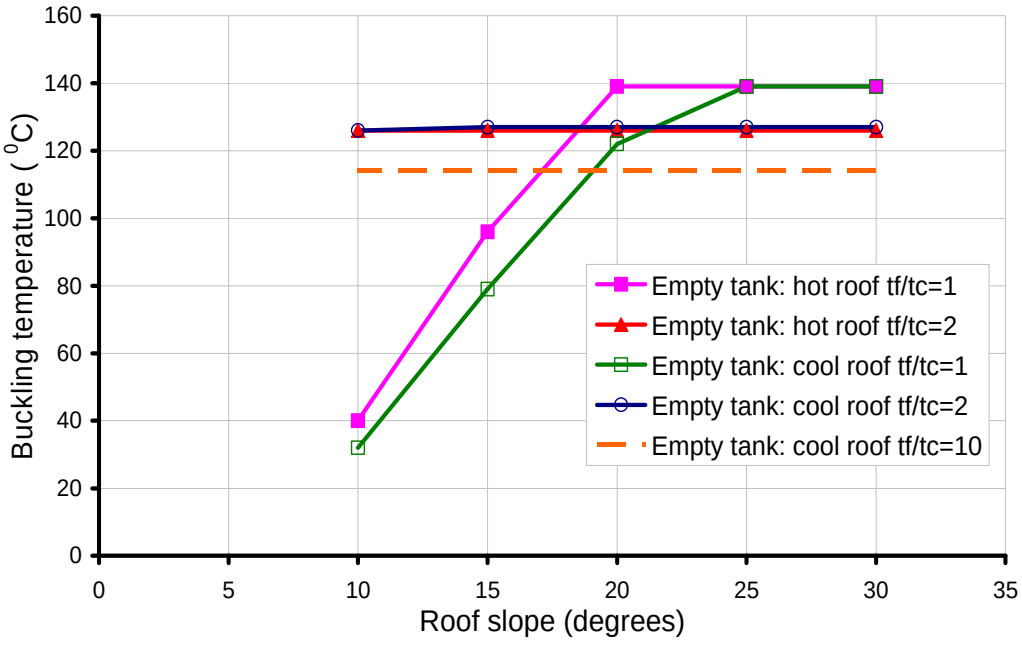

Figure 7-29 The effect of roof slope on the buckling temperature of an empty tank

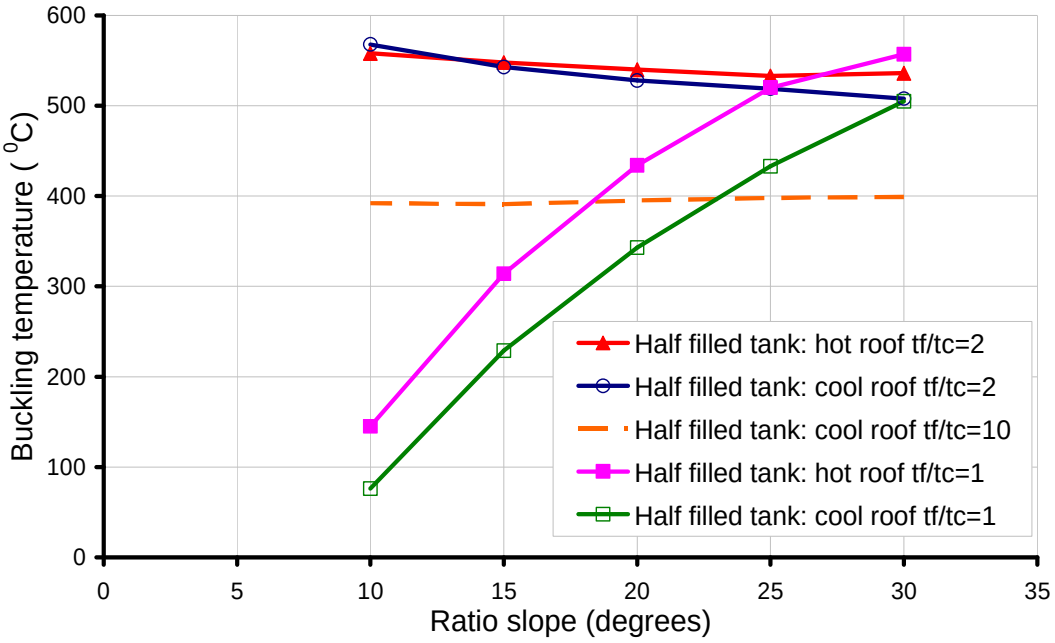

Figure 7-30 The effect of roof slope on the buckling temperature of a half-filled tank

7.4.4 Effect of heating range

If the size of the adjacent tank fire is changed, the target tank is exposed to heating in a zone of different size. The circumferential range of the heated zone models this effect. Here, characteristic angles θ_0 of 30°, 60°, 90° and 120° were investigated. The buckling temperatures of the empty and half filled tanks are shown in Figure 7-31.

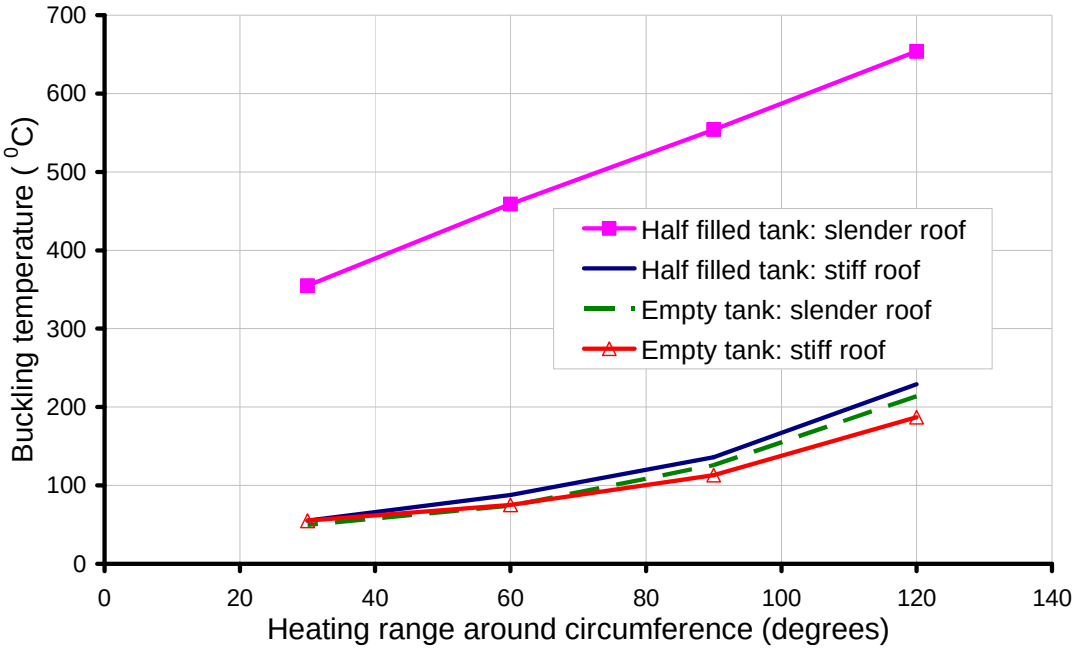

Figure 7-31 The effect of heating ranges on the buckling temperature

It can be seen that the buckling temperature increases with an increase in the characteristic angle. The stiff roof tank displays a much lower buckling temperature than the tank with slender roof. This can be understood by examining the axial membrane stress pattern in the tank (Figure 7-32). A narrow band of elevated temperature (θ_0=30º) leads to higher compressive stresses on the most heated meridian. By contrast, a wider zone leads to a relatively uniform temperature increase that produces lower compressive stresses but spread over a wider zone. Thus the narrowly defined heated zone leads to buckling at a lower temperature because larger compressive stresses are induced, and over a zone large enough for a buckle to form.

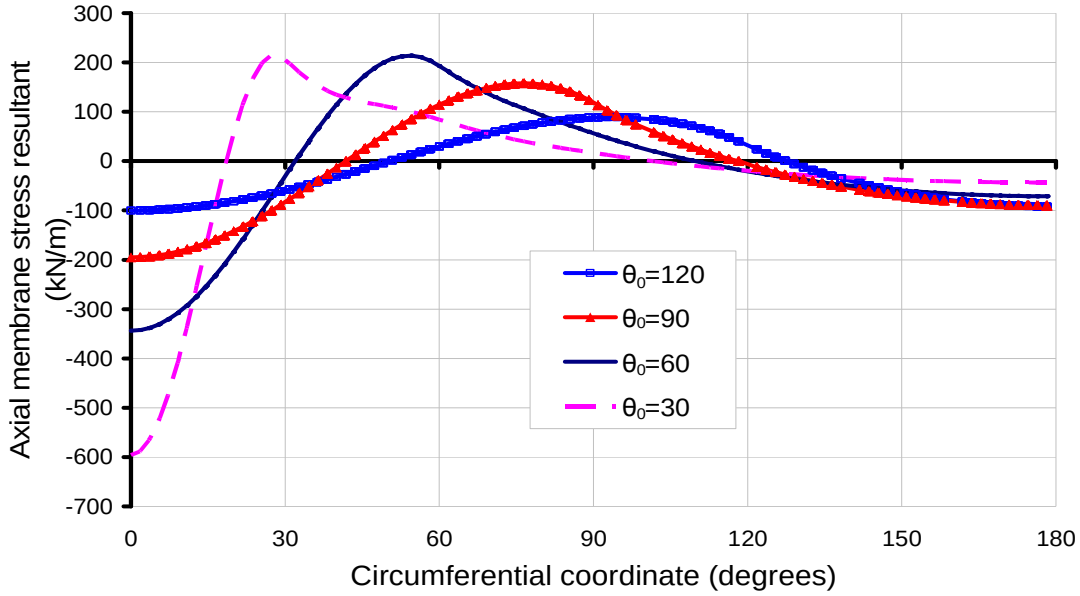

Figure 7-32 Effect of heating ranges θ_0 on axial membrane stress around circumference in an empty tank (stresses taken at the mid-height of the tank)

The post buckling modes of an empty tank and a half filled tank are shown in Figure 7-33 - Figure 7-36. The buckle always forms in the heated zone. When the tank is exposed to a narrow band of heating, buckles concentrate within the small band. When the heated zone is wider, buckles spread over a wider range. The position of the buckles corresponds to the largest axial force developed in the tank. Buckling occurs near the bottom boundary if the tank roof is light, but with a very heavy restraint from the roof, they may develop at the top of the wall. In a partially filled tank, buckling occurs near the liquid surface and then spreads into the empty part. The presence of liquid in the tank generally increases the buckling temperature as a result of the beneficial effect of internal pressure which causes circumferential tension.

θ_0=30° θ_0=60° θ_0=90° θ_0=120°

Figure 7-33 Post buckling modes in an empty tank with a slender roof (t_f=2t_c)

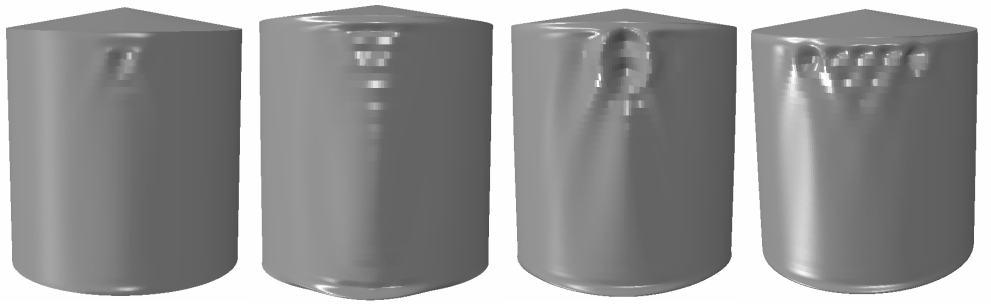

θ_0=30° θ_0=60° θ_0=90° θ_0=120°

Figure 7-34 Post buckling modes in an empty tank with a very stiff roof (t_f=100t_c)

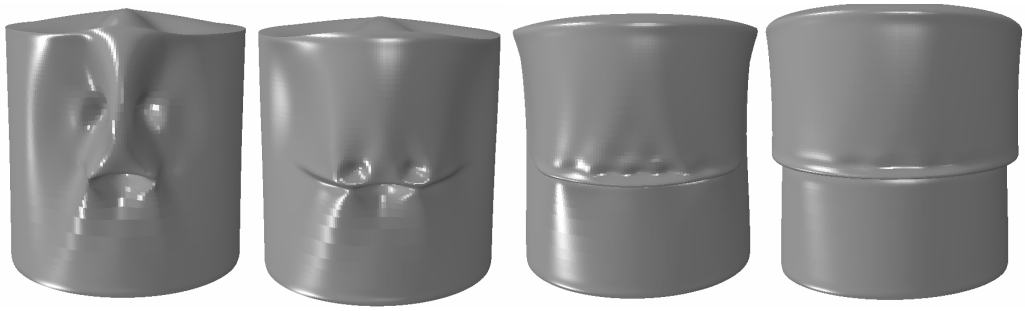

θ_0=30° θ_0=60° θ_0=90° θ_0=120°

Figure 7-35 Post buckling modes in a half filled tank with a slender roof (t_f=2t_c)

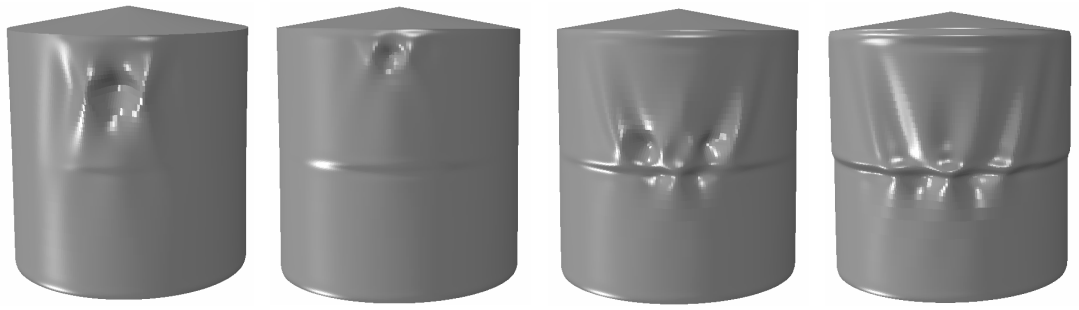

θ_0=30° θ_0=60° θ_0=90° θ_0=120°

Figure 7-36 Post buckling modes in a half filled tank with a very stiff roof (t_f=100t_c)

7.4.5 Effect of liquid level

The liquid surface level inside the tank has a significant influence on the buckling behaviour. The buckling temperature rise variation with the liquid surface level is shown Figure 7-37 for two tanks: one with a slender roof whose post-buckling modes are shown in Figure 7-38and the other with a very stiff roof whose post-buckling modes are shown in Figure 7-39. As the liquid surface rises, the buckling temperature generally rises too. In slender roofed tanks, the buckling temperature ceases to increase when a certain filling level is reached. When the liquid level is near the bottom, the buckling temperature is slightly lower than that for the condition of an empty tank. Buckling always occurs near the liquid surface and spreads into the empty part, as shown in Figure 7-38 and Figure 7-39.

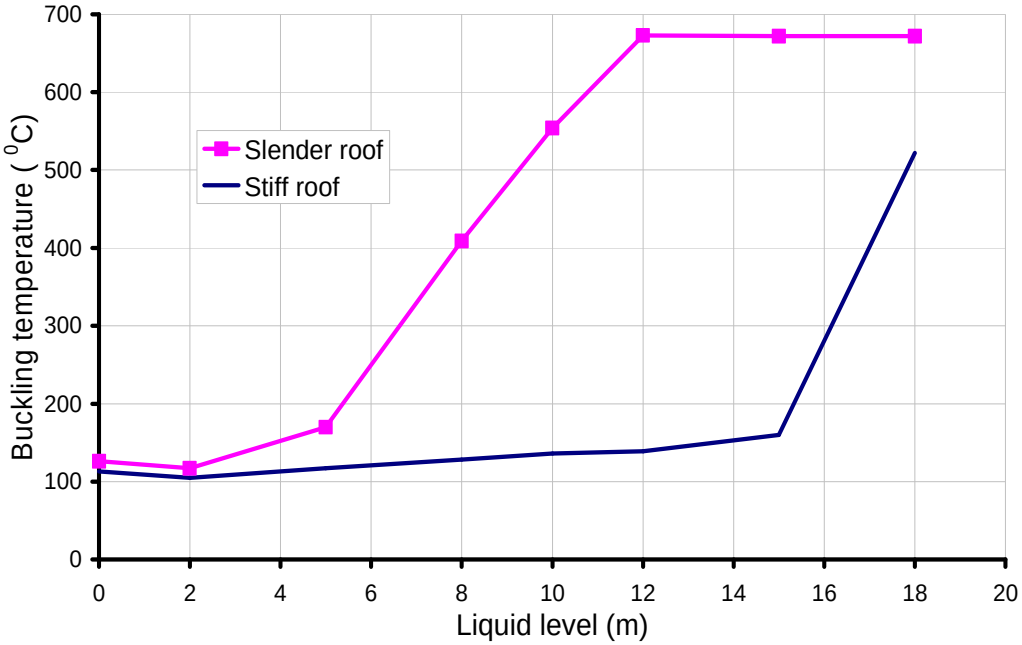

Figure 7-37 The effect of liquid surface level on the buckling temperature

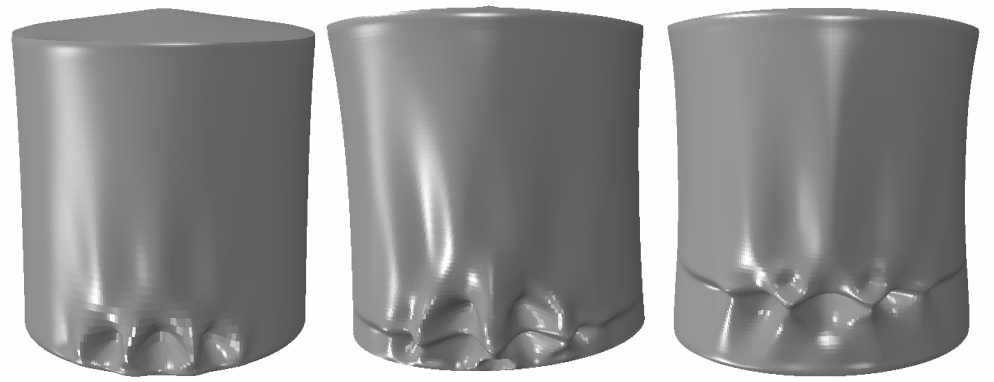

(a) Liquid level=0m (b) Liquid level=2m (c) Liquid level=5m

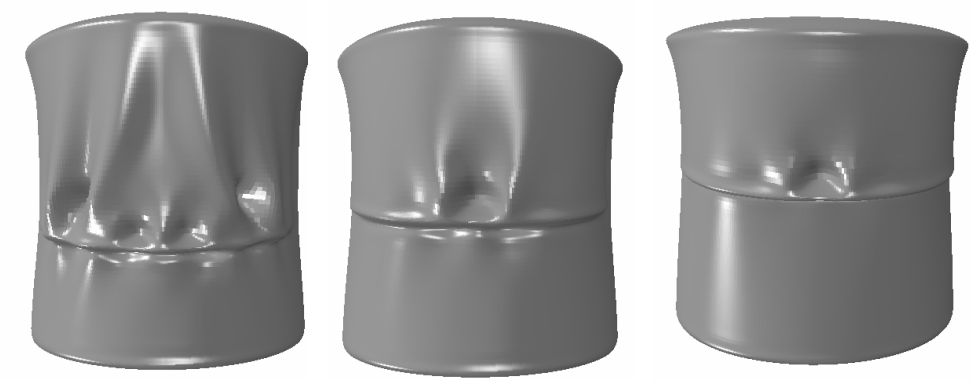

(d) Liquid level=8m (e) Liquid level=10m (f) Liquid level=12m

Figure 7-38 Post buckling modes in a slender roof tank (t_f=2t_c) with different liquid surface levels

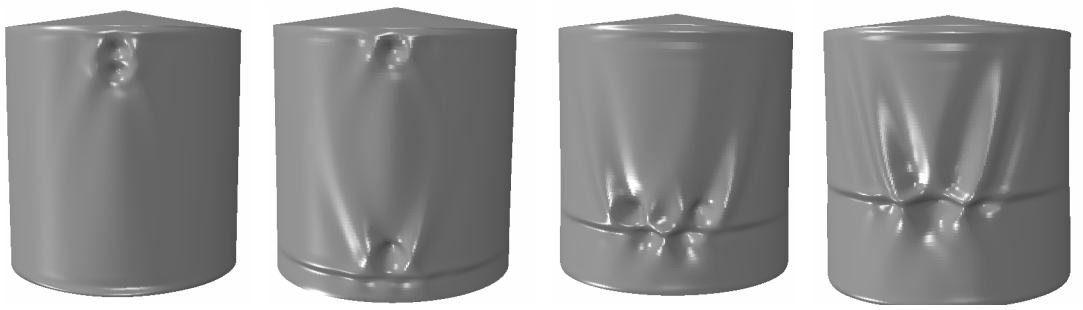

(a) Liquid level=0m (b) Liquid level=2m (c) Liquid level=5m (d) Liquid level=8m

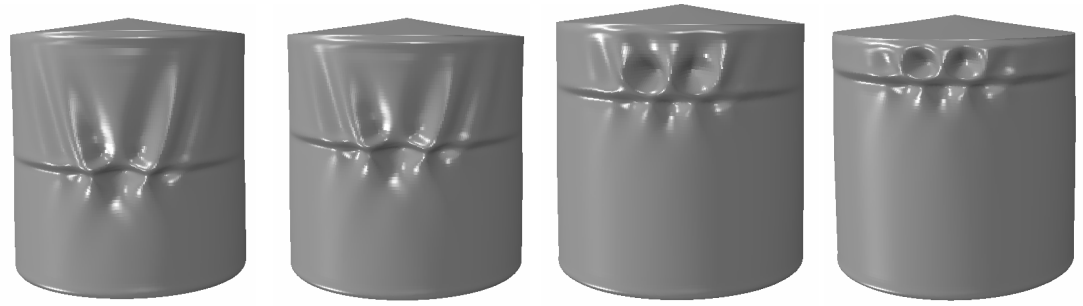

(e) Liquid level=10m (f) Liquid level=12m (g) Liquid level=15m (h) Liquid level=18m

Figure 7-39 Post-buckling modes in a stiff roof tank (t_f=1000t_c) with different liquid surface levels

7.4.6 Effect of tank radius-to-thickness ratio

The slenderness of a shell structure is simply measured by the ratio of the shell wall thickness to its radius. It is naturally important to explore the buckling temperature of tanks with different radius to thickness ratios *r/t*. The buckling temperature generally decreases with an increase in *r*/*t* ratio (Figure 7-40), as shown by the progressive fall in buckling temperature with decreasing tank diameter. The buckling modes also do not appear to change as the tank aspect ratio is changed (Figure 7-41).

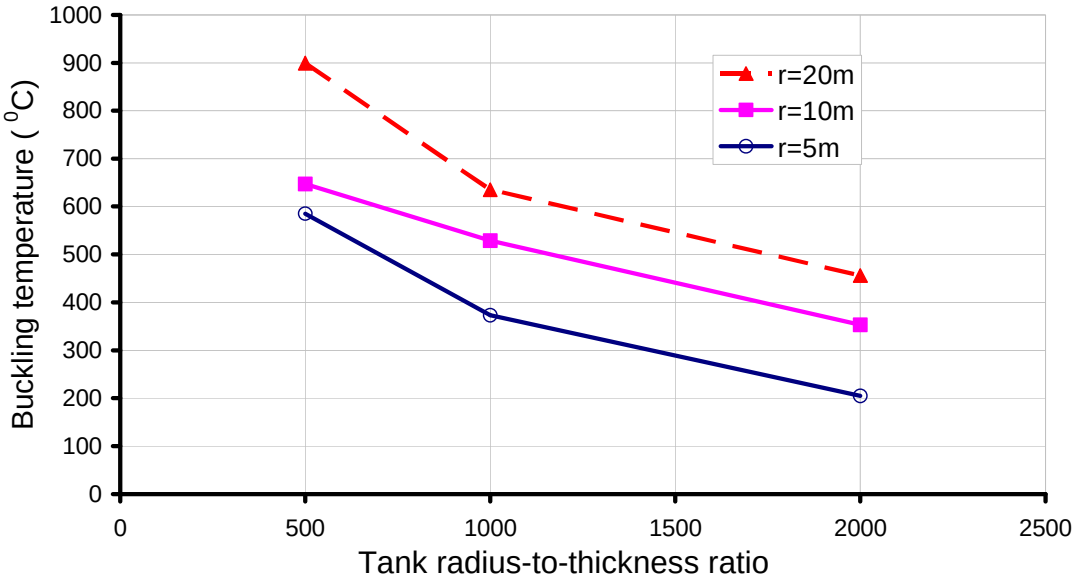

Figure 7-40 Buckling temperature of half-filled tanks with different aspect ratios (t_f/t_c=10)

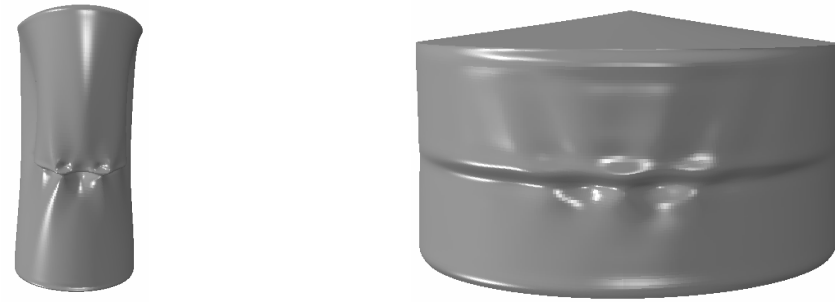

(a) R=5m (b) R=20m

Figure 7-41 Post-buckling modes of half filled tanks with different aspect ratios (r/t=1000)

7.4.7 Effect of transition zone

The geometrically linear analytical study presented in Chapter 4 has suggested that the size of transition zone has a significant effect on the compressive circumferential

stresses near the liquid level. Hence, the influence of this transition length to the buckling behaviour is evaluated in this section. Figure 7-42 illustrates that the buckling temperature increases with increase of transition length, the rate of increasing is more pronounced under a heating regime with a transition length larger than 0.5m. The results demonstrate that the induced compressive circumferential stresses have certain effect on the prediction of buckling temperature. Thus, in cases where an accurate transition length is unknown, the presumed value for this parameter should be carefully selected. For this study, as according to the heat transfer analysis in Chapter 5, a transition length of 0.2m is deemed to be accurate.

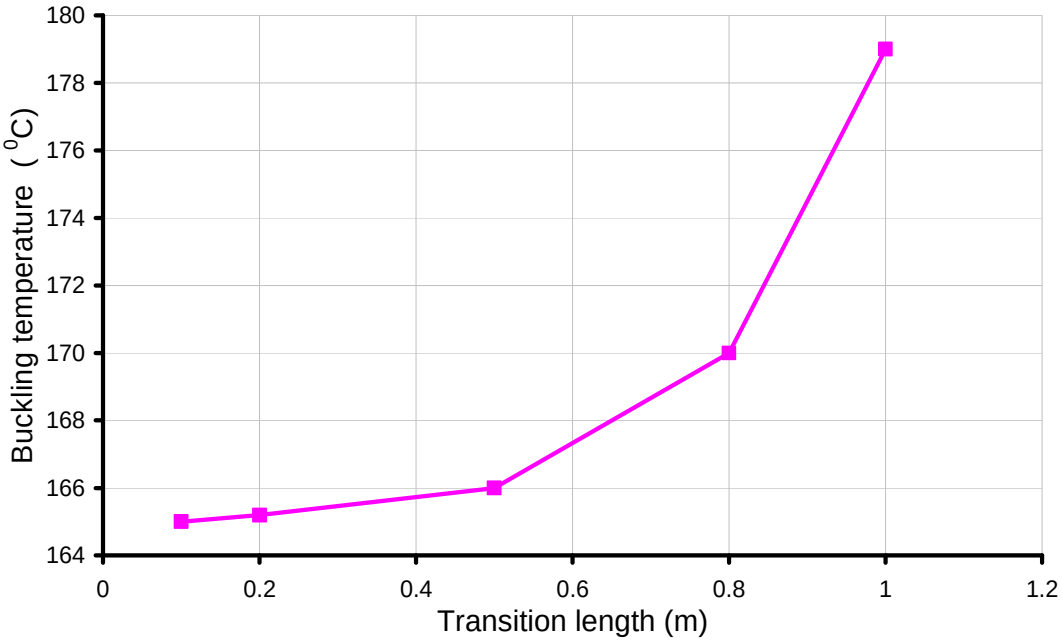

Figure 7-42 Effect of transition length on the buckling temperature

7.5 Conclusions

The behaviour of a typical petroleum storage tank that is severely heated by its proximity to an adjacent tank that is on fire has been explored in this chapter. The different analysis procedures were used to investigate the behaviour of the tank under

such scenario. By contrast geometrically nonlinear analysis showed a good prediction for the current problem.

The results show that the tank can buckle when exposed to a rather low increase in temperature. The significance of tank geometry, liquid surface level, size of the heated zone and fire condition for the buckling temperature rise were all explored in this chapter.

The following conclusions are drawn:

1. The failure of tanks subject to heating from an adjacent tank is caused by buckling, leading to large post-buckling deformations which can easily lead to local rupture and ignition of the contents.

2. Buckling always occurs on the hot side of the tank. The buckling is caused by vertical compressive stresses induced by the restraint to differential thermal expansion provided by the cooler parts of the wall.

3. The extent of the heated zone around the tank circumference has a significant effect on the buckling temperature rise. A narrow band of heating results in buckling at a lower temperature, with the buckling mode occurring over a narrower zone.

4. The presence of liquid in the tank can significantly increase the buckling temperature and this increase is steadily enhanced as the liquid surface level is increased.

5. In a partially filled tank, the buckling temperature rise is sensitive to the condition of whether the roof been heated or not; while this is not the case for an empty tank.

6. The buckling temperature decreases with an increase in the radius to thickness ratio of the tank wall, the relationship being approximately linear with the tank diameter.

7. The stiffness of roof significantly affects the stress state in the cylindrical wall. For realistically flexible roofs, buckling occurs near the base or the fluid surface level.

However, if a very stiff upper boundary condition is used, the analysis predicts that the maximum compressive stress will occur near the roof and buckling is found at that location.

8. For realistically flexible roofs, the slope of the roof has certain influence on the buckling temperature. Tank tends to buckle under a high temperature with a steep slope. The roof angle is not shown much influence for stiff roof tanks.

9. In general with practical roof structures, buckling is expected to begin in the roof, to develop large deformations that are not visible from the ground, and to stabilise before buckling of the wall ensues.

Chapter 8

8. Realistic post-buckling analysis of tanks

8.1 Introduction

Chapter 7 has presented a detailed thermal buckling analysis of the target problem using the conventional numerical buckling analysis method – the arc-length method (i.e., the Riks method in Abaqus). A shortcoming in the analysis has been identified when using this method: the increasing temperature, applied as the thermal loading, has to reduce once the structure passes over the buckling point that corresponds to the buckling temperature defined for the target structure. While in reality, the post-buckling procedure of the structure should be accompanied by a continuously ascending temperature variation as usually the thermal loading (e.g., due to fire) may develop to a much higher temperature than the buckling temperature of a structure. In particular, when the temperature-induced material degradation is concerned, the predicted buckling behaviour of the structure experiences unrealistic recovered material properties (e.g., increased elastic modulus and yield stress) as the temperature reduces artificially, instead of further weakened properties due to increasing temperature. This limitation of Riks method has been shown to effectively

prohibit continuing the calculation to capture the successive buckling events in the tanks problem. Specifically, for a tank with slender roof, the roof usually buckles first, followed by wall buckling. Such a successive buckling process cannot be successfully simulated by the conventional static analysis using the Riks method.

The chapter presents a solution to the above problem that includes a successive buckling under continuously elevated thermal loading. The analysis method used in this chapter is the conventional nonlinear static analysis incorporating an “Artificial Damping”. The analysis procedure and theory of the “Artificial Damping Method” (ADM) is explained first. Calculations of a tank buckling problem carried using this method in Abaqus will be shown and compared with that obtained from the Riks method. It will be shown that such numerical procedure can successfully capture the interested successive buckling behaviour and shows certain merits over the Riks method in dealing with thermal buckling problems.

8.2 Analysis procedure

In a nonlinear analysis the nonlinear response is found by iterating at each time step for a loading as a function of time. In general FEM codes such as Abaqus/Standard, the simulation was undertaken as a number of time increments and finds the approximate equilibrium configuration at the end of each time increment. However, nonlinear static problems can be unstable. If the instability manifests itself in a global load-displacement response with a negative stiffness, the problem can be treated as a buckling or collapse problem.

8.2.1 Limitations of the Riks method

A powerful method of dealing with non-linear problem is the arc-length method that has been widely used in both research and practice. In Abaqus it is called the Riks method. The Riks method is generally used to predict unstable, geometrically nonlinear collapse of a structure. This method has some limitations. It is only valid for cases where the loading changes proportionaly over the complete structure.

Furthermore, the Risk method cannot trace the behaviour to a higher loading level after the analysis process enters an unstable path with negative stiffness. For an oil tank buckling problem, technically this means, if the tank buckles at a temperature which is lower than the peak value that could be developed in the tank structure under a real fire scenario, the Riks method will fail to realistically trace the structural behaviour above the temperature of the first buckling. The analyses in the previous chapter showed that the roof of the tank often buckle easily at around a temperature rise of as small as 40°C. It is noted that the buckling of roof may not necessarily influence the stability of the whole tank structure while the main concern is more about the buckling of tank wall. Clearly, by using the Riks method, no information on the wall behaviour could be obtained in such a situation; for example, whether the wall is going to buckle after the roof buckling or not and what the buckling mode would be.

There is also a technical restriction in using the Riks algorithm in the current version of Abaqus when trying to read data from a previous loading step that is of a different analysis type such as heat transfer analysis. Evidently it will be useful to conduct thermal buckling analysis of a structure using thermal loading information obtained directly from a heat transfer analysis of the same structure. The temperature distribution and magnitude predicted from the previous step of heat transfer analysis were stored in an Abaqus data file that are usually readable (using Keywords *FILE) for the subsequent loading steps. However, this gateway isn't valid if the the Riks method is used in the next simulation step.

8.2.2 The Artificial Damping Method (Simulia 2008)

"*When a structural stability problem is concerned, if the instability is localised, there will be a local transfer of strain energy from one part of the structure to its neighbouring parts. This class of problems has to be solved either dynamically or with the aid of an artificial damping; for example, by using dashpots.*" (Simulia 2008). Although the dynamic approach has an advantage in dealing with nonlinear

problem because the inertia terms provide stability to the system, this approach is time consuming and computationally cost ineffectively.

"Abaqus/Standard provides an automatic mechanism for stabilising the unstable quasi-static problems through the automatic addition of a volume-proportional damping to the model.

The applied damping factors can be constant over the duration of a step, or they can vary with time to account for changes over the course of a step. Automatic stabilization with a constant damping factor is triggered by including automatic stabilization in any nonlinear quasi-static procedure. Viscous forces of the form

$$F_v = cM^* v \tag{8-1}$$

are added to the global equilibrium equations

$$P - I - F_V = 0 \tag{8-2}$$

where M^* is an artificial mass matrix calculated with unity density, c is a damping factor, $v = \Delta u / \Delta t$ is the vector of nodal velocities, and Δt is the increment of time (which may or may not have a physical meaning in the context of the problem being solved), P is the total applied load, and I is the structure's internal force.

While the model is stable, the viscous forces and, therefore, the viscous energy dissipated are negligible compared with the strain energy of the system. Thus, the additional artificial damping has no effect on the structural behaviour. If a local region becomes unstable, the local velocities increase and, consequently, part of the strain energy released is dissipated by the applied damping.

Normally the examined structure is stable at the beginning of the step and that instabilities may develop in the course of the step. Such condition is assumed in the numerical implementation of the damping parameter. The first increment of the step is stable without the need to apply a damping. The damping factor is then determined

in such a way that the dissipated energy for a given increment with characteristics similar to the first increment is a small fraction of the extrapolated strain energy. The fraction is called the dissipated energy fraction and has a default small value of 0.0002 but the user is free to assign an even smaller or larger value. The damping factor is controlled by the convergence history and the ratio of the energy dissipated by the viscous damping to the total strain energy. If the convergence behaviour is problematic because of instabilities or rigid body modes, Abaqus/Standard automatically increases the damping factor. On the other hand, Abaqus/Standard may also reduce the damping factor automatically if instabilities and rigid body modes subside. " (Simulia 2008)

The above described Artificial Damping Method was deemed a suitable tool for solving the current problem of thermal buckling of oil tanks; hence it was tested and then adopted in the calculations presented in this and next chapters.

8.3 Predicting the thermal buckling behaviour

The predictions of the thermal buckling of oil tank structure using the Artificial Damping Method are presented below. As explained in the previous section, within the stable regime of a structure, the applied artificial damping should be extremely small so that the structural behaviour is not affected. Therefore, the predicted behaviour should be not different from that obtained from the Riks method in and only in the pre-buckling part. Hence, a way of validating the functionality of the ADM is to compare it's predictions to that of the Riks method.

8.3.1 Model and thermal loading pattern

The tank dimensions are the same as that adopted in chapter 7, which are 20m in diameter and 20m high with a uniform wall thickness of 0.01m (Figure 8-1a). Two roof thickness $t_f=t_c$ and $t_f=2t_c$ were studied in this analysis to represent a slender roof and a stiffer roof case respectively. The tank was assumed to be empty. Two roof conditions were considered, cool and hot respectively. The temperature distribution

pattern is assumed to follow the "smooth-edge" pattern as expressed in Eq. 7-1 with $\theta_0 = 90^0$ (Figure 8-1b).

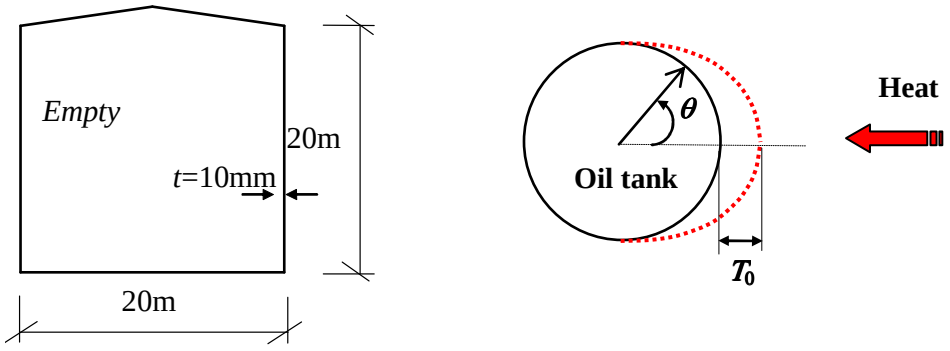

a) Tank dimensions

b) Temperature distribution: smooth-edge (θ_0=90°)

Figure 8-1 Numerical model

The geometric nonlinear elastic analysis (GNA) was adopted, so that the material nonlinearity due to plasticity is neglected in the calculations. It is noted that the material nonlinearities due to thermal effect (e.g., temperature dependent elastic modulus and thermal expansion coefficient) are still taken into accounted.

8.3.2 Examination of the predictions

Figure 8-2 shows the evolution of energy dissipation fraction (the ratio of the energy dissipated through artificial damping to the total strain energy of the system) as the thermal loading rises to 200°C. The horizontal coordinate is the maximum temperature developed in the tank in each time step. It can be seen that in the early stage of the loading process, the energy dissipation fraction is almost zero, which corresponds to the situation that the deformation of the system is rather small so that the virtual nodal velocities in Eq. 8-1 were all very small producing a negligible damping effect. The whole system remains almost in the original configuration, i.e. no buckling occurred. As the loading process continued with the maximum temperature reaches ~128°C, the energy dissipation fraction suddenly jumps up to a

large value, which suggests a rapid increase of structural deformation resulting in a large amount of energy dissipated by the artificial damping. This effect indicates that the structure experienced a sudden change of configuration – corresponding to an event of buckling. Numerically, large artificial damping is produced in order to satisfy static equilibrium of the whole system and enable the continuation of the quasi-static simulation. After the jump the energy fraction gradually reduces and approaches a small value until further buckling occurs. The temperature at the point of jumping is therefore the predicted buckling temperature which will be explored in more detail below.

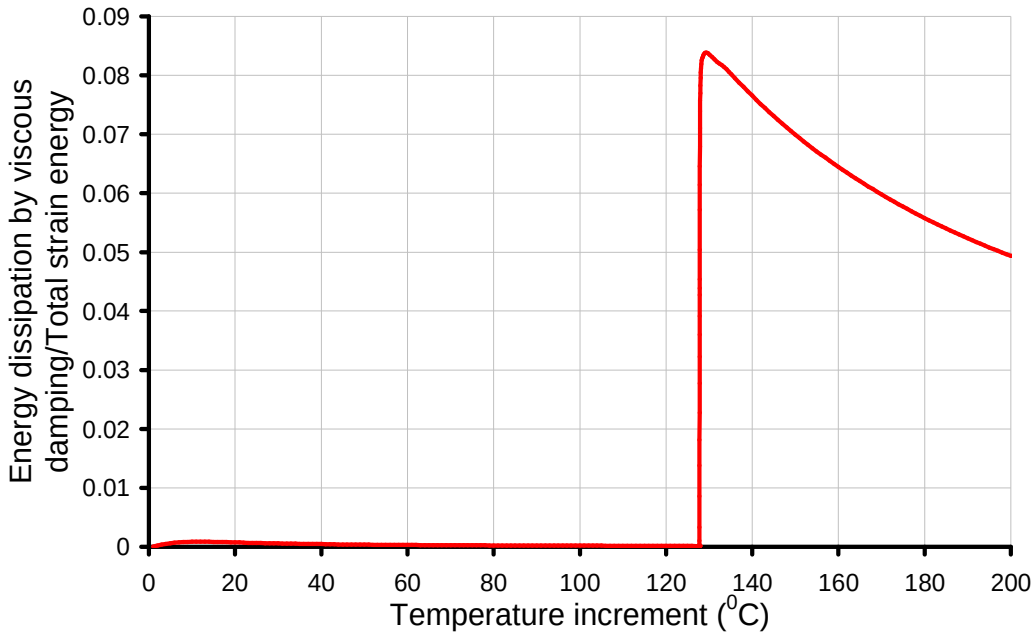

Figure 8-2 Evolution of energy dissipation fraction (t_f=2t_c, cool roof)

Figures 8-3a and b show the thermal loading vs. radial and vertical displacements curves of a node at z=10m on the most heated meridian (θ=0) for the cool roof condition. In each figure, two curves are compared: one obtained from Riks analysis (dash line with symbols) and the other form the ADM analysis (solid line). It can be seen in Figure 8-3, the prediction from the Riks method consists typically an ascending branch followed by a descending branch. The peak corresponds to the

buckling temperature. The ADM predicts exactly the same output in the pre-buckling range (i.e. before buckling point) and the same buckling temperature as the Riks method. This indicates a good consistency between the two methods in the pre-buckling regime as expected.

However, discrepancy started to develop once buckling occurs. Due to the inherent limitation, the Riks method fails to trace a higher temperature. The ADM successfully traces the post-buckling behaviour with an increasing temperature. It can be seen from Figure 8-3, the tank experiences a rapid development of deformation within a tiny increment of temperature. The temperature keeps increasing although the velocity of the examined node changes direction at times.

Figure 8-4 shows the same pair of curves for the case of a hot roof. It is interesting to note that the curves are almost identical as those of the cool roof case. This suggests that for the current empty tank with relatively stiff roof, the buckling behaviour has little sensitivity to the thermal condition of the roof, as confirmed by both the Riks and the ADM procedures.

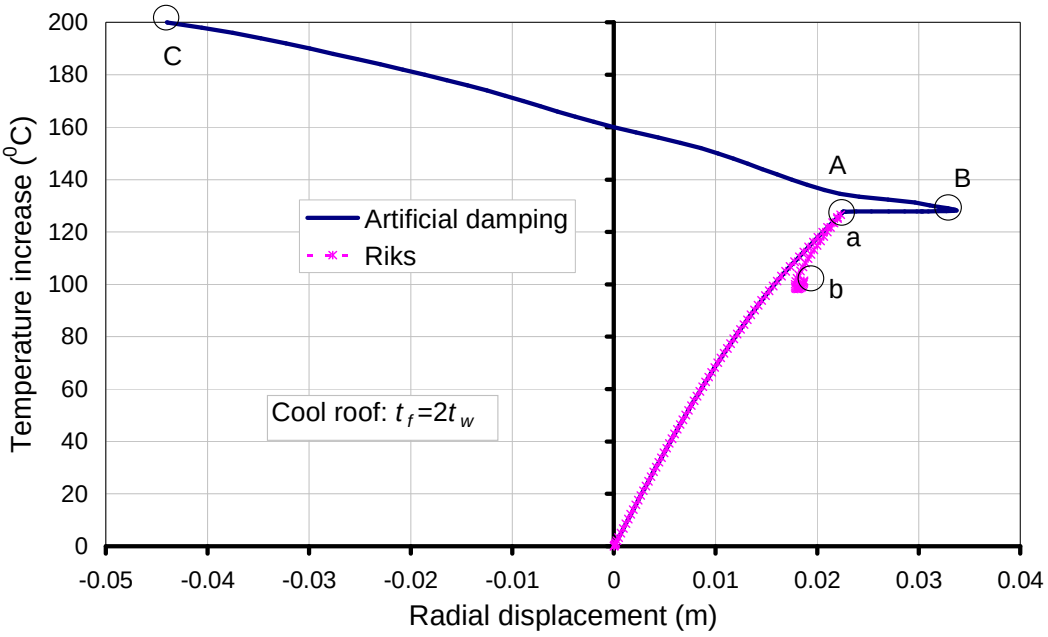

(a) Radial displacement

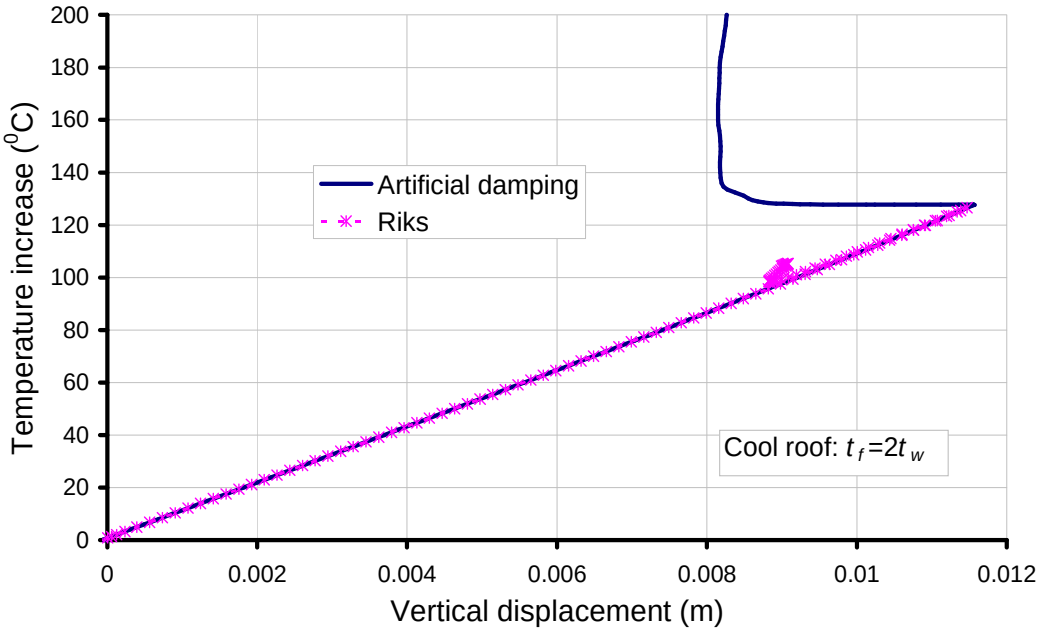

(b) Vertical displacement

Figure 8-3 Temperature vs. radial displacement curves of node at θ=0°, z=10m from Artificial Damping Method and Riks method (cool roof; $t_f=2t_c$)

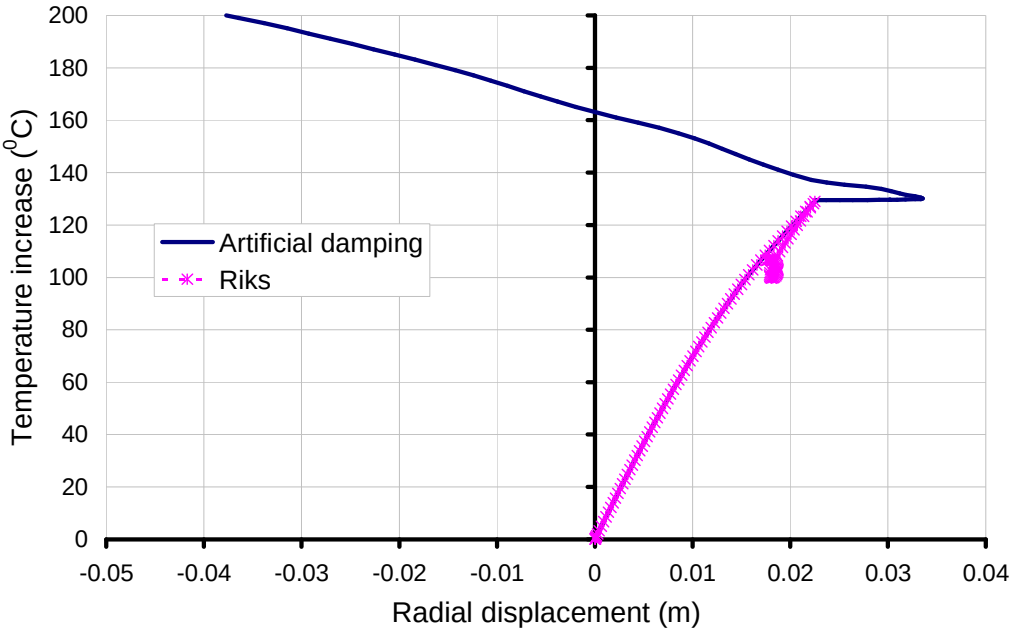

(a) Radial displacement

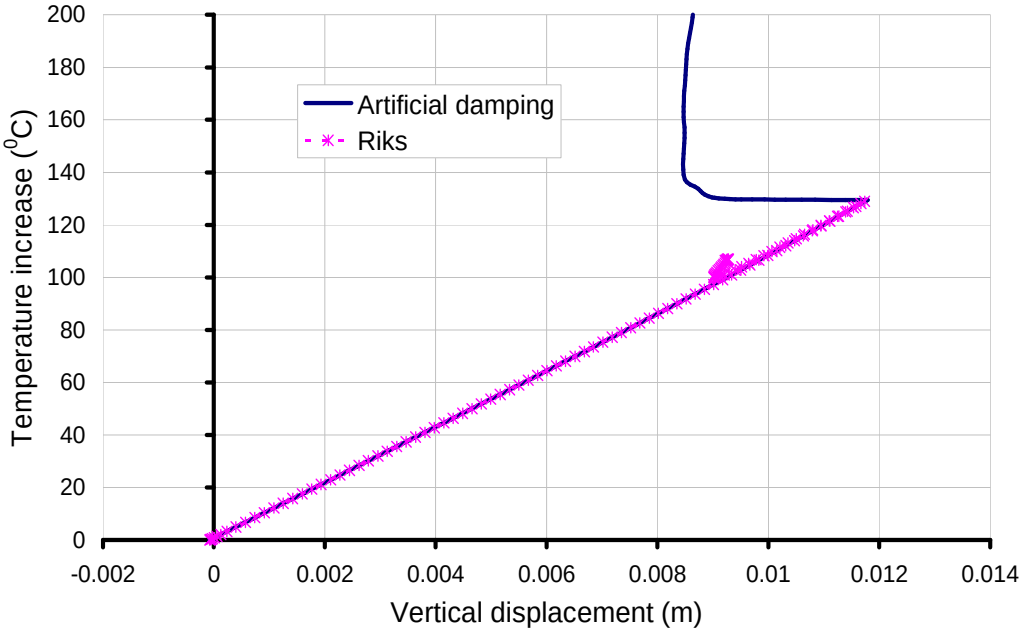

(b) Vertical displacement

Figure 8-4 Temperature rise - radial displacement curves of node at θ=0°, z=10m from Artificial Damping Method and Riks method (hot roof; t_f=2t_c)

It is of interest to show the deformed shape of the tank structure at each of the key stages. The configurations predicted by the ADM and the Riks method are shown in Figures 8-5 for the cool roof case. These configurations correspond to the points *A*, *B* and *C* or points *a* and *b* denoted in Figure 8-3a. The two methods are consistent to each other in predicting that buckles initialised near the bottom boundary of the tank, and then spread upward to a larger region of the tank wall. However, the exact deformation modes from the two methods slightly differ from each other and a larger difference lies in the number of buckles and area of the buckles. Note that the deformations shown in the contour of Figure 8-5 are scaled up by a factor of 5 from both methods.

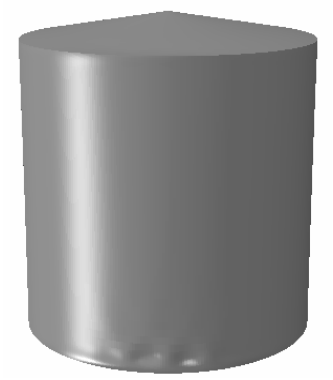

Stage *A* (ADM)

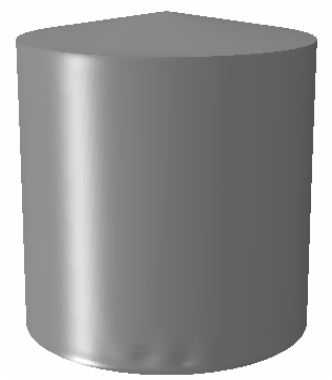

Stage *a* (Riks)

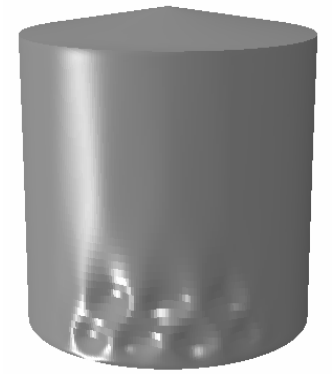

Stage *B* (ADM)

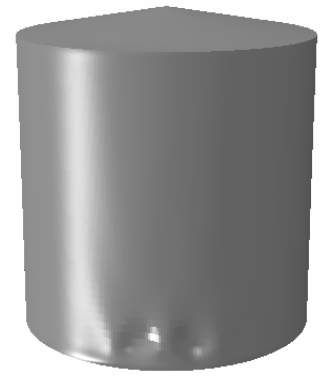

Stage *b* (Riks)

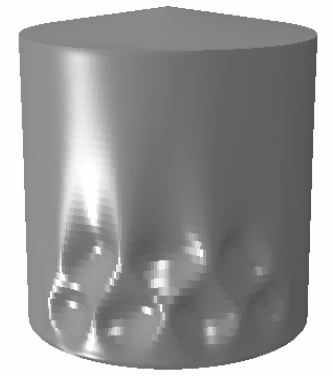

Stage *C* (ADM)

Figure 8-5 Deformation of the tank at some critical stages (t_f=2t_c, cool roof, scale factor = 5)

8.3.3 Predictions of successive buckling behaviour

The advantage of using Artificial Damping Method is more obvious in modelling the cases that involve multiple occurrences of buckling along the thermal loading path. Such a situation is typical in the thermal buckling of tanks with slender roof (e.g., t_f=t_c) where the tank roof often buckles before the tank wall.

Figure 8-6 shows the evolution of energy dissipation fraction during the thermal loading process in the slender roof case. In the cool roof case (solid line), the first jump (sudden increase of the fraction magnitude), occurs at a temperature rise of 36°C (part $A \rightarrow B$), which is much lower than that of the stiff roof case (128°C). By observing the deformation of the tank, it is seen that this sudden increase of energy dissipation is due to the buckling of the roof (Figure 8-7a) instead of the wall in stiff roof case (Figure 8-5a).

It is important to note that the buckling temperature of the roof (i.e. 36°C) is far lower than the magnitude that could develop during a real fire accident. Therefore, information on behaviour of the whole structure after the buckling of roof is of great interest to the safety evaluation of the collapse of the tank. It is shown that such information may be successfully obtained by using the Artificial Damping Method. As shown in Figure 8-6, three more jumps can be identified in the traced range (till 400°C) of energy dissipation history, though their magnitudes appear much smaller than the first jump. Among the four jumps, the last jump ($C \rightarrow D$) is of special significance, as it corresponds to the buckling of the tank wall, confirmed by the deformation shape (Figure 8-5d). The middle two jumps are less significant as they correspond to another two successive buckling in the roof. As a result, Figure 8-6 has clearly exhibited two important jumps at points *A* and *C*, corresponding to the first roof buckling and wall buckling respectively.

The dotted line in Figure 8-6 shows the case of hot roof has higher buckling temperatures for both roof and wall compared to the cold roof case. This suggests that for the empty tank with relatively slender roof, the thermal condition of the roof has some effect but not significant influence on the buckling behaviour of the tanks.

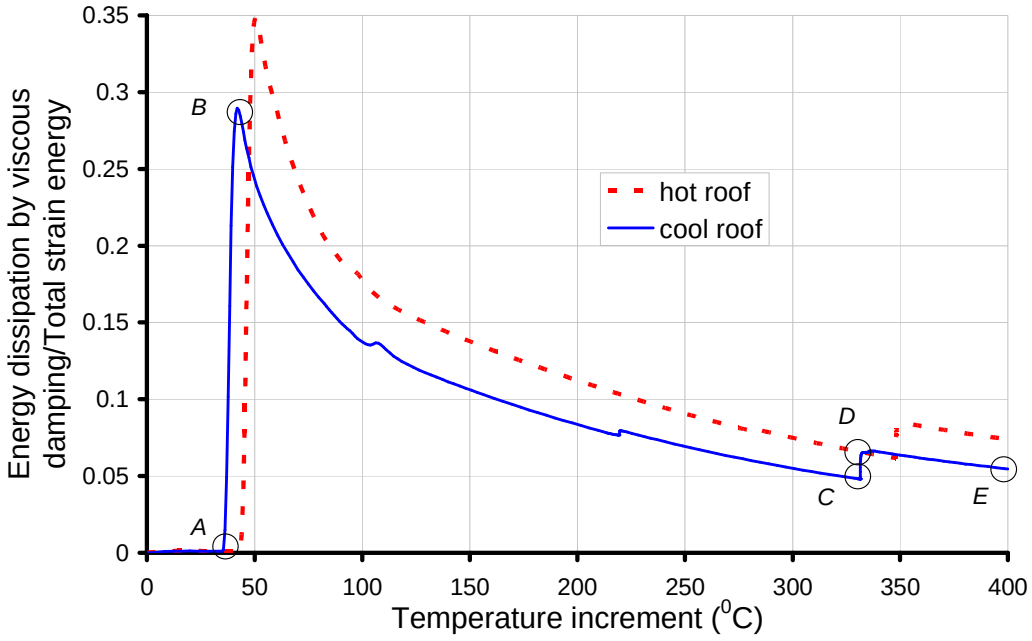

Figure 8-6 Dissipated energy fraction history (t_f=2t_c)

Figure 8-7 illustrates the evolution of deformation mode of the tank at different stages as denoted in Figure 8-6. When temperature rises up to a certain value, the roof of the tank starts buckling (Figure 8-7 a). The viscous energy then rises up until the system is stable again (Figure 8-7 b). As soon as a stable state is achieved, the viscous energy starts decreasing. During that time the buckle developed bigger (Figures 8-7 a&b), involving another two successive roof buckling. The buckle in the roof changes from one wave on the heated side to three big waves covers the whole roof (Figure 8-7 c). At about 330°C, the tank wall starts buckling (Figure 8-7 d), the viscous energy rises up once more and the buckles in the tank wall developed further until the system stable again, then the viscous energy decreases until the temperature reached the end of the traced thermal loading range (Figure 8-8 e).

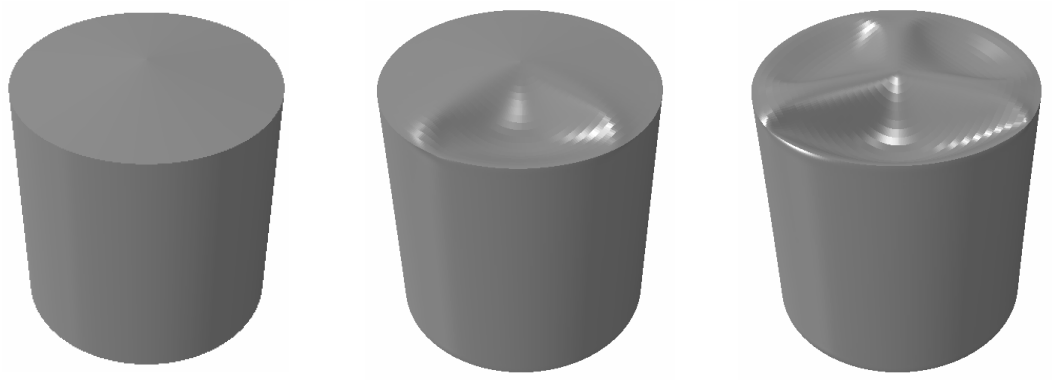

(a) Stage *A* (*T*=36°C) (b) Stage *B* (*T*=43°C) (c) Stage *C* (*T*=331°C)

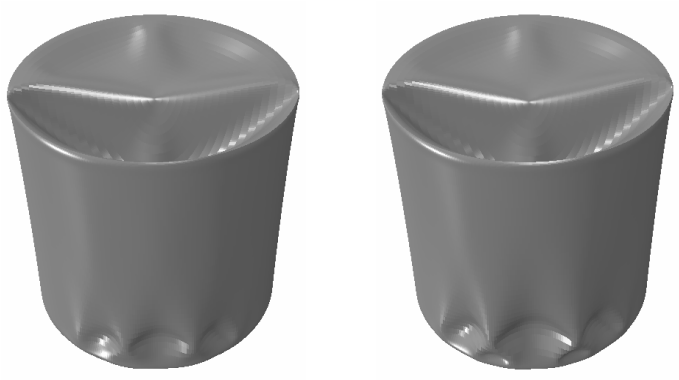

(d) Stage *D* (*T*=338°C) (e) Stage *E* (*T*=400°C)

Figure 8-7 Roof buckling followed by shell buckling of a thin roof tank (t_f=t_c, cool roof)

The loading-displacement results obtained by using the ADM (solid curve with symbols) and the Riks method (solid curve) are compared in Figure 8-8. The Riks method predicted that the roof buckled at less than 35°C of temperature rise, after which the loading process drops down and no further results above this buckling temperature were provided. The ADM simulation continued after passing the roof buckling and distinctly displays another buckling event occurring in the cylindrical wall at around 330°C manifested as a rapid increase of radial displacement within a tiny increase of temperature (at the point *C* in the solid curve, Figure 8-8). However, the 2nd and 3rd buckling events in the roof do not manifest clearly in this curve. This is due to the fact that the temperature vs. displacement curve varies from node to

node and different in radial and vertical directions. The rapid motion of buckling sometimes may not appear so obviously in curves extracted from some nodes or in some directions in the structure. This phenomenon can be further seen from the current example. The radial-displacement curves in Figures 8-8 a and b manifest clearly the buckling point is at 36°C, but it is not that obvious in the curve of the vertical displacement in Figures 8-6 c and d. As a result, the identification of the buckling occurrences requires additional examinations of the energy dissipation fraction history or the deformation modes. It is recommended here that the energy dissipation fraction history can be regarded as a more reliable way to identify the buckling events.

It may be noticed that in Figure 8-6b the roof buckling temperature predicted by the ADM is close to but still slightly higher (by ~3°C) than that predicted by the Riks method. As discussed earlier, one expects the same buckling temperature value from both methods, as in the stiff roof case where tank wall buckles first (see Figure 8-3). This slight discrepancy is in some extent due to numerical accuracy but can also be caused by some other issues that remain unsolved. A tentative explanation is that the buckling mechanism of tank wall is of type of bifurcation while that of the roof is of limit point buckling. The artificial damping may slightly defer the motion resulted from a limit point buckling, but it cannot alter the position of the onset of bifurcation. This can be understood as that bifurcation type of buckling involves a switch of the deformation mode /configuration while the limit point buckling mainly continues the original deformation mode, say, no change of configuration.

It can be concluded from the above analysis that both methods can predict the buckling load and buckling mode of the first buckling. Hence, if only such information is interested, then both methods are applicable. When the post-buckling behaviour especially successive buckling events are of interest, the Artificial Damping Method is more useful than the conventional Riks method.

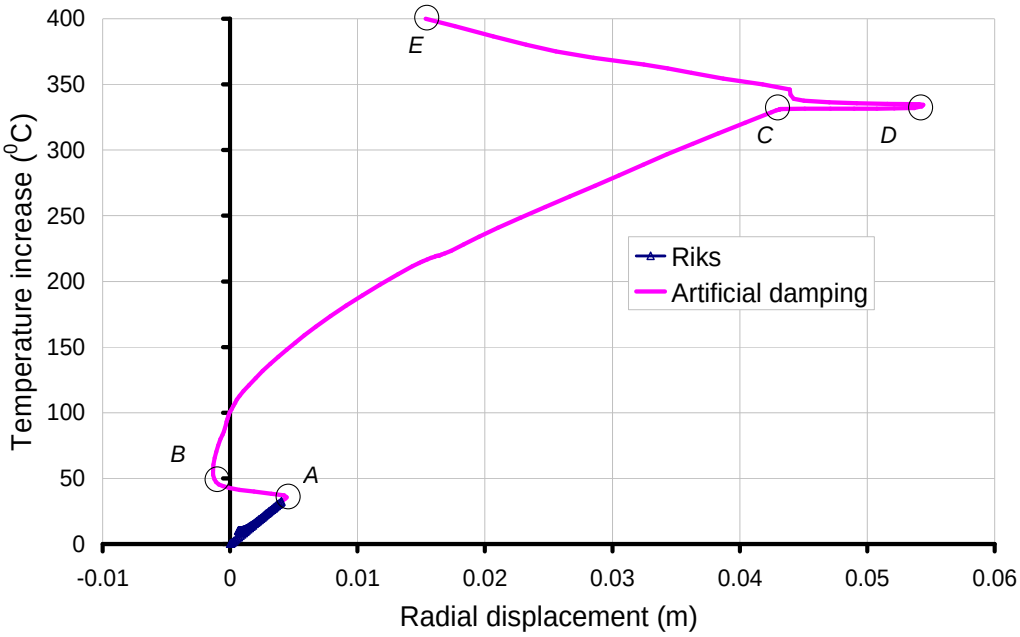

(a) Radial displacement

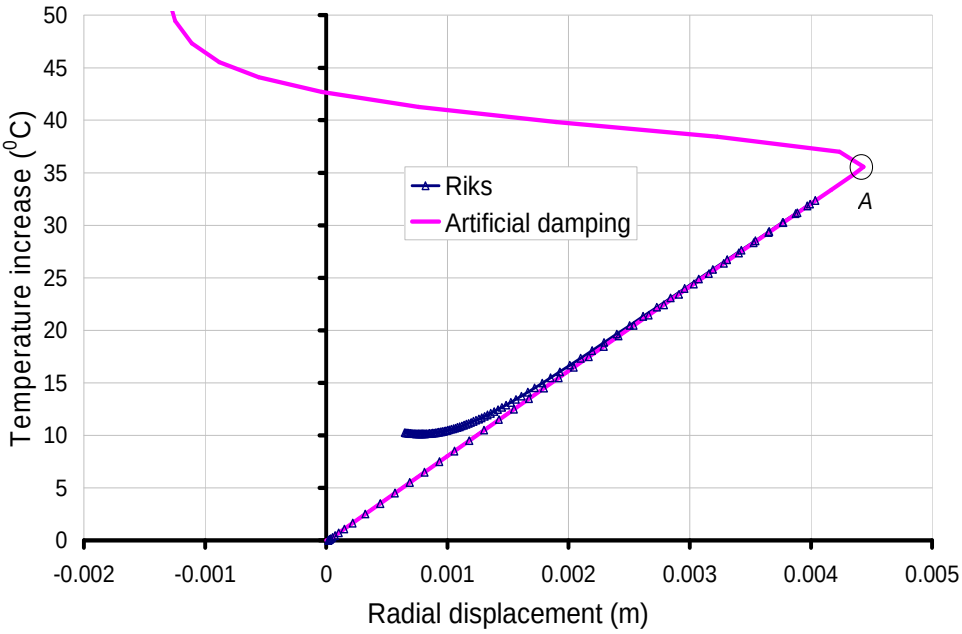

(b) Close-up view of (a)

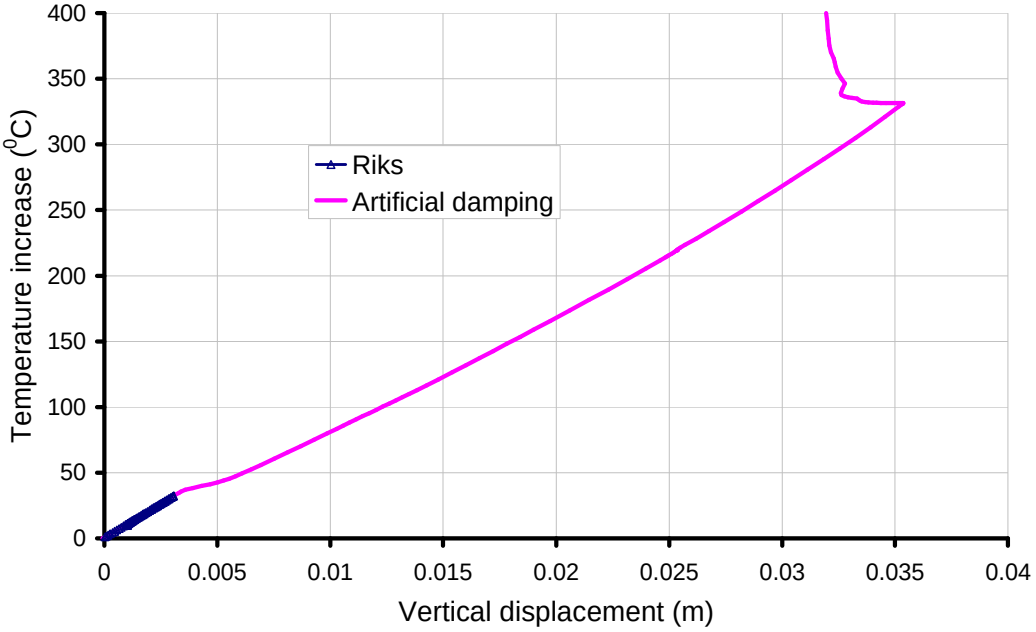

(c) Vertical displacement

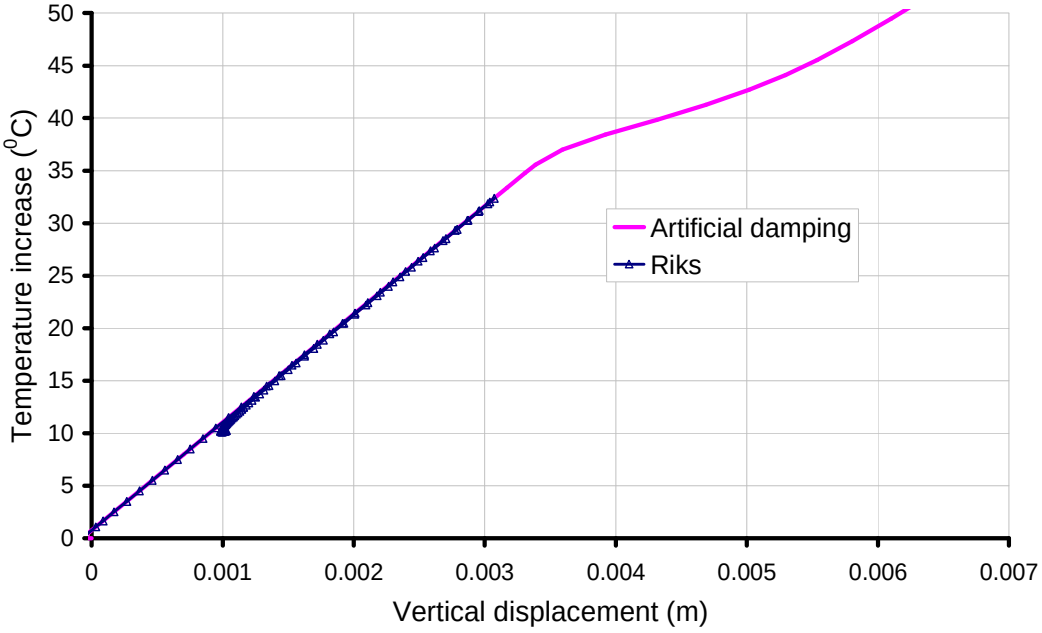

(d) Close-up view of (c)

Figure 8-8 Temperature vs. radial displacement curves of node at θ=0°, z=10m (t_f=t_c, cool roof)

8.4 Selection of suitable numerical parameters

In order to achieve consistent and reliable numerical output, the sensitivity of the predictions on some numerical parameters needs to be evaluated. In this section two important input parameters in using the Artificial Damping Method are investigated: the initial dissipated energy fraction and size of numerical stepping increment.

8.4.1 Initial value of dissipated energy fraction

According to the numerical mechanism of the ADM, a certain amount of (artificial) damping force is applied to the system to help the structure to pass through the local instabilities without being terminated due to convergence difficulties. The magnitude of the damping force hence influences the structural response. Ideally, the damping is best to be zero in the period when the structure is stable so that its perturbation to the structural behaviour is negligible. Then the damping force is expected to increase to an appropriate magnitude to achieve adequate numerical stability when buckling occurs. As introduced earlier, in Abaqus the initial damping factor is given by the input initial dissipated energy fraction while the value of the damping factor may be updated automatically according to the convergence condition and the input value of the initial dissipated energy fraction.

The effect of the input initial dissipated energy fraction on the tank behaviour is shown in Figure 8-9. A large artificial damping (e.g. input initial fraction of 0.0005) would lead to a large perturbation to the structural behaviour. With the input fraction decreased, the predictions appeared to converge to a stable value, except when a too small value (e.g. 0.00002) was input where the code failed to effectively update the damping factor to achieve static equilibrium. For the results presented in this chapter and Chapter 9, an input initial dissipated energy fraction of no larger than 5×10^{-5} was employed.

When using ADM, it has been argued by some researchers that the energy dissipation fraction should be limited to a relatively small value throughout the whole process so that the damping force can be deemed not too large to distort the

global structural behaviour (e.g., Simulia 2008; Kobayashi and Mihara 2009). It is important to clarify here that this statement is usually satisfied in problems where the instabilities are localised within small zone or secondary component of overall structure, or with relatively lower magnitude (e.g., surface wrinkling). However, for problems where instabilities occur in a relatively large component and particularly involving rigid body rotations (e.g., tank roof buckling studied here), it is not feasible to restrain the energy dissipation fraction from increasing to a rather high value in the post-buckling stage (e.g., ~8.5% in Figure 8-2). This is because the damping force applied to the buckled component (e.g., tank roof) has to be updated larger to keep the static equilibrium of the system.

Indeed for post-buckling problems where inertial effects are important, a full dynamic simulation with realistic damping treatment is desired, rather than a static simulation using the Riks method or the ADM. According to its algorithm (Section 8.2.2), an ADM simulation in some extent corresponds to a dynamic simulation with heavy damping such that dynamic motions of the instable components are fully damped and the deformation only develops in a static fashion. It is worth mentioning that some comparison studies have been conducted where ADM analysis, dynamic analysis and experimental measurements were compared. For example, Kobayashi and Mihara (2009) have provided a test study of the successive buckling behaviour of elastic cylindrical shells under axial compression. Their results demonstrated a good agreement between the ADM and dynamic explicit simulation and both methods matched well with the experimental data of Yamaki (1984).

It may be concluded that the ADM predictions are expected to be in close agreement with those of a full dynamic analysis if the artificial damping is small or the real damping is large. If the real damping is small but the applied artificial damping is large, the predicted post-buckling path may be distorted, and the degree of this distortion is related to the damping value: the larger the artificial damping the more the distortion. The post-buckling predictions obtained using the ADM need therefore be treated with caution especially when large artificial damping is involved. Due to the scope of this study, the verification of the ADM results for the oil tank thermal

buckling problem using dynamic study or experimental study has not been conducted, but it would be a worthwhile topic for future study.

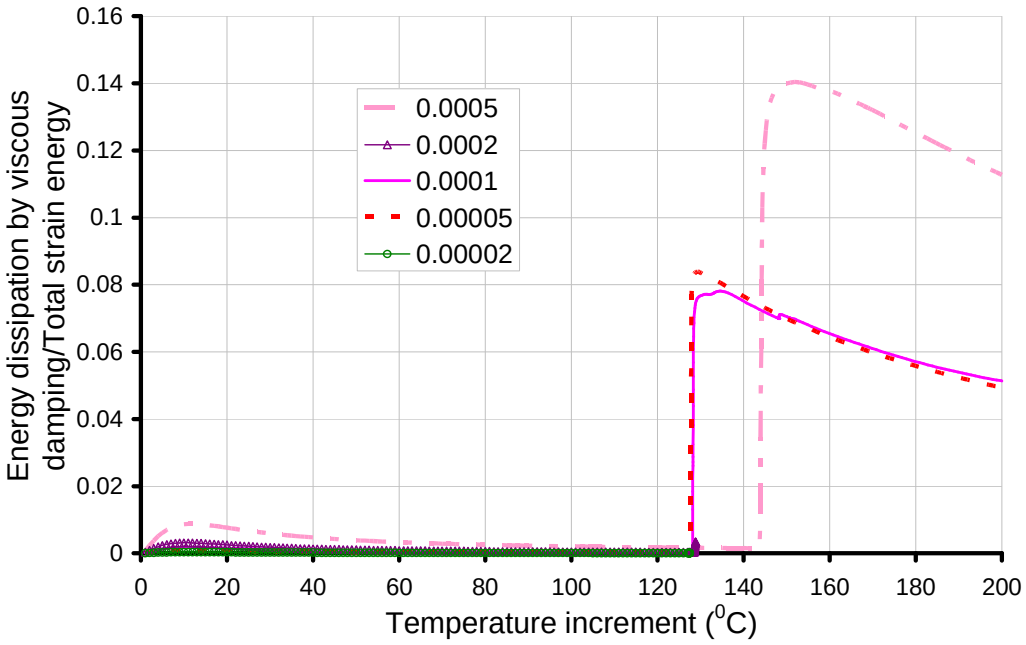

Figure 8-9 Evolution of energy dissipation fraction with different input initial values (t_f=2t_c, cool roof)

8.4.2 Loading increment

It has been well appreciated that the size of loading increment has a noticeable effect on the Riks predictions of buckling behaviour for some structures, particularly for those having a dense distribution of bifurcation points along the primary equilibrium path. If the increment is too large, the incremental loading process may miss some bifurcation points and continue on the primary equilibrium path that is no longer stable as the missed branch of buckling path is of lower potential energy. As a result, for nonlinear buckling modelling of such structures, the adopted time increment should be small enough to avoid missing the first bifurcation point which is actually the controlling point.

It is shown here that such sensitivity on increment size also exists in the simulation using the ADM. Figure 8-10 shows the evolution of energy dissipation fraction along with thermal loading process when using different temperature increment sizes. In this particular example, relatively large increment size tends to miss the earlier bifurcation points until the increment size equals to 1 degree. It is noted, the positions of bifurcation point can still be indicated by the occurrences of negative eigenvalues of the global stiffness matrix as that in the Riks analysis.

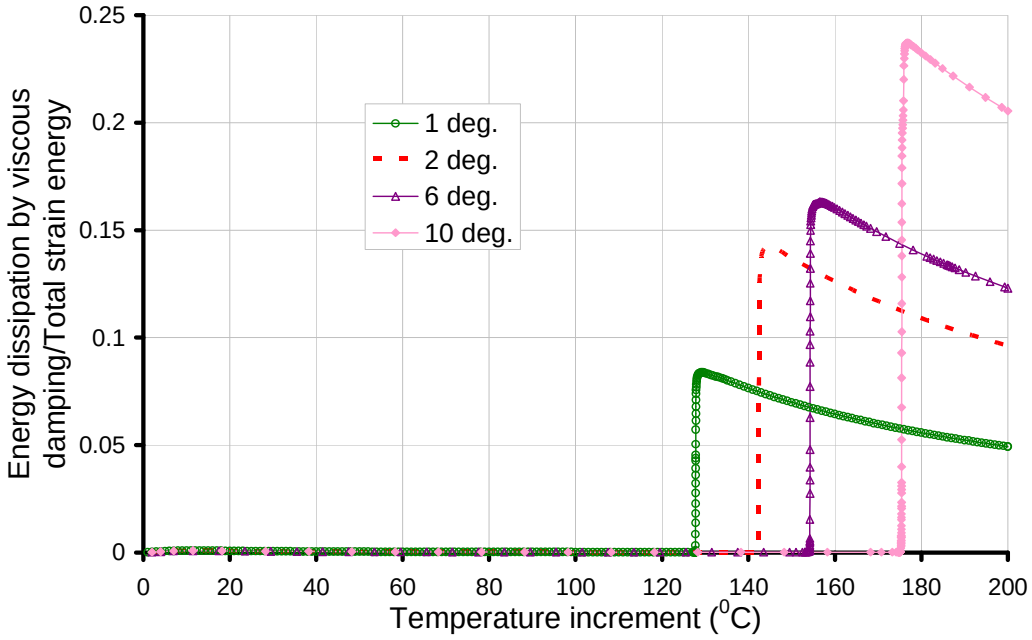

Figure 8-10 Effect of step size on the buckling temperature prediction (t_f=2t_c, cool roof)

8.5 Conclusions

This chapter has presented the prediction of thermal buckling behaviour of oil tanks using the Artificial Damping Method. Due to the limitations of the Riks method in dealing with buckling analysis under fire loading, the Artificial Damping Method is a superior method when the post-buckling behaviour is required to be accurately captured. The ADM was employed and tested against the results from Riks method.

The results show the predicted buckling temperature for the first buckling occurrence matches very well from both methods.

The buckling point in the ADM can be identified to be at the point when the value of the energy dissipation fraction suddenly jumps up to a large value in the energy dissipation fraction history curve.

Two important input parameters were shown to have significant influence on the accuracy of numerical output. The initial dissipated energy fraction needs to be chosen as a proper value. If it is too large, the result may be inaccurate; if it is too small then Abaqus would fail to continue. The loading increment is another key parameter which needs to be chosen carefully, as a large increment tends to miss earlier bifurcation points.

The empty tank with relatively stiff roof buckles at about 126°C when subjected to a smooth edge temperature pattern regardless of roof was heated or not. For the slender roof case, roof buckling mode was predicted at only around 40°C temperature rise and then followed by a tank wall buckling mode at around 300°C. The latter situation can only be predicted by using the ADM. Hence, when the post-buckling behaviour especially successive buckling events are interested, the ADM is more useful than the conventional Riks method.

Chapter 9

9. Buckling behaviour of tank structures under various thermal and geometrical parameters

9.1 Introduction

This chapter presents numerical examinations of tank behaviours under various fire scenarios. The temperature distributions predicted directly from numerical heat transfer analysis in Chapter 5 were adopted. Proposed algebraic models of temperature pattern from Chapter 6 were also tested.

This chapter is organised as follows. Firstly, the effects of material nonlinearity are investigated in Section 9.2. Two types of wall thickness treatment (i.e., uniform thickness and stepwise-varying thickness) are then tested in Section 9.3. In these two sections, the simplified algebraic models given in Section 6.5 were adopted, where an ambient temperature of 0°C was assumed. The sensitivity of the structural behaviour to heat transfer parameters is then studied in Section 9.4. The tank behaviours under various fire scenarios, particularly buckling temperature and failure

mode, are studied in Section 9.5. Also in this section, the tank behaviours predicted by using the proposed algebraic expression are compared with that by using direct heat transfer analysis predictions. Lastly, the effects of filling levels of the target tank are investigated in Section 9.6.

The numerical method adopted in this chapter is the Artificial Damping Method (ADM) that has been introduced and examined in Chapter 8. The simulations were carried out in Abaqus (Simulia 2008). Material plasticity was ignored in the simulations, except those in Section 9.2 where the effects of material plasticity are examined. The tank model was assumed to have dimensions the same as that in Chapter 7, which is 20m high and 20m in diameter with uniform wall thickness (t_c =0.01m) and roof thickness (t_f=2t_c), unless otherwise stated. The studied fire scenario in Section 9.4 to Section 9.6 is the same as the reference case studied in Chapter 5 Section 5.5.2 with a flame height of 20m for the fire column.

9.2 Effect of material nonlinearity - GMNA vs. GNA

Although for thin shell structures the elastic buckling load usually provides a rather accurate measure of the strength, effect of material plasticity should be evaluated. Due to the high local stresses near the boundary induced by large temperature gradient, plastic yielding could occur and affect both the pre-buckling and post-buckling behaviours. The geometric and material non-linear analysis (GMNA) was conducted to examine the influence of the plasticity on the tank buckling behaviour. The tank material plasticity was assumed to obey a von Mises yielding surface with no hardening (ie. elastic-perfectly plastic). As have been revealed in Chapter 7 using Riks method, material yielding may delay the onset of buckling. Same phenomenon has been obtained by using the Artificial Damping Method as shown in Figure 9-1 where the relation between the buckling temperature of a tank and the yielding stress of steel is displayed. As the material strength increases, the buckling temperature of the GMNA quickly approaches that of the pure elastic analysis (GNA). Interestingly, the GMNA predicted higher buckling temperature than that of the GNA, indicating that the material nonlinearity may improve the thermal stability of the tank in the

studied scenario. For a tank with a yielding stress less than $\sigma_y = 240$ MPa, no buckling behaviour was captured within the studied typical fire temperature range (0~1000°C).

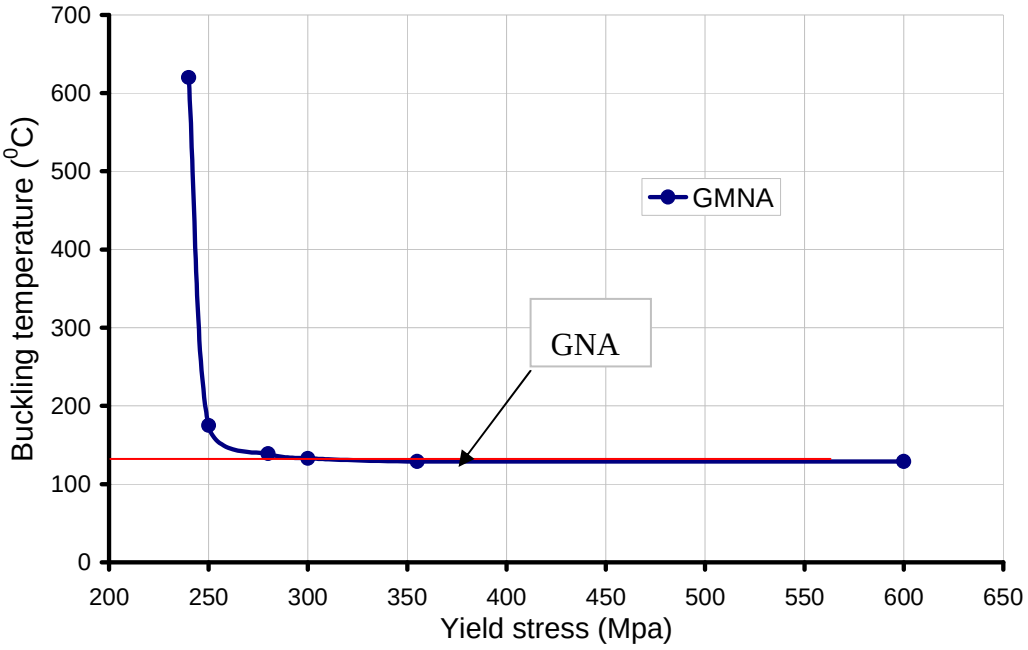

Figure 9-1 Effect of material nonlinearity on the tank buckling temperature

It is of interest to examine the history of dissipated viscous energy fraction along the heating process with different material strengths. Figure 9-2 shows that the overall value of dissipated viscous energy fraction actually decreases with the decrease of the yielding stress. As the magnitude of the artificial damping is dependent on the rate of the deformation (Eq. 8-1), a smaller damping corresponds to a smaller change of structural configuration during the buckling process. This phenomenon indicates that local movement of the wall in the buckled area can be reduced by the plastic strain, so that the artificial damping required to sustain the equilibrium of the system is less.

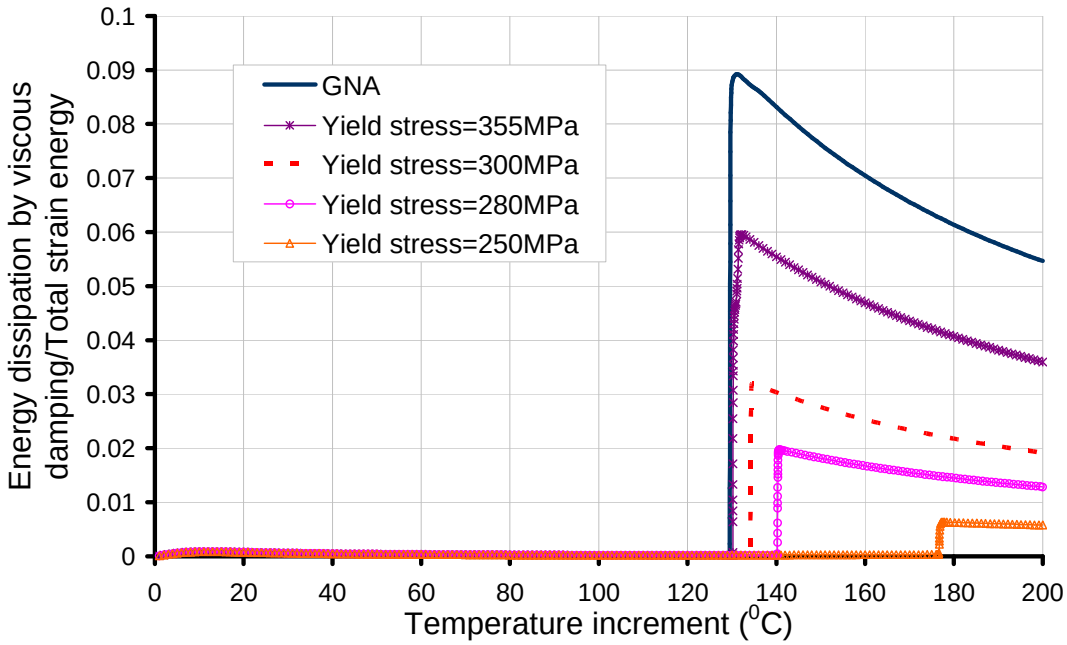

Figure 9-2 History of dissipated energy fractions of an GMNA analysis

The equivalent plastic strain contour at T=200°C for the case of $\sigma_y = 300$ MPa is shown in Figures 9-3. It can be seen that plastic strain localised in a circumferential strip just above the bottom edge that is also the lower border of the buckles.

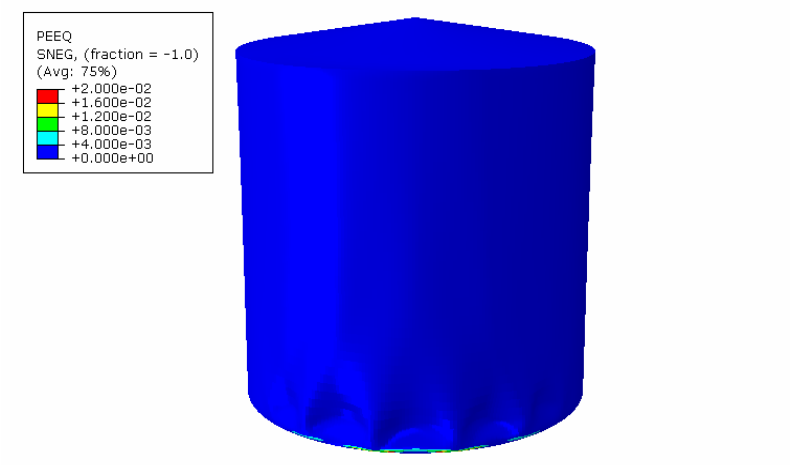

(a) Whole view

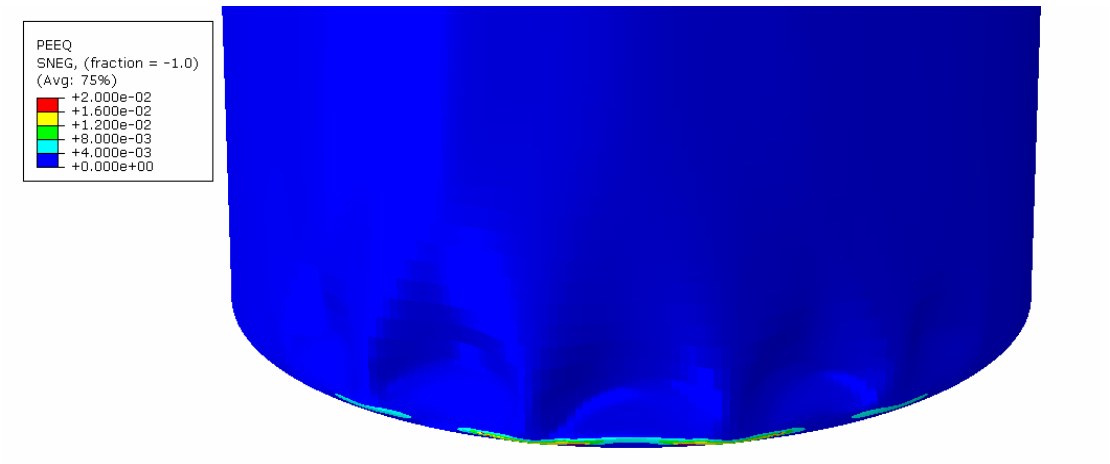

(b) Close-up look near the boundary

Figure 9-3 The equivalent plastic strain contour at *T*=200°C from a GMNA analysis ($\sigma_y = 300$ MPa)

9.3 Effect of wall thickness – uniform vs. stepped thickness

Uniform wall thickness was assumed in all the previous simulations in this thesis. However, in real tank designs the wall is often constructed with a stepped thickness. The differences in the resulted tank behaviours between these two designs were therefore investigated.

A chart of recommended wall thickness for different tank dimensions has been provided in Table A-2a of API 650 (2007). According to this table, the dimensions of the example tank were chosen to be 17.8m high and 18m in diameter. The values of the wall thickness for the stepped wall case were also chosen from the same source, which are repeated in Figure 9-4. For the uniform wall thickness case, 9mm was adopted. A 9mm thickness was adopted for the roof in both cases.

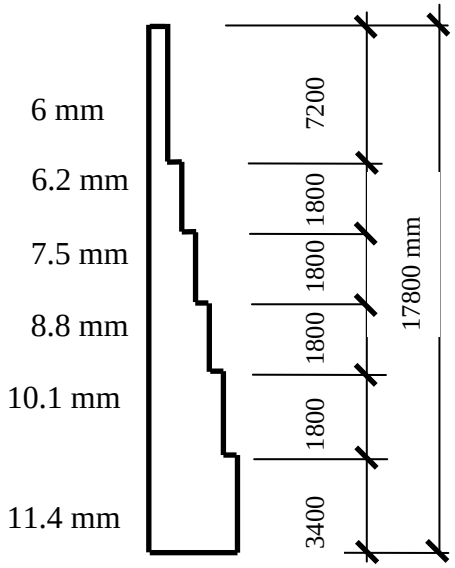

Figure 9-4 Stepped wall profile

The predicted dissipated energy fraction curves and temperature-displacement curves of these two cases are compared in Figure 9-5 and Figure 9-6 respectively. The deformation modes at some critical stages are compared in Figure 9-7. It can be seen that buckling occurs slightly earlier in the tank with a stepped wall design (T=48°C) than that with a uniform wall design (T=51°C). In both cases, roof buckling occurred at a very early stage and is followed by wall buckling. In both cases, buckling modes of the roof started with one big buckle that later evolved into three buckles during the successive buckling process. However, the positions of the buckles in the tank wall are different. In the stepped wall, serious buckling occurred in the upper part of the tank where the wall thickness is thinner, while no buckling can be observed near the bottom boundary. By contrast, in the uniform wall, buckling started near the bottom boundary and then spread to a larger area.

For convenience, uniform wall was taken as a reference case and adopted in all the rest of the simulations.

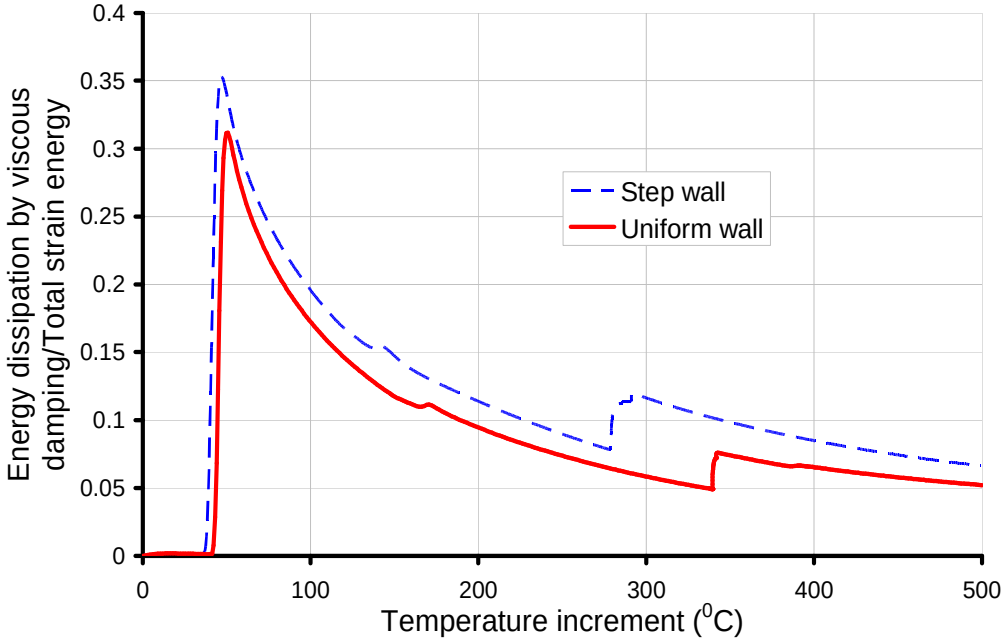

Figure 9-5 History of dissipated energy fractions (uniform wall vs. stepped wall)

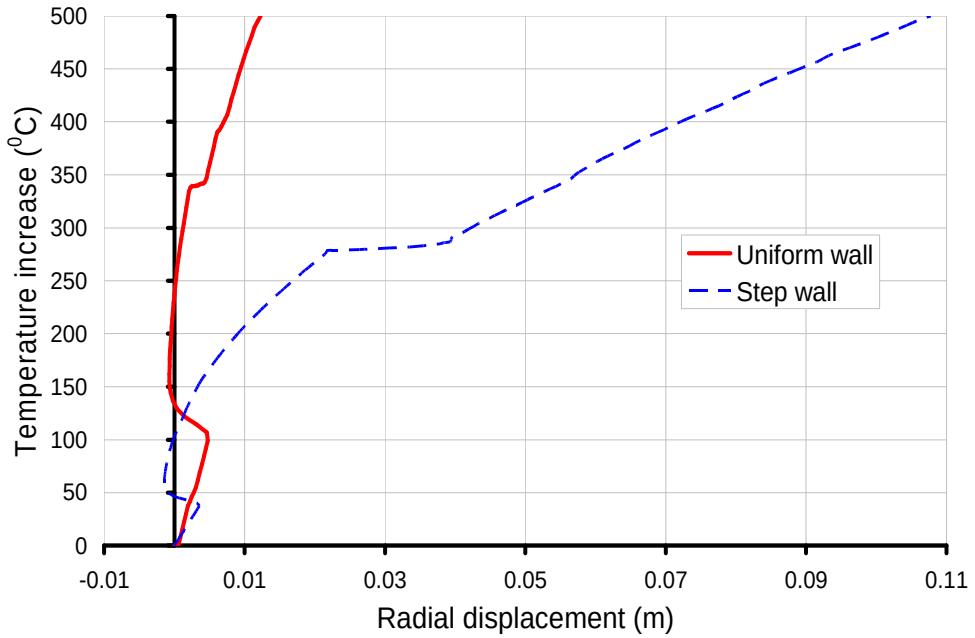

(a) Radial displacement-temperature curve

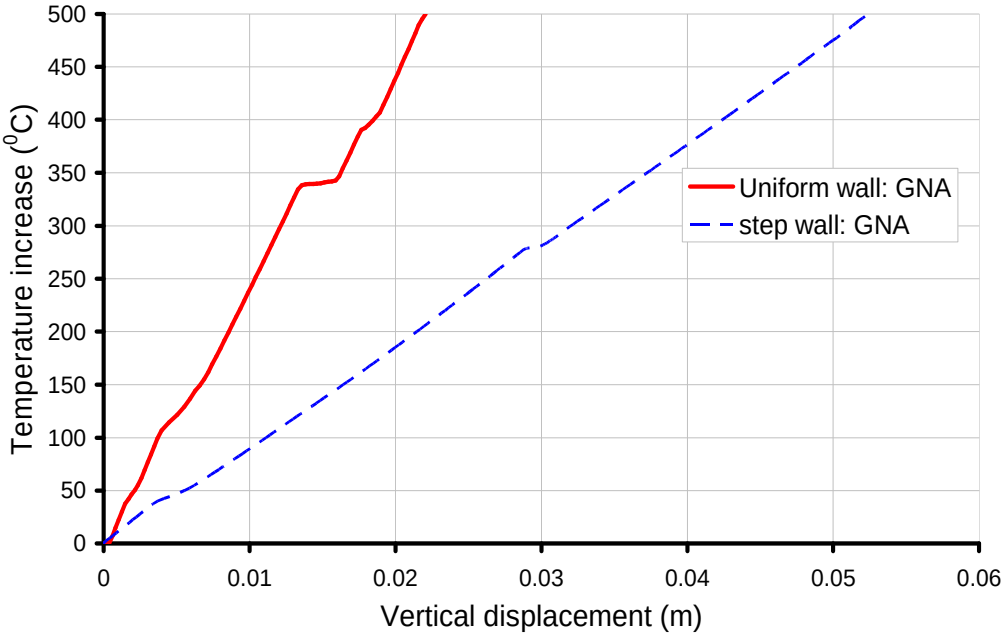

(b) Vertical displacement-temperature curve

Figure 9-6 Temperature rise - displacement curve of the node at θ=0°, z=9m (uniform wall vs. stepped wall)

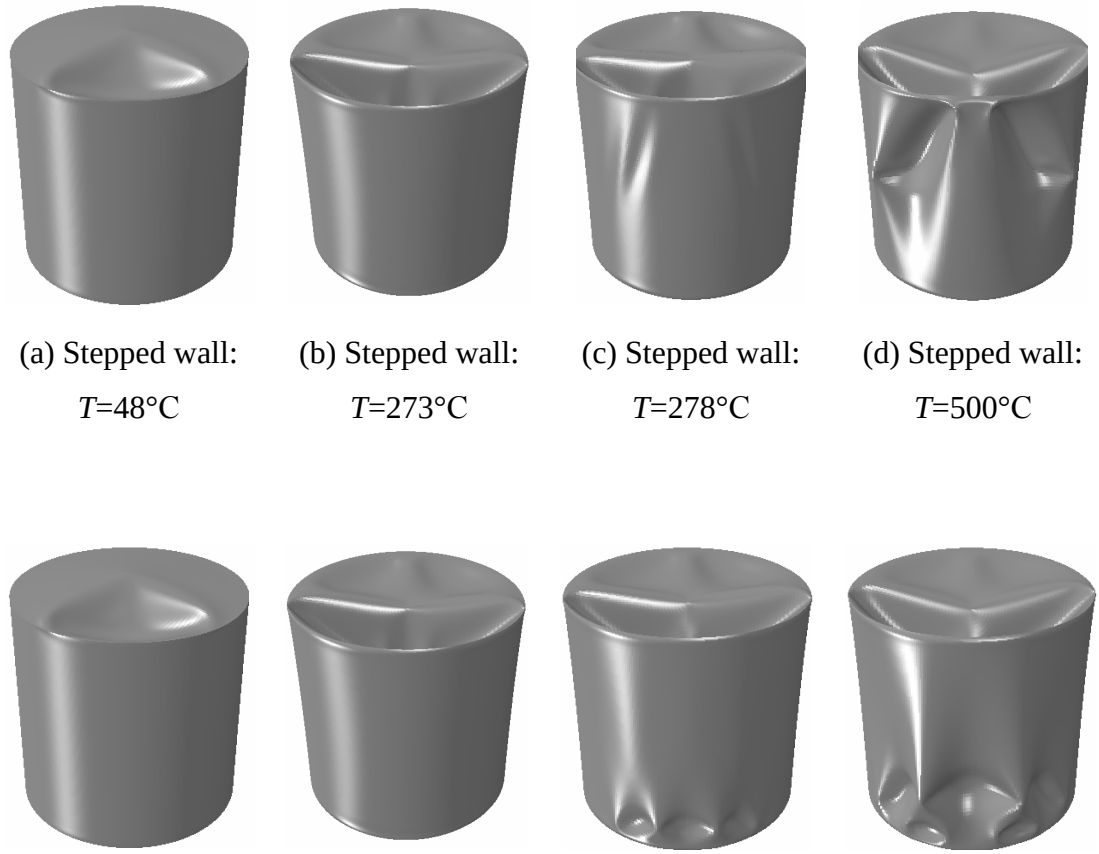

(a) Stepped wall: T=48°C (b) Stepped wall: T=273°C (c) Stepped wall: T=278°C (d) Stepped wall: T=500°C

(e) Uniform wall: T=51°C (f) Uniform wall: T=339°C (g) Uniform wall: T=344°C (h) Uniform wall: T=500°C

Figure 9-7 Deformations in an empty tank (uniform wall thickness vs. stepped wall thickness; deformation scale factor =5)

(a) A tank in Buncefield during the fire

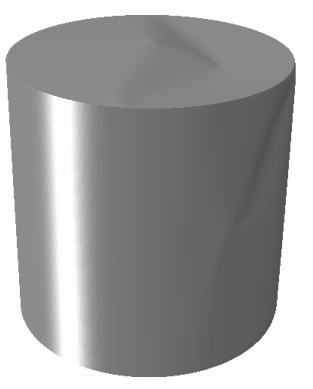

(b) Side view of the tank in Figure 9-7 d; deformation not being scaled

Figure 9-8 Comparison of tank deformation modes (Buncefield accident vs. numerical prediction)

It is interesting to have a qualitative comparison of the buckling modes between the above numerical model (Figure 9-8b) and the tank in Buncefiled accident (Figure 9-8a). Although the geometry and material properties of the two tanks are different, the failure modes show similar salient characteristics. The roofs of both tanks have buckled under fire heating. The tank wall facing the fire has buckles but the back side of the tank is intact in both cases. This illustrates thermal buckling due to heating from adjacent fires could be another reason of causing the tank failure in the Buncefiled accident.

9.4 Sensitivity study of heat transfer parameters

Some important parameters used in the heat transfer analysis on the predicted temperature in the tank have been examined in Chapter 5 Section 5.5.3. Two heat transfer parameters were shown to significantly affect the final temperature distribution pattern, which are surface emissivity and convective heat transfer coefficient of liquid. In addition, varying flame height of the fire can also significantly alter the vertical temperature distribution, as illustrated in Section 5.5.2.

Therefore, this section conducts structural analyses to evaluate the effect of these parameters on the buckling behaviour of the tanks.

9.4.1 Flame height

Figure 9-9 shows variation of buckling temperature when the flame height was varied from 10m to 40m. Intuitively, higher flame height provides larger radiation so likely lead to a lower buckling temperature. However, Figure 9-9 shows an opposite trend: the tank tends to buckle earlier under fire with shorter flame rather than that with taller flame.

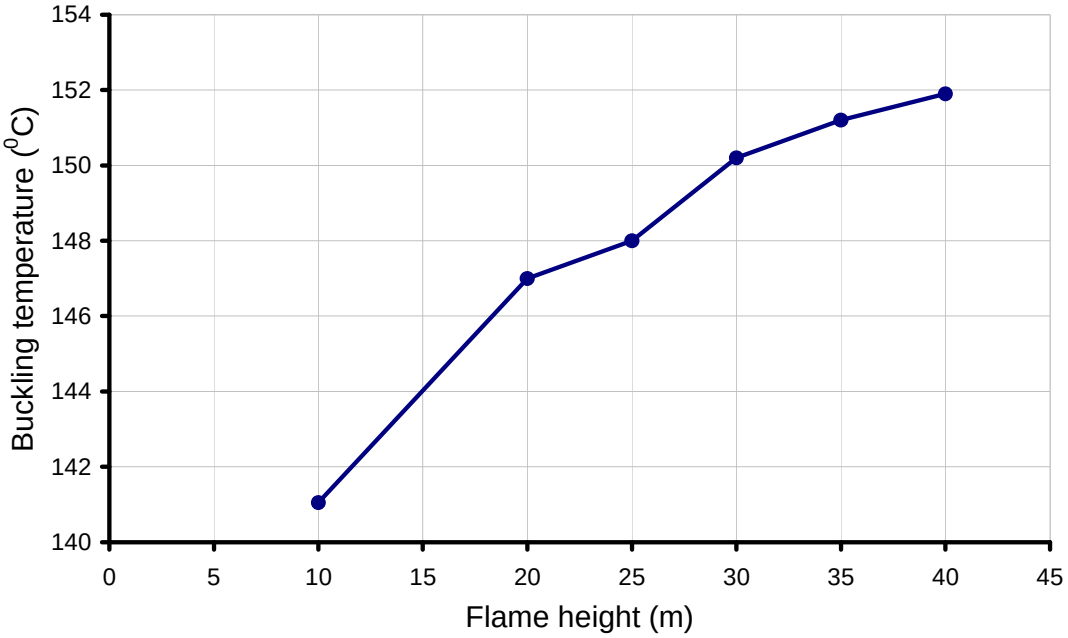

Figure 9-9 Effect of flame height on the buckling temperature of an empty tank; D=D_f=20m, d=6.67m, H_{f0}=0m

This counter-intuitive observation can be explained by examining the thermal strains developed in the tank under such fire loadings. When a tank is heated from one side, the heated part expands under the restraint from the cold part. If the flame height is low, the temperature of the roof keeps cool (Figure 9-10 a), thus the heated part gets restraint not only from the back of the tank but also from the cold roof. Consequently, larger axial compressive stress is resulted on the hot part (Figure 9-

11). By contrast, if the flame height is high, although the maximum temperature developed in the tank is higher, the roof would also have been heavily heated (Figure 9-10 b) thus the restraint it exerts to wall is significantly reduced. This results in a reduced compressive stress in the heated part and higher buckling temperature.

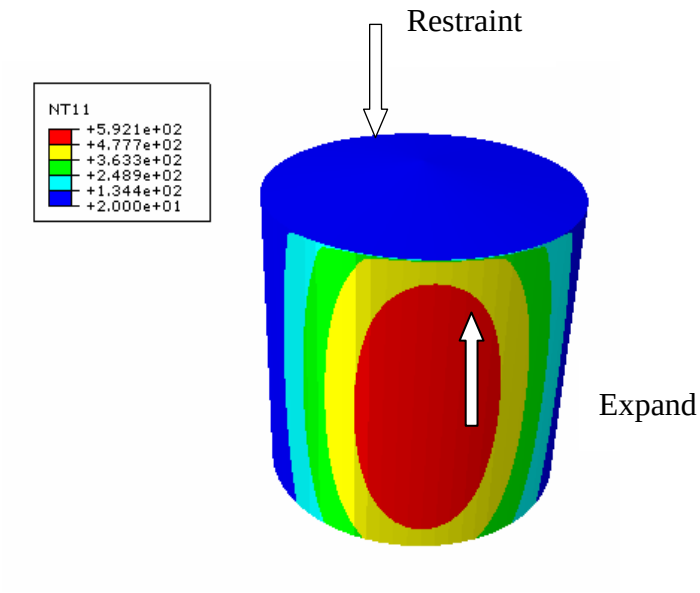

(a) Flame height H_f=20m

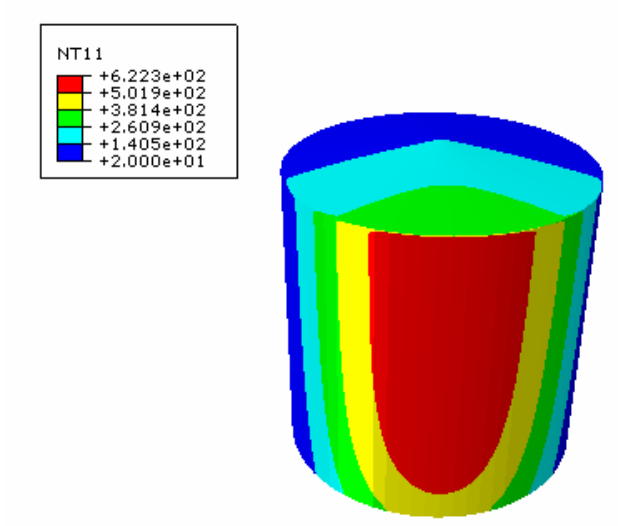

(b) Flame height H_f=40m

Figure 9-10 Temperature distribution contours in an empty tank exposed to an adjacent tank fire arising from ground level; D=D_f=20m, d=6.67m, H_{f0}=0m

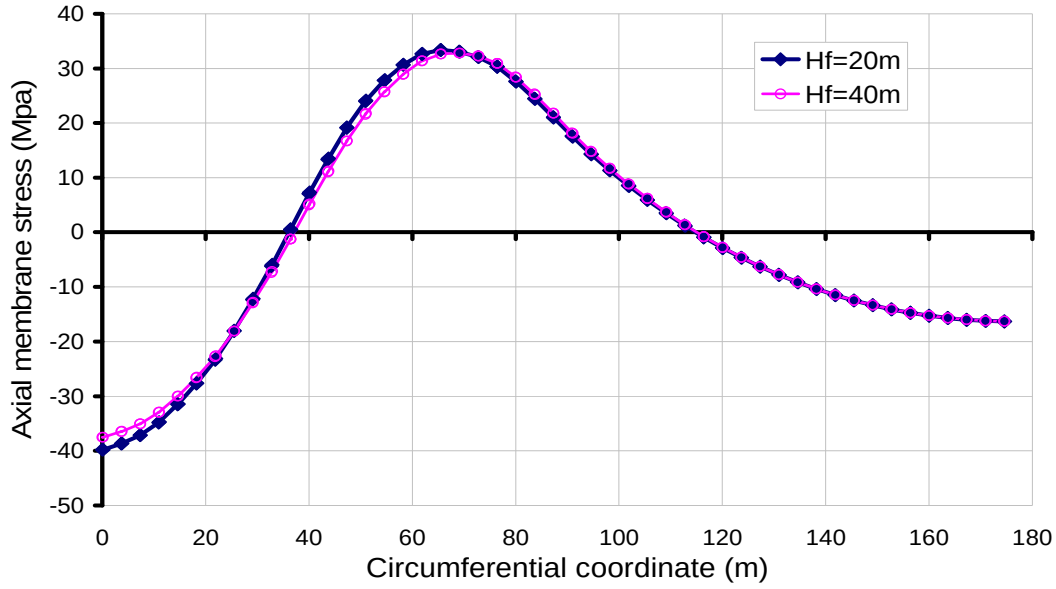

Figure 9-11 Axial membrane stress distribution around circumference at mid-height of the tank (T=100°C); D=D_f=20m, d=6.67m, H_{f0}=0m

9.4.2 Emissivity of the tank surface

The emissivity of a material is the relative ability of its surface to emit energy by radiation. Effect of surface emissivity on temperature distribution in tanks has been shown in Chapter 5 Figures 5-27&28. Surface with larger values of emissivity tends to develop higher temperature. However, the predicted buckling temperature is shown to increase with increasing of emissivity (Figure 9-12). This is mainly due to a less intensive temperature gradient around circumference resulted from higher values of emissivity (Figure 5-27).

Omitting the inner surface radiation in the analysis is shown having no effect on the prediction of buckling temperature for tanks constructed with surfaces of small values of emissivity; while for tank surface with lager values of emissivity, ignoring the inner surface radiation may produce lower buckling temperature but the variation is not very pronounced.

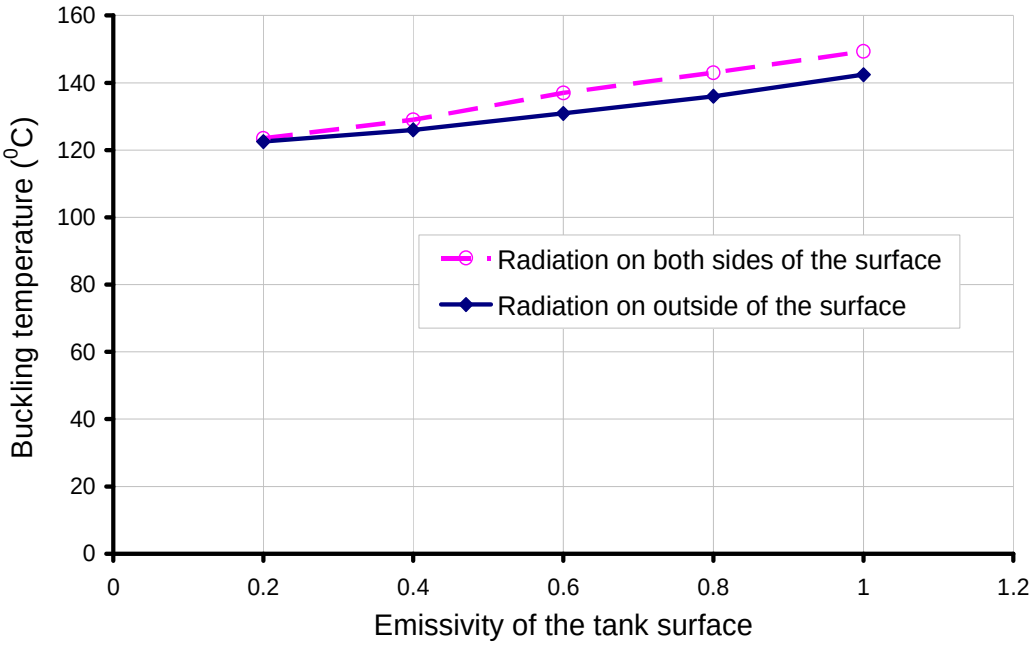

Figure 9-12 Effect of surface emissivity on the buckling temperature (empty tank); D=D_f=20m, d=6.67m, H_f=20m, H_{f0}=0m

The deformation of the tank predicted in the final stage (after reached steady state) for tanks with emissivity of 0.2 and 1 are shown in Figure 9-13. The deformation of the tank concentrated in a narrower region for surface with lower emissivity (Figures 9-13 a&c) than that with higher emissivity (Figure 9-13 b&d). This reflects the development of a more intensive temperature gradient around circumference with lower emissivity. Whether taking account inner surface radiations into the analysis did not make noticeable difference on predicted buckling modes.

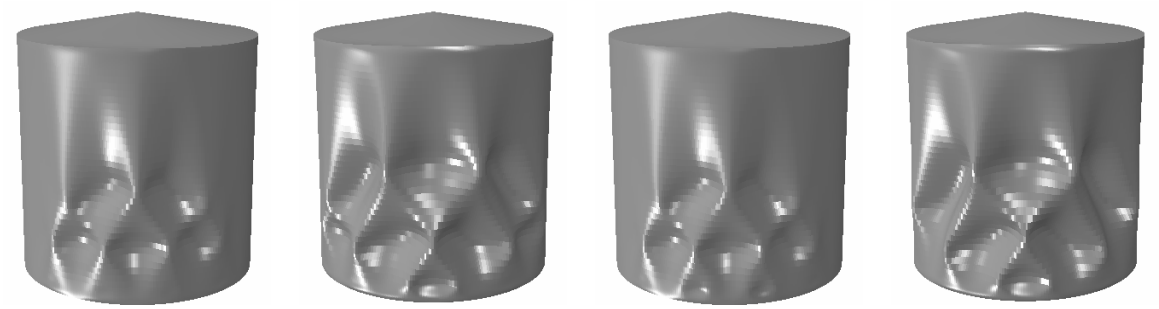

(a) ε_{out}=0.2; ε_{in}=0.2 (b) ε_{out}=1; ε_{in}=0=1 (c) ε_{out}=0.2; ε_{in}=0 (d) ε_{out}=1; ε_{in}=0

Figure 9-13 Steady state deformations in an empty tank with various values of surface emissivity (deformation scale factor =5); D=D_f=20m, d=6.67m, H_f=20m, H_{f0}=0m

9.4.3 Convective heat transfer coefficient of liquid h_{liq}

The value of convective heat transfer coefficient h_{liq} depends on the type of fluid and their properties, and varies in a range of 50 to 1000. Liquid with larger value of heat transfer coefficient cools the tank surface better and the tank therefore can resist buckling in a larger chance (Figure 9-14). This indicates that the assumption made in Chapter 7 by treating the temperature of the tank wall in contact with liquid as ambient temperature would overestimate the buckling temperature, especially when the liquid is with small value of heat transfer coefficient.

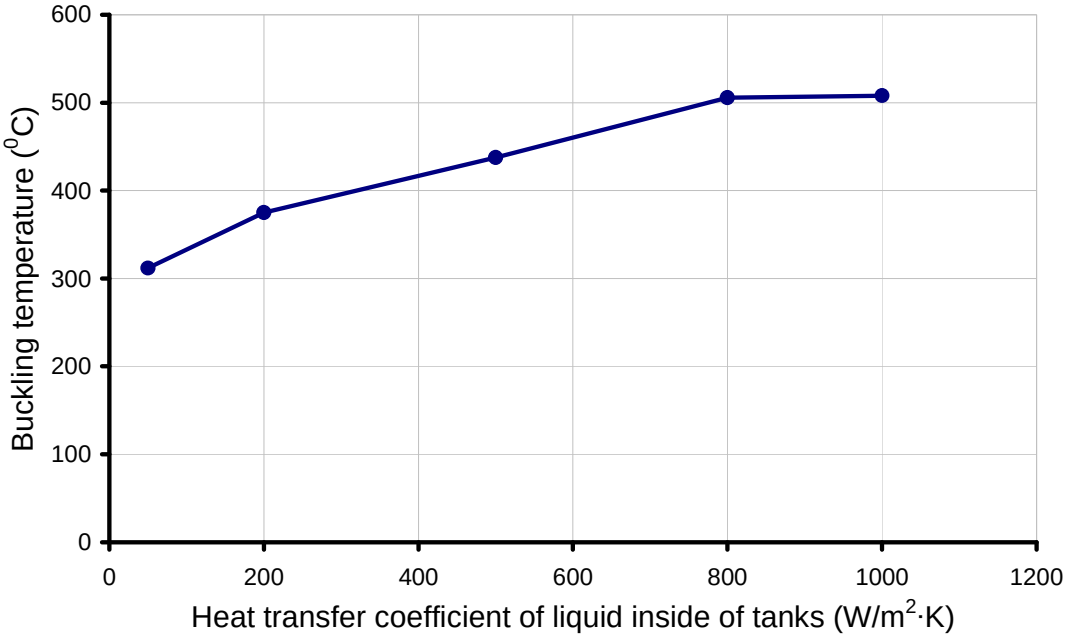

Figure 9-14 The effect of heat transfer coefficient of the liquid inside of the tank on the buckling temperature; $D=D_f$=20m, d=6.67m, H_f=20m, H_{f0}=0m

9.5 Buckling behaviours under various fire scenarios

One objective of this section is to investigate the buckling behaviour of a tank under various fire scenarios. The dimensions of the tank and fire are chosen as the same as in the reference case studied in Chapter 5 Section 5.5.2. Flame height was chosen to be the same as that of the tank (H_f=20m). Two magnitudes of roof stiffness were investigated which were $t_f=2t_c$ and $t_f=t_c$. The other objective of this section is to compare the predicted structural behaviours under the proposed algebraic temperature model from Chapter 6 Section 6.2 with that under the temperature distribution obtained directly from numerical heat transfer analysis.

9.5.1 Effect of vertical fire location

The effect of vertical fire locations in the burning tank on the buckling temperature is shown in Figure 9-15, where the studied vertical location of the base of fire ranges from the ground level to the roof level. Figure 9-15 illustrates that the buckling

temperature increased with rise of vertical fire location under both temperature distributions (i.e., from heat transfer analysis prediction and from proposed algebraic model). The proposed temperature model is shown to be able to provide accurate predictions for fires rising near the ground level but underestimates the buckling temperature for fires starting from higher level. The discrepancy is due to the assumption made in the proposed temperature model that the heating range is constant through the full tank height. In fact, as studied in Chapter 5 Section 5.5.5, the circumferential temperature distribution varies significantly when fire starts at a high level above ground, therefore the discrepancy of the predicted buckling temperature is more pronounced under those conditions.

The effect of vertical fire location can be seen similar to that of flame height discussed in Section 9.4.1. Figure 9-16 shows the temperature contour of an empty tank under an adjacent fire starting from roof level. Smaller temperature gradient was induced near the roof edge in this case, compared to that in lower fire location cases. As the heated part of the tank wall would receive less restraint from the cold part, it could expand more freely, which therefore leads to a higher buckling temperature.

It is interesting to note that no buckling was captured if the fire starts above 0.6 times of tank height under temperature pattern directly obtained from heat transfer analysis (Figure 9-15).

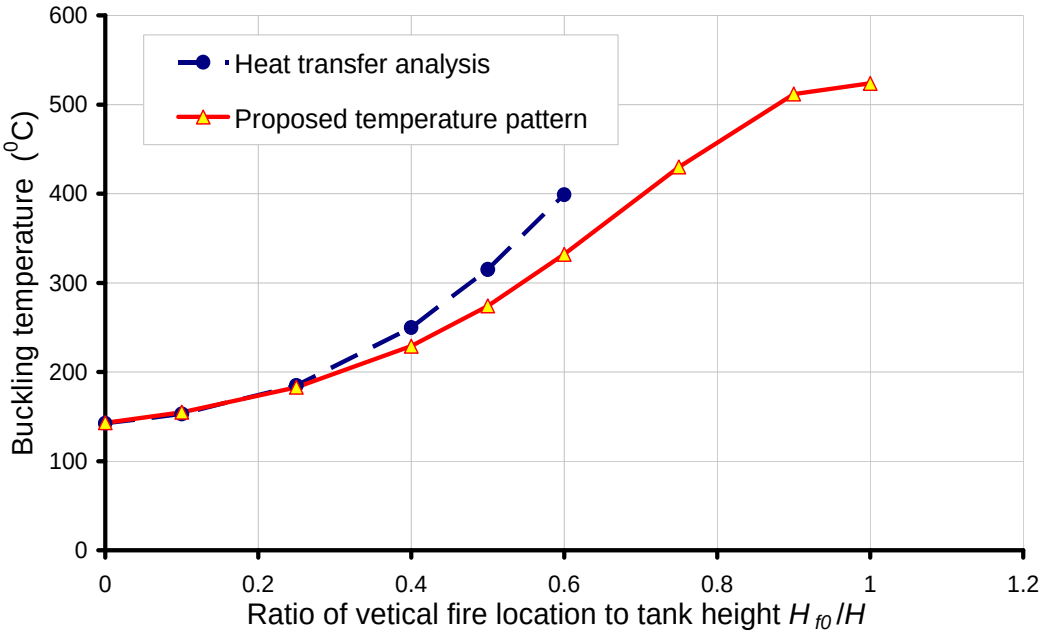

Figure 9-15 Buckling temperature of an empty tank exposed to adjacent tank fire starting from various vertical locations (t_f=2t_c); D=D_f=20m, d=6.67m, H_f=20m

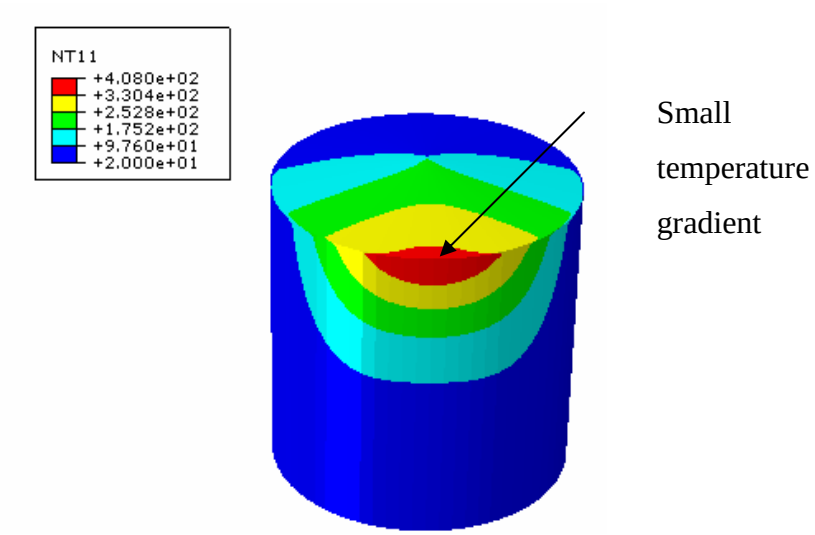

Figure 9-16 Temperature contour in an empty tank exposed to adjacent tank fire starting from roof level; D=D_f=20m, d=6.67m, H_f=20m

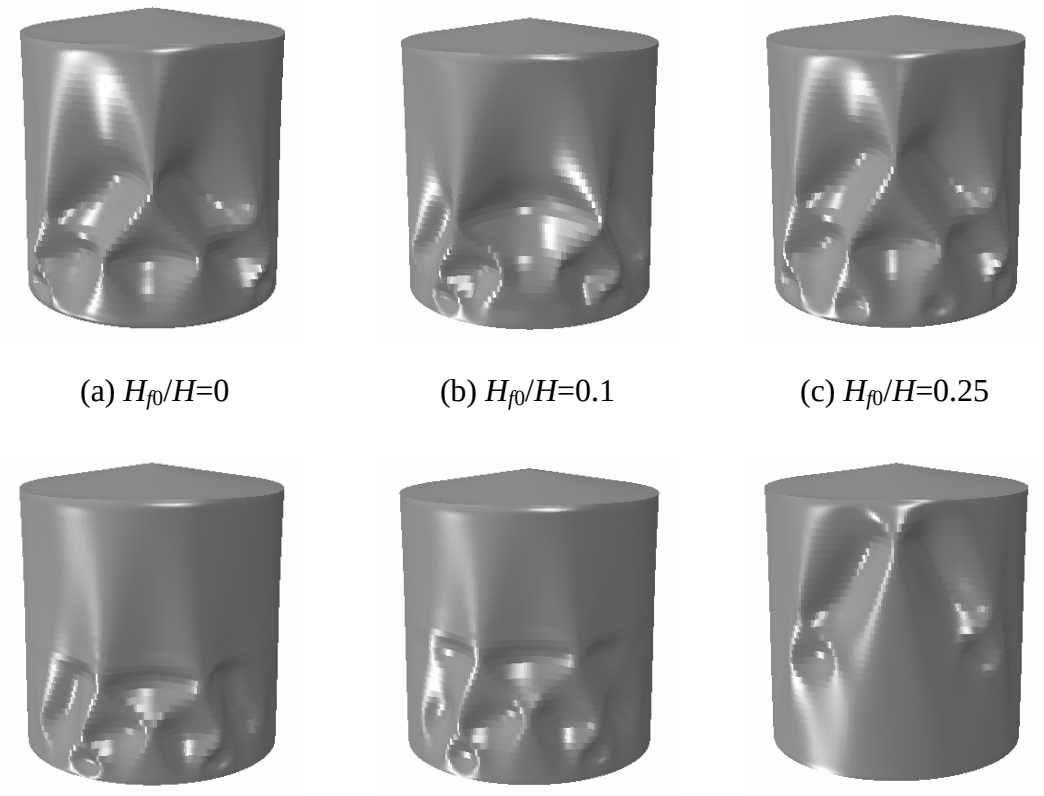

(a) H_{f0}/H=0 (b) H_{f0}/H=0.1 (c) H_{f0}/H=0.25

(d) H_{f0}/H=0.4 (e) H_{f0}/H=0.5 (f) H_{f0}/H=0.6

Figure 9-17 Steady state deformations in an empty tank under an adjacent fire starting from various vertical locations (t_f=2t_c); deformation scale =5; D=D_f=20m, d=6.67m, H_f=20m

The predicted tank deformations under different fire vertical locations are shown in Figure 9-17. Buckles are shown to almost spread over the entire heated side of tank wall, except when fire started from very high level where buckling concentrated on the upper part of the tank.

The results of thin roof case (t_f=t_c) are shown in Figures 9-18&19. Similar to the case of t_f=2t_c, buckling temperature is shown to increase with the rise of fire vertical location. The roof may easily to buckle at very low temperature. Tank wall buckling occurred later than roof buckling. When the base of fire is above 0.4 times of the tank height from the ground, no tank wall buckling was predicted. By comparing Figure 9-15 and Figure 9-18, it can be seen that the buckling of the tank wall is

significantly postponed in a slender-roof condition (t_f=t_c), and this effect was more pronounced under fires starting from a higher vertical location.

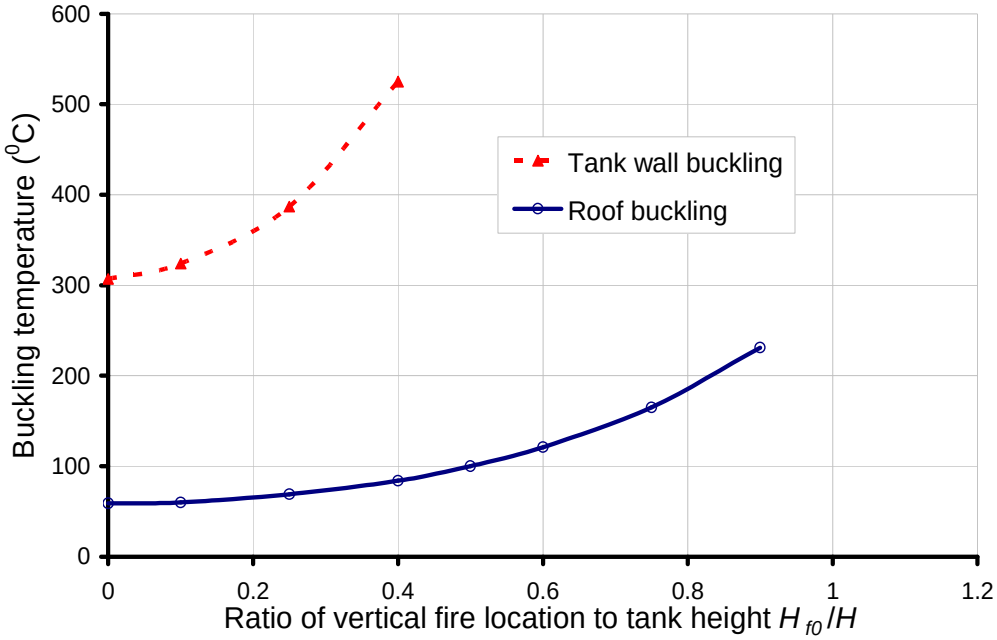

Figure 9-18 Buckling temperature of an empty tank exposed to an adjacent fire starting from different vertical locations (t_f=t_c); D=D_f=20m, d=6.67m, H_f=20m

The predicted tank deformations under fire starting from different vertical levels are compared in Figure 9-19. Roof buckling always occurred and showed three apparent buckles, irrespective of the fire's vertical starting level. In cases involving wall buckling, buckles are seen to spread to a rather large portion of the front face.

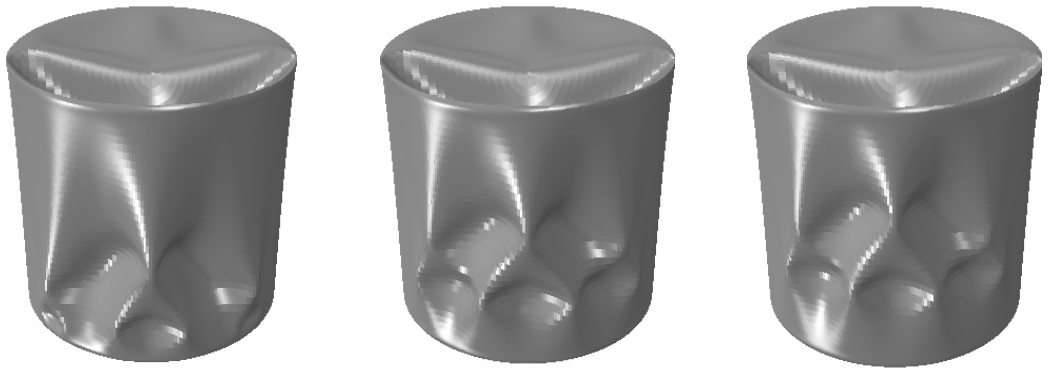

(a) H_{f0}/H=0 (b) H_{f0}/H=0.1 (c) H_{f0}/H=0.25

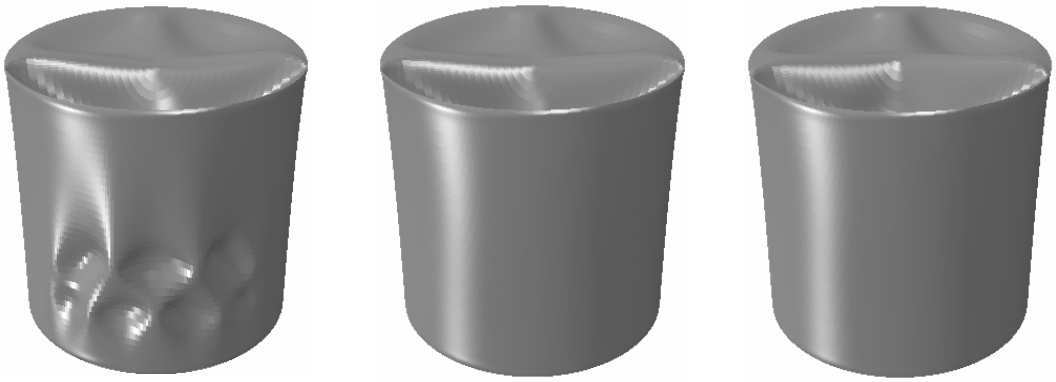

(d) H_{f0}/H=0.4 (e) H_{f0}/H=0.5 (f) H_{f0}/H=0.6

Figure 9-19 Steady state deformations of an empty tank under an adjacent fire starting from various vertical locations (t_f=t_c); deformation scale factor=5; D=D_f=20m, d=6.67m, H_f=20m

9.5.2 Effect of horizontal fire distance

The effect of horizontal distance between the tank and the fire column was investigated by placing the fire away from the tank in a range from 3m to 30m. The tank-fire distance referred here is the clear separation between the tank wall and the fire periphery. It can be seen from Figure 9-20 that the buckling temperature of the tank with roof thickness t_f=2t_c is not very sensitive to the horizontal location of the fire as that to the vertical fire location. It has been shown in Chapter 5 Section 5.5.6 that varying the tank-fire distance effectively changes the maximum temperature induced in the target tank, but does not alter much the temperature distribution

pattern. As the required temperature for inducing an empty tank to buckle is rather low, it can be easily achieved at any tank-fire distance. As a result, the predicted buckling temperature does not show much sensitivity to the horizontal fire location.

Figure 9-20 also compares the results using temperature distribution obtained from heat transfer analysis and the proposed temperature model. Though both curves are rather flat, one shows an ascending trend while the other shows a descending trend. When the fire is placed farther from the tank, the temperature gradient around the circumference of the tank would become less significant (Figure 5-41a), and therefore the tank tends to buckle at a higher buckling temperature; but the temperature distribution along vertical coordinate is getting more uniform (Figure 5-41c) which will result in a lower buckling temperature. The predicted variation of buckling temperature with change of tank-fire distance shown in Figure 9-20 demonstrates that the change of temperature pattern around circumference plays a dominative role in determining the buckling temperature of the whole structure. However, in the proposed temperature model, the heating range through the full tank height was fixed to one value. Thus, the vertical temperature variation dominates the prediction, and gives a wrong trend of variation of buckling temperature with change of tank-fire distance. The treatment of heating range up the vertical coordinate of the tank in the temperature model needs to be improved in the future.

The predicted buckling modes are similar in all the simulations and are shown in Figure 9-21a.

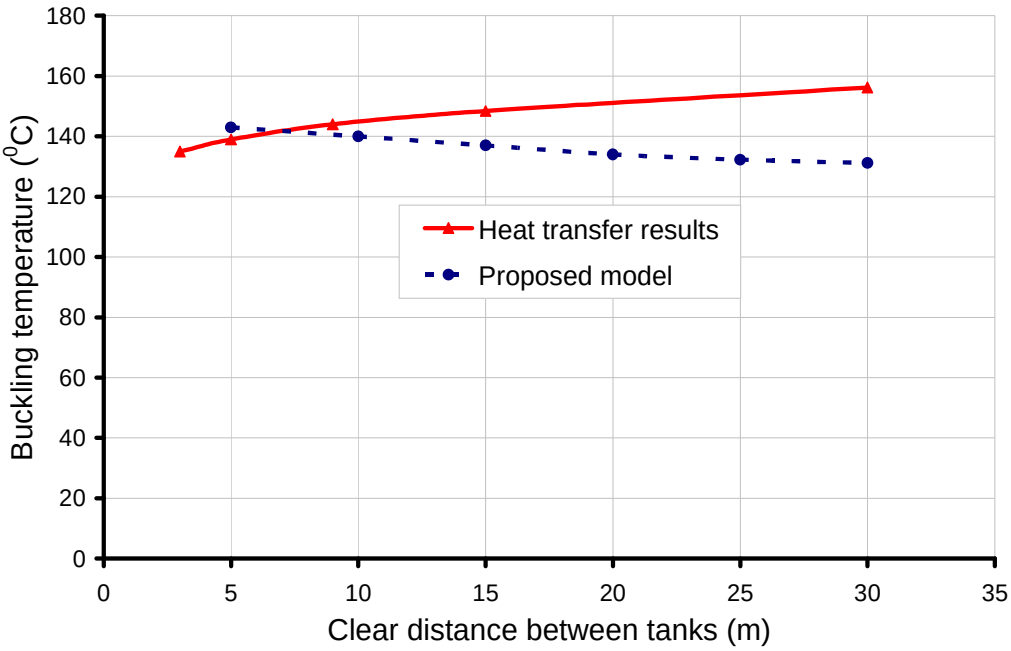

Figure 9-20 Buckling temperature of an empty tank under various tank-fire distances (t_f=2t_c); D=D_f=20m, H_f=20m, H_{f0}=0m

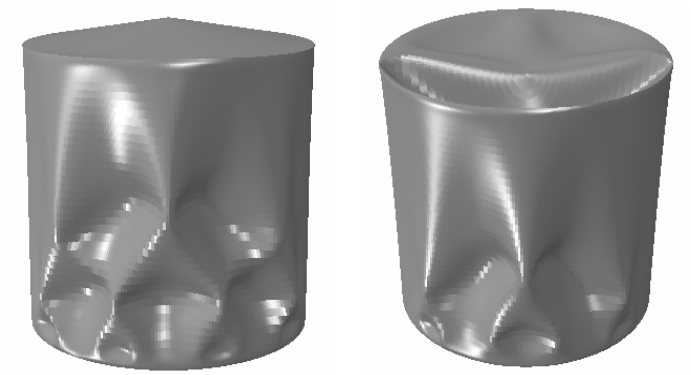

t_f=2t_c t_f=t_c

Figure 9-21 Steady state deformations of an empty tank under an adjacent fire; deformations are the same for various tank-fire distances; deformation scale factor =5; D=D_f=20m, d=6.67m, H_f=20m, H_{f0}=0m

The effect of tank-fire distance on the buckling temperature of a slender-roof tank is shown in Figure 9-22. The buckling temperature of the tank wall is shown to increase with the increase of the tank-fire distance, while the buckling temperature of roof is

shown not sensitive to tank-fire distance at all. The same tank wall buckling trend was predicted in the case with a roof thickness of $t_f=2t_c$. The typical buckling mode is shown in Figure 9-21b.

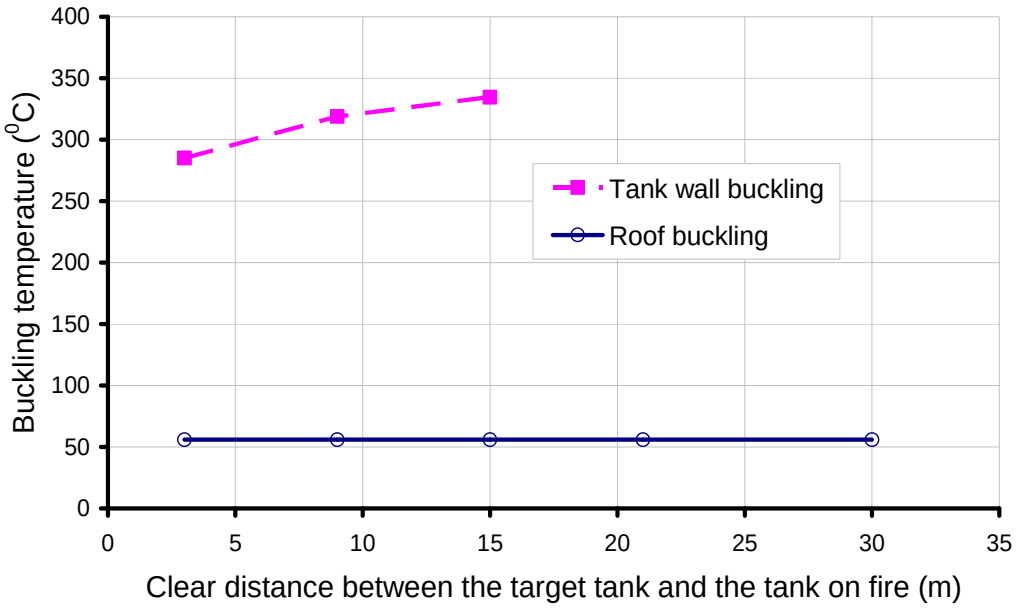

Figure 9-22 Buckling temperature of an empty tank under various tank-fire distances ($t_f=t_c$); $D=D_f$=20m, H_f=20m, H_{f0}=0m

9.5.3 Effect of fire diameter

The effect of fire scale was investigated by changing the fire diameter from 0.5 to 5 times of the target tank diameter. The spacing between the fire and the target tank was fixed as that of the reference case in Section 5.5.2. The results show that fire diameter has a significant influence on the value of buckling temperature (Figure 9-23). A tank tends to buckle earlier when exposed to a fire with smaller diameter. Changing fire diameters mainly influences the circumferential heating range (see Chapter 5). The effect of the heating range on the predicted buckling temperature has been discussed in Chapter 7 Section 7.4.4.

The proposed temperature model is shown to be able to accurately predict the buckling temperature for all studied fire diameters (Figure 9-23). The small

discrepancy in the predicted results from the two temperature distributions is believed due to the simplification of the heating range made in the proposed temperature distribution function.

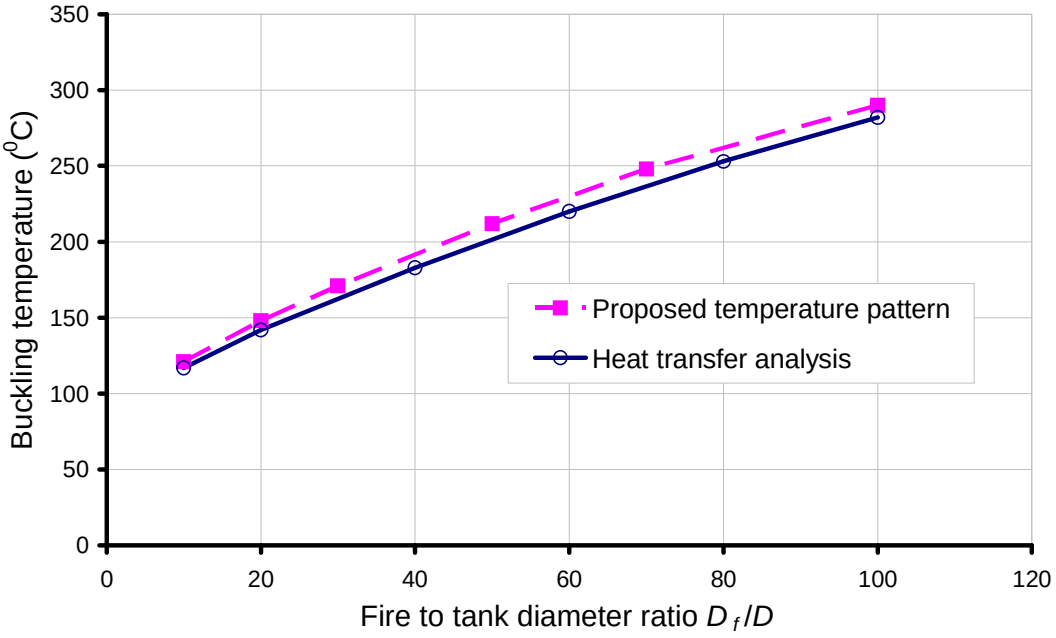

Figure 9-23 Buckling temperature of an empty tank under an adjacent fire with various fire diameters (t_f=2t_c); D=20m, d=6.67m, H_f=20m, H_{f0}=0m

The predicted buckling modes of the tank under a fire with a diameter of 0.5, 2.5 and 5 times of its own diameter are compared in Figure 9-24. The buckles tended to spread in a slightly wider circumferential range under fires with larger diameter. Furthermore, the numbers of buckle developed in the tank at the final stage are lesser under fires with larger diameter.

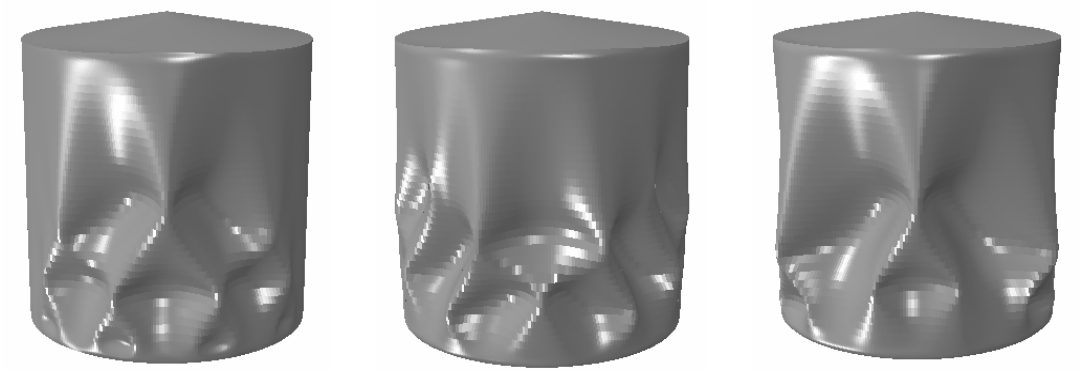

(a) D_f/D=0.5 (b) D_f/D=2.5 (c) D_f/D=5

Figure 9-24 Steady state deformations in an empty tank under fires with various diameters (t_f=2t_c); deformation scale factor =5; D=20m, d=6.67m, H_f=20m, H_{f0}=0m

The results of the slender-roof case (t_f=t_c) are shown in Figures 9-25&26. Similar as in the stiff-roof case (t_f=2t_c), the bucking temperature is shown to rise with the increase of the fire diameter. The developed temperature distribution around the tank circumference was more uniform when the fire diameter was larger. Roof buckling was predicted with all fire diameters, while wall buckling was only found with large fire diameters. The influence of the fire diameter on the buckling temperature was much weaker for the roof than the wall (Figure 9-25). Deformation shape of the roof is shown not to change with the change of fire diameters. The tank wall is shown to deform in a wider area under larger fire diameters (Figure 9-26).

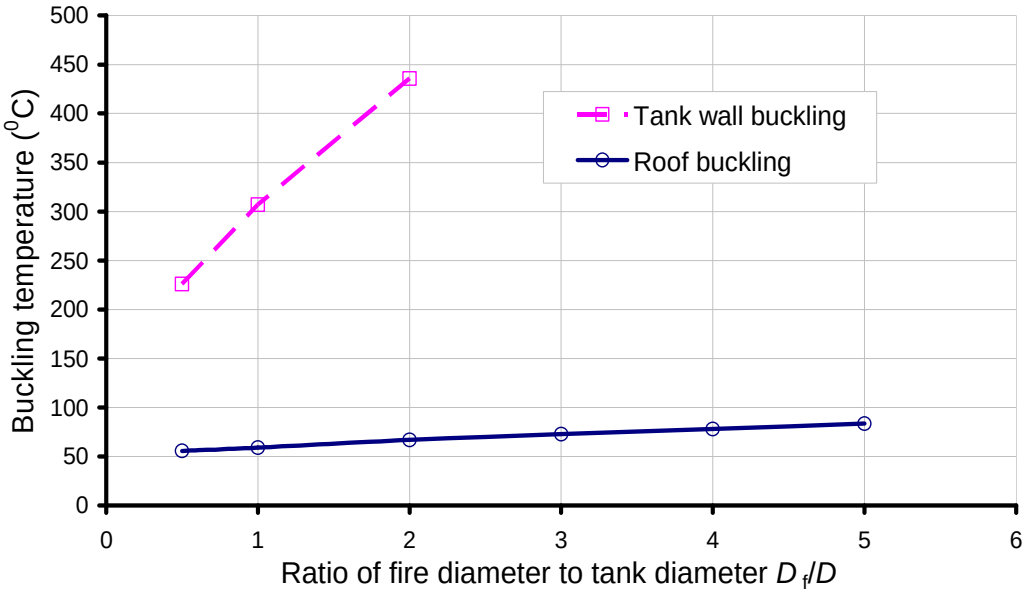

Figure 9-25 Buckling temperature of an empty tank under an adjacent fire with various fire diameters (t_f=t_c): comparison of roof and wall buckling; D=20m, d=6.67m, H_f=20m, H_{f0}=0m

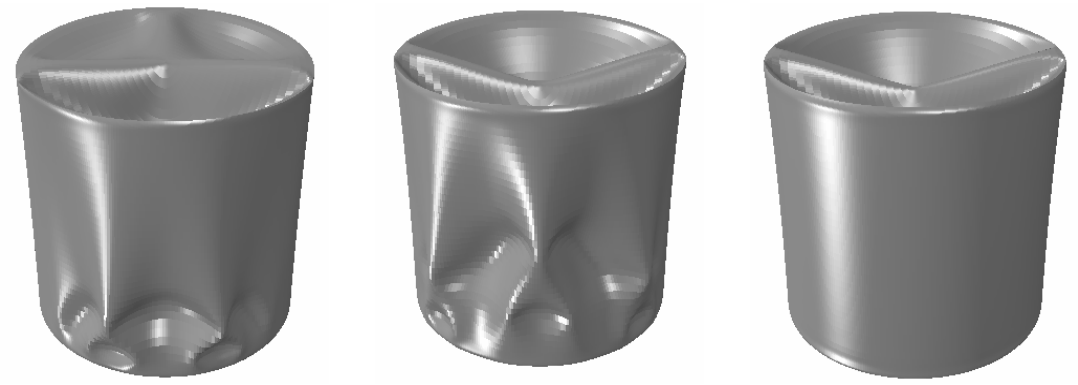

(a) D_f/D=0.5 (b) D_f/D=2.5 (c) D_f/D=5

Figure 9-26 Steady state deformations of an empty tank under fire with various diameters (t_f=t_c); deformation scale factor =5; D=20m, d=6.67m, H_f=20m, H_{f0}=0m

9.6 Effect of filling level in target tank

The liquid inside of the tank can cool the tank wall significantly and the degree of this cooling effect depends on the liquid properties. The results below are based on a type of liquid with a heat transfer coefficient of 320W/m^{2}K.

Figure 9-27 shows that for a stiff-roof tank (t_f=2t_c), the buckling temperature rose with the increase of the liquid level and no buckling occurred when the liquid level exceeded 0.6 times of tank's height. The buckling always occurred in the tank wall above the liquid level on the heated face (Figure 9-28).

The predicted results using the proposed algebraic temperature model match well with that using heat transfer analysis prediction. This validates the applicability of using of a linear function and a 0.2m transition zone to represent the temperature change above the liquid level in the proposed temperature expression.

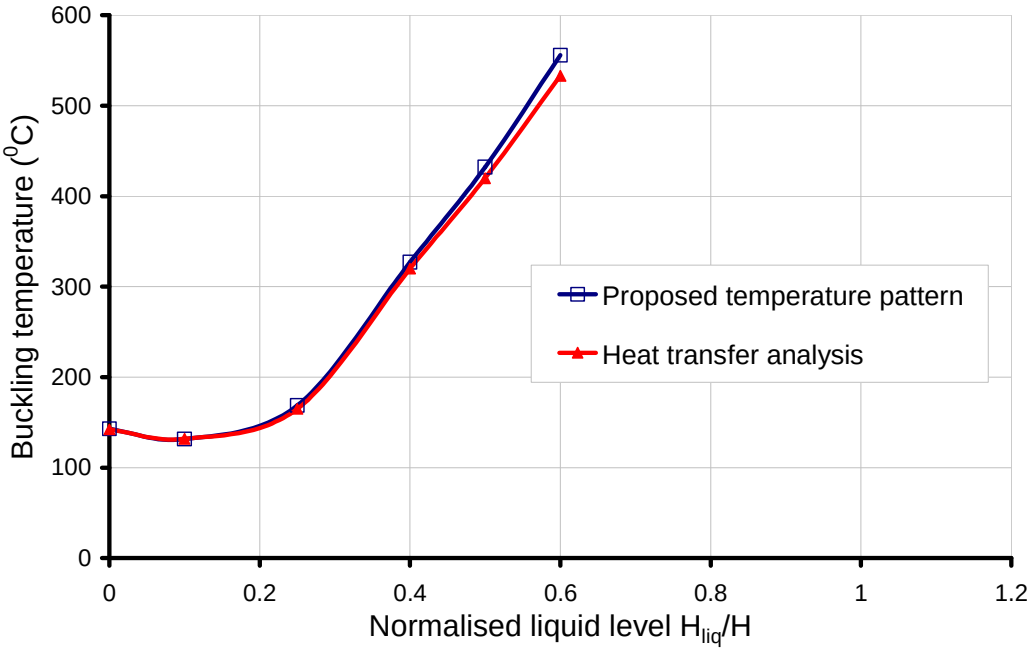

Figure 9-27 Buckling temperature of a tank filled with various levels of liquid (t_f=2t_c); D=D_f=20m, d=6.67m, H_f=20m, H_{f0}=0m

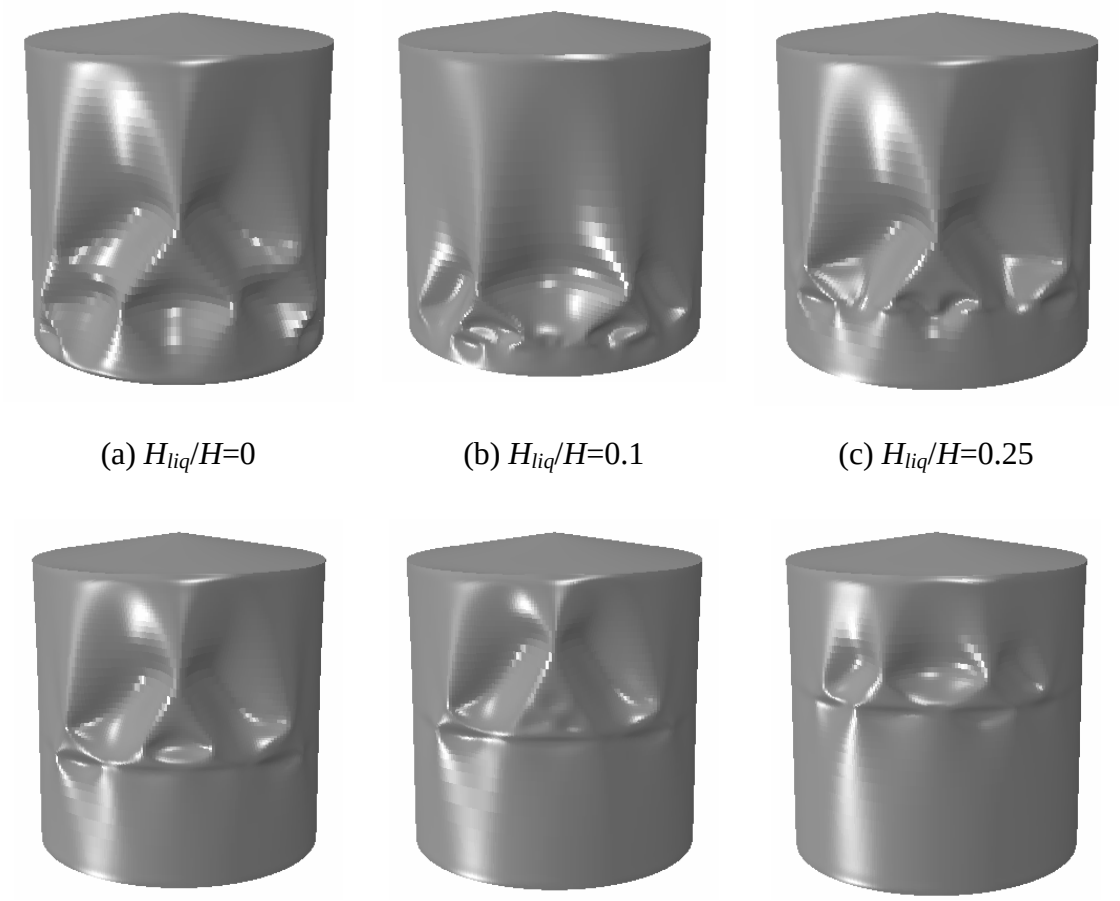

(a) H_{liq}/H=0 (b) H_{liq}/H=0.1 (c) H_{liq}/H=0.25

(d) H_{liq}/H=0.4 (e) H_{liq}/H=0.5 (f) H_{liq}/H=0.6

Figure 9-28 Steady state deformations of a tank filled with various levels of liquid (flame height=20m; t_f=2t_c); deformation scale factor =5; D=D_f=20m, d=6.67m, H_f=20m, H_{f0}=0m

For tanks with a slender roof (t_f=t_c), the buckling temperature shows the same trend as that in the stiff-roof case (t_f=2t_c), as shown in Figure 9-29. When the liquid level was lower than 0.4 times of the tank height, both the roof and the tank wall buckled, otherwise, only roof buckling mode was predicted. The deformation shapes of the tank wall in slender roof tanks (Figure 9-30) are similar to that in stiff roof tanks (Figure 9-28). In addition, the roof deformation pattern did not show much sensitivity to the liquid level.

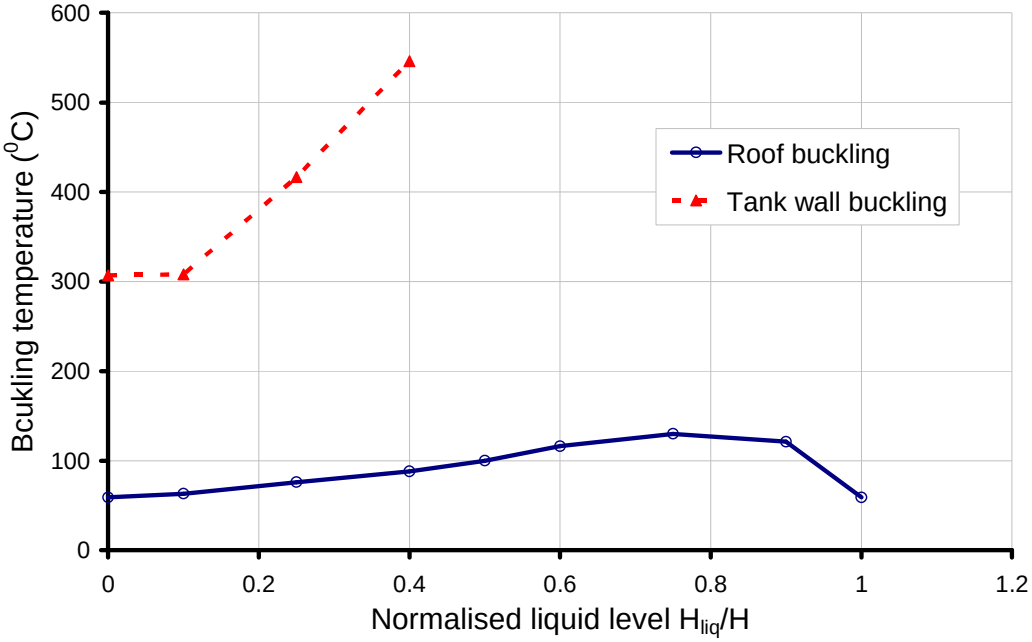

Figure 9-29 Buckling temperature of a tank filled with various levels of liquid (t_f=t_c); D=D_f=20m, d=6.67m, H_f=20m, H_{f0}=0m

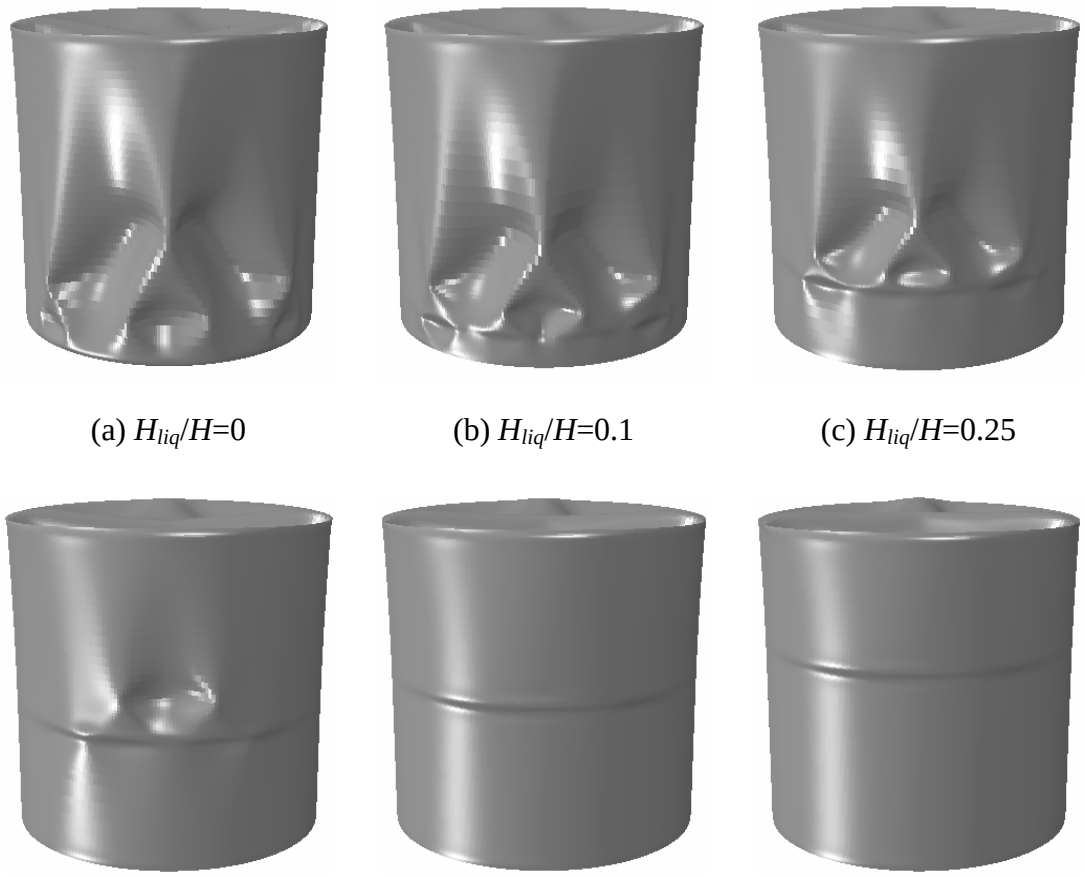

(a) H_{liq}/H=0 (b) H_{liq}/H=0.1 (c) H_{liq}/H=0.25

(d) H_{liq}/H=0.4 (e) H_{liq}/H=0.5 (f) H_{liq}/H=0.6

Figure 9-30 Steady state deformations of a tank filled with various levels of liquid (t_f=t_c); deformation scale factor =5; D=D_f=20m, d=6.67m, H_f=20m, H_{f0}=0m

9.7 Conclusions

A parametric study was conducted in this chapter to investigate the tank behaviour under various thermal and geometrical parameters. The following conclusions were obtained.

1) Geometrically non-linear elastic analysis (GNA) gives the lower bound of predicted buckling temperature of tanks compared with geometrically and materially

nonlinear analysis (GMNA). Tanks wouldn't have buckling failure if they are constructed with material of low yield stress.

2) The positions of the buckles in the tank designed with stepped wall thickness might be in the upper part of the tank where the wall thickness is thinner. By contrast, buckling usually starts near the bottom boundary and then spreads upward in tanks with uniform wall thickness. Buckling may occur earlier in the tank with a stepped wall design than that with a uniform wall thickness.

3) Three variables identified in heat transfer analysis most affecting the temperature distribution in the tank were examined. Their effects on the structural behaviour of the tank were investigated. It was found that the tank tends to buckle earlier under a fire with low flame height rather than high flame height, due to the heated roof being less able to restrain the expansion of the heated wall. The assumption of omitting the inner surface radiation in the analysis was found to have no effect on the prediction of buckling temperature for tanks constructed with low values of surface emissivity, but will underestimate the buckling temperature for tanks with high emissivity material, although the influence is not very pronounced. Whether including the inner surface radiation in the analysis does not make much difference on the predicted buckling modes. Liquid with larger heat transfer coefficient cools the tank surface better so the tank has better ability to resist buckling.

4) Buckling behaviour of tanks under various fire scenarios was examined. The results showed that buckling temperature increases significantly with rise of vertical fire location, which indicates the fire starting from ground can be seen as the worst situation for the tank. Horizontal fire locations were shown not sensitive to the buckling temperature. Tanks exposed to a fire with a diameter larger than its own was shown to have a higher buckling temperature. The liquid level is the most influential parameter on preventing buckling of the oil tank. Liquid inside of the tank on the one hand cools the tank wall and on the other hand stables the structure, thus high level of liquid in the tank is the best way to prevent buckling failure under such circumstances. Deformations of the tank were found to further develop from near the boundary or liquid level to covering the most heated face above the liquid level.

5) Tank wall tends to buckle much earlier in a stiff roof tank than in a slender roof tank. In a slender roof tank, roof buckling occurs at very early stage of heating.

6) The effect of the proposed temperature model in Chapter 6 on the prediction of buckling behaviour was examined under various fire scenarios. The proposed model was shown to be able to provide rather accurate predictions for fires rising near the ground level but underestimate the buckling temperature for fires starting from higher level. The proposed expression can also provide accurate predictions for partially filled tank with various liquid levels and under fires with various diameters. The proposed model is less accurate if the tank-fire distance is large, but the discrepancy is acceptable.

It is vital that appropriate failure criteria are precisely defined for oil tanks for specific industrial considerations. If the criteria are not well defined, it is difficult to assess whether a tank would fail eventually under certain hazardous loading, such as thermal loading from an adjacent fire.

As shown by the results of this chapter, a slender-roof tank buckles in the roof after a very low temperature rise. However, this local buckling of the roof does not affect the integrity of the tank, and only when the wall buckles is the integrity seriously at risk. The wall buckles at a much higher temperature. Even after the tank wall has begun to buckle, it still cannot be said that the tank completely loses all strength. However, large deformations progressively develop in the tank wall after buckling, and before long the severe deformations are likely to induce a local rupture. Even a small rupture of the steel wall would result in the loss of the stored contents, causing a much greater fire than that which caused the tank itself to be heated. It is therefore good design practice to ensure that wall buckling does not occur. This is a safer criterion than one that limits the extent of yielding or the absorption of strain energy.

Local yielding of the steel near the boundary may also result in a catastrophic consequence. The bottom boundary edge of the tank facing the fire first begins to yield and then the stresses are redistributed. With the temperature continuing to rise, the yielded area expands and will eventually lead to a large local rotation with high

local strains, which can very possibly lead to overall large deformations of the tank and local rupture. An appropriate criterion in terms of strain energy absorption, or maximum plastic strain must be developed before this concept can be transformed into a reliable design calculation.

More research is required on this problem in order to define the failure criteria for the oil tank under such non-uniform heating. Acceptable failure criteria such as the maximum acceptable strains, deformations, buckle areas and residual stresses, should be developed. There is a significant challenge in defining appropriate criteria to predict when rupture of the tank may be expected to occur, and this should be given priority in future research on the problem.

Chapter 10

10. Conclusions and future work

10.1 Introduction

Fire is one of the main hazards associated with storage tanks containing flammable liquids. These tanks are usually closely spaced and in large groups, so where a petroleum fire occurs, adjacent tanks are susceptible to damage leading to further development of the fire. The structural behaviour such as thermal stability and failure modes of the tanks under such fire scenario are very important to the safety design and assessment of oil depots. However, no previous studies on this problem are known to the best knowledge of the author.

This thesis has presented a systematic exploration of the potential thermal and structural behaviours of an oil tank when one of its neighbour tanks is on fire. Analytical and numerical simulations were carried out to reveal stresses and deformations induced in the tank. The thermal patterns developed in oil tanks and the underlying mechanism responsible for the buckling of tank structure was explored.

The influences of various thermal and geometrical parameters on the buckling temperature of the tanks were investigated.

The following summaries the work done and conclusions achieved in this thesis as well as outlook of further work on this topic.

10.2 Conclusions

10.2.1 Background knowledge and literature review

The background knowledge of the research was first provided in this thesis.

A recent review of storage tank failures occurred in refineries and chemical plants have showed that fire and explosion are the two major causes of such accidents. The recent fire at the Buncefield Oil Storage Depot near London in 2005 has once again drawn a great attention to the fire safety issue of storage tanks.

Pool-fire is the most common type of fires occurring in oil tanks. Knowledge on pool fire and its theoretical models was then reviewed. Emphasis was put on the solid flame model which was later chosen to describe the adjacent tank fire in the numerical simulations. The key parameters which affect the predictions by solid flame models include flame shape, average surface emissive power and the view factor calculation method. Assumptions and correlations widely used to determine these factors were reviewed.

Most of the storage tanks are thin steel shell structures. It is well known that thin shells are susceptible to buckling failure. Fundamental knowledge on shell buckling and previous research on thermal buckling was briefly reviewed. Codes and standards relevant to tank design are summarised at the end of Chapter 2.

Previous thermal buckling research involves temperature distribution patterns that is very simple in form (e.g., linear variation, axisymmetric) and is usually based on significant assumptions. To the best knowledge of the author, there has been no

specific research concerned with the thermal buckling under fire loading, where large temperature gradients occur both around the circumference and along the meridian of the cylindrical shell and the conical roof. Furthermore, the structural geometries considered in these studies are usually a simple cylindrical shell without any connected boundary structures (e.g., the end plate and stiffeners). As for an oil tank, the roof offers only a semi-rigid restraint to the thermal expansion of cylindrical wall, thus the thermal buckling behaviour of a roofed tank under fire heating was still to be revealed.

10.2.2 Analytical solution for a cylindrical tank under axisymmetric thermal loading

This research began in Chapter 3 with deriving analytical solutions for stresses and deformations in a partially filled roofless cylindrical tank under axisymmetrical heating involving thermal discontinuity at the liquid level. When a partially filled tank is heated by an adjacent tank fire, a large temperature gradient occurs in the wall at the liquid surface level due to the large thermal inertia of the stored fluid. An evaluation of these stresses is necessary for the prediction and control of the structural failure in such a situation.

The material properties of the steel are temperature dependent, especially the elastic modulus of steel reduces rapidly with an increase of temperature. Therefore, previous studies of the cylindrical shell problem adopting a constant elastic modulus (Fluegge 1973) are not valid for the current scenario and may be un-conservative. The analytical solutions were derived by conducting linear elastic analysis (LA) based on the classical theory of shells. The solution was validated by comparing its results with the finite element (FE) predictions.

The results of a partially filled tank and an empty tank exposed to fire were analysed as two illustrative examples. The former represents the situation where an abrupt temperature discontinuity occurs in the tank wall at the liquid level, while the latter represents the scenario where the temperature rise is uniform along the whole tank height. The results have demonstrated that large compressive circumferential

membrane stresses occur near the boundary for an empty tank and near the liquid level for a partially-filled tank when it is subjected to fire loading.

A parametric study was performed using the analytical solution to investigate the effects of radius to thickness ratio and temperature gradient on the stress and deflection in the tank wall. These parameters were both shown to have significant effects on the deflections and stresses in the tank walls. The maximum radial displacements developed in the empty tank and half-filled tank are very similar, while the maximum value of the circumferential stress developed in the empty tank can be significantly larger than that in the half-filled tank.

10.2.3 A cylindrical tank under axisymmetric thermal loading with a transition zone near the liquid level

The thermal loading on the tank assumed in Chapter 3 contains an abrupt change of temperature at the oil surface level, which is a simplification of the real situation. A transition zone in which the temperature increases linearly from a low value at the lower segment of the tank wall which is in contact with the stored liquid to a high temperature of the upper segment is obviously more realistic to represent the temperature distribution in a partially-filled tank. An analytical solution for the improved representation of temperature distribution on the partly-filled tank was therefore derived in Chapter 4. The solution for the stresses and displacements has also been numerically validated by the finite element predictions. The results have shown that rather than adopting precisely the temperature dependent elastic modulus for the transition zone, using a constant average value in the transition zone appears to give satisfactory prediction of the stress and displacement with minimal errors. The introduction of the temperature transition zone has led to a reduction of local bending and circumferential membrane stresses at the liquid surface level presented in Chapter 3. The local bending is sensitive to the size of the transition zone: a larger transition zone leads to less local bending effect.

10.2.4 Heat transfer modelling of a non-uniformly heated tank

In order to evaluate the structural response to an adjacent tank fire heating, the temperature distribution of the tank must be established. The assessment of fire hazard associated with pool fires involves primarily steady-state thermal radiation. Detailed techniques for modelling tank pool fires were presented and an upright cylinder was chosen to represent the shape of tank fire in Chapter 5. Wind effect was neglected in this analysis.

The temperature distribution in the tank was obtained by conducting a heat transfer analysis in Abaqus. All three heat transfer mechanisms which are radiation, convection and conduction were taken into account. The model in Abaqus was validated against analytical solution for a 2D scenario.

Parameters and assumptions used in the adopted pool fire model were carefully examined. Among those studied variables, the value of heat transfer coefficient of the liquid was found to have a significant effect on the predicted temperature. A large value results in lower temperature in the tank wall. The assumption of neglecting radiation at the inner surface of the tank is acceptable only when emissivity of that surface is small.

A detailed study of temperature pattern induced in the tank began with a study of a typical tank under a typical fire scenario which is taken as the reference case, where an empty tank exposed to an adjacent tank fire of the same dimension and starting from the ground. Results have shown that the predicted temperature in the target tank has large spatial gradients around the circumference. Only about half of the tank is heated and the temperature pattern around the circumference has a cosine-like distribution. The temperature along the vertical coordinate is not uniform either.

Effects of various fire scenarios and tank conditions on the temperature distribution in the tank were studied afterwards. The difference between a partially filled tank and an empty tank was found only lying along the vertical coordinate. The temperature of the tank wall elevates suddenly within a very short distance from a

low value below the liquid level to a high value above the liquid level. The length of such a transition zone is almost independent of the liquid level. The temperature of the tank wall in contact with liquid follows the same pattern predicted in a fully filled tank while the empty part of wall follows the same pattern predicted in a fully filled tank or an empty tank respectively.

It is discovered that the vertical fire location mainly influences the temperature pattern in the vertical direction of the target tank wall. However, the pattern of temperature around the circumference was also found to vary significantly at different heights of the tank when the fire starts from a high level above ground. The horizontal distance between the tank and fire significantly influences the maximum temperature induced in the tank. It does not change the temperature distribution pattern around the circumference and only slightly changes the vertical temperature distribution. The fire diameter mainly influences the size of heating range around the circumference, but not much of the temperature pattern along the vertical direction. The maximum temperature induced in the tank wall increases with the fire diameter when the tank-fire separation is fixed. However, the trend is in the opposite when the fire is placed at the minimum allowed distance according to the code NFPA 30.

10.2.5 Simple temperature distribution models for heated tanks

It is useful to devise a simple analytical model of the temperature distribution induced in a tank when it is exposed to an adjacent tank fire. By using a simple algebraic expression, one will be able to conduct structural analysis directly and don't have to run a heat transfer analysis beforehand to seek the temperature pattern. Two temperature distribution models have been proposed for the target tanks in Chapter 6: a rigorous model based on a semi-analytical solution and a simple model simplified from it. Both are in the form of the maximum temperature multiplied by two functions, one representing the circumferential temperature distribution and another representing the vertical temperature distribution. The heating range is assumed to be constant along the vertical direction in the proposed models. All variables in the proposed models possess practical meanings such as the diameter of

the fire, location of fire and liquid level inside of the target tank. The proposed models have been shown to be able to accurately describe the numerically predicted temperature rise in the tank under various kinds of fire scenarios.

In the simplified model the temperature distribution around the circumference remains the same as that in the rigorous model while the temperature rise along the vertical coordinate is further simplified. This model can also largely capture the most silent features of the temperature rise pattern. It has an advantage of simplicity and could provide a conservative structural analysis result. This second model can be used for preliminary structural analyses.

10.2.6 Buckling behaviour of a tank under a simplified temperature distribution

As the structural failure mode of the tank exposing to fire radiation is still unknown, numerical simulations have been conducted in Chapter 7 by using the second temperature distribution model.

Different analysis procedures were adopted. The linear bifurcation analysis (LBA) was conducted first to estimate the buckling temperature. However, this method would not produce accurate predictions as the nonlinear prebuckling deformation has a significant effect under thermal loading. Geometrically non-linear analysis (GNA) and geometrically and materially non-linear analysis (GMNA) were conducted afterwards. By contrast, GNA is shown to predict a lower bound of buckling temperature for the current problem. The arc-length method (Riks subroutine) was employed to trace the buckling failure.

It is found that oil tanks can easily buckle under rather moderate temperature rises. The causes of such buckling failures are the reduced modulus of steel at elevated temperatures, coupled with thermally-induced stresses due to the restraint of thermal expansion. Since the temperatures reached in such structures can be several hundred Centigrade degrees, any restraint to thermal expansion can lead to the development of compressive stresses. The high susceptibility of thin shell structures to buckling

under low compressive stresses means that this type of failure can be easily provoked. This buckling results in large post-buckling deformations which can easily lead to local rupture and ignition of the contents.

The significance of the liquid surface level, the size of the heated zone and fire condition for the buckling temperature rise were all explored. It was found that buckling always occurs on the hot side of the tank. The extent of the heated zone around the tank circumference has a significant effect on the buckling temperature rise. A narrower band of heating results in buckling at a lower temperature, with the buckling mode occurring over a narrower zone. The presence of liquid in the tank can significantly increase the buckling temperature and this increase is steadily enhanced as the liquid surface level is increased.

An investigation on the effects of tank geometry and roof condition was also conducted. In a partially filled tank, the buckling temperature rise is sensitive to the condition of whether the roof is heated; while this is not the case for an empty tank. The buckling temperature decreases with an increase in the radius to thickness ratio of the tank wall. The stiffness of the roof significantly affects the stress state in the cylindrical wall. For realistically flexible roofs, buckling occurs either near the base or the fluid surface level. However, if the roof is very stiff, the analysis predicts that the maximum compressive stress occurs near the roof where buckling occurs. The slope of the roof is shown to influence the buckling temperature only when the roof is flexible. The tank tends to buckle under a higher temperature with a steeper slope. In general, with practical roof structures, buckling is expected to begin in the roof, developing large deformations that are not visible from the ground, and stabilise before buckling of the tank wall ensues.

10.2.7 Realistic post-buckling analysis of tanks

Although the arc-length method adopted in the above analysis can accurately predict the buckling temperature, the temperature loading has to reduce once the structure passes the buckling point which is often much lower than the temperature could practically be reached under a fire radiation scenario. In practice, the temperature

does not reduce in the event of buckling. It is of interest to investigate the post-buckling behaviour in this case. Another nonlinear static analysis method incorporating an “artificial damping” (the artificial damping method or ADM) was adopted to simulate the post-buckling behaviour in Chapter 8.

The numerical mechanism of this procedure was introduced and two important input parameters which affect the accuracy of the results were discussed. Predictions of the first buckling temperature by the Riks method and the ADM were found to be identical. After the first buckling point, successive buckling events (as what happens in a tank with a slender roof where roof buckled first and followed by a cylindrical wall buckling at a higher temperature) can be successfully captured by using the ADM.

10.2.8 Buckling behaviour of tank structures under various thermal and geometrical parameters

Due to the advantages of the ADM, it was adopted to examine the tank behaviour with various thermal and geometrical parameters. The main conclusions drawn are as follows.

The buckling temperature increases significantly with an increase of the vertical fire location, which indicates that the fire starting from ground is the worst situation for tanks. The horizontal fire location was shown to be not sensitive to the buckling temperature. Tanks exposed to a fire with a diameter larger than its own is shown to have a higher buckling temperature.

Tanks with liquid inside are not prone to buckling failure, due to two effects: the liquid cools the hot steel surface and its pressure provides stabilization. The buckling initially occurs near the boundary for an empty tank or around the liquid level for a partially filled tank, and then develops further to the heated area without in contact of liquid.

The stiffness of the roof relative to the tank wall affects the location of buckling and also the buckling temperature. Cylindrical tank wall buckling occurs earlier in the

tank with a relatively stiff roof. For a slender roof, roof buckling occurs at a very early stage of heating and followed by cylindrical wall buckling; by contrast, the roof remains its stability in a stiff roof tank.

The position of buckling in the tank wall also depends on the wall thickness profile. In a stepped wall thickness design, buckling of the tank wall is likely to occur in the upper part of the tank where the wall thickness is very thin. By contrast, with uniform wall thickness, buckling usually starts near the bottom boundary and then propagates upward. Buckling may occur earlier in the tank with a stepped wall design than one with a uniform wall thickness.

The proposed rigorous temperature model was examined under various fire scenarios. It was shown to be able to provide rather accurate predictions for fire rising near the ground level. However, it may underestimate the buckling temperature when fire starts from a higher level. The proposed model can also provide accurate predictions for cases with various liquid levels and fire diameters. The proposed model is less accurate if the tank-fire distance is large, but the discrepancy is acceptable.

10.2.9 Summary

In summary, this thesis provides a systematic exploration of the thermal and structural behaviour of an oil tank exposed to an adjacent fire. It has shown that an oil tank may suffer thermal buckling under partial heating, and it is shown that the buckling temperature rise could be rather low (e.g. less than 130°C when the tank is empty).

In a thermal buckling scenario, buckling initially occurs either on the roof or near the bottom boundary of the tank wall, depending on the relative stiffness of the roof and the wall. A slender-roof tank tends to experience roof buckling at a rather small temperature rise, followed by a major buckle in the tank wall when the temperature rises much higher. This postponed buckling in the tank wall effectively guarantees that the main body of the tank could stand a longer heating, which could also

improve the endurance time for fire fighting. Thus, a slender roof design is beneficial, as also is probably a weak roof to wall joint.

It has also been shown that the amount of liquid stored in the tank can affect the thermal resistance. A fuller tank can resist buckling much longer than a partially filled tank, which suggests that it might be better to have a tank fully filled rather than to leave them partially filled. A corollary of this final statement is that tanks would resist buckling failures in fires much better if water were used beneath the contained oil to ensure that the tank is always full. This would be a significant safety measure, and would enhance the survivability of oil tank farms in major conflagrations.

10.3 Future research

In order to further explore this topic and bring it towards industrial tank safety assessment and design stage, there are some important issues worthy of study in the future.

It is vital that appropriate failure criteria are precisely defined for oil tanks for specific industrial considerations, such as the maximum allowed strain, deformation, buckle area and residual stress, etc.

An accurate prescription of loading and boundary conditions is vital to a structural analysis. For predicting the oil tank behaviour under fire radiation loading, this issue is particularly true and crucial. As the radiation loading exerted by fire is subjected to numerous factors, most of which are dealt in current literature and in this study with significant assumptions and idealisations. As a result, any effort that can improve the determination of these factors is worthwhile. Related aspects at least include the following:

The adopted fire model in this thesis is a one zone solid flame model. Other solid flame models such as two-zone model which may produce a more non-uniform vertical temperature distribution can be further examined.

The study mainly tackles the target problem within a quasi-static regime. The time-dependent temperature variation from fire needs to be considered in future research, and the transient response analysis for the oil tanks needs to be conducted accordingly.

Another issue is related to fire under wind condition. When wind is present, the flame is tilt and the objects at downwind direction may suffer intensive radiation. This effect needs to be more accurately investigated in the future.

The flammable liquid was assumed to be stable and remain at the ambient temperature in the heat transfer analysis in this thesis. This needs to be justified by conducting further heat transfer analysis with models inclusive of liquid.

The tank model used in this thesis is an idealised cylindrical tank without roof-wall rings. Furthermore, the detailed profile of roof structure was simplified and approximated by using a homogeneous and isotropic conical shell. A detailed tank design with possible rafters or columns would be helpful for accurate prediction of tank behaviour, particularly the buckling mode in the roof, in future studies.

A lack of experimental study is another limitation of this research. Currently, the study of large pool fires is still an immature and active research being undertaken in the field of fire dynamics. In addition, conducting large scale of tests is extremely costly even if possible. Once sufficient progress has been made in pool fire studies, an experimental study of thermal buckling behaviour of tank under fire condition may be undertaken accordingly, though appearing rather challenging from the current research state point of view.

11. References

1 Abir, D., and Nardo, S. V. (1959). "Thermal buckling of circular cylindrical shells under circumferential temperature gradients." *Journal of Aerospace Science*, 26(6): 803-808.

2 Anderson, M. S. (1962a). "Combinations of temperature and axial compression required for buckling of a ring-stiffened cylinder." National Aeronautics and Space Administration.

3 Anderson, M. S. (1962b). "Thermal buckling of cylinders." Collected Papers on Instability of Shell Structures-1962.

4 Anderson, M. S., and Card, M. F. (1962). "Buckling of ring-stiffened cylinders under a pure bending moment and a nonuniform temperature distribution." National Aeronautics and Space Administration

5 API 650 (2007). Welded steel tanks for oil storage. American Petroleum Institute

6 Arbocz, J. (1987). "Post-buckling behaviour of structures numerical techniques for more complicated structures." *Buckling and Post-buckling*: 83-142.

7 Ari Gur, J., Baruch, M., and Singer, J. (1979). "Buckling of cylindrical shells under combined axial preload, nonuniform heating and torque " *Experimental Mechanics*, 19: 406-410.

8 Atallah, S., and Allan, D. S. (1971). "Safe separation distances from liquid fuel fires." *Fire Technology*, 7(1): 47-56.

9 Babrauskas, V. (1983). "Estimating large pool fire burning rates." *Fire Technology*, 19(4): 251-261.

10 Babrauskas, V. (1986). "Free burning fires." *Fire Safety Journal*, 11(1-2): 33-51.

11 Baker, W. E., Cox, P. A., Westine, P. S., Kulesz, J. J., and Strehlow, R. A. (1982). "Explosion hazards and evaluation."

12 Bejan, A., and Kraus, A. D. (2003). Heat transfer handbook. Wiley-Interscience.

13 Belov, V. K. (1978). "Experimental study of shell stability under heating and loading." *Izv. Vyssh. Uchebn. Zaved. Aviats. Tekh. (USSR)*, 21(2): 5-8.

14 Beyler, C. L. (1995). "Fire hazard calculations for large, open hydrocabon fires (Third Edition)." *The SFPE Handbook of Fire Protection Engineering*, National Fire Protection Association, Quincy, Massachusetts**:** 3-268:3-313.

15 Beyler, C. L. (2004a). "Fire hazard calculations for large, open hydrocabon fires." *The SFPE Handbook of Fire Protection Engineering***:** 3-268:3-313.

16 Beyler, C. L. (2004b). "Industrial fire protection engineering." *Fire Technology*, 40(3): 297-298.

17 Bijlaard, P. P., and Gallagher, R. H. (1960). "Elastic instability of a cylindrical shell under arbitrary circumferential variation of axial stress." *J. Aerospace Sci*, 27(11): 854-858.

18 Board, B. M. I. I. (2010). "Buncefield investigation." http://www.buncefieldinvestigation.gov.uk/index.htm.

19 Brendel, B., and Ramm, E. (1980). "Linear and nonlinear stability analysis of cylindrical shells." *Computers & Structures*, 12(4): 549-558.

20 BS EN14015:2004 (2004). Specification for the design and manufacture of site built, vertical, cylindrical, flat-bottomed, above ground, welded, steel tanks for the storage of liquids at ambient temperature and above. British Standards Institute.

21 Burgess, D., and Hertzberg, M. (1974). "Radiation from pool flames." *Heat transfer in flames*. N. H. Afgan and J. M. Beers. New York, NY, John Wiley & Sons, Ch.27.

22 Bushnell, D. (1971a). "Analysis of ring-stiffened shells of revolution under combined thermal and mechanical loading." *AIAA Journal*, 9: 401-410.

23 Bushnell, D. (1971b). "Effect of ring out-of-plane bending stiffness on thermal buckling prediction for ring-stiffened cylinders." *AIAA Journal*, 9(8): 1653-1654.

24 Bushnell, D. (1973). "Nonsymmetric buckling of cylinders with axisymmetric thermal discontinuities." *AIAA Journal*, 11: 1292-1295.

25 Bushnell, D. (1981). "Buckling of shells-pitfall for designers." *AIAA Journal*, 19(9): 1183-1226.

26 Bushnell, D. (1985). Computerized buckling analysis of shells. Springer.

27 Bushnell, D., and Smith, S. (1971). "Stress and buckling of nonuniformly heated cylindrical and conical shells(Computer program for thermal stress and buckling analysis of nonuniformly heated segmented ring-stiffened cylindrical and conical shells)." *AIAA Journal*, 9: 2314-2321.

28 Chang, J. I., and Lin, C. C. (2006). "A study of storage tank accidents." *Journal of Loss Prevention in the Process Industries*, 19(1): 51-59.

29 Chang, L. K., and Card, M. F. (1970). "Thermal buckling of stiffened cylindrical shells." *AIAA/ASME 11th Structural Dynamics, and Materials Conference*, New York, 260-272.

30 Chang, L. K., and Card, M. F. (1971). "Thermal buckling analysis for stiffened orthotropic cylindrical Shells."

31 Chen, J. F., Rotter, J. M., and Teng, J. G. (2006). "A simple remedy for elephant's foot buckling in cylindrical silos and tanks." *Advances in Structural Engineering*, 9(3): 409-420.

32 Crowl, D. A., and Louvar, J. F. (2002). Chemical process safety. Prentice Hall PTR.

33 Davie, F. M., Nolan, P. F., and Hoban, T. W. S. (1994). "Case histories of incidents in heated bitumen storage tanks." *Journal of Loss Prevention in the Process Industries*, 7(3): 217-221.

34 DiNenno, P. J. (1995). The SFPE Handbook of Fire Protection Engineering. National Fire Protection Association Quincy, MA.

35 Ding, X., Coleman, R., and Rotter, J. M. (1996). "Surface profiling system for measurement of engineering structures." *Journal of Surveying Engineering*, 122: 3-13.

36 DNV (2007). PHAST professional user manual. DNV Software, Oslo.

37 Drysdale, D. (1999). An introduction to fire dynamics. Wiley Chichester et al.

38 EN1993 1-2 (2007). Eurocode 3: Design of steel structures, Part 1-2: General rules - Structural fire design. Brussels, CEN.

39 EN1993 1-6 (2007). Eurocode 3: Design of steel structures, Part 1-6: General rules - Strength and stability of shell structures. CEN.

40 EN1993 4-2 (2007). Eurocode 3- Design of steel structures, Part 4-2: Tanks. Brussels, CEN.

41 Engelhard, W. F. J. M. (2005). "Heat flux from fires." *Methods for the Calculation of Physical Effects due to Releases of Hazardous Materials (Liquids and Gases)*. R. A. P. M. W. C.J.H. van den Bosch. RAMP, Netherlands.

42 Eslami, M. R., and Javaheri, R. (1999). "Buckling of composite cylindrical shells under mechanical and thermal loads." *Journal of Thermal Stresses*, 22(6): 527-545.

43 Eslami, M. R., and Shahsiah, R. (2001). "Thermal buckling of imperfect cylindrical shells." *Journal of Thermal Stresses*, 24(1): 71-89.

44 Eslami, M. R., and Shariyat, M. (1997). "Elastic, plastic, and creep buckling of imperfect cylinders under mechanical and thermal loading." *Journal of Pressure Vessel Technology*, 119: 27-36.

45 Eslami, M. R., Ziaii, A. R., and Ghorbanpour, A. (1996). "Thermoelastic buckling of thin cylindrical shells based on improved stability equations." *Journal of Thermal Stresses*, 19(4): 299-315.

46 Fewtrell, P., and Hirst, I. L. (1998). "A review of high-cost chemical/petrochemical accidents since Flixborough 1974." *IchemE Loss Prevention Bulletin*, 140: 1-12.

47 Fluegge, S. (1973). Stresses in shells. Springer-Verlag, Berlin.

48 Frum, Y., and Baruch, M. (1976). "Buckling of cylindrical shells heated along two opposite generators combined with axial compression." *Experimental Mechanics*, 16(4): 133-139.

49 Gellatly, R. A., Bijlaard, P. P., and Gallagher, R. H. (1965). "Thermal stress and instability of sandwich cylinders on rigid supports." *J. Aircraft*, 2(1): 44-48.

50 Gould, P. L. (1999). "Analysis of plates and shells." Prentice Hall.

51 Greiner, R., and Guggenberger, W. (2004). "Tall cylindrical shells under wind pressure." *Buckling of Thin Metal Shells*: 198.

52 Heskestad, G. (1995). The SFPE Handbook of Fire Protection Engineering

53 Hill, D. W. (1959). "Buckling of a thin circular cylindrical shell heated along an axial strip." Stanford Univ., Calif.

54 Hoff, N. J. (1957a). "Buckling at high temperature." *Journal of the Royal Aeronautical Society*, 61(563): 756-774.

55 Hoff, N. J. (1957b). "Buckling of thin cylindrical shell under hoop stresses varying in axial direction " *American Society of Mechanical Engineers -- Transactions -- Journal of Applied Mechanics*, 24 (3): 405-412.

56 Hoff, N. J. (1965). "A non-linear model study of the thermal buckling of thin elastic shells." *J Appl Mech*, 32(1): 71-75.

57 Hoff, N. J., Chao, C. C., and Madsen, W. A. (1964). "Buckling of a thin-walled circular cylindrical shell heated along an axial strip." *Journal of Applied Mechanics*, 31: 253-258.

58 Hoff, N. J., and Ross, B. (1967). "A new solution of the buckling problem of thin circular cylindrical shells heated along an axial strip." *Resent Progress in Applied Mechanics*, The Folke Odqvist Volume: 251-271.

59 Holman, J. (1990). Heat Transfer. New York: McGraw-Hill, Inc.

60 Holst, J., Rotter, J. M., and Calladine, C. R. (1996). "Geometric imperfections and consistent residual stress fields in elastic cylinder buckling under axial compression." 199-216.

61 Holst, J., Rotter, J. M., and Calladine, C. R. (2000). "Imperfections and buckling in cylindrical shells with consistent residual stresses." *Journal of Constructional Steel Research*, 54(2): 265-282.

62 Howell, J. R., Daun, K., Erturk, H., and Sandia National Labs Albuquerque, N. M. (2001). "An annotated bibliography of thermal radiation validation data for fire applications." Sandia National Laboratories.

63 Hutchinson, J. W. (1974). "Plastic buckling." *Advances in applied mechanics*, 14: 67-144.

64 Hutchinson, J. W., and Koiter, W. T. (1970). "Postbuckling theory." *Appl. Mech. Rev*, 23(12): 1353–1366.

65 Incropera, F. P., DeWitt, D. P., Bergman, T. L., and Lavine, A. S. (1996). "Fundamentals of heat and mass transfer."

66 Islam, M. N., Kormi, K., and Al-Hassani, S. T. S. (1992). "Dynamic response of a thin-walled cylinder to side pressure pulse." *Engineering Structures*, 14(6): 395-412.

67 Johns, D. J. (1962). "Local circumferential buckling of thin circular cylindrical shells." Collected papers on instability of shell structures**:** 267-276.

68 Johns, D. J. (1965). Thermal stress analyses. Pergamon Press.

69 Johnson, A. D. (1992). "A model for predicting thermal radiation hazards from large-scale LNG pool fires." *Major Hazards Onshore and Offshore*, Machester, 507-524.

70 Johnson, D. (1987). "Surface to Surface Radiation in the Program TAU." Taking Account of Multiple Reflection, United Kingdom Atomic Energy Authority Report

71 Johnson, D. M. (2010). "The potential for vapour cloud explosions-lessons from the buncefield accident." *Jounal of Loss Prevention in the Process Industries*, 23(6): 921-927.

72 Johnson, T. F., and Card, M. F. (2009). "Stiffening and mechanical load effects on thermal buckling of stiffened cylindrical shells." *Journal of Spacecraft and Rockets*, 46(1): 203-209.

73 Keene, F. W., and Hetnarski, R. B. (1990). Bibliography on thermal stresses in shells. Hemisphere Publ. Corp.

74 Koiter, W. T. (1945). Over de stabiliteit van het elastisch evenwicht (PhD thesis (in Dutch) thesis). University of Delft

75 Lees, F. P. (1996). "Loss Prevention in process industries. ." London: Butterworths.

76 Lehr, W., and Simecek-Beatty, D. (2004). "Comparison of hypothetical LNG and fuel oil fires on water." *Journal of hazardous materials*, 107(1-2): 3-9.

77 Li, S. C., Du, Y. L., Zhang, X. K., and Yang, J. T. (2004). "Statistics and analysis of oil tank fires." *Fire science and technology*, 23(2): 117-121.

78 Lorenz, R. (1908). "Achsensymmetrische Verzerrungen in Duennwandigen Holhlzylindern." *VDI-Zeitschrift 52*, 52: 1706-1713.

79 Ma, S. (1989). "Thermal buckling of antisymmetric angle-ply composite circular cylindrical shells." 113-120.

80 Madding, R. P. (2002). "Temperature dependence of the graybody approximation to emissivity for some common materials." 37-43.

81 McGrattan, K. B., Baum, H. R., and Hamins, A. (2000). "Thermal radiation from large pool fires." NIST Technology Administration U.S. Department of Commerce.

82 Mercx, W. P. M., and van den Berg, A. C. (1997). "Methods for the Calculation of Physical Effects (The Yellow book)." *The Netherlands Organisation (TNO), The Netherlands*.

83 Moulin, D., Combescure, A., and Acker, D. (1989). "A review of thermal buckling analysis methods." *Nuclear engineering and design*, 116(3): 255-263.

84 Mudan, K. S. (1984). "Thermal radiation hazards from hydrocarbon pool fires." *Progress in Energy and Combustion Science*, 10: 59-80.

85 Mudan, K. S., and Croce, P. A. (1988). "Fire hazard calculations for large open hydrocarbon fires." *SFPE Handbook of Fire Protection Engineering*: 2-45.

86 NFPA-58 (2008). "Liquefied petroleum gas code." National fire protection association, Quincy, MA.

87 NFPA 30 (1996). "Flammable and Combustible Liquids Code." National fire protection association, Quincy, MA.

88 Panda, S. K., and Singh, B. N. (2011). "Large amplitude free vibration analysis of thermally post-buckled composite doubly curved panel using nonlinear FEM." *Finite Elements in Analysis and Design*, 47(4): 378-386.

89 Planas Cuchi, E., Vílchez, J. A., and Casal, J. (1999). "Fire and explosion hazards during filling/emptying of tanks." *Journal of Loss Prevention in the Process Industries*, 12(6): 479-483.

90 prEN 14015-1 (2000). Specification for the Design and Manufacture of Site Built. Vertical. Cylindrical. Flat-Bottomed. Above Ground. Welded. Metallic Tanks for the Storage of Liquids at Ambient Temperature and Above - Part 1: Steel Tanks.

91 Pritchard, M. J., and Binding, T. M. (1993). "FIRE 2: a new approach for predicting thermal radiation levels from hydrocarbon pool fires." *IChemE Symposium Series No.130*: 491-505.

92 Property-Risk-Consulting (2003). "The 100 largest losses 1972-2001 large property damage losses in the hydrocarbon-chemical industries." J. C. Coco.

93 Raj, P. K. (2005). "Exposure of a liquefied gas container to an external fire." *Journal of hazardous materials*, 122(1-2): 37-49.

94 Rew, P. J., and Hulbert, W. G. (1996). "Development of pool fire thermal radiation model." *HSE Contract Research Report*.

95 Rew, P. J., Hulbert, W. G., and Deaves, D. M. (1997). "Modelling of thermal radiation from external hydrocarbon pool fires." *Process safety and environmental protection*, 75(B 2): 81-89.

96 Robertson, A. (1928). "The strength of tubular struts." *Proceedings of the Royal Society of London. Series A, Containing Papers of a Mathematical and Physical Character*, 121(788): 558-585.

97 Ross, B. (1966). "An analog study of the thermal buckling behavior of thin cylindrical shells." *AIAA J*, 4(8): 1437-1439.

98 Ross, B., Hoff, N. J., and Horton, W. H. (1966). "The buckling behavior of uniformly heated thin circular cylindrical shells." *Experimental Mechanics*, 6(11): 529-537.

99 Ross, B., Mayers, J., and Jaworski, A. (1965). "Buckling of thin cylindrical shells heated along an axial strip." *Experimental Mechanics*, 5(8): 247-256.

100 Rotter, J. M. (1985). "Membrane theory of shells for bins and silos." *Design of Steel Bins for the Storage of Bul Solids, School of Mining and Civil Engineering, University of Sydney*: 135-147.

101 Rotter, J. M. (1987). "Bending theory of shells for bins and silos." *Transactions of Mechanical Engineering, Institution of Engineers, Australia, Vol. ME12*, 3: 147-159.

102 Rotter, J. M. (1988). "Calculated buckling strengths for the cylindrical wall of 10000 tonne silos at Port Kembla." Investigation report S663.

103 Rotter, J. M. (1996). "Elastic plastic buckling and collapse in internally pressurised axially compressed silo cylinders with measured axisymmetric imperfections: interactions between imperfections, residual stresses and collapse." 119–140.

104 Rotter, J. M. (1997). "Design standards and calculations for imperfect pressurised axially compressed cylinders." 354-360.

105 Rotter, J. M. (1998). "Shell structures: the new European standard and current research needs." *Thin-walled structures*, 31(1-3): 3-23.

106 Rotter, J. M. (2002). "Shell buckling and collapse analysis for structural design." *New approaches to structural mechanics, shells, and biological structures*. C. R. Calladine, H. R. Drew and S. Pellegrino, Kluwer Academic Pub**:** 355-378.

107 Rotter, J. M. (2004). "Buckling of cylindrical shells under axial compression." *Buckling of Thin Metal Shells*. J. G. Teng and J. M. Rotter. Spon, London**:** 42-87.

108 Ruiz, C., Salvatorelli-D'Angelo, F., and Thompson, V. K. (1989). "Elastic response of thin-wall cylindrical vessels to blast loading." *Computers & structures*, 32(5): 1061-1072.

109 Sengupta, A., Gupta, A. K., and Mishra, I. M. (2010). "Engineering layout of fuel tanks in a tank farm." *Journal of Loss Prevention in the Process Industries*.

110 SFPE (1999). Engineering guide for assessing flame radiation to external targets from pool fires. Bethesda, Maryland.

111 Shahsiah, R., and Eslami, M. R. (2003). "Thermal buckling of functionally graded cylindrical shell." *Journal of thermal stresses*, 26(3): 277-294.

112 Shell FRED 4.0 (April 2004). Fire, Release, Explosion, and Dispersion, Hazard Consequence Modelling Package, Technical Guide and User Guide.

113 Shokri, M., and Beyler, C. L. (1989). "Radiation from large pool fires." *Journal of Fire Protection Engineering*, 1(4): 141-149.

114 Siegel, R., and Howell, J. R. (2002). Thermal radiation heat transfer. Taylor & Francis Group.

115 Simitses, G. (1986). "Buckling and postbuckling of imperfect cylindrical shells- A review." *Applied Mechanics Reviews*, 39(10): 1517-1524.

116 Simitses, G. J., Shaw, D., Sheinman, I., and Giri, J. (1985). "Imperfection sensitivity of fiber-reinforced, composite, thin cylinders." *Composites Science and Technology*, 22(4): 259-276.

117 Simulia (2008). "Abaqus Analysis Users Manual: Version 6.8." Dassault Systèmes.

118 Song, C. Y., Teng, J. G., and Rotter, J. M. (2004). "Imperfection sensitivity of thin elastic cylindrical shells subject to partial axial compression." *International journal of solids and structures*, 41(24-25): 7155-7180.

119 Southwell, R. V. (1914). "On the general theory of elastic stability." *Philosophical Transactions of the Royal Society of London. Series A, Containing Papers of a Mathematical or Physical Character*, 213: 187-244.

120 Sparrow, E. M., and Cess, R. D. (1978). Radiation heat transfer. Hemisphere Publishing Corp., Washington D.C.

121 Sunakawa, M. (1962). "Deformation and buckling of cylindrical shells subjected to heating." University Tokyo. Re. Inst. .

122 Teng, J. G., and Lou, Y. F. (1997). "Post-collapse bifurcation analysis of shells of revolution by the accumulated arc-length method." *International journal for numerical methods in engineering*, 40(13): 2369-2383.

123 Teng, J. G., and Rotter, J. M. (1992). "Buckling of pressurized axisymmetrically imperfect cylinders under axial loads." *Journal of engineering mechanics*, 118: 229-247.

124 Teng, J. G., and Rotter, J. M. (2004). Buckling of thin shells. Taylor & Francis Group, London and New York.

125 Teng, J. G., and Song, C. Y. (2001). "Numerical models for nonlinear analysis of elastic shells with eigenmode-affine imperfections." *International journal of solids and structures*, 38(18): 3263-3280.

126 Thangaratnam, R. K., Palaninathan, R., and Ramachandran, J. (1990). "Thermal buckling of laminated composite shells." *AIAA Journal (American Institute of Aeronautics and Astronautics);(USA)*, 28.

127 Thomas, P. H. (1963). "The size of flames from natural fires." Elsevier, 844-859.

128 Thornton, E. A. (1993). "Thermal buckling of plates and shells." *Applied Mechanics Reviews*, 46(10): 485-506.

129 Timoshenko, S. (1910). "Einige stabilitatsprobleme der elastizitatstheorie." *Z. Math. Phys*, 58(4): 378-385.

130 Timoshenko, S., and Woinowsky-Krieger, S. (1959). Theory of plates and shells. McGraw-Hill New York.

131 Tvergaard, V. (1976). "Buckling behaviour of plate and shell structures." Amsterdam, North-Holland Publishing Co., 233-247.

132 TWG8.4 Shells (2008). Buckling of Steel Shells - European Design Recommendations 5th edition. ECCS

133 Walton, W. D. (1993). "In-situ burning of oil spills: Meso-scale experiments and analysis." *Proceedings of the 16th Arctic and Marine Oil Spill Program (AMOP) Technical Seminar*, Calgary, Alberta, 679-734.

134 Wilson, W. M., and Newmark, N. M. (1933). The strength of thin cylindrical shells as columns. Bulletin No. 255, University of Illinois

135 Wolfram, S. (1999). The mathematica book. Cambridge University Press, Cambridge, UK.

136 Yamaki, N., and Kodama, S. (1972). "Buckling of circular cylindrical shells under compression–report 3: solutions based on the Donnell type equations considering prebuckling edge rotations." *Report of the Institute of High Speed Mechanics*, 25: 99–141.

137 Zabetakis, M. G., and Burgess, D. S. (1961). Research on the hazards associated with the production and handling of liquid hydrogen. US Dept. of the Interior, Bureau of Mines.

138 Ziegler, F., and Rammerstorfer, F. G. (1989). "Thermoelastic stability." *Thermal Stresses III*. R. B. Hetnarski, Elsevier, Amsterdam**:** 107–191.

12. Appendix

Some examples of Abaqus input file for heat transfer and thermal buckling analyses that have been used in this study are included here. Note that only the key keyword lines are given while the node and element information have been omitted in order to save space.

12.1 Heat transfer analysis

```
*HEADING
HEAT TRANSFER AND VIEWFACTOR CALCULATION
*PREPRINT, ECHO=NO, HISTORY=NO, MODEL=NO, CONTACT=NO
*NODE, NSET=N-CYLINDER
    1, 0.100000000E+02, 0.000000000E+00, 0.000000000E+00
    2, 0.612303177E-15,-0.100000000E+02, 0.000000000E+00
.....Omitted
*NODE, NSET=N-HEATER
  4664, 0.366666667E+02, 0.000000000E+00, 0.000000000E+00
  4665, 0.266666667E+02,-0.100000000E+02, 0.000000000E+00
.....Omitted
*ELEMENT, TYPE=DS4, ELSET=E-CYLINDER-HIGH
     1,     1,     3,   193,   116
     2,     3,     4,   270,   193
.....Omitted
*ELEMENT, TYPE=DS4, ELSET=E-HEATER
  4537,  4664,  4666,  4856,  4779
  4538,  4666,  4667,  4933,  4856
.....Omitted
*ELSET,ELSET=E-CYLINDER
E-CYLINDER-HIGH
*ELSET,ELSET=EALL
E-HEATER
E-CYLINDER
*NSET,NSET=N-CYLINDER-BASE
  1692,
  1710,
.....Omitted
*ELSET,ELSET=E-0
```

```
      1,
      2,
```

.....Omitted

```
*SHELL SECTION,ELSET=EALL,MATERIAL=STEEL
 0.100000000E-01
*MATERIAL,NAME=STEEL
*CONDUCTIVITY
 0.458000000E+02
*DENSITY
 0.785000000E+04
*SPECIFIC HEAT
 0.460000000E+03
*SURFACE,NAME=SURF,PROPERTY=PROP1
E-HEATER,SNEG
E-CYLINDER,SNEG
*SURFACE,NAME=SURF-INNER-HIGH,PROPERTY=PROP1
E-CYLINDER-HIGH,SPOS
*SURFACE,NAME=SURF-OUTER-HIGH,PROPERTY=PROP1
E-CYLINDER-HIGH,SNEG
*CAVITY DEFINITION,NAME=CAV1,AMB= 0.200000000E+02
SURF
*SURFACE PROPERTY,NAME=PROP1
*EMISSIVITY
 0.100000000E+01
*PHYSICAL CONSTANTS,STEFANB= 0.566900000E-07,ABSOLUTE ZERO=-0.273150000E+03
*RESTART,WRITE,FREQ=5
*STEP,INC=20
RADIATION VIEWFACTOR CALCULATIONS
*HEAT TRANSFER,STEADY STATE
1.,1.
*RADIATION VIEWFACTOR,REFLECTION=NO,VTOL=.001,SYMMETRY=R-SYMMETRY
*RADIATION SYMMETRY,NAME=R-SYMMETRY
*REFLECTION,TYPE=PLANE
0,0,0,1,0,0
0,0,10
*BOUNDARY
N-HEATER,11,,915.
*SFILM
```

SURF-INNER-HIGH,F, 0.200000000E+02, 0.250000000E+02

SURF-OUTER-HIGH,F, 0.200000000E+02, 0.250000000E+02

*NODE PRINT

NT,COORD,

RFLE,

*NODE FILE

NT,

*OUTPUT,FIELD

*NODE OUTPUT

NT,COORD

*RADIATION FILE

RADFL,RADFLA,RADTL,RADTLA,VFTOT,FTEMP

*OUTPUT,FIELD

*RADIATION OUTPUT

RADFL,RADFLA,RADTL,RADTLA,VFTOT,FTEMP

*END STEP

12.2 Thermal buckling analysis (Riks)

*HEADING

AN OIL TANK EXPOSED TO AN ADJACENT FIRE

*PREPRINT, ECHO=NO, HISTORY=NO, MODEL=NO, CONTACT=NO

*NODE, NSET=N-CYLINDER
```
     1, 0.100000000E+02, 0.000000000E+00, 0.000000000E+00
     2, 0.612303177E-15, 0.100000000E+02, 0.000000000E+00
```

.....Omitted

*NODE, NSET=N-ROOF
```
17196, 0.994848457E+01, 0.173651444E+00, 0.200088163E+02
17197, 0.995000000E+01, 0.000000000E+00, 0.200088163E+02
```

.....Omitted

*ELEMENT, TYPE=S4R, ELSET=E-CYLINDER
```
     1,     1,     3,   241,   212
     2,     3,     4,   270,   241
```

.....Omitted

*ELEMENT, TYPE=S4R, ELSET=E-TOP
```
16921,  5946,  5947, 17196, 17197
16922, 17197, 17196, 17198, 17199
```

.....Omitted

*ELSET, ELSET=E-PRES

*NSET,NSET=N-BOT

```
      1,
      2,
```

.....Omitted

```
*NSET,NSET=N-TOP
  5916,
  5946,
```

.....Omitted

```
*NSET,NSET=N-SYM
      1,
    122,
```

.....Omitted

```
*MATERIAL, NAME=STEEL1
*DENSITY
 0.785000000E+04
*ELASTIC
 0.210000000E+12, 0.300000000E+00, 0.000000000E+00
 0.210000000E+12, 0.300000000E+00, 0.100000000E+03
 0.189000000E+12, 0.300000000E+00, 0.200000000E+03
 0.168000000E+12, 0.300000000E+00, 0.300000000E+03
 0.147000000E+12, 0.300000000E+00, 0.400000000E+03
 0.126000000E+12, 0.300000000E+00, 0.500000000E+03
 0.651000000E+11, 0.300000000E+00, 0.600000000E+03
 0.273000000E+11, 0.300000000E+00, 0.700000000E+03
 0.189000000E+11, 0.300000000E+00, 0.800000000E+03
 0.141750000E+11, 0.300000000E+00, 0.900000000E+03
 0.945000000E+10, 0.300000000E+00, 0.100000000E+04
 0.472500000E+10, 0.300000000E+00, 0.110000000E+04
*EXPANSION
 0.123000000E-04, 0.000000000E+00
 0.125000000E-04, 0.100000000E+03
 0.129000000E-04, 0.200000000E+03
 0.133000000E-04, 0.300000000E+03
 0.137000000E-04, 0.400000000E+03
 0.141000000E-04, 0.500000000E+03
 0.145000000E-04, 0.600000000E+03
 0.149000000E-04, 0.700000000E+03
 0.141000000E-04, 0.800000000E+03
 0.134000000E-04, 0.900000000E+03
 0.141000000E-04, 0.100000000E+04
```

0.146000000E-04, 0.110000000E+04
*MATERIAL, NAME=STEEL2
*DENSITY
0.392500000E+04
*ELASTIC
0.210000000E+12, 0.300000000E+00, 0.000000000E+00
0.210000000E+12, 0.300000000E+00, 0.100000000E+03
0.189000000E+12, 0.300000000E+00, 0.200000000E+03
0.168000000E+12, 0.300000000E+00, 0.300000000E+03
0.147000000E+12, 0.300000000E+00, 0.400000000E+03
0.126000000E+12, 0.300000000E+00, 0.500000000E+03
0.651000000E+11, 0.300000000E+00, 0.600000000E+03
0.273000000E+11, 0.300000000E+00, 0.700000000E+03
0.189000000E+11, 0.300000000E+00, 0.800000000E+03
0.141750000E+11, 0.300000000E+00, 0.900000000E+03
0.945000000E+10, 0.300000000E+00, 0.100000000E+04
0.472500000E+10, 0.300000000E+00, 0.110000000E+04
*EXPANSION
0.123000000E-04, 0.000000000E+00
0.125000000E-04, 0.100000000E+03
0.129000000E-04, 0.200000000E+03
0.133000000E-04, 0.300000000E+03
0.137000000E-04, 0.400000000E+03
0.141000000E-04, 0.500000000E+03
0.145000000E-04, 0.600000000E+03
0.149000000E-04, 0.700000000E+03
0.141000000E-04, 0.800000000E+03
0.134000000E-04, 0.900000000E+03
0.141000000E-04, 0.100000000E+04
0.146000000E-04, 0.110000000E+04
*SHELL SECTION, ELSET=E-CYLINDER, MATERIAL=STEEL1
0.100000000E-01
*SHELL SECTION, ELSET=E-TOP, MATERIAL=STEEL2
0.200000000E-01
*BOUNDARY
N-BOT, 1,3
*BOUNDARY

N-SYM, YSYMM

*TRANSFORM,NSET=N-CYLINDER,TYPE=C

0,0,0,0,0, 0.200000000E+02

*ORIENTATION,NAME=ORI-1,SYSTEM=CYLINDRICAL

0,0,0,0,0, 0.200000000E+02

1

*RESTART,WRITE,FREQUENCY=1

***

*STEP,NLGEOM=YES,INC=100000

*STATIC

1.0,1.0,1.0E-5,1.0

*DLOAD

E-CYLINDER,GRAV,9.8,0,0,-1.

E-TOP,GRAV,9.8,0,0,-1.

*OUTPUT, FIELD,FREQ=1

*NODE OUTPUT

CF, COORD, RF, U

*ELEMENT OUTPUT

HP, LE, P, PE, PEEQ, PEMAG, S, SF, STH

*OUTPUT,HISTORY,FREQ=1

U

*END STEP

*STEP,NLGEOM,INC=120

*STATIC,RIKS

0.001,1,1E-50,0.012,1

*MONITOR,NODE=NODE-CONTROL, DOF=1

*TEMPERATURE

```
     1, 0.150000000E+03
     2, 0.562372771E-30
```

.....Omitted

*OUTPUT, FIELD,FREQ=1

*NODE OUTPUT

CF, COORD, RF, U, NT

*ELEMENT OUTPUT

HP, LE, P, PE, PEEQ, PEMAG, S, SF, STH

*OUTPUT,HISTORY,FREQ=1

U

*END STEP

12.3 Thermal buckling analysis (ADM)

*STEP,NLGEOM,INC=3000

*STATIC, STABILIZE=0.00005

0.001,1,1E-5,0.001

*MONITOR,NODE=NODE-CONTROL, DOF=1

*TEMPERATURE,FILE=N.ODB,INTERPOLATE

*OUTPUT, FIELD, VARIABLE=PRESELECT,FREQUENCY=5

*NODE OUTPUT

CF, COORD, RF, U,NT

*ELEMENT OUTPUT

HP, LE, P, PE, PEEQ, PEMAG, S, SF, STH,E,EE,IE,THE,CE

*OUTPUT,HISTORY,VARIABLE=PRESELECT,FREQUENCY=1

*ENERGY PRINT,FREQUENCY=1

*END STEP